Dissertation

submitted to the

Combined Faculty for the Natural Sciences
and for Mathematics

of the

Ruperto-Carola University of Heidelberg,
Germany

for the degree of

Doctor of Natural Sciences

Put forward by
Dipl. Phys. Stefan Wagner, born in Memmingen

Date of oral examination: 02.07.2014

ENERGY NON-LINEARITY STUDIES AND PULSE SHAPE ANALYSIS OF LIQUID SCINTILLATOR SIGNALS IN THE DOUBLE CHOOZ EXPERIMENT

Referees:

Prof. Dr. Manfred Lindner
Prof. Dr. Werner Hofmann

For my family.

Abstract

The Double Chooz reactor neutrino experiment measures the neutrino mixing angle θ_{13} with a liquid scintillation detector. It uses the $\bar{\nu}_e$ flux as well as their energy spectrum in the analysis of θ_{13}, which requires a detailed knowledge of the energy scale. In particular the non-linear scintillator response caused by ionization quenching and Čerenkov light has to be accurately reproduced in the Monte Carlo. To this end the relevant properties of the liquid scintillators are investigated experimentally and theoretically.

For the data analysis the pulse shape of the scintillator emission is exploited for particle identification. A novel classifier is presented which characterizes the pulse shape in Fourier space. It allows to distinguish between the detector volumes as well as to reduce the stopping muon background. A more advanced version of this technique is then investigated for pulse shape discrimination between e^+ and e^- events. It has a high efficiency for $\bar{\nu}_e$ and can be used to reject remaining background in the Double Chooz analysis. The method thus increases the signal-to-background ratio, which may be a tremendous advantage for analyses with neutron captures on Hydrogen.

<p style="text-align:center">★   ★   ★</p>

Das Double Chooz Reaktorneutrinoexperiment misst den Mischungswinkel θ_{13} mit Hilfe eines Flüssigszintillationsdetektors. In der θ_{13}-Analyse werden sowohl der Fluss der $\bar{\nu}_e$ als auch deren Energieverteilung verwendet, was eine genaue Kenntnis der Energieskala erfordert. Insbesondere muss die durch Fluoreszenzlöschung und Čerenkov-Effekt nichtlineare Szintillatorantwort in der Simulation genau reproduziert werden. Zu diesem Zweck werden die Szintillatoreigenschaften experimentell und theoretisch untersucht.

In der Datenanalyse werden die Pulsformen der Szintillationssignale zur Teilchenidentifikation verwendet. Ein neuartiger Klassifikator wird vorgestellt, der die Pulsform im Fourier-Raum beschreibt. Er kann zwischen den Detektorvolumina unterscheiden, sowie den Beitrag von stoppenden Myonen reduzieren. Eine weiterentwickelte Version zur Unterscheidung von e^+ und e^- anhand ihrer Pulsformen wird untersucht. Sie kann verwendet werden um einen Teil des verbleibenden Untergrunds zu entfernen, während $\bar{\nu}_e$-Ereignisse kaum betroffen sind. So wird das Signal-zu-Untergrund-Verhältnis verbessert, was einen bedeutenden Vorteil für Analysen mit Neutroneneinfang auf Wasserstoff darstellt.

Contents

INTRODUCTION

Neutrinos are widely considered probes for physics beyond the Standard Model. One of their many curious properties is the ability to oscillate between flavors. These oscillations are described with help of the PMNS matrix, which contains three mixing angles for the different oscillation modes. The mixing angle θ_{13} has received particular attention due to its smallness and its importance for theory and experiment. Double Chooz is a reactor neutrino experiment dedicated to measuring θ_{13} and it observes the disappearance of electron antineutrinos emitted from two nuclear reactors. Currently, Double Chooz takes data with one detector only and has determined a value of $\sin^2(2\theta_{13}) = 0.109 \pm 0.030(\text{stat}) \pm 0.025(\text{syst})$[1] for the mixing angle. When the second detector takes data as well, many uncertainties related to the reactor and the detector efficiency will decrease. This thesis focuses on scintillator-related aspects of Double Chooz and is divided into three parts.

The first part begins with an overview over the basics of neutrino oscillations in Chapter 1, followed by a presentation of the Double Chooz experiment in Chapter 2. The detector concept and design are described as well as the data analysis and the past results. Chapter 3 starts with the microphysical processes of light creation and propagation in general organic liquid scintillators. Then it gives an overview over the development and the large-scale production of the Double Chooz liquid. Chapter 4 covers a more theoretical work to describe the effect of *ionization quenching* in liquid scintillators. A new model is developed, which aims to make more precise statements about the energy non-linearity induced by this phenomenon. In principle, the model also allows to deduce previously separate quantities from one single parameter.

The second part centers around the Monte Carlo simulation of the optical properties and the energy non-linearities introduced by ionization quenching and the Čerenkov effect. Chapter 5 presents the energy reconstruction scheme and how different detector-related effects are corrected in data and Monte Carlo respectively. Then, in order to refine the simulation of optical properties in the Monte Carlo, various scintillator properties are experimentally determined. The laboratory measurements are described in Chapter 6. Among the properties studied are the molar

extinction coefficients of the liquids, the reemission probability of the scintillators, and the quantum yields of the fluorescent substances. Then, in Chapter 7, the experimental results are incorporated into the Monte Carlo software and their effects on the non-linearity of the simulated detector response are studied.

The last part is about the analysis of Double Chooz data. It starts with a new unsupervised machine-learning approach in Chapter 8. An algorithm is developed which automatically groups detector data into *clusters* and can be used for a rejection of non-physics events. It is also useful for an optimization of the pulse shape-based classifier presented in Chapter 9. There, a classification variable is constructed from the Fourier power spectrum of the scintillation events. It can cleanly distinguish between events from the different scintillator volumes in Double Chooz and identify remaining non-physics events. Furthermore, it is shown that the variable can be used to reduce the stopping muon background in the experiment. It can also be optimized to perform different tasks. Finally, in Chapter 10, the scintillation pulse shapes are used to discriminate between different particles. An artificial neural network identifies non-linear patterns in the Fourier power spectrum and is used for a separation of positrons and electrons. The technique may be used to suppress a major part of the electron and gamma background, while maintaining a high efficiency for positron events. This would be a tremendous advantage for the Double Chooz data analysis, but may also be of interest for other liquid scintillator experiments.

PART I

NEUTRINO PHYSICS AND SCINTILLATORS

NEUTRINO PHYSICS

1.1 NEUTRINO OSCILLATIONS

Neutrino oscillations arise from the situation that mass and flavor states do not coincide. Both the flavor and the mass states form orthonormal bases in the Hilbert space and one can change between bases with help of a matrix $\boldsymbol{U}$, a rotation matrix which maps the flavor basis onto the mass basis.[1] In the most general case $\boldsymbol{U}$ can be complex and, as a rotation matrix, must be unitary. In this picture a neutrino flavor state can be written as a superposition of the mass states

$$|\nu_\alpha\rangle = \sum_k \boldsymbol{U}_{\alpha k} |\nu_k\rangle \tag{1.1}$$

where $\boldsymbol{U}_{\alpha k}$ are the elements of the matrix $\boldsymbol{U}$. It is called the *neutrino mixing matrix* or *PMNS matrix*.[2]

In the instant of a neutrino's creation it is encountered in a pure flavor state, as described by equation (1.1). In the radioactive β-decay, for example, the neutrino is initially in a pure electron neutrino flavor state. The oscillation phenomenon occurs when the neutrino travels through space and time. In natural units the time evolution of the initial flavor state is given by

$$|\nu_\alpha(t)\rangle = \sum_k e^{-iE_k t} \boldsymbol{U}_{\alpha k} |\nu_k\rangle \tag{1.2}$$

where t is the time elapsed since the creation and

$$E_k = \sqrt{\boldsymbol{p}^2 + m_k^2} \tag{1.3}$$

is the relativistic energy of the mass state $|\nu_k\rangle$. If all neutrino masses were exactly equal, E_k would also be equal for all mass eigenstates and they would evolve identically according to equation (1.2). There would be no oscillations in this

---

[1] If flavor and mass states were identical, $\boldsymbol{U}$ would be the unity matrix and the time evolution would not create any special effects. Neutrino oscillations would then not be possible.

[2] Named for Pontecorvo, Maki, Nakagawa and Sakata for their works on neutrino oscillations.

scenario. In the case of different neutrino masses, however, equations (1.2) and (1.3) do lead to different evolutions of the states. In consequence, the originally pure flavor state from equation (1.1) changes its composition with time and gains contributions from the other flavor states as well. At the moment of its detection the evolved flavor state $|\nu_\alpha(t)\rangle$ is collapsed onto a final flavor eigenstate $\langle\nu_\beta|$. Since the final state can also be described by a superposition of mass eigenstates, this projection yields

$$\langle\nu_\beta|\nu_\alpha(t)\rangle = \sum_j \langle\nu_j|\,U^\dagger_{j\beta} \cdot \sum_k e^{-iE_k t}\,U_{\alpha k}\,|\nu_k\rangle = \sum_n e^{-iE_n t}\,U^\dagger_{n\beta}U_{\alpha n} \tag{1.4}$$

where $U^\dagger$ is the conjugate transpose of U. For the second equality the orthonormality of the states $\langle\nu_a|\nu_b\rangle = \delta_{ab}$ was used.

Equation (1.4) gives the quantum-mechanical amplitude to encounter the neutrino, which was created with flavor α and energy E, with the flavor β after a time t. The probability $P_{\alpha\to\beta}$ to detect the neutrino with flavor β is the square of the absolute value of the amplitude:

$$
\begin{aligned}
P_{\alpha\to\beta} &= \left|\langle\nu_\beta|\nu(t)\rangle\right|^2 = \left|\sum_n e^{-iE_n t}U^\dagger_{n\beta}U_{\alpha n}\right|^2 \\
&= \sum_m\sum_n e^{-i(E_m-E_n)t}\,U^\star_{\beta n}U_{\alpha n}U_{\beta m}U^\star_{\alpha m}
\end{aligned}
\tag{1.5}
$$

where the property $|z|^2 = z\,z^\star$ was used. For each combination of m and n there is a complementary summand where m and n are swapped. Summing these pairs cancels the imaginary part.

$$
\begin{aligned}
P_{\alpha\to\beta} &= \sum_{m\leqslant n}\mathrm{Re}\left\{e^{-i(E_m-E_n)t}U^\star_{\beta n}U_{\alpha n}U_{\beta m}U^\star_{\alpha m}\right\} \\
&= \sum_{m\leqslant n}\cos\left[(E_m-E_n)t\right]\mathrm{Re}\left\{U^\star_{\beta n}U_{\alpha n}U_{\beta m}U^\star_{\alpha m}\right\} \\
&= \sum_{m\leqslant n}\left|U^\star_{\beta n}U_{\alpha n}U_{\beta m}U^\star_{\alpha m}\right|\cos\left[(E_m-E_n)t - \arg\left(U^\star_{\beta n}U_{\alpha n}U_{\beta m}U^\star_{\alpha m}\right)\right]
\end{aligned}
\tag{1.6}
$$

The probability $P_{\alpha\not\to\alpha}$ is called the *oscillation probability*, while $P_{\alpha\to\alpha} = 1 - P_{\alpha\not\to\alpha}$ is the *survival probability*.

For measurements of neutrino oscillations it is often more helpful to express these probabilities in terms of the length traveled by the neutrino instead of the time. Here we can use the fact that neutrinos are essentially always highly relativistic, thanks to their extremely small masses. Under this circumstance, equation (1.3) can be approximated as

$$E_k \approx p + \frac{m_k^2}{2p} \approx E + \frac{m_k^2}{2E} \tag{1.7}$$

	parameter	value
Mass differences		
	Δm_{12}^2	$\left(7.50^{+0.19}_{-0.20}\right) \cdot 10^{-5}$ eV^2
	Δm_{23}^2	$\left(2.32^{+0.12}_{-0.08}\right) \cdot 10^{-3}$ eV^2
	Δm_{13}^2	$\approx \Delta m_{23}^2$
Mixing angles		
	$\sin^2\left(2\theta_{12}\right)$	$0.857^{+0.023}_{-0.025}$
	$\sin^2\left(2\theta_{23}\right)$	> 0.95 (95 % CL)
	$\sin^2\left(2\theta_{13}\right)$	0.095 ± 0.010

Table 1.1: Neutrino oscillation parameters. The values cited here are taken from [2]. In the case of Δm_{13}^2 and Δm_{23}^2 the sign is still unknown and only the absolute value is given.

Furthermore, as neutrinos move at nearly the speed of light c, the elapsed time t since creation can be replaced by the length L travelled by the neutrino, so the oscillation probability (1.5) can be written as

$$P_{\alpha \to \beta} = \sum_{m \leqslant n} \left| U_{\beta n}^{\star} U_{\alpha n} U_{\beta m} U_{\alpha m}^{\star} \right| \cos \left[\left(\frac{\Delta m_{mn}^2}{2E} L \right) - \arg \left(U_{\beta n}^{\star} U_{\alpha n} U_{\beta m} U_{\alpha m}^{\star} \right) \right] \tag{1.8}$$

1.1.1 PMNS-matrix and mixing angles

In the above considerations only very general assumptions about the mixing matrix U were made. The first restriction may be to consider only three neutrino families, which requires U to be a 3×3-matrix. If a fourth flavor were to be taken into account (for instance, a *sterile neutrino*; see Section 1.2.4), the mixing matrix must also have four dimensions. The most common parametrization of U is

$$U = \begin{pmatrix} 1 & 0 & 0 \\ 0 & c_{23} & s_{23} \\ 0 & -s_{23} & c_{23} \end{pmatrix} \begin{pmatrix} c_{13} & 0 & s_{13}\,e^{-i\delta} \\ 0 & 1 & 0 \\ -s_{13}\,e^{i\delta} & 0 & c_{13} \end{pmatrix} \times \tag{1.9}$$

$$\begin{pmatrix} c_{12} & s_{12} & 0 \\ -s_{12} & c_{12} & 0 \\ 0 & 0 & 1 \end{pmatrix} \begin{pmatrix} e^{i\alpha_1/2} & 0 & 0 \\ 0 & e^{i\alpha_2/2} & 0 \\ 0 & 0 & 1 \end{pmatrix}$$

where c_{ij} is short for $\cos\theta_{ij}$ and s_{ij} correspondingly for $\sin\theta_{ij}$. The θ_{ij} are a measure of the oscillation amplitude and are called *neutrino mixing angles* in
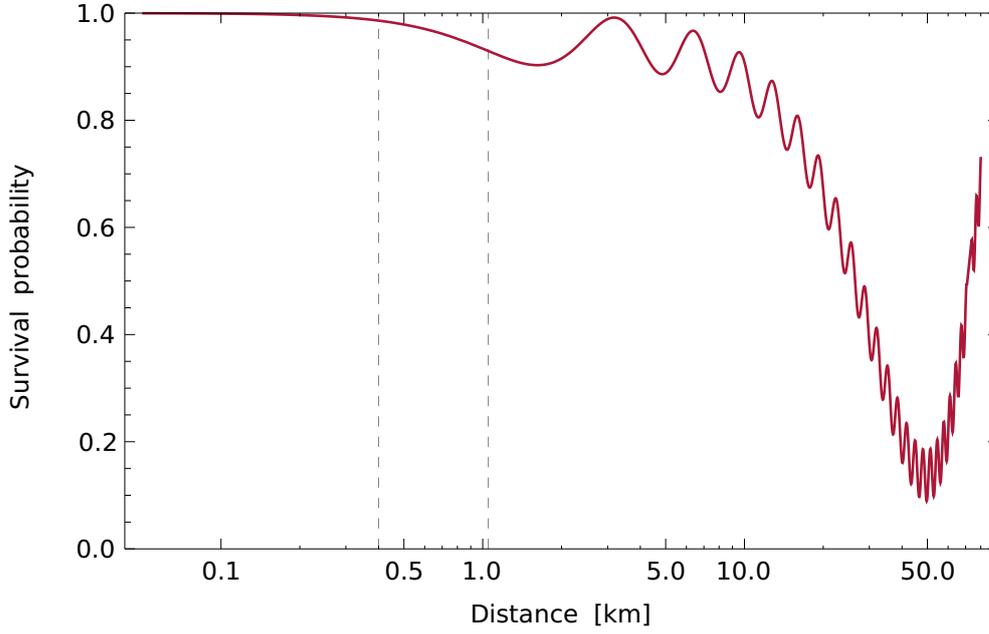
Figure 1.1: Survival probability (1.10) of an electron (anti)neutrino of 3 MeV kinetic energy in dependence of the distance travelled. The oscillation parameters are taken from Table 1.1. The dashed lines show the mean distances of the two Double Chooz detectors from the reactor cores (see Chapter 2).

analogy to the mixing angles in the quark sector. The parametrization also contains a complex phase δ for the possibility of CP violation, as well as two phases α_1 and α_2 for the case that neutrinos should turn out to be Majorana particles. When this parametrization of U is used with equation (1.8), the survival probability of an electron neutrino becomes

$$
\begin{aligned}
P_{\nu_e \to \nu_e} = 1 &- 4\cos^2\theta_{12}\,\cos^4\theta_{13}\,\sin^2\theta_{12}\,\sin^2\!\left(\frac{\Delta m_{12}^2}{4E}L\right) \\
&- 4\cos^2\theta_{12}\,\cos^2\theta_{13}\,\sin^2\theta_{13}\,\sin^2\!\left(\frac{\Delta m_{13}^2}{4E}L\right) \\
&- 4\sin^2\theta_{12}\,\cos^2\theta_{13}\,\sin^2\theta_{13}\,\sin^2\!\left(\frac{\Delta m_{23}^2}{4E}L\right)
\end{aligned}
\tag{1.10}
$$

As of the time of this writing, only the complex phases α_1, α_2 and δ are unknown quantities. All mixing angles have been determined experimentally, the latest being θ_{13}. The value of θ_{13} remained unknown for a long time and there was the question if it could zero. The best upper limit came from the CHOOZ experiment and was $\sin^2 2\theta_{13} < 0.19$ (at 90% CL).[3] The situation changed dramatically when the recent reactor antineutrino experiments started data taking. The Double Chooz reactor neutrino experiment found a first hint at a non-zero θ_{13} in 2012.[4] This was confirmed soon after with results from the reactor neutrino experiments Daya Bay[5] and RENO.[6] as well as with new results from Double Chooz.[1] All

experiments have improved their results further and a combined value of the three experiments is $\sin^2 2\theta_{13} = 0.095 \pm 0.010$, as given in [2]. Thanks to these experimental efforts θ_{13} has become the best known mixing angle to date.

The mixing angle θ_{12} is known from measurements of oscillations of solar and reactor neutrinos. The best value $\sin^2 2\theta_{12} = 0.857^{+0.023}_{-0.025}$ comes from a combined fit to data from the KamLAND experiment and solar neutrino measurements.[7] The third mixing angle θ_{23} was measured in experiments with atmospheric and accelerator neutrinos. The best limit $\sin^2 2\theta_{23} > 0.95$ (90% CL) was determined by the Super-Kamiokande experiment, using a two-neutrino oscillation analysis.[8]

The values for the mixing angles and the squared mass differences are summarized in Table 1.1. Based upon these values the survival and oscillation probability of an electron antineutrino in the three-neutrino case are illustrated in Figure 1.1.

1.2 OPEN QUESTIONS

Their extremely small mass and the weak interaction probability of neutrinos frequently pose challenges for the measurement of neutrino properties. Their mere existence took about 26 years to be proven experimentally and many questions concerning them are still unresolved today.

1.2.1 *Dirac and Majorana nature*

The discovery of neutrino oscillations showed that neutrinos have mass. Together with their lack of electrical charge their non-zero mass opens up the possibility that neutrinos are *Majorana fermions* instead of *Dirac fermions*, i.e. that they are their own antiparticles.

A promising experimental way to search for the Majorana nature of neutrinos is the *neutrinoless double beta decay*. In the ordinary double beta decay an isotope simultaneously emits two electrons and two electron antineutrinos. This decay can be observed when the single beta decay would lead to a daughter nucleus with higher binding energy and is energetically forbidden. This is for example the case in ^{76}Ge, which decays via double beta decay into ^{76}Se. As there are four particles involved in the decay, the two electrons exhibit a continuous energy spectrum.

The neutrinoless double beta decay is only possible if the neutrino is indeed a Majorana particle. The process can be imagined as an annihilation of the two neutrinos and only the two electrons are emitted. This process would violate total lepton number conservation by two numbers. As there are no neutrinos emitted, the two electrons receive the total decay energy. Experiments like GERDA look for a peak at the end of the double beta energy spectrum. In a first analysis by the GERDA collaboration no peak could be found.[9] The sensitivity of the experiment will be increased by a factor of 10 in its second phase.

1.2.2 Neutrino mass

From the day of their postulation it was clear that neutrinos can only have a very tiny mass (otherwise it would have been visible in the endpoint of the β-spectrum), and for a long time it was widely believed that neutrinos are in fact massless. The discovery of neutrino oscillations then showed that neutrinos have non-zero mass[3] and allowed to measure the squared mass differences, but the absolute mass scale remains still unknown. The current best limit on the *effective neutrino mass*

$$m_{\bar{\nu}_e}^{\text{eff}} = \sqrt{\sum_i |U_{ei}|^2 \, m_{\nu_i}^2} \qquad (1.11)$$

was determined in the Mainz and Troitsk experiments via the end point of the tritium β^--spectrum. They found an upper limit of 2.3 eV (95% CL) [10] and 2.2 eV (95% CL) [11] respectively. The KATRIN experiment improves on this method and has a projected sensitivity of 0.2 eV.[12]

All these experiments work with electron antineutrinos. As the effective mass involves the PMNS-matrix U, it could be different for electron neutrinos if there is CP-violation in the lepton sector. The best experimental limit on $m_{\nu_e}^{\text{eff}}$ comes from a measurement with electron capture on ^{163}Ho (which involves a neutrino, rather than an antineutrino) and is 225 eV.[13] The upcoming experiments MARE and ECHO intend to improve this limit and make use of Rhenium and Holmium respectively.[14;15]

1.2.3 Neutrino mass hierarchy

Closely related to the neutrino masses is the question of the neutrino mass hierarchy, i.e. the ordering of the mass eigenvalues. This question is equivalent to determining the signs of the squared mass differences Δm_{ij}^2 between the neutrino flavors i and j. It is already known that Δm_{21}^2 is positive, i.e. $m_2 > m_1$. The signs of Δm_{13}^2 and Δm_{23}^2 are still unknown.[2]

The mass hierarchy is of special interest, since the direct experimental discovery of all three absolute neutrino masses may still lie in the far future. Together with a known mass hierarchy, however, it is sufficient to measure the mass of a single neutrino eigenstate to know the absolute masses of the other two as well.

1.2.4 Sterile neutrinos

In the past decades a number of experiments measured the neutrino flux from nuclear reactors at very short distances (between about 9 and 92 m). At these

---

[3]More precisely, according to equations (1.2) and (1.3) they cannot all have the *same* mass. So at least one neutrino mass state must be non-zero, but in principle one state could still have zero mass.

distances any oscillations can be neglected and the detectors observed the unoscillated neutrino output. However, a recent re-evaluation of the neutrino output from nuclear reactors predicts a higher neutrino flux by about 3 %.[16] If this is correct, the experiments have effectively measured a deficit even at short distances. A hypothetical fourth neutrino flavor was suggested in order to resolve this anomaly.[17] It would not participate in the weak interaction and is called *sterile neutrino*. The "sterility" is required to avoid a clash with the number of neutrino flavors predicted by the Z-Boson lifetime. These observations constrain the number of weakly-interacting neutrinos (with a mass below half of the Z-Boson mass) to three, but a non-interacting neutrino could circumvent this restriction.

New experiments like STEREO are dedicated to confirm or reject this hypothesis.[18] The Near Detector of Double Chooz can also help to confine the parameter space for sterile neutrinos, since it will provide an accurate measurement of the still unoscillated neutrino flux from the reactors.

1.2.5 *Investigation of CP-violation*

As already mentioned before, equation (1.5) represents the oscillation of neutrinos, not antineutrinos. In the case of antineutrinos the formula has to be conjugated and U is replaced by $U^\star$. If the CP-violating phase δ in equation (1.9) is not equal to zero, $U^\star$ is different from U. In consequence, CP-violations could manifest in a different oscillation behavior of neutrinos and antineutrinos.[4]

This holds under the assumption that the neutrino mixing angle θ_{13} is not zero. According to the connection between δ and θ_{13}, which is apparent in the parametrization (1.9) of the mixing matrix, all terms with δ would vanish in the case of $\theta_{13} = 0$ and neutrino oscillations would be CP-conserving independent of δ. But since the recent reactor neutrino experiments Double Chooz, Daya Bay and Reno found a rather "large" value of θ_{13}, this opens up the possibility of investigating CP-violations with the help of oscillations of neutrinos and antineutrinos.

---

[4] U and $U^\star$ are also different if α_1 or α_2 are non-zero, but these parameters do not have any impact on the oscillation behavior.

CHAPTER 2

THE DOUBLE CHOOZ EXPERIMENT

2.1 EXPERIMENTAL CONCEPT

Double Chooz aims at a precision measurement of the mixing angle θ_{13}. The basic experimental concept is to use a nuclear reactor as an intense source of electron antineutrinos and place two detectors in different distances from the source. The *Far Detector*, is placed close to the oscillation maximum, where it monitors the reactor neutrino flux. The result is compared to the original neutrino flux expected from data of the reactor's thermal power, and a value for θ_{13} can be obtained from the deficit. This is the experimental situation of the first phase of the experiment. In this single-detector configuration the result for θ_{13} depends critically on the knowledge of the reactor power and the $\bar{\nu}_e$ detection efficiency, and the uncertainties of these quantities directly influence the error on the mixing angle.

In a second phase, the use of a *Near Detector*, liberates the measurement from the knowledge of the absolute reactor power (and the associated uncertainty). It is placed close to the reactor core, at a distance at which the amount of oscillated $\bar{\nu}_e$ is still negligible, and thus serves as a reference for the original neutrino flux. In the two-detector configuration θ_{13} can be extracted from the relative decrease of the $\bar{\nu}_e$ flux between the two detectors[1] as well as from the distortion of the energy spectrum. As Near and Far Detector are of identical design, the uncertainties on the detection efficiency are significantly reduced and the overall error on θ_{13} decreases considerably.

The one-reactor scenario is an ideal case. Most commercial power plants operate several reactors, and in the case of Double Chooz there are two cores. This makes the measurement somehow more complex, but in the case of only two cores

---

[1] Of course, the flux is corrected for the isotropic emission of the $\bar{\nu}_e$ and the resulting r^{-2}-dependence of the flux with increasing distance from the reactor.

iso-lines can be exploited. The iso-lines are imaginary curves around the reactor cores, along which the ratio of the fluxes of the two reactors is constant. If both detectors are located on the same iso-line, the uncertainties on the reactor power still cancel, as in the one-reactor case: should one reactor change its thermal power output, both detectors observe the same fractional change in the $\bar{\nu}_e$ flux. Iso-lines do not exist any more for general arrangements of three or more reactor cores and it is more difficult to determine the relations between the observed fluxes in the detectors.

The two-reactor setup has a second advantage over arrangements with more cores. Due to maintenance or refuelling, reactor cores have to be shut down from time to time. With only two reactors it is possible that both cores are shut down at the same time. Such *off-off*-times are very valuable, since they allow to measure the pure background content in absence of neutrino signals. Such a situation is the less likely, the more reactors there are.

2.1.1 Reactor cores

The experiment is located at the grounds of the Chooz Nuclear Power Station in the village of Chooz in the French Ardennes. The plant operates two pressurized water reactors with 4.4 GW$_{th}$ thermal power each, which serve as the neutrino sources for the experiment. This translates into a neutrino production rate of about $2.3 \cdot 10^{20}$ s^{-1} per reactor. The two reactor cores are currently the most powerful units in the world, which ensures a very intense neutrino flux at only two sources. As outlined before, the use of only one or two cores is favorable for the experiment's systematic error budget.

    The Far Detector is located at a mean distance of 1057 m from the two reactor cores. It is placed in an underground laboratory with 300 m w.e. overburden and is taking data since April 2011. At the time of writing, the Near Detector is being constructed at a mean distance of 415 m from the reactors. The laboratory housing the detector was newly erected and has an overburden of 75 m w.e.

2.1.2 Neutrino detection

Double Chooz is a so-called *disappearance experiment*, meaning that it searches for a deficit in the electron antineutrino flux coming from the reactors. The survival probability of the $\bar{\nu}_e$ is given by equation (1.10).[2] In the case of Double Chooz, this formula can be written in a simpler form. Due to the short baseline and the

---

[2]To be exact, equation (1.10) was derived from equation (1.8) for the particular case of neutrinos, but it is not automatically valid for antineutrinos with which we are concerned here. To obtain the survival and oscillation probabilities for antiparticles, the quantities in equation (1.8) have to be conjugated. If the CP-violating phase is zero, the result is the same. If not, there is a difference between oscillations of neutrinos and oscillations of antineutrinos.

small mass splitting Δm_{12}^2, and the approximation $\Delta m_{23}^2 \approx \Delta m_{13}^2$, one obtains

$$P_{\bar{\nu}_e \to \bar{\nu}_e} = 1 - \sin^2 2\theta_{13} \, \sin^2 \left(\frac{\Delta m_{23}^2}{4E} L \right) \tag{2.1}$$

The mixing angle θ_{13} can be obtained with help of this relation. L is the distance between reactor and detector, the mass splitting Δm_{23}^2 is known from the MINOS experiment $2.32^{+0.12}_{-0.08} \cdot 10^{-3}$ eV^2,[19] and the neutrino energy E can be determined from the reactor power and the fuel composition. The survival probability $P_{\bar{\nu}_e \to \bar{\nu}_e}$ is determined by comparing the measured number of reactor neutrinos to the number of expected neutrinos in the case of no oscillations, where the latter is again obtained from reactor data. When the Near Detector is employed, $P_{\bar{\nu}_e \to \bar{\nu}_e}(E)$ can be obtained from a comparison of the two detectors.

The detectors themselves are large-scale liquid scintillator detectors. They observe the reactor antineutrinos via the inverse β-decay

$$\bar{\nu}_e + \mathrm{H}^+ \longrightarrow \mathrm{e}^+ + \mathrm{n}^0 \tag{2.2}$$

in which an electron antineutrino converts a Hydrogen nucleus at rest into a positron and a neutron. While both reaction products are created at the same time, the positron deposits its energy nearly instantly, while the neutron first thermalizes and is then captured on a nucleus some 10^{-5} to 10^{-4} s later.

The inverse β-decay reaction is identified by its characteristic signature of a prompt positron event and a correlated delayed neutron capture signal. The coincidence of these two signals in time and space as well as the high event energy of 8 MeV of the Gd-deexcitation allow for a very clean selection of IBD events from the general background.

The large number of Hydrogen nuclei in the hydrocarbon-based scintillator presents a vast number of reaction targets. The cross section for the IBD reaction per proton is given as

$$\sigma_{\mathrm{IBD}} = K(E_{\bar{\nu}_e} - \Delta m_{n,p}) \sqrt{(E_{\bar{\nu}_e} - \Delta m_{n,p})^2 - m_e^2} \tag{2.3}$$

where $K = (9.559 \pm 0.009) \cdot 10^{-48}$ m^2 MeV^{-2}.[20] The energy of the neutrino is $E_{\bar{\nu}_e}$, m_e is the electron mass, and $\Delta m_{n,p}$ is the difference between the neutron mass m_n and the proton mass n_p. The cross section for this process is comparably large and shown qualitatively in Figure 2.1. The plot also displays the energy spectrum of the emitted reactor neutrinos and the "pure" spectrum of the detected neutrinos. The actual shape of the detected spectrum is different: The visible energy, i.e. the energy deposited by the IBD positron and its annihilation gammas is given by

$$E_{\mathrm{vis}} \approx E_{\bar{\nu}_e} - \Delta m_{n,p} + m_e \approx E_{\bar{\nu}_e} - 0.782 \text{ MeV} \tag{2.4}$$

when the energy of the IBD neutron is neglected.
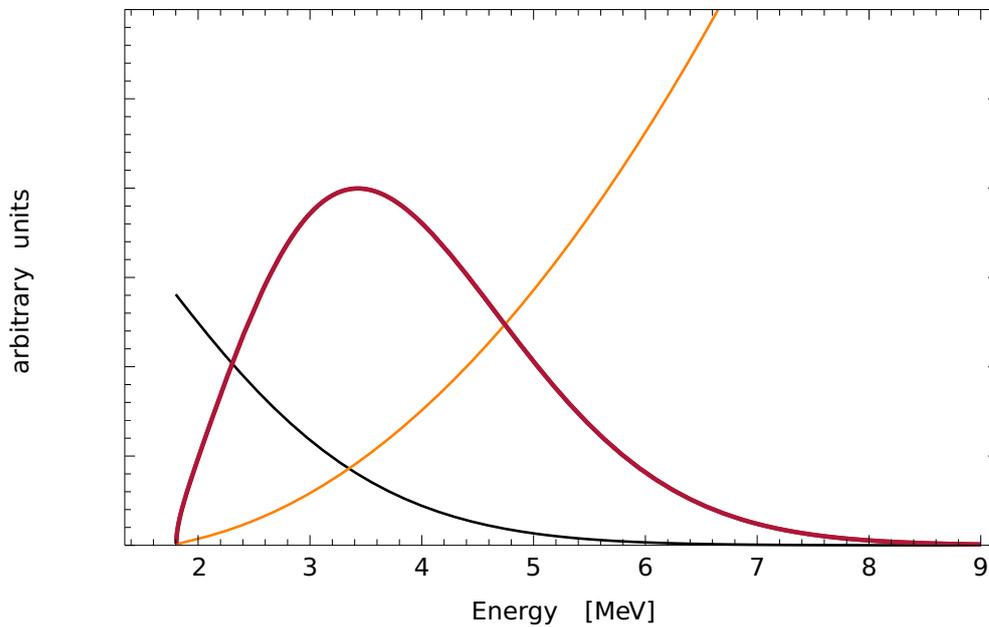
Figure 2.1: Energy spectrum of the electron antineutrinos as emitted from the reactor (black), the cross section for the IBD reaction (orange), and the resulting detectable neutrino energy spectrum (red).[16]

2.2 DETECTOR DESIGN

Double Chooz uses two liquid scintillator detectors for the detection of the reactor antineutrinos. Both detectors have an identical design in order to reduce systematic uncertainties as much as possible. Each detector consists of four concentric cylindrical volumes, as illustrated in Figure 2.2, each of which contains a mixture of organic liquids to fulfil their purpose. The volumes are described in the following.

Neutrino Target: The innermost volume is the *Target*, the principal detection volume for reactor antineutrinos. It consists of 10.3 m³ of a novel Gadolinium-loaded organic liquid scintillator in a transparent acrylic vessel of 8 mm thickness.

The protons of the Hydrogen-rich organic liquid serve as the IBD reaction targets. The positron from equation (2.2) immediately deposits its energy in the scintillator and produces a *prompt signal*. For the purpose of the detection of the neutron, the scintillator is doped with Gadolinium. After thermalization in the liquid the neutron is captured on Gadolinium, and the daughter nucleus immediately deexcites via emission of several gammas, creating the *delayed signal*.

The addition of Gadolinium brings significant advantages. As the element has the highest capture cross section for thermal neutrons of all elements,
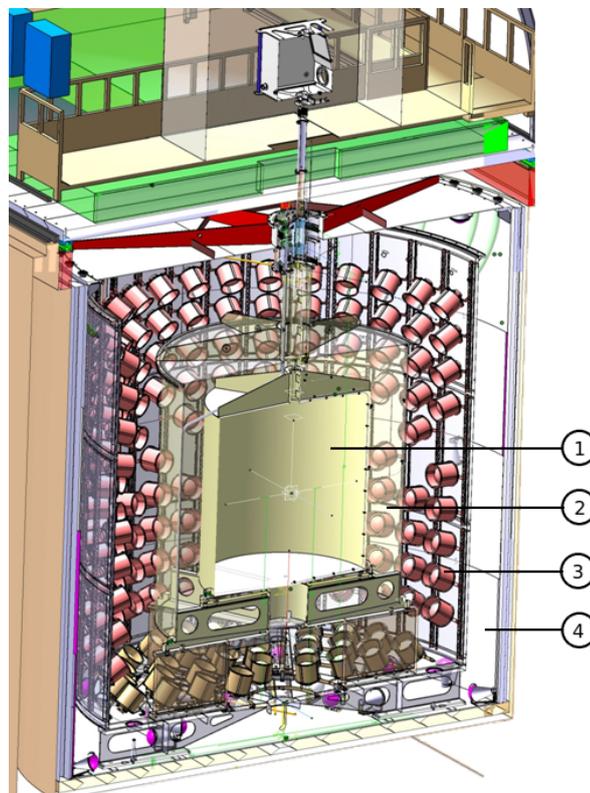
Figure 2.2: Simplified cross-sectional drawing of the Double Chooz detector. The three volumes of the *Inner Detector* can be seen: the *Neutrino Target* (1) where the IBD reactions occur, the *Gamma Catcher* (2), and the non-scintillating *Buffer* (3) as a shielding of the inner two volumes. The Buffer vessel is a 3 mm steel tank, on which the Inner Detector PMTs are mounted on the inside. The Inner Detector is surrounded by the *Inner Veto* (4), which serves as an active veto against cosmic muons and external radiation.

the associated mean capture time is very short. At the given concentration it is only $\approx 30\ \mu s$, which is about a factor of six shorter than in the case of neutron capture on Hydrogen ($\approx 180\ \mu s$). This allows to select IBD events with a short coincidence time cut relative to the prompt event, which in turn reduces the number of accidental coincidences. The total deexcitation energy of Gadolinium is also very high. The roughly 8 MeV emitted energy place the neutron signal well above typical background energies, resulting in a very high signal-to-background ratio. Again, this allows for a very clean energy cut to separate the IBD signal from the background.

Gadolinium is present at a concentration of 1 g/l, leading to an efficiency of about 85 % for neutron capture on a Gd-nucleus. In the remaining cases the

capture occurs mainly on Hydrogen nuclei. Neutron captures on Carbon also occur, but they only give a minor contribution.

Gamma Catcher: The *Gamma Catcher* consists of 22.3 m^3 of Gadolinium-free liquid scintillator and is contained in a 12 mm thick acrylic vessel. Its primary purpose is to detect deexcitation gammas from the neutron capture on Gadolinium which escape from the Target volume. This is important for an accurate reconstruction of the event energy, especially if an event took place near the Target wall. For the Gd-analysis the volume can also be considered an additional shielding for the Target, protecting it from externally incident fast neutrons.

In the Hydrogen analysis (presented in Section 2.3) the Gamma Catcher also serves as an additional neutrino detection volume. In this analysis the IBD reactions are detected via neutron capture on Hydrogen, which predominantly occurs in the Gamma Catcher (as the process does not have to compete with capture on Gadolinium). This selection has the advantage of a far greater detection volume, but has a larger background contamination than the Gd-analysis, but due to the longer time window required and a lower energy of the delayed event it selection has a larger background contamination than the Gd-analysis. The Gamma Catcher is also closer to the detector walls and is not as well shielded from external background as the Target.

The scintillator liquids used in the Target and the Gamma Catcher are described in detail in Chapter 3.

Buffer: The Gamma Catcher is surrounded by the *Buffer,* a 105 cm thick layer of non-scintillating, highly transparent liquid. It contains roughly 100 m^3 of a mixture of different mineral oils and shields the two scintillating inner volumes from background originating in the surrounding rock and the outer detector materials. The Buffer liquid is accommodated in a 3 mm steel tank, which also supports the 390 Hamamatsu 10″-photomultiplier tubes (PMTs) of the Inner Detector. The scintillation light produced in the inner two volumes traverses the Buffer liquid and is detected at the PMTs. The coverage at the Buffer surface is about 13 %.

Inner Veto: The *Inner Veto* serves to detect external radiation entering the Inner Detector volumes (most importantly cosmic muons) and is the main instance for active background reduction in Double Chooz. It consists of 90 m^3 scintillator liquid with high light yield. When an ionizing particle enters the detector, it has to cross the Inner Veto and creates a scintillation signal. Such events can be easily rejected by applying a veto when Inner Detector events coincide with signals from the Inner Veto. The volume is optically separated from the other three volumes by the Buffer steel vessel. The Veto-sided wall of the Buffer steel tank is coated with highly reflective foil in order to minimize light losses in the Inner Veto volume. It is observed by 78 Hamamatsu 8″-PMTs.

There is an additional 15 cm steel shielding around the detector to protect it from natural radioactivity originating in the rocks. Both detectors are placed underground with an overburden of about 300 m w.e. for the Far Detector and about 115 m w.e. for the Near Detector. The overburden significantly reduces the cosmic muon flux reaching the detectors. Still, radioisotopes created by the remaining muons are the dominating source of correlated background in Double Chooz. For this reason there is an additional active veto above the detector, the *Outer Veto*. It consists of several layers of plastic scintillator strips and enables a muon track reconstruction. This way it is possible to know if a muon has passed close to the detector and this information can be used to even veto cosmogenic background which is not detected by the Inner Veto, most prominently *stopping muons* and *fast neutrons*, as described in Section 2.5.

2.3 SELECTION AND DATA ANALYSIS

For the measurement of θ_{13} Double Chooz has pursued different analysis approaches. The two main paths are the *Gadolinium analysis* [1] and the *Hydrogen analysis*, [21] which detect neutrons via capture of the IBD neutron on Gadolinium and Hydrogen respectively.

Gadolinium analysis The selection criteria for the Gadolinium analysis are presented in Table 2.1. A pre-selection is performed, which cleans the sample of short-lived muon-induced radioisotopes and undesired non-physics events (see Section 2.5). Among the remaining events the candidates for antineutrinos are selected by the time coincidence between the prompt positron and the delayed neutron of the IBD reaction. The mean time for neutron thermalization and capture on Gadolinium is about 30 μs, so the coincidence window of $\Delta T \in [2, 100]$ μs contains most IBD events, but is short enough to keep the contamination with accidentals low. The high energy window of the delayed event, made possible by the high Gadolinium deexcitation energy, further reduces backgrounds. Finally, to reduce the number of correlated background events in the selected sample, some additional cuts are applied: A *multiplicity cut* around the delayed event, an additional 0.5 s veto after high-energy muons, and a veto when an event is coincident to an Outer Veto signal.

With this selection 8249 candidates were selected during the 227.93 live days in [1]. The expectation in the no-oscillation case was 8937 events. In an analysis of the neutrino rate and their energy spectrum (see Section 2.4) the value of $\sin^2 2\theta_{13} = 0.109 \pm 0.030(\text{stat}) \pm 0.025(\text{syst})$ was obtained.

Hydrogen analysis The Hydrogen analysis offers a bigger detection volume, in exchange for a higher background contamination. Table 2.2 summarizes the

Pre-selection	
	$\Delta T_{\mathrm{muon}} > 1$ ms
	$T_{\mathrm{rms}} < 40$ ns
	$Q_{\mathrm{max}}/Q_{\mathrm{tot}} < 0.09$
Coincidence	
	$\Delta T \in [2, 100]$ μs
	prompt event: $E_{\mathrm{prompt}} \in [0.7, 12.2]$ MeV
	delayed event: $E_{\mathrm{delayed}} \in [6.0, 12.0]$ MeV
	multiplicity cut: no event in $[-100, 400]$ μs around delayed event
Purity	
	No coincidence in the Outer Veto
	$\Delta T_{\mathrm{muon}} > 500$ ms after muon with $E_\mu > 600$ MeV

Table 2.1: Selection criteria for the Gadolinium analysis.[1]

criteria for the Hydrogen selection. The pre-selection is the same as for the Gadolinium analysis, but the other criteria have to be adapted to the different time constants and energies involved in the neutron capture on Hydrogen. The delayed energy window is lowered to $E_{\mathrm{delayed}} \in [1.5, 3.0]$ MeV, while the coincidence time is opened to $\Delta T \in [10, 600]$ μs. Both changes significantly increase the amount of background leaking into the selection. As a countermeasure an additional spatial coincidence cut is introduced, which removes a large part of the accidental background contribution. Again, a multiplicity cut and a veto for coincidences with the Outer Veto are used to reduce correlated backgrounds.

The selection found a total of 36680 IBD candidates in 240.1 live days. About half of the events are background. 36284 events were expected in the case of $\theta_{13} = 0$. The analysis of the neutrino rate and the shape of the energy spectrum found $\sin^2 2\theta_{13} = 0.097 \pm 0.034(\mathrm{stat}) \pm 0.034(\mathrm{syst})$.

Reactor rate modulation A different analysis approach is *reactor rate modulation* analysis.[22] As the reactor site in Chooz only operates two reactors it is sometimes the case that only one reacor is in operation. There was even a phase of 7.53 live days in which both reactors were simultaneously off.[23] Such a situation is unique to Double Chooz and can be used to determine θ_{13} independent of the non-neutrino background. In this approach the neutrino flux is analyzed with respect to the relative reactor power instead. In a graphical representation the measured flux data points form a line, where the slope is a measure for the neutrino survival probability, and serves to determine θ_{13}. Accidental and correlated

Pre-selection	
	$\Delta T_{\text{muon}} > 1$ ms
	$T_{\text{rms}} < 40$ ns
	$Q_{\text{max}}/Q_{\text{tot}} < 0.09$
Coincidence	
	$\Delta T \in [10, 600]$ μs
	prompt event: $E_{\text{prompt}} \in [0.7, 12.2]$ MeV
	delayed event: $E_{\text{delayed}} \in [1.5, 3.0]$ MeV
	multiplicity cut: no event in $[-600, 1000]$ μs around delayed event
	spatial cut: $\Delta R < 900$ mm
Purity	
	No coincidence in the Outer Veto

Table 2.2: Selection criteria for the Hydrogen analysis.[21]

backgrounds just cause an offset of the curve, but do not influence the slope, so the analysis does not require a background model. The analysis makes use of neutrino candidates according to both the Gadolinium and the Hydrogen selection and finds a value of $\sin^2 2\theta_{13} = 0.102 \pm 0.028(\text{stat}) \pm 0.003(\text{syst})$.[22] It is the first measurement of the mixing angle that is independent of the background model.

2.4 RATE*SHAPE ANALYSIS

The value of θ_{13} is extracted from the so-called *final fit*, i.e. a fit of the theoretical prediction to the measured data, after all other analysis steps have finished. In Double Chooz the fit involves the neutrino rate as well as their energy spectrum, called *rate+shape analysis*. To perform a rate+shape analysis, the spectrum of the selected events is first divided into k bins[3] with $k = 36$ in [1]. The resulting histogram is fitted with a predicted distribution depending on θ_{13}. The best fit is obtained by minimizing the test quantity χ^2 given by

$$\chi^2 = N \, \boldsymbol{M}^{-1} \, N^T \; + \; \sum_k \lambda_k$$

$$= \sum_{i,j}^{k} N_i \, \boldsymbol{M}_{i,j}^{-1} \, N_j \; + \; \lambda_1 \; + \; \lambda_2 \; + \; \lambda_3 \tag{2.5}$$

where $\boldsymbol{M}_{i,j}^{-1}$ is the inverse of the experiment's covariance matrix. The N_i are the differences of predicted and measured neutrino events in bin i. The contributions

---

[3]A rate-only analysis can be considered a special case of a rate+shape analysis in which the complete spectrum is contained in a single bin.

of different backgrounds are subtracted from the number of measured events, so that the N_i are given as

$$N_i = N_i^{\text{data}} - \sum_b^{\text{backg.}} N_i^b - N_i^{\text{pred.}} \qquad (2.6)$$

where N_i^b is the contribution of a specific background to the ith bin and $N_i^{\text{pred.}}$ contains the expected number of neutrinos from both reactors. The λ_k in equation (2.5) are pull terms according to [24]. They allow variations of the associated quantities in exchange for a penalty, which is inversely proportional to their uncertainty σ_k^2. The three pull terms are given in the following:

$$\lambda_1 = \left(\frac{\Delta m_{23}^2 - \Delta m_{23,\,\text{MINOS}}^2}{\sigma_{\text{MINOS}}} \right)^2 \qquad (2.7)$$

accounts for the uncertainty on the squared mass difference Δm_{13}^2 of the first and third neutrino mass eigenstates. As it is seen in equation (2.1), this parameter directly influences the oscillation behavior. It is known from experimental data that $\Delta m_{13}^2 \approx \Delta m_{23}^2$ within their respective errors,[2] so a value of Δm_{23}^2 can be used instead of Δm_{13}^2. The MINOS result $\Delta m_{23,\,\text{MINOS}}^2 = 2.32^{+0.12}_{-0.08} \cdot 10^{-3}$ eV^2 is used as the central value.[19]

$$\lambda_2 = \left(\frac{\epsilon_{\text{corr.}} - 1}{\sigma_{\text{corr.}}} \right)^2 \qquad (2.8)$$

is a pull term for the uncertainty of the contributions of the correlated backgrounds, which are mainly due to the cosmogenic isotopes ^{9}Li and ^{8}He. Because correlated background events pass the coincidence cuts, their respective energy spectra add to the neutrino spectrum, therefore deforming the expected oscillation pattern. And finally,

$$\lambda_3 = \left(\frac{\alpha_{\text{E}} - 1}{\alpha_{\text{E}}} \right)^2 \qquad (2.9)$$

is a pull term for the uncertainty of the energy scale. The energy scale directly influences the fit to the neutrino spectrum and it is of crucial importance to the quality of the rate+shape result.

2.5 BACKGROUND IN DOUBLE CHOOZ

With a rate of about 50 IBD events per day in Double Chooz, the contribution of background events is a major topic in the experiment. For a successful analysis of θ_{13} the possible backgrounds can be either identified and rejected with help of characteristic features, or their contribution is studied and included in the final analysis. Double Chooz is faced with a number of background sources.

2.5.1 Accidentals

Accidental backgrounds are two subsequent unrelated events in the detector which by chance pass the selection cuts. They mostly come from radioactive decay events in the detector material or the surrounding rocks.

The rate of accidental events is greatly limited by the Gd-deexcitation energy of ≈ 8 MeV, since there are only very few backgrounds with such high energies. The short neutron capture time and the associated small ΔT between prompt and delayed event, further reduce the number of accidental events.

In the H-analysis the longer time window and, above all, the much lower energy of the delayed event (≈ 2.2 MeV) lead to a larger contamination of the IBD sample with accidental coincidences. One measure to reduce the number of accidentals is to impose an additional ΔR cut on the distance between the prompt and delayed event. In an IBD reaction the positron and the neutron originate at the same point and deposit their energies relatively close to each other, while accidentals can occur at very different vertices within the detector. Nevertheless, in the Hydrogen analysis the contribution of accidentals remains significant. Chapter 10 shows an approach to considerably reduce the number of accidental and correlated backgrounds by electron-positron discrimination with help of pulse shape differences.

2.5.2 Muons and cosmogenic correlated backgrounds

The vast majority of cosmic muons can be rejected with help of the coincidence signal in the Inner Veto, and/or an energy threshold in the Inner Detector, as muons are generally characterized by very large energy depositions. Muons also create radioactive isotopes directly within the detector material. A *muon veto* of 1 ms after each muon effectively removes these muon-induced radioactive decay events.

Cosmogenic radioisotopes The detector material is essentially composed of Hydrogen and Carbon. Scattering processes of high-energy muons off Carbon nuclei can create a multitude of radioisotopes along the muon's track. Most of these radionuclides are not critical for Double Chooz, as they either have a half-life well below 1 ms and are rejected by the muon time cut, or their decay yields only a single signal and they would be considered accidental background.

The notable exceptions are ^{9}Li and ^{8}He. They have relatively long half-lives of 178.3 ms and 119 ms respectively, and can therefore not be vetoed completely. [4] Both ^{9}Li and ^{8}He are β-n-emitters, i.e. they decay via emission of an electron and

---

[4] At a muon rate of about 46 s^{-1} the mean time difference between two subsequent muon events in the detector is about 22 ms, much shorter than the half-lives of the isotopes.

a neutron:

$$^9\text{Li} \longrightarrow e^- + \bar{\nu}_e + n + 2\alpha$$
$$^8\text{He} \longrightarrow e^- + \bar{\nu}_e + n + {}^7\text{Li}$$
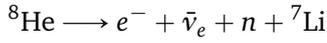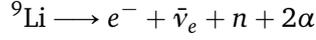
The β^--decay gives a prompt signal in the detector, while the neutron is captured on Gadolinium or Hydrogen and provides a delayed signal.[5] These events look like IBD reactions and are hard to reject on an event-by-event basis. The usual strategy is to subtract the correlated backgrounds statistically from the final antineutrino sample. The uncertainties on their expected rate and spectrum contribute to the error on θ_{13}.

Recently, a likelihood-technique was developed to identify ^9Li and ^8He on an event-by-event basis. It uses the IV/OV muon track reconstruction, as well as time and vertex information of the event relative to previous muon tracks.[25] Since both cosmogenic isotopes decay via emission of an electron (instead of a positron), an e^-/e^+ pulse shape discrimination could also be used for an event-by-event rejection of these two correlated backgrounds, possibly in conjunction with the likelihood technique.

Stopping muons Muons entering the detector are normally detected by the scintillation signal in the Inner Veto or the high energy deposition in the Inner Detector (with a threshold at 20 MeV). An exception are *stopping muons*. They enter the detector through the chimney (and are not detected by the Inner Veto) and stop close to the entrance point. This way the visible energy deposition in the Inner Detector stays below the energy threshold and the muon appears as an ordinary physics event. After its 2.2 μs life time, the muon decays via

$$\mu^+ \longrightarrow e^+ + \bar{\nu}_\mu + \nu_e$$
$$\mu^- \longrightarrow e^- + \nu_\mu + \bar{\nu}_e$$
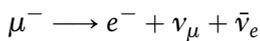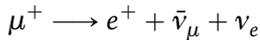
Due to the three-body process the charged leptons are created with a continuous spectrum of energies; the rest is taken away by the two neutrinos. If the charged particle receives only small kinetic energy, it can also pass the energy threshold and provides a delayed event.

The Outer Veto helps to identify stopping muon events, as it can also track muons entering through the chimney. Another approach exists in which the uneven distribution of scintillation photons in the case of chimney events is exploited. The inhomogeneous distribution over the PMTs affects the vertex reconstruction and can be measured with a quality parameter.[26] Again, pulse shape discrimination can also provide a very good handle on this type of background, as shown in Chapter 9.

---

[5] The two alpha particles in the decay of ^9Li are created by the instantaneous decay of the daughter nucleus ^8Be. They only have kinetic energies in the keV-range and their scintillation light is so strongly quenched that the alphas remain practically invisible. As the alphas do not contribute to the scintillation signal, they cannot be used for pulse shape discrimination of the ^9Li decay.

Fast neutrons   Cosmic muons can also create *fast neutrons* along their tracks. This is especially important when a muon passes close to the detector, but does not cross the Inner Veto and is therefore not tagged. A fast neutron created in the rock or steel shielding can then enter the detector. Hard collision events, where the neutron scatters off a Hydrogen nucleus and transfers a substantial amount of its energy to the latter, are relatively rare and the neutron might pass the Inner Veto undetected. Eventually, it can reach the Gamma Catcher or the Target volume, and collide with a Hydrogen nucleus. As a charged particle, the recoil proton deposits its kinetic energy locally and creates a flash of scintillation light, mimicking a prompt event. The neutron then thermalizes and is captured on Gadolinium or Hydrogen, which is the delayed event. Like stopping muons, the prompt event produced by fast neutrons has a continuous and rather flat energy distribution.

2.5.3   *Light noise*

Light noise is an entirely different kind of background. In such events the signals do not originate from particle interactions, but from the PMTs themselves. Even though there have been various experimental investigations of this effect (for example [27] or [28]), there is no final consensus as to the origin of light noise.

Light noise contributes mostly to the accidental background in Double Chooz. Even though there are many sub-categories of light noise with somewhat different properties, most light noise events can be removed with dedicated cuts. Two reliable rejection variables are the $Q_{\mathrm{max}}/Q_{\mathrm{tot}}$ and T_{RMS}. The first one monitors if the light is distributed evenly over the PMTs or concentrated at a single PMT, which would be a strong indicator for light noise; the second one detects distortions in the PMT hit time distribution. Several new cuts are also being studied (see Chapter 8).

Due to the fundamentally different creation mechanism, most light noise events have very unusual pulse shapes. They can also be identified and rejected with pulse shape discrimination (PSD) methods.

A small fraction of light noise events also creates correlated background. This happens when the light burst is longer than the time window of the DAQ. In this case the signal is still strong enough at the end of the time window and triggers the DAQ again immediately. These correlated light noise events are characterized by extremely short time differences ΔT between the prompt and the delayed event. They can be removed very effectively by imposing a lower limit on the coincidence time window used in the θ_{13} analyses. However, novel pulse shape-based PID approaches might be able to reject correlated light noise without the need of a lower cut on ΔT. New techniques to deal with light noise are presented in Chapter 9.

CHAPTER 3

Scintillation and scintillator production

Organic liquid scintillators are a common choice for large-scale neutrino detectors and used in many modern experiments. They combine fast response times on the nanosecond timescale with high light yield, allowing for good timing and energy resolutions. They are highly adaptable to a variety of problems, since it is easy to adjust properties by changing the mixture or by adding additives. For instance, they can be doped with materials with high neutron capture cross sections for increased neutron detection capability. It is furthermore possible to purify liquid scintillators and achieve high radiochemical and optical purity. The former is a general requirement in modern low-background experiments; the latter is especially important for super-sized detector projects to ensure that the scintillation light originating anywhere in the fiducial volume can reach the photodetectors and is not absorbed by impurities. Moreover, their comparably low costs makes it possible to construct detectors with very large fiducial masses, which makes them a choice for neutrino detectors. The current reactor antineutrino experiments, as well as planned kiloton neutrino detectors use organic liquid scintillators.

The principles of scintillation are the basis for the ionization quenching model (Chapter 4), the Monte Carlo simulation of the optical model (Chapters 6 and 7), and pulse shape-based data analysis techniques (Chapters 9 and 10). In this section I summarize the scintillation mechanism in a generic three-component organic liquid scintillator, consisting of the solvent and two fluorescent solutes. This configuration is already sufficiently complex to investigate all processes that play a role, namely energy migration in the solvent, energy transfer from the solvent to the fluor, and radiative transfer between fluors. In Section 3.6 the scintillation mechanism is revisited for the specific case of the Double Chooz scintillators.

3.1 LIGHT CREATION IN ORGANIC LIQUID SCINTILLATORS

Solvent The base material of a liquid scintillator is an aromatic solvent. Aromatic molecules feature one or more ring systems, in which the electrons are delocalized in a π-orbital extending over the entire ring. This ring system is where scintillation occurs. The energy levels of the π-orbital are displayed schematically in Figure 3.1. The transition from the first excited state to the ground state of the π-system takes place via the emission of an optical photon. Transitions between higher excited states are non-radiative.[29]

Solutes Liquid scintillator mixtures employ at least one dissolved fluorescent substance, commonly called *fluor*. In general, fluors should only be present in small concentrations in order to avoid significant self-absorption losses of the scintillation light.

Fluors shift the light towards longer wavelength, which is based on the vibrational states associated with the electronic states of the molecule (see Figure 3.1). When a photon is absorbed, the electron is elevated from S_0 to an excited vibrational sub-state of S_1. The subsequent relaxation to the vibrational ground state of S_1 is non-radiative. Then the molecule deexcites radiatively to an excited vibrational sub-state of S_0, which again relaxes to the ground state without emission of a photon. Compared to the originally absorbed photon, the energy of the re-emitted photon is reduced by the energies lost in the relaxation of the vibrational states (of the order of 0.1 eV). The associated shift to a higher wavelength is called the *Stokes shift*. Rotational states of the molecule only have energy differences of the order of meV and are negligible.

It is possible to add also a secondary fluor as a wavelength shifter, in order to move the wavelengths of the primary scintillation light farther away from the absorption bands of the scintillator mixture and closer to the sensitive region of the photodetection devices.

3.1.1 *Primary excitation*

When a charged particle traverses the scintillator material it interacts electromagnetically with the electron shells and leaves behind a trail of excited and ionized molecules. The molecules can be excited into either singlet or triplet states, where singlet states are primarily formed when the energy transfer to the molecule is small and the electron is elevated into a higher electronic state. Triplet states, on the other hand, are more likely to be created when the energy transfer is large and the electron is temporarily torn from its molecule. When an electron falls back to the ion it populate a triplet state with a chance of 3/4.[30]

Normally the molecules are initially excited into a higher electronic state (S_n or T_n, with $n > 1$), but they undergo a rapid radiationless decay into the S_1 or T_1 state within several picoseconds. From a practical point of view it can be
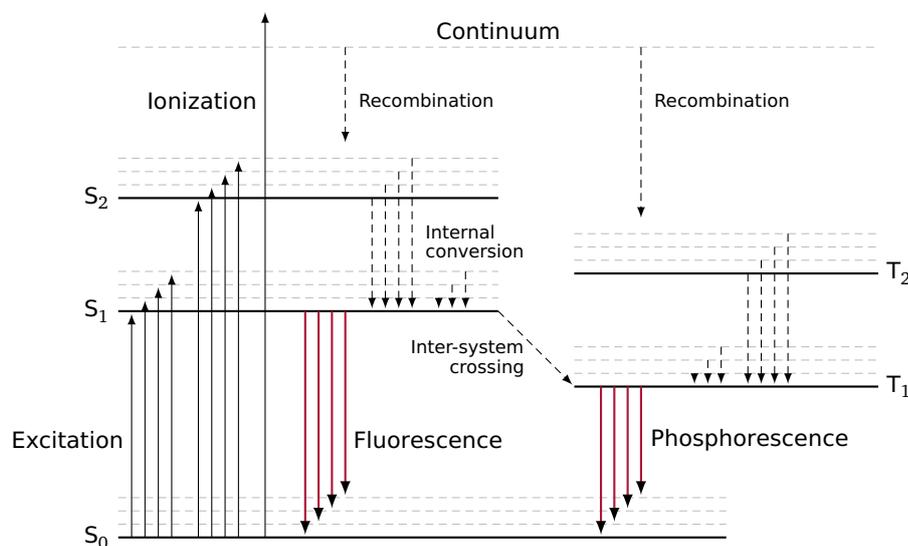
Figure 3.1: Schematic display of singlet and triplet states in the π-system of a fluorescent molecule, which is responsible for scintillation. An incident particle can excite an electron into a higher singlet state (and its vibrational sub-states) or into the continuum. In the latter case, singlet or triplet states are excited upon recombination. The higher excited states rapidly deexcite by *internal conversion* without photon emission to the lowest excited singlet or triplet state S_1 or T_1. The T_1 state can also be populated by *inter-system crossing*. The radiative decay of the S_1 and T_1 states lead to fluorescence and phosphorescence respectively.

assumed that all molecules are encountered only in their lowest excited singlet or triplet states. These electronic states have a longer mean life time. The S_1 state typically has a life time on the nanosecond time scale, while the decay of the T_1 state is suppressed by selection rules and decays with phosphorescence time scales (usually $\gg 10^{-8}$ s). Its lifetime can be greatly reduced by interactions with surrounding molecules, though.

3.1.2 *Excitation energy migration*

After an ionizing particle passed through the material, it leaves numerous ionized and excited molecules in its wake. Since the fluors are usually only present at low concentrations, the particle excites almost exclusively the bulk matter. The solvent itself usually does not emit scintillation light, so the excitation energy has to move through the solvent to eventually reach a fluor.

The dominant process for this energy migration is excimer formation.[31] The excited solvent molecule $A^\star$ interacts with an unexcited adjacent solvent molecule A and form and temporarily forms an excimer, i.e. $A^\star + A \rightarrow A^\star A$. The probability for this process to occur depends on the alignment of the two molecules.

Excimers form when the molecules are nearly parallel to each other, and the formation probability decreases with increasing angle between the molecules. The excimer is very short-lived and dissociates on a nanosecond time scale. When it breaks apart into its monomers again, the excitation energy can remain with the previously unexcited molecule and the energy has migrated. The net reaction is then $A^\star + A \rightarrow A + A^\star$. This process is repeated with the next neighboring molecule and the excitation energy effectively moves through the medium. Migration by diffusion, in which an excited solvent molecule itself moves through the medium, is also possible, but usually only plays a minor role. During migration several processes can occur. [32]

- If the excitation comes close enough to an unexcited fluor molecule, the energy can be transferred to the fluor, either radiatively or non-radiatively. This mechanism is described in the next paragraph.

- Depending on the type of molecule, $A^\star$ can also directly undergo photon emission. This is typically less likely than energy transfer to the primary fluor, but still gives a contribution.

- If impurities or non-scintillating components are present, the excitation energy can be transferred to these quenching agents. The energy is then lost for scintillation. In Double Chooz this may happen due to the non-scintillating Gd-complex in the Target.

- Another effect, which is explained in detail in Chapter 4, is *ionization quenching*. If the local density of excited solvent molecules is very high, two excited molecules can interact, effectively reducing the number of excitations available for scintillation. The associated processes are schematically $A^\star + A^\star \rightarrow A + A$ and $A^\star + A^\star \rightarrow A + A^{\star\star} \rightarrow A + A^\star$.

- If neither of the above processes has taken place within the mean lifetime of the excited state, the energy dissipates into heat and is again lost for scintillation.

3.1.3 Energy transfer to the solute

If the excitation energy comes close enough to a fluor molecule, it can be propagated to the latter by the same process of excimer formation. However, if the excited molecule is already fluorescent, there is a second transfer path which is very effective at short ranges: A fluorescent *donor* can transfer its energy to an *acceptor* molecule via the so-called *Förster resonance energy transfer* (FRET). This process is non-radiative, i.e. no real photons are exchanged.

This transfer takes place with 50 % probability if the distance between the bulk molecule and the fluor is equal to the Förster radius:

$$R_F^6 = \frac{9 \ln 10}{128\, \pi^5 N_A} \cdot \frac{\kappa^2 \phi}{n^4} \int_0^\infty \epsilon(\lambda)\, f(\lambda)\, \lambda^4\, \mathrm{d}\lambda \tag{3.1}$$

In this equation $\epsilon(\lambda)$ and $f(\lambda)$ are the absorption spectrum of the acceptor and the emission spectrum of the donor respectively, and ϕ is the donor's quantum yield (see also Section 6.6), and n is the refractive index of the medium. It is a function of the wavelength, but can usually be considered constant over the whole range of the absorption and emission spectra. κ is a factor describing the mutual alignment of the donor and the acceptor molecules. It is 2/3 when there is no preferred orientation of the molecules. The Förster radius of a donor-acceptor system is typically somewhere between 1 and 10 nm. It can also be translated to a *critical concentration* c_0, at which the mean distance of the fluor molecules is equal to R_F. It is given as

$$c_0 = \frac{3}{4\pi R_F^3 N_A} \tag{3.2}$$

3.1.4 *Transfer from primary to secondary fluor*

The concentrations of the solutes are usually low, so that the mean distances between their molecules is very large compared to the Förster radius. Therefore, a non-radiative energy transfer between them only plays a minor role and the dominant transfer mode is radiative. This is, the primary fluor deexcites via the emission of a real photon, which propagates through the medium and is absorbed by the secondary fluor. This is facilitated if the respective emission and absorption spectra have a large overlap.

While the photon travels through the medium it is subject to optical processes, including absorption on other molecules. To increase the effectiveness of the energy transfer to the secondary fluor, one could in principle raise the concentration of the secondary fluor. In this case the mean distances between the donors and acceptors would decrease, and the process would become more and more non-radiative until the situation reduces again to the radiationless Förster transfer, as described in the previous paragraph. In fact, both transfer mechanisms can be considered the long- and short-range manifestations of the same phenomenon.[33] However, it is generally recommended to keep the fluor concentrations low, since high concentrations also lead to significant self-quenching (in case of the primary fluor) or self-absorption (in case of the secondary fluor), and in consequence a loss of scintillation light.

3.2 PULSE SHAPE DISCRIMINATION

The whole process of primary excitation, energy migration and light emission happens within 10^{-8} to 10^{-7} s. The flashes of scintillation light are very short, but their shape contains valuable information.

In general, the pulses feature a *fast* component, which gives rise to a short peak, and a *slow* component responsible for an extended "tail" after the initial

peak. The excited singlet states usually have a mean lifetime well below 10 ns and their decays yield a short flash of light.

The slow component is created in a more complicated manner. The excited T_1 triplet states have a much longer lifetime on phosphorescence time scales. In fact, the lifetime would normally be too long to be of any relevance for scintillation. But frequent interactions with surrounding molecules can reduce the excitation lifetime significantly. In an interaction between two molecules in a triplet state, one excitation can be converted into a S_1 singlet state, while the second molecule falls back to its ground state.[1] This process thus leads to a postponed population of the S_1 state, which then decays radiatively and creates the *slow* component of the scintillation pulse.

The pulse shape is governed by the ratio of singlet to triplet states. As already stated in Section 3.1.1, singlet and triplet states are populated by different mechanisms. If singlet or triplet states are favored depends mostly on the mean energy transfer of the particle, i.e. of $\langle dE/dx \rangle$. As long as $\langle dE/dx \rangle$ is low, molecules are merely excited and assume a singlet state. When it is high, molecules are ionized and assume a triplet state upon recombination with an electron.

Since the mean differential energy loss function $\langle dE/dx \rangle$ varies between different types of incident particles, they excite different amounts of singlet and triplet states, ultimately leading to different proportions of the fast and slow scintillation component. Conversely, the different pulse shapes allow to draw conclusions about the incident particle. This is routinely exploited for *pulse shape discrimination* (PSD) and *particle identification* (PID). PSD is expected to work the better, the more the particles differ in their energy deposition mechanism. For example, electrons and alpha particles, which are described by entirely different energy loss mechanisms, may exhibit large differences and can often be successfully identified by their pulse shapes. Figure 3.2 shows the pulse shape differences between electrons and alpha particles in the Double Chooz scintillators, and the influence of the fast and slow component is clearly visible.

The differentiation between similar particles is far more challenging (and often outright impossible). In the particular case of electrons and positrons, there are some differences in the energy loss function of the two particles,[34] but they are far too small to have a significant impact on the scintillation pulse shapes. However, an important characteristic of positrons is the annihilation at the end of their paths. The annihilation creates two gamma photons, which are not present in the case of the electron. This may lead to a slight distortion of the signal, as compared to electron pulses.[2] Chapter 10 presents a technique to exploit these

---

[1]Strictly speaking, this is also a case of ionization quenching.

[2]There is also the possibility of positronium formation. This process can lead to a delayed annihilation of the positron, which can cause a more severe distortion of the pulse shape. This can also be exploited for a PSD of electron and positron events[99] (see also Chapter 10).
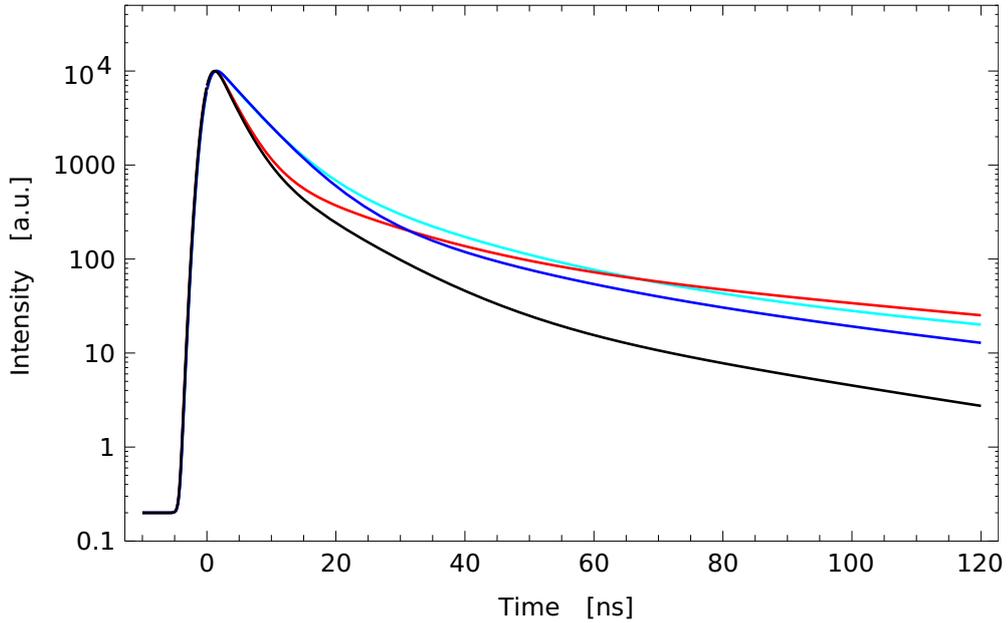
Figure 3.2: Normalized scintillation waveforms of the Double Chooz scintillators to different particles. The black and blue curves show the waveforms of the Target for electrons and alpha particles respectively; the waveforms of the Gamma Catcher are shown in blue (electrons) and cyan (alphas). For better comparability the different curves are normalized to the same value. These curves were obtained in timing measurements performed under laboratory conditions. It can be clearly seen that the differences between electrons and alpha particles are largest in the delayed component.[35]

differences and to distinguish positrons from the background of electrons and gammas, and so to isolate the IBD signal.

Furthermore, the pulse shape can also be modified due to the localization of the event, especially in large detectors. Pulses should generally be corrected for the time-of-flight from the event vertex to the PMTs, but effects due to the geometry can still have an influence (for instance, reflections at detector structures). Serious distortions can be created by the time-of-flight correction, if the event vertex is not properly reconstructed. If this predominantly happens for a certain class of events, this can be taken advantage of. In Chapter 9 such position-induced distortions of the pulse shape will be used to perform a reduction of the stopping muon background in Double Chooz.

3.3 SCINTILLATOR RESPONSE AND NON-LINEARITIES

The *response function* of a scintillator is the amount of light produced as a function of the incident particle's kinetic energy. In principle, the response function scales linearly with the particle energy: The light output increases with the number

of primary excitations in the material, and hence with the energy deposited by the incident particle. There are, however, two important effects that lead to a nonlinear energy dependence of the light output, namely *ionization quenching* and the *Čerenkov effect*.

Ionization quenching: The process of ionization quenching takes place during the phase of energy migration (see Section 3.1.2). In contrast to other light loss mechanisms, the reduction due to ionization quenching depends on the particle's kinetic energy.

As long as the local density of excited molecules is low, the distances between them are too large for any interaction to occur, and the excitations can migrate undisturbed. In this case there is no light loss due to ionization quenching. At the end of the particle's track, however, the mean energy loss $\langle dE/dx \rangle$ increases sharply (*Bragg peak*). The density of excited molecules becomes large enough that interactions between them are likely.[3]

Particles with rather low initial energy deposit their energies with large $\langle dE/dx \rangle$, and the total light output is significantly quenched. More energetic particles, on the other hand, deposit most of their energy with small $\langle dE/dx \rangle$. The high $\langle dE/dx \rangle$ at the end of their track contributes less to their total light yield. The process of ionization quenching leads to a non-linear relation between the energy of the ionizing particle and the light produced by the scintillator. A theoretical treatment of the effect is presented in Chapter 4.

Čerenkov effect: The *Čerenkov effect* is strictly speaking not a scintillator-related issue. But in practice the two processes cannot be separated and Čerenkov light might as well be treated as a scintillator nonlinearity.

Čerenkov light is only created if the speed of the incident particle is larger than the speed of light in the medium. For electrons travelling through a medium with $n = 1.4$, this threshold is at about 219 keV. The refractive index $n(\lambda)$ of the material is a function of the wavelength λ and increases sharply towards the UV region.

In Double Chooz the Čerenkov effect is only of concern in respect to electrons and positrons.[4] Heavy particles, like protons and alphas, only emit Čerenkov radiation when their kinetic energy is above several hundred MeV, which is outside the scope of Double Chooz.

Ionization quenching reduces the light at low particle energies, while the Čerenkov effect adds to the light yield at higher particle energies. Together, both effects contribute that in proportion less light is created for particles of lower energies. The

---

[3] The dependence on $\langle dE/dx \rangle$ is the "traditional" explanation of the ionization quenching effect. The study in Chapter 4 suggests that the decisive quantity is the total ionization cross section σ_p of the primary particle rather than $\langle dE/dx \rangle$. The quantities are related, but nevertheless distinct.

[4] Gamma photons deposit their energies in multiple Compton scatter events in the detector. The Compton electrons also emit Čerenkov radiation if their kinetic energy is high enough, so the effect also plays a role for gammas.

nonlinearities introduced by the two effects and their treatment in the simulation are examined more closely in Chapter 7.

3.4 TARGET AND GAMMA CATCHER DESIGN

The knowledge of the scintillation mechanism was used in the design of the Double Chooz scintillators. Details about the scintillator design can be found in [36; 37; 38]. The following list gives an overview over the general requirements and design criteria of the Double Chooz scintillators.

Long-term stability: The Target contains a metal-organic Gadolinium complex for neutron detection. Such complexes, however, can be very sensitive. Great efforts were made to develop a stable compound (see Paragraph 3.4.1). The whole scintillator production chain took place in a controlled environment without contact to oxygen or other substances and materials that could have a negative impact on the scintillator stability. In addition, the scintillators were tested and tuned for compatibility with the acrylics.

Optical properties: In a large-volume detector the liquids have to be very transparent for the emitted scintillation light to reach the PMTs. The attenuation lengths for wavelengths of the scintillation spectrum should be comparable to the detector dimensions or larger. This is achieved by using high-purity materials and, if necessary, additional purification steps to remove absorbent impurities. In addition, the fluorescent components which are responsible for the scintillation performance, were chosen such that the scintillation light could be efficiently shifted to higher wavelengths. This minimizes absorption losses and also increases the light detection efficiency at the PMTs. Light yield quenching due to the presence of the metal-organic complex also has to be minimized.

Radiopurity: The use of high-purity materials is not only of concern for the optical properties, but also to minimize the rate of internal radioactive background. Dodecane and PXE were already tested for radiopurity by KamLAND and Borexino respectively and found to meet the Double Chooz requirements.[39;40] The efforts thus concentrated on the solutes. The activity of the solutes was measured by means of neutron activation analysis, atomic absorption spectroscopy and gamma spectroscopy. With specialized treatments of the substances their activity could be minimized. The radioisotope content of the complete scintillator mixtures is dominated by remaining natural Potassium, which was measured to be below 2 ppb.

Precise proton number: The Hydrogen nuclei are the targets for the IBD reaction. Their number in the detector, the *proton number*, is therefore an essential parameter for the experiment. It is especially important, as Double Chooz only takes data with the Far Detector in the first phase of the experiment. In

this arrangement the uncertainty of the proton number directly contributes to the error budget, and has to be known very precisely. First and foremost, this was achieved by utilizing only substances with a well-defined chemical structure. For example, *linear alkyl benzene* (LAB), which is a recent choice for large-scale neutrino detectors, was not considered suitable for this purpose. Instead, Double Chooz opted for pure *n-dodecane* ($C_{12}H_{26}$) as the solvent. During production the components were precisely weighed, to have an exact knowledge of the composition of the mixtures. Later, in the two-detector phase, the Near Detector (with identical proton number) acts as a reference, and the uncertainties of the proton number largely cancel. Section 3.7 is concerned with the proton number in more detail.

Light yield and density matching: As Double Chooz uses a two-part Inner Detector, the light yields of the two scintillators have to be adjusted to each other. If the light yields did not match within a narrow tolerance range, this would lead to distortions in the energy reconstruction of detector events. At the same time all liquids must have the same density. Differences in the liquid density would cause unwanted buoyancy forces between the volumes, which in turn would create mechanical stress on the acrylic vessels. The Gamma Catcher composition was adjusted by adding the mineral oil Ondina 909, so that it matches the Target in light yield and density, and tuning of the PXE and PPO concentrations.

Safety considerations: It was also taken care of minimizing safety hazards. Both dodecane and PXE have comparably high flash points and low toxicity, and the scintillator mixtures fulfil the requirements.

The final compositions of the liquids are given in Table 3.1. For completeness it also includes the Buffer and Inner Veto liquids, which were produced by TUM, Munich.

3.4.1 *Gadolinium complex*

Gadolinium is characterized by an extremely large thermal neutron capture cross section. With 254000 barn the isotope ^{175}Gd has the highest cross section of all stable nuclides (and the second largest of all known nuclides, after the unstable ^{135}Xe). The isotopic composition of natural Gadolinium is shown in Table 3.2. It consists of seven isotopes, which have a combined mean cross section that is about five orders of magnitude larger than that of Hydrogen. After capturing a thermal neutron, the daughter nucleus instantaneously deexcites via the emission of several Gammas and releases a total energy of about 8 MeV. The high decay energy places the signal from neutron captures on Gadolinium well above typical background events (most background has energies below 3 MeV). This enables a very clean selection of neutron capture events and predestines Gadolinium for an efficient neutron detection.

	name	content	chemical name	CAS number
Target				
	Dodecane	80 %$_{\text{vol}}$	n-dodecane	112-40-3
	PXE	20 %$_{\text{vol}}$	o-phenylxylylethane	6196-95-8
	PPO	7 g/l	2,5-diphenyloxazole	92-71-7
	bis-MSB	20 mg/l	1,4-bis(2-methylstyryl)benzene	13280-61-0
	Gd(thd)$_3$	4.5 g/l	Gd(III)-tris-(2,2,6,6-tetra-methyl-heptane-3,5-dionate)	14768-15-1
	THF	0.5 %$_{\text{wt}}$	tetrahydrofuran	109-99-9
GC				
	Dodecane	30 %$_{\text{vol}}$	n-dodecane	112-40-3
	Ondina 909	66 %$_{\text{vol}}$	mineral oil	8042-47-5
	PXE	4 %$_{\text{vol}}$	o-phenylxylylethane	6196-95-8
	PPO	2 g/l	2,5-diphenyloxazole	92-71-7
	bis-MSB	20 mg/l	1,4-bis(2-methylstyryl)benzene	13280-61-0
Buffer				
	Cobersol C70	46.5 %$_{\text{vol}}$	mixture of n-alkanes	64771-72-8
	Ondina 917	53.5 %$_{\text{vol}}$	mineral oil	8042-47-5
Veto				
	Cobersol C70	50 %$_{\text{vol}}$	mixture of n-alkanes	64771-72-8
	LAB	50 %$_{\text{vol}}$	linear-alkyl-benzene	67774-74-7
	PPO	2 g/l	2,5-diphenyloxazole	92-71-7
	bis-MSB	20 mg/l	1,4-bis(2-methylstyryl)benzene	13280-61-0

Table 3.1: Composition of the Double Chooz liquids. Please note that the concentration of 4.5 g/l of the Gd-complex Gd(thd)$_3$ is equivalent to 1 g/l Gadolinium in the Target. scintillator.

Gadolinium itself is not soluble in the scintillator. To bring it into a soluble form a metal-organic complex is produced. The Chooz and Palo Verde experiments have shown that the creation of a stable complex is far from trivial.[3;41] For example, Chooz suffered from a rapid degradation of its rare-earth complex, which decisively limited the experiment lifetime. Consequently, highest priority was given to the development of a chemically stable and durable Gadolinium complex. Extensive studies with a number of possible organic ligands were per-

isotope	NA	$\sigma(n^0_{\mathrm{therm}})$	$\sum E_\gamma$
^{152}Gd	0.20 %	735 b	6.247 MeV
^{154}Gd	2.18 %	85 b	6.438 MeV
^{155}Gd	14.80 %	60900 b	8.536 MeV
^{156}Gd	20.47 %	1.5 b	6.360 MeV
^{157}Gd	15.65 %	254000 b	7.937 MeV
^{158}Gd	24.84 %	2.2 b	5.942 MeV
^{160}Gd	21.86 %	0.77 b	5.635 MeV

Table 3.2: Isotopic composition of natural Gadolinium.[45] Due to the overwhelmingly large thermal neutron cross section, the line at 7.937 MeV dominates the deexcitation spectrum.

formed.[36;42;43;44] The decision ultimately was taken in favor of β-diketonates because of their superior stability and the possibility to sublimate the resulting compounds.[37] This is a big advantage, since a sublimation procedure can be used to increase the purity of the chemical.

Beta-diketones (in IUPAC nomenclature *1,3-diketones*) are a class of diketones, in which the two carbonyl groups are separated by one carbon atom. This configuration is especially advantageous, since it allows both carbonyl groups to bind together to the central ion. The specific diketone used in Double Chooz is *2,2,6,6-tetra-methyl-heptane-3,5-dione* (abbreviated as *thd*), i.e. a heptane skeleton with a carbonyl group at the third and fifth carbon atom, and two methyl groups at the second and sixth carbon atom.

Together with a central Gadolinium atom the *thd* diketones form the metal-organic complex *Gd(III)-tris-(2,2,6,6-tetra-methyl-heptane-3,5-dionate)*, abbreviated Gd(thd)$_3$. In this compound the central Gadolinium atom is encompassed by three *thd* ligands. The two coordinate bonds that each ligand forms with the Gadolinium atom lead to special chemical stability of the compound, based on the chelate effect. The rather large *thd* ligands also occupy much of the space surrounding the Gadolinium atom, protecting it from other molecules.

3.4.2 *Neutrino Target design*

The composition of the Target was decided first. Due to the presence of the Gd-complex this scintillator has the most design constraints; while there is more flexibility to adjust the other liquids.

The solvent is a mixture of 20 %$_{\mathrm{vol}}$ PXE and 80 %$_{\mathrm{vol}}$ n-dodecane. *PXE*, or *o-phenylxylylethane*, is an organic solvent characterized by a high flash point (at 145 °C) and low toxicity, and is considered as "non-hazardous".[39] This makes

the compound favorable in terms of safety aspects. PXE is a fluorescent compound with an emission spectrum in the UV range. In high concentrations, however, it would be aggressive to the acrylics. For material compatibility it is diluted with *n-dodecane*.

Dodecane is available very clean and in industrial quantities. It has a very high transparency for light at the scintillation wavelengths and is compatible with many other chemicals. Additionally, the fraction of Hydrogen atoms in pure dodecane can be easily calculated from its chemical sum formula ($C_{12}H_{26}$). This is essential for a precise knowledge of the proton number, as it is required in Double Chooz. Mineral oils, which are also a commonly chosen as scintillator solvents, are admixtures of different hydrocarbons with varying structures and sum formulas, and do not fulfill this requirement.

The complex $Gd(thd)_3$, described in the previous paragraph, is added to the mixture for the efficient detection of neutrons. On the other hand, the complex absorbs strongly in the region of the PXE emission and reduces the scintillation light yield. But due to the very large cross section of Gadolinium, low concentrations already lead to a high neutron detection efficiency. A concentration of 4.5 g/l of the complex $Gd(thd)_3$, which is equivalent to a concentration of 1 g/l Gadolinium, is sufficient for a good neutron capture efficiency while maintaining a high light yield.

The solutes PPO and bis-MSB are added to shift the emission spectrum to higher wavelengths and towards the sensitive region of the PMT photocathode. The fluors were chosen such that their absorption spectra largely overlap with the emission spectrum of the previous component, so that the light is efficiently "passed on" from component to component. This is displayed in Figures 3.3 and 3.4. It can also be seen in the graphic that the absorption spectrum of PPO overlaps partly with the one of $Gd(thd)_3$. This means that PPO competes with the Gd-complex for the primary scintillation light. Due to its larger concentration it intercepts much of the light before it can be absorbed by $Gd(thd)_3$ and shifts it to higher wavelengths, where the complex does not absorb any more.

3.4.3 *Gamma Catcher design*

The Target is the reference for the design of the other Double Chooz liquid. The Gamma Catcher has to be matched to the Target in terms of density and light yield. Both properties have to be adjusted simultaneously, since a change of one property also influences the other. Details about the adjustment procedure are given in [35]

The main difference between Target and Gamma Catcher is the lack of the Gd-complex in the latter. Since the complex acts as a quencher, this would lead to a light yield difference between the two liquids if the composition was otherwise
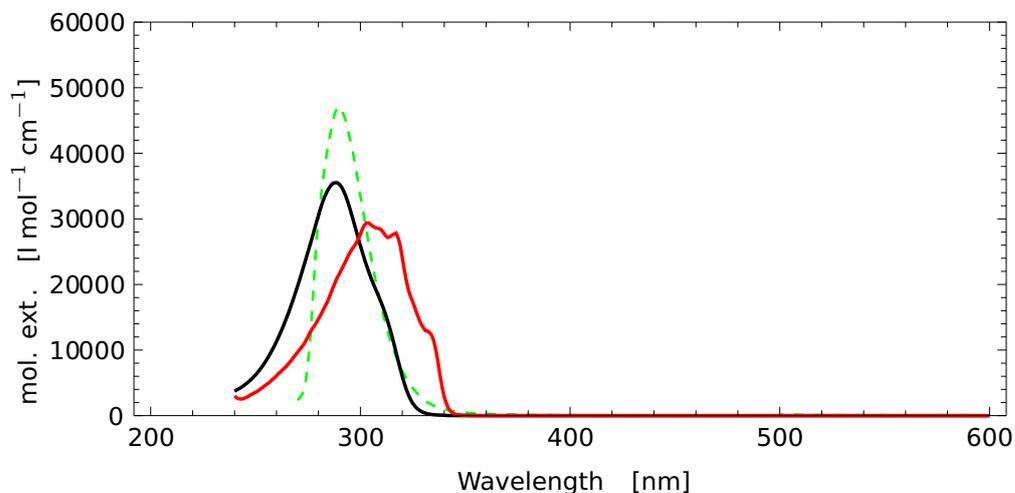
Figure 3.3: Absorption spectra of PPO (red) and the Gd-complex Gd(thd)$_3$ (black). The spectra were taken separately for each component in low concentrations. The position of the PXE emission peak is shown with the green curve (in arbitrary units). It is seen that both PPO and Gd(thd)$_3$ compete in the region of the PXE emission.
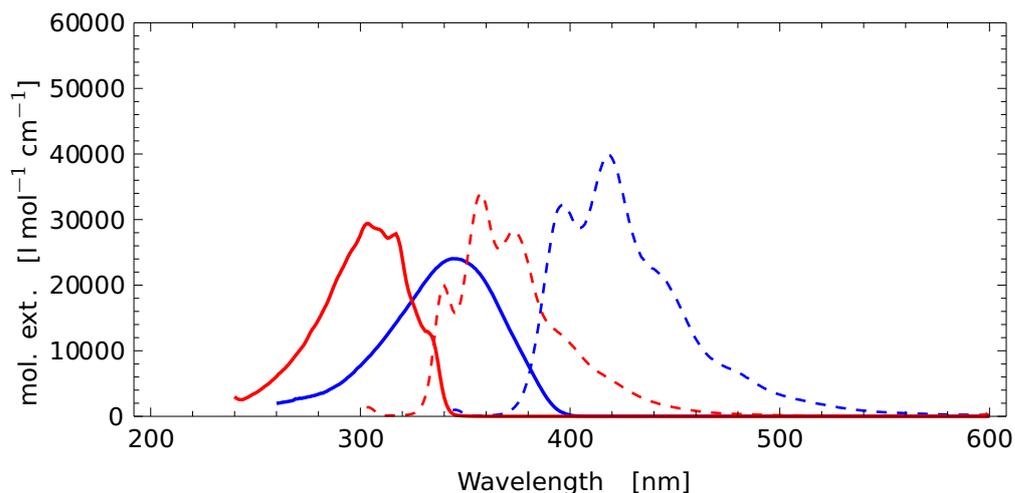
Figure 3.4: Absorption spectra (continuous lines) and emission spectra (dashed) of PPO (red) and bis-MSB (blue). The spectra were taken separately for each component in low concentrations. In the complete scintillator mixtures non-radiative transfer processes are important (see Section 3.6) and the emission spectrum of the whole mixture is different from the spectrum of the components.

equal. This would be problematic for the reconstruction of the event energy from the amount of scintillation light, since it would then depend strongly upon the event position. The Gamma Catcher must therefore have a different composition

than the Target in order to reduce the light yield to the Target level.[5] This is achieved by lowering the PXE ratio and the PPO concentration.

Changing the ratios of the substances, on the other hand, also changes the density of the mixture. If the difference in density is too large, it could result in large net pressure on the fragile acrylic vessels, which might take damage. In consequence, the reduction of the amount of PXE – which has a rather high density [6] of 0.984 kg/l – must be compensated by another liquid with a density between that of PXE and dodecane (with 0.747 kg/l). The mineral oil *Ondina 909* is used for this purpose. It has a density of 0.811 kg/l, high transparency at scintillation wavelengths and good viscosity values. The use of mineral oils is possible in the Gamma Catcher. In the Gd-analysis the main detection volume is the Target, and the requirement of a very precisely known proton number is alleviated for the Gamma Catcher. A detailed light yield model, presented in [38], helped in the design of the Gamma Catcher. The model is based upon the different energy transfer paths that are possible in the current scintillator configuration. The density and light yield adjustment was achieved with a solvent mixture of 30 % dodecane, 66 % Ondina 909 and 4 % PXE. The fluors PPO and bis-MSB are present at concentrations of 2 g/l and 20 mg/l respectively. All four Double Chooz liquids have a density of 0.804±0.001 kg/l at 15 °C.

A version of the Gamma Catcher with 5 g/l PPO was also studied. The concentration would be above the *critical concentration* of the mixture, so that the light yield would be practically independent of the actual PPO concentration. However, this possibility was later scrapped in favor of the 2 g/l version. The larger difference to the Target fluor concentration makes the scintillation process "slower", leading to a different pulse shape. How the differences in the scintillation pulse shapes of the Gamma Catcher and the Target can be exploited for pulse shape discrimination is shown in Chapter 9.

3.5 SCINTILLATOR PRODUCTION

The scintillators for the Neutrino Target and Gamma Catcher volumes were designed and produced at MPIK, Heidelberg. The large-scale production of the Target and the Gamma Catcher is described in [37] and summarized in the following.

Each detector requires 10.3 m^3 of Target and 22.3 m^3 of Gamma Catcher liquid. For the production of the two scintillators on a multi-ton scale, a dedicated scintillator hall was built at the MPIK. The hall houses several transportable

---

[5]In fact, the light yield of the Gamma Catcher is tuned slightly below the Target level, since there is a higher light collection efficiency in the outer volume. The lower light yield serves to compensate the higher detection efficiency, so that the observed light yield is homogeneous over the whole Inner Detector scintillator volume.

[6]The density values given here refer to a temperature of 23 °C.

24.000 l tank containers in a standard 20′ ISO frame for storage of the chemicals and shipment of the scintillators to the detector site in Chooz.

An especially designed liquid handling system was installed in the hall, which allows to move the chemicals to virtually any desired container. The liquids can be transferred between storage and mixing volumes without contact to air or to other materials which could degrade the quality of the chemicals. All materials in contact with the Target components are made of inert fluorinated hydrocarbons. Furthermore, a gas system provides a steady supply of nitrogen at operating pressures of the liquid pumps as well as at low pressures for bubbling and maintaining a nitrogen blanket in the tanks. The liquids could so be kept under a nitrogen atmosphere at all times.

Mixing of the liquid takes place in the 600 l *mixing tank* made of PVDF. It is equipped with an electric stirring unit for a thorough mixing of the liquids and a precision scale to weigh the components. Also, in the case of the Target scintillator, a special *weighing tank* is used during production. It serves the purpose to measure the exact mass of the scintillator, leading to a small uncertainty of the proton number (see Section 3.7).

3.5.1 Preparation

Dodecane was purchased from Japan Energy. It is the same product which was already used in KamLAND and has shown excellent optical and radiochemical properties. PXE was produced at Dixie Chemicals, Houston and was already very clean compared to industrial standards. To improve the optical and radiochemical purity further, PXE was processed in an additional column purification step at the MPIK. In this step the liquid was pressed through a column containing layers of powders with different pH (to remove acid, basic and neutral impurities from PXE) and filter materials (to hold back the particles of the column material). This way, the attenuation length of PXE could be improved from 2.9 m to over 8 m.

The metal-organic complex was produced at *Sensient Imaging Technologies*, Wolfen. The powder was sublimed to increase its purity. Until the production of the liquids began, the compound was stored in an underground laboratory to reduce exposure to cosmic radiation. It was kept in glass bottles under an inert Argon atmosphere and additionally sealed in air- and light-tight aluminized bags.

PPO was produced at Perkin-Elmer, where additional purification steps were added to the synthesis of the material to meet the purity specifications. Bis-MSB was purchased from Sigma-Aldrich and did not require any further processing.

3.5.2 Mixing

Even though Gadolinium in the form of $Gd(thd)_3$ is equipped with organic ligands, the complex still dissolves very reluctantly in the scintillator. To overcome this problem several concentrated solutions were prepared under laboratory condi-
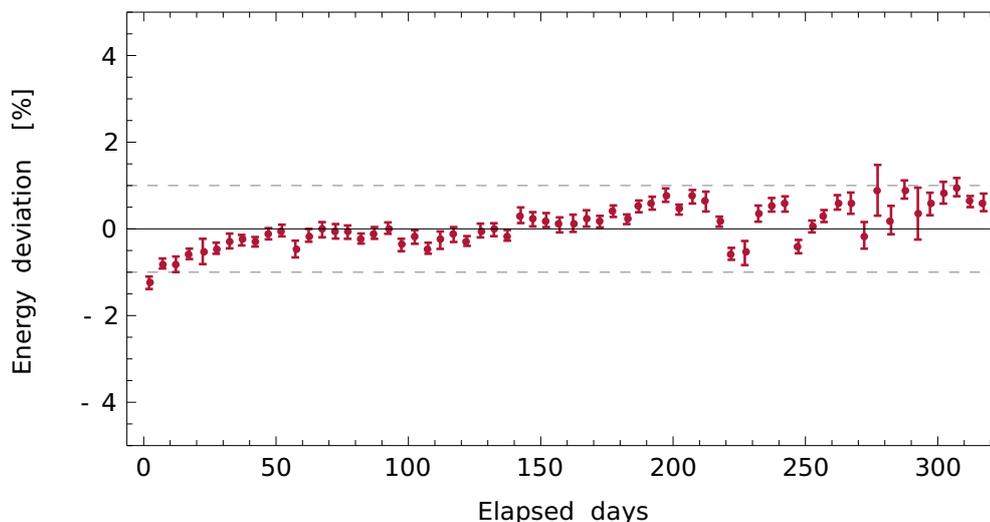
Figure 3.5: Detector stability over the runtime. The relative position of the Gadolinium neutron capture peak is shown as measured with spallation neutrons. The peak position remained stable within 1 %. This way the plot demonstrates the good stability of the scintillator. [1]

tions before mixing them with the other liquids. The Gd(thd)$_3$ powder was first dissolved in pure THF in the chemistry lab at MPIK. The mixture was magnetically stirred for several days until the powder was completely dissolved. These concentrated solutions were then added to dodecane in the mixing tank. In all transfer steps the liquids were pumped through PVDF tubes from one compartment into the other, so that no contact to oxygen could occur. The THF used to dissolve the Gd-complex remained in the solution. In the mixture it acts as a stabilizing agent, which prevents other molecules (most importantly water) from docking to the Gd-complex and potentially leading a degradation of the compound.

In a second step the fluors PPO and bis-MSB were dissolved in PXE in high concentrations. This mixture was then transferred to the weighing tank and added to the dodecane/Gd-solution. Finally, the remaining PXE was added to the mixture. Between the individual steps samples of the mixture were taken and their optical properties checked.

The design and production of the scintillator has lead to a very stable scintillator. Figure 3.5 shows the stability of the Target in the running detector as monitored with spallation neutrons captured on Gadolinium (see Chapter 5). The light yield remained stable within 1 %.
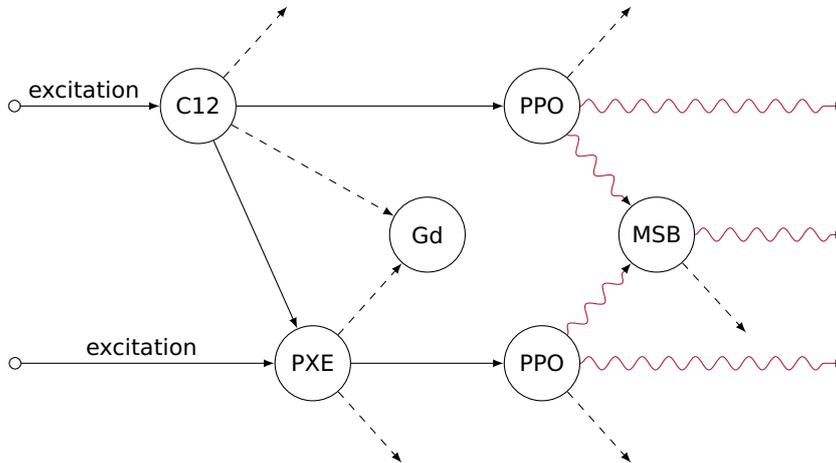
Figure 3.6: Depiction of energy transfer paths in the Target scintillator.[38] The solid lines represent predominantly non-radiative transfers, while the wavy red lines represent emission of optical photons (radiative transfers). Dashed lines are processes which lead to light loss in the scintillator. These are mostly thermal deexcitations (which affect all molecules), but also transfers from dodecane and PXE to the Gadolinium complex, which acts as a quencher. The radiated spectrum is a combination of the PPO and the bis-MSB emission spectra. The absorption and emission spectra involved in the non-radiative dodecane/PXE→PPO system are shown in the fist part of Figure 3.3; the relevant spectra for the radiative processes of PPO and bis-MSB are shown in Figure 3.4.

3.6 THE SCINTILLATION PROCESS IN THE DOUBLE CHOOZ SCINTILLATORS

This section is a reprise of Section 3.1 for the specific case of the Double Chooz scintillators. It explains the energy transfer mechanism and the characteristics arising from their composition, which were also used for the scintillator model in [38].

The transfer paths in the Double Chooz scintillators are depicted in Figure 3.6. The overall energy transfer chain is dodecane/PXE→PPO→bis-MSB. At the very beginning is the excitation of the bulk matter by the primary particle. This is either dodecane or PXE.[7] Due to their small concentrations, the direct excitation of the fluors by the primary particle is extremely rare and can be neglected.

Dodecane transfers its excitation energy predominantly to PXE. The transfer dodecane→PPO has a smaller probability but is still relevant, while a direct excitation of bis-MSB from dodecane is negligible. The concentration of PPO in the mixture is higher than the critical concentration c_0, which is given by the

---

[7]In the Gamma Catcher there is also Ondina 909, but for the scintillation mechanism it only acts as transparent bulk matter and can be treated like dodecane.

Förster radius (3.1) of the PXE-PPO-system. This leads to a predominantly non-radiative energy transfer from PXE to PPO. This is important in this region, since PXE has an emission spectrum in the near UV, where the scintillator also shows strong absorption by the Gd-complex.

The energy transfer from PPO to bis-MSB is mostly radiative, but a non-radiative component is still present. In the case of radiative transfer, a photon is emitted with the PPO spectrum. It then propagates through the scintillator and is eventually absorbed on bis-MSB.

The step-by-step transfer leads to a strong dependence of the scintillation spectrum on the path length. If the path between light creation and detection is very short, the PPO→bis-MSB transfer is not complete and most photons are emitted with the PPO spectrum. The detected spectrum, however, will not be a pure PPO emission spectrum. Since there is still non-radiative energy transfer to bis-MSB, there is already a contribution of the bis-MSB spectrum at this stage. The detected spectrum is thus a combination of both. It was found that this combined spectrum is consistent with a linear combination of 70 % PPO and 30 % bis-MSB. [46] This is the *primary spectrum* of the scintillator, as used in the simulation.

With increasing path lengths that the photons have to travel through the scintillator, more and more are absorbed and re-emitted by bis-MSB. This way the spectrum shifts towards longer wavelengths. The dependence of the scintillation spectrum on the path length is shown in Figure 3.7

When the energy follows the PXE → PPO → bis-MSB chain, the scintillator shifts from non-radiative to radiative behavior. This is accompanied by ever higher emission wavelengths of the components. In consequence, the scintillator can be divided into two regions: a predominantly non-radiative domain at short wavelengths, and a radiative domain at higher wavelengths. The transition between the two regimes is at around 340 nm. Below this threshold there is no emission; above 340 nm the primary emission spectrum begins.

This behavior is important for the simulation of the scintillator in the Monte Carlo. The micro-physical processes in the non-radiative domain cannot and need not be simulated. The real photons occurring in the radiative domain, however, are subject to optical processes (like absorption, reemission or reflection) and have to be tracked individually. Therefore, to achieve an efficient simulation of scintillation, the two domains are treated differently in the Monte Carlo (see also Section 6.1).

3.7 PROTON NUMBER

In this section special attention is given to the number of Hydrogen nuclei in the fiducial volume, the so-called *proton number*. The proton number is a critical
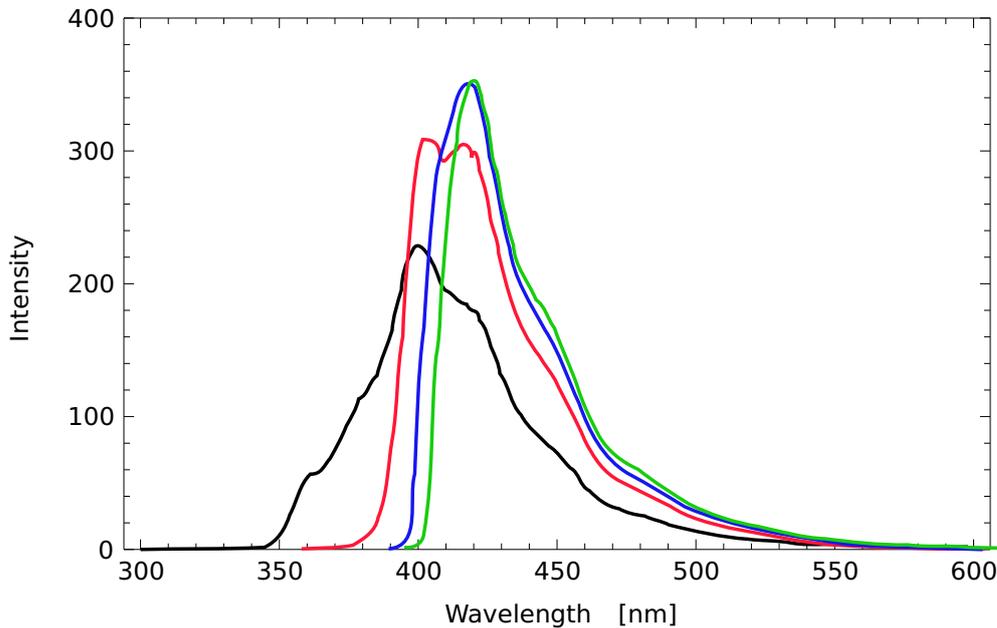
Figure 3.7: Change of the scintillation spectrum with the path length in the scintillator. The black line shows the measured primary spectrum, which is used in the Monte Carlo. The other curves are simulations of how the spectrum evolves with the path length in the scintillator. The effect of bis-MSB is clearly visible: after 1 cm most of the light is already shifted to the bis-MSB spectrum (red line). After 10 cm the spectrum is nearly completely shifted (blue); a further increase of the path length to 50 cm has only a small additional effect on the spectrum (green). [35]

parameter for the experiment. It determines the number of reaction targets for the inverse beta decay and its uncertainty is directly related to the uncertainty of the neutrino flux. A one percent lower proton number would lead to a one percent decrease of the detected number of neutrinos.

To have precise control over the amount of the components in the mixtures, the substances were weighed during mixing. It was also monitored how much Target liquid entered the detector. Immediately before filling the detector the Target liquid was stored in the underground neutrino laboratory in a dedicated weighing tank, which is equipped with a high-precision scale. The variations of the gravitational acceleration with the location were measured and compensated. By weighing the tank at the beginning and the end of the filling procedure, the mass of Target liquid that is actually in the detector was determined with a precision of 0.04 %. [1]

From this information the absolute number of protons can be calculated as

$$N_p = f_p \frac{m_{\text{Target}}}{m_H} \tag{3.3}$$

where m_{Target} and m_H are the mass of the Target liquid in the detector and of a single Hydrogen atom respectively. This calculation also requires f_p, the Hydrogen fraction (by mass) of the mixture.

When the precise chemical structure of component i is known, its Hydrogen fraction f_i can be calculated from the measured masses and the chemical structure via

$$f_i = \frac{n_{H,i} M_H}{M_i} \tag{3.4}$$

where $n_{H,i}$ is the number of Hydrogen atoms in the compound and M_H and M_i are the molar masses of (atomic) Hydrogen and the component i. The Hydrogen fraction of the mixture is then

$$f_p = \sum_i \frac{m_i}{m_{\text{Target}}} f_i \tag{3.5}$$

where i runs over all components.

3.7.1 Target

In the case of the Target the Hydrogen fractions of the single components can be calculated precisely from their elementary compositions. The error of its proton number is dominated by the uncertainty on the component masses. The total mass of the Target scintillator could be determined with high accuracy with help of the weighing tank.

To estimate the uncertainty of the number of Hydrogen nuclei in the detector two cases were considered: one, where all variations go in the direction of a higher proton number, and one where they all lead to a lower number. These scenarios were taken as the boundary cases and determine the uncertainty of the value. They serve as very conservative estimates and the actual uncertainty on the Hydrogen fraction is supposedly smaller.

High Hydrogen fraction: The masses of both dodecane and PXE have an uncertainty of 10 kg. In the high proton number case there would be an additional 10 kg of dodecane in the scintillator, and in turn 10 kg less of PXE. The content of the stabilizing agent THF is also modified. THF is very volatile and some evaporation losses into the Nitrogen blanket on the liquids are likely. In this scenario, it was assumed that the volatile THF completely evaporated from the scintillator during filling. A contribution of impurities was unlikely in this scenario, since hydrocarbons are among the chemicals with the highest hydrogen to carbon ratio. It is hard to conceive any reasonable contamination

that would raise the Hydrogen fraction, so impurities were disregarded here. Under these assumptions the mass percentage of Hydrogen atoms in the Target liquid is 13.62 %.

Low Hydrogen fraction: For the lower bound of the Hydrogen fraction the opposite assumptions were made. The PXE mass was increased by 10 kg, in exchange for 10 kg less dodecane. This time evaporation losses of the THF were neglected, so that it contributes with full 49 kg to the mixture mass. In this scenario the possibility of impurities with a low Hydrogen fraction also had to be considered. It was assumed an impurity content of 10 kg in PXE, which amounts to 0.4 % of its total mass, and 30 kg dodecane (0.5 %, according to the test results by Japan Energy[47]). From the data sheets and gas chromatography–mass spectrometry measurements it can be inferred that the impurities are chemically similar to the substances themselves. It appears conservative to assume that the Hydrogen fractions of the impurities are only half as big as those of dodecane or PXE. Contribution from possible impurities of the solutes are negligible. In this case the mass fraction of Hydrogen becomes 13.56 %.

In bulk quantities n-dodecane is refined from mineral oil and can have a small content of alkanes with different lengths. It was also tested how the presence of these alkanes would impact the proton number. The specification of the n-dodedcane by Japan Energy state that the content of undecane and tridecane is each 0.2 %.[47] Both alkanes have practically the same ratio of Hydrogen to Carbon atoms (of about 2:1) and even the maximum amount of undecane or tridecane impurities would only have a negligible effect on the Hydrogen fraction. From the above considerations the value for the Target is then (13.59 ± 0.03) %.

For an experimental cross-check samples of the Target were sent to *BASF Kompetenzzentrum Analytik*, Ludwigshafen, for a CHN-analysis. This procedure involves a combustion of the sample in an oxygen-loaded atmosphere and a chemical analysis of the reaction products, from which the elementary composition of the original sample is deduced. The CHN-analysis found a Hydrogen mass percentage in agreement with the above value within the measurement's uncertainty (about 1 %).

The total number of Hydrogen nuclei is then determined from the Target mass measurement. The Hydrogen fraction of (13.59 ± 0.03) % translates to $(6.747 \pm 0.020) \cdot 10^{29}$ protons in the Target.[4]

3.7.2 *Gamma Catcher*

The mass of the Gamma Catcher liquid was calculated from the liquid density and the volume of the acrylic recipient. From measurements of its dimensions, it was found to hold a volume of 33.210 ± 0.065 m^3, including the slightly cone-

shaped top and bottom lids. The error is mostly due to a slight ellipticity of the mantle structure. The Target vessel and its acrylic supporting structures occupy 10.668 m^3 within the volume (with negligible error), so that the total Gamma Catcher volume is 22.542 m^3 with 0.3 % uncertainty.[48] Consistent results were found in a flow meter mass measurement with slightly lower precision compared to the geometrical calculation.[49]

The Hydrogen fraction of the Gamma Catcher cannot be calculated with equation (3.5), since the main component Ondina 909 does not have a well-defined chemical structure. It was instead experimentally determined via CHN-analysis at BASF, where a Hydrogen mass fraction of 14.6 % was found with a 1 % uncertainty on the value.

Since Ondina 909 is the only component without a well known chemical structure, it might be favorable to perform the CHN-analysis on the mineral oil only, and calculate the Hydrogen fractions of the other components via equation (3.4). This alternative approach was also tested and found to give a result in accordance with the above value. However, this method did not significantly improve the uncertainty of the proton number, since Ondina 909 is by far the compound with the largest amount in the mixture.

All in all, it can be concluded that a CHN analysis cannot determine the proton number with the same level of precision as with mass measurements and calculation from the chemical composition.[37] This is reflected in the larger uncertainty on the proton number of 1.01 % for the Gamma Catcher,[?] compared to 0.3 % for the Target.[4]

The Hydrogen analysis, which also makes use of the Gamma Catcher as an IBD reaction volume, has been unforeseen at the time when the scintillators were designed. Otherwise, it might have been advantageous to use other pure n-alkanes instead of Ondina 909. On the other hand, as long as data is only taken with the Far Detector, in both the Gadolinium and the Hydrogen analysis the uncertainty of the Gamma Catcher proton number is not a dominating contribution to the error budget.

3.7.3 Buffer

The Hydrogen fraction of the Buffer liquid was also determined via a CHN analysis, again conducted at BASF, Ludwigshafen. The result of the measurement was (14.80 ± 0.15) %. The value is mainly important in spill-in/out studies for the Hydrogen analysis.[49] Since this effect has only a small overall impact on θ_{13}, the given value is sufficiently accurate.

3.7.4 Two-detector case

The experimental concept of Double Chooz is to have two identical detectors at different distances from the reactor cores. In this setup the Near Detector is used as a reference and many uncertainties in the analysis of θ_{13} are greatly reduced.

To guarantee an identical Hydrogen fraction in both detectors, the Target scintillator was produced in one single batch for both detectors. When the Far Detector was filled, the batch was split in half and one part was used for the filling. The second half is stored until the filling of the Near Detector begins. Thus, the same mixture is used for both detectors. When data taking with both detectors commences, the errors on the Hydrogen fraction cancel (since they are equal) and the uncertainty of the proton number is then given only by the weight measurements of the two Target masses. This will reduce the uncertainty of the proton number to 0.06 % for the Gd-analysis. [49]

CHAPTER 4

A THEORY OF IONIZATION QUENCHING

4.1 BIRKS' FORMULA

The knowledge of the scintillator response function is an important matter in many scintillator experiments. Even though the scintillation response is reasonably linear for higher particle energies, it is well known that it becomes nonlinear at low particle energies due to *ionization quenching*. In 1951 Birks introduced a semi-empirical formula to model this nonlinearity.[30;50] According to this model the mean differential light yield $\langle \mathrm{d}L/\mathrm{d}x \rangle$ is

$$\left\langle \frac{\mathrm{d}L}{\mathrm{d}x} \right\rangle = \frac{L_0 \left\langle \frac{\mathrm{d}E}{\mathrm{d}x} \right\rangle}{1 + kB \left\langle \frac{\mathrm{d}E}{\mathrm{d}x} \right\rangle}, \tag{4.1}$$

where L_0 is a normalization factor for the light output per MeV deposited in the medium by the primary particle. kB is a parameter product which describes the strength of the quenching effect and is often called *Birks-parameter*. Even though Birks originally developed his model only for inorganic crystal scintillators, it is successfully applied to practically all types of scintillators, including organic liquid scintillators. It is probably the most widely used formula to describe the ionization quenching phenomenon.

Under some circumstances, e.g. for incident heavy ions, the formula may not be accurate enough. In such cases higher orders of $\langle \mathrm{d}E/\mathrm{d}x \rangle$ are routinely employed. For example, the particle physics simulation software FLUKA[51] uses a model

$$\left\langle \frac{\mathrm{d}L}{\mathrm{d}x} \right\rangle = \frac{L_0 \left\langle \frac{\mathrm{d}E}{\mathrm{d}x} \right\rangle}{1 + B \left\langle \frac{\mathrm{d}E}{\mathrm{d}x} \right\rangle + C \left\langle \frac{\mathrm{d}E}{\mathrm{d}x} \right\rangle^2} \tag{4.2}$$

with two parameters B and C, which was motivated by Chou.[52]

In his model Birks only considers a single primary particle. In reality, how-ever, an incident charged particle of sufficiently high energy ejects electrons from the atomic shells of the material, which can themselves excite and ionize further molecules. These secondary electrons typically receive low kinetic energies and their light is consequently quenched very much. If one then attempts to fit equation (4.1) to measured data, the fit will try to compensate the additional loss of light by increasing the value of kB. If instead a detailed simulation is carried out with explicit creation of secondary electrons, the result is better adapted to the physical situation and lower than in the first case.[35]

In a more thorough treatment of the micro-physical processes Voltz and Laustriat[53] find

$$\left\langle \frac{\mathrm{d}L}{\mathrm{d}x} \right\rangle = L_0 \left\langle \frac{\mathrm{d}E}{\mathrm{d}x} \right\rangle e^{-B\left\langle \frac{\mathrm{d}E}{\mathrm{d}x} \right\rangle} \tag{4.3}$$

for the special case of incident electrons. In their model this equation can be derived from from a more general case

$$\left\langle \frac{\mathrm{d}L}{\mathrm{d}x} \right\rangle = L_0 \left[(1-F)A_s^{(1)} \left\langle \frac{\mathrm{d}E}{\mathrm{d}x} \right\rangle e^{-B_s(1-F)\left\langle \frac{\mathrm{d}E}{\mathrm{d}x} \right\rangle} \right. \\ \left. + FA_s^{(2)} \left\langle \frac{\mathrm{d}E}{\mathrm{d}x} \right\rangle + A_t \left\langle \frac{\mathrm{d}E}{\mathrm{d}x} \right\rangle e^{-B_t\left\langle \frac{\mathrm{d}E}{\mathrm{d}x} \right\rangle} \right] \tag{4.4}$$

It uses several parameters F, $A_s^{(1)}$, $A_s^{(2)}$, A_t, B_s and B_t, but they are not explicitly given in their paper. This model also predicts an explicit particle dependence of ionization quenching and in an experimental campaign the authors have found that equation (4.4) reproduces the data more closely than equation (4.1).[54] Its rather complicated structure and the large number of adjustable parameters have nevertheless impeded a widespread usage of this model.

In the following analytical expressions will be developed for the mean differential light yield $\langle \mathrm{d}L/\mathrm{d}x \rangle$ and the total light yield $L(E)$ in dependence of the initial particle energy E.

The issues with Birks' semi-empirical model prompted the development of a new ionization quenching model, which is presented in the following.

4.2 THE QUENCHING PROCESS

Ionization quenching affects the scintillation light yield especially at low energies, while at higher kinetic energies the light yield becomes linear with the energy of the particle. For electrons this is already the case from about 200 keV upwards,[30] so we look at particles of relatively low energies here.

Several assumptions about ionization quenching are made. First it is assumed that the processes involved act before the creation of radiative photons. Other

processes which reduce the radiative photon yield are not attributed to ionization quenching any more, but to other quenching effects such as self-absorption.

Three classes of interactions between an excited molecule $A^\star$ and surrounding molecules can be distinguished:

- **Energy migration:** $A^\star$ interacts with an unexcited molecule of the same type A and passes the energy on to the latter. The excitation thus migrates through the medium until it comes close enough to an unexcited fluorescent molecule, to which it can transfer its energy. The fluor then converts the energy into a scintillation photon with a certain efficiency η.

- **Ionization quenching:** On the way through the medium the excitation energy is intercepted by another excited molecule $X^\star$. The interaction leaves one or both molecules in the ground state. The excitation energy of one or both molecules is then lost for scintillation. I follow the terminology of Birks and the term "ionization quenching" shall (without further specification) refer collectively to all interactions between excited molecules which reduce the number of excitations before they can reach a fluor. [30]

- **Non-radiative deexcitation:** If neither of the above processes has taken place within the mean lifetime τ of the excited state, the excitation energy dissipates into heat. These losses are generally attributed to the overall efficiency of the scintillator.

The requirement of two excited molecules also distinguishes ionization quenching from other types of light reduction processes, like *oxygen quenching*, *impurity quenching* or *self-quenching*. These processes affect the scintillator light yield independent of the particle energy and can be considered part of the scintillator light yield.

4.3 MEAN DISTANCE BETWEEN EXCITED MOLECULES

For simplicity it is assumed that two excited molecules interact if and only if they are produced within a distance R from each other. This ansatz has already been used quite successfully by Voltz et al. [53] Under this assumption ionization quenching is equivalent to an instantaneous reduction of the primary number of excited molecules, followed by an undisturbed propagation of the remaining electronic excitations or their non-radiative deexcitation respectively. R can therefore be considered the *critical distance* for ionization quenching.

Even though there are various micro-physical processes which cause ionization quenching, they always involve interactions between two excited molecules. This is different from energy migration, where an excited molecule interacts with a previously unexcited molecule and transfers its electronic excitation energy to the latter. An overview over processes relevant for ionization quenching can be found in [53].

The value of R depends on a variety of factors. For example, a higher fluor concentration or a large Förster radius leads to a higher probability for the excitation to reach a fluor molecule before it is quenched. Hence R decreases and L increases. On the other hand, a short excitation decay time reduces R and L, since an excited molecule has less time to encounter another excited molecule or a fluor.

The exact relations between these quantities and R are, however, most complex and it is very complicated to calculate R from them. It is more practical to obtain R from a fit to experimental data.

It is now of interest how many excited molecules have a distance greater than R from each other and in this way survive the ionization quenching phase. A particle traversing the scintillator creates excitations and ionizations along its path. The mean distance between two ionized molecules can be derived from the total ionization cross section. The probability density ρ for the ionization of a molecule by the primary particle after a distance x follows an exponential distribution and is given by

$$\rho(x) = n\,\sigma_p\,e^{-x\,n\,\sigma_p} \tag{4.5}$$

where σ_p is the energy-dependent total ionization cross section of the primary particle and n the number of atoms per unit volume (the number of electrons Z per atom is included in σ_p). The subscript p denotes the type of the incident particle. For the probability P that the particle traverses at least a distance R between two subsequent ionization processes then follows

$$P(x > R) = n\,\sigma_p \int_R^\infty e^{-x\,n\,\sigma_p}\,\mathrm{d}x = e^{-R\,n\,\sigma_p} \tag{4.6}$$

Under the above assumption of a hard distance threshold for quenching, this is equivalent to the fraction of unquenched excitations, i.e. the amount of molecules which "survive" ionization quenching and are available for scintillation light emission. The quantity shall be called *emission factor* for future reference.

In the context of this model the light loss due to ionization quenching is completely governed by this term. The general behavior of ionization quenching can already be qualitatively studied on the basis of this quantity. At high particle energies σ_p is small and practically constant over a wide range and the emission factor is close to 1. This is, nearly all of the excited molecules survive ionization quenching. Then, when the particle has only a small kinetic energy left, σ_p grows and the emission factor decreases just as expected.

4.4 LIGHT YIELD AS A FUNCTION OF PARTICLE ENERGY

To calculate the absolute amount of light emitted, we also have to know how many excitations the primary particle created in the first place. The mean number

of excitations within a short path of length $\mathrm{d}x$ is the inverse of the mean free path λ:

$$\left\langle \frac{\mathrm{d}N}{\mathrm{d}x} \right\rangle_p = \frac{1}{\lambda_p} = n\,\sigma_p \tag{4.7}$$

where n is the density of atoms of the material. The mean number of photons created in $\mathrm{d}x$ is then obtained by multiplying the above equation by the emission factor (4.6) and the *scintillation efficiency* η of the scintillator[1]

$$\left\langle \frac{\mathrm{d}L}{\mathrm{d}x} \right\rangle_p = \eta\,n\,\sigma_p\,e^{-Rn\sigma_p} \tag{4.8}$$

η contains all effects which take place after ionization quenching (such as the efficiency of energy migration, the quantum yields of the fluors, energy-independent quenching processes mentioned in Section 4.2 as well as absorption processes) and is independent of the particle energy. Equation (4.8) in an expression for the differential light yield. The *total* amount of light produced along the entire particle track (as a function of the initial energy of the incoming particle) is obtained by taking the integral of (4.8) over the distance. However, since x itself is a function of the energy, the integration variable has to be changed to E prior to integration. With

$$\mathrm{d}x = \mathrm{d}E \cdot \left\langle \frac{\mathrm{d}E}{\mathrm{d}x} \right\rangle_p^{-1} \tag{4.9}$$

we arrive at

$$\langle L \rangle_p = \eta\,n \int_0^E \frac{\sigma_p}{\langle \mathrm{d}E/\mathrm{d}x \rangle_p}\,e^{-nR\sigma_p}\,\mathrm{d}E \tag{4.10}$$

for the total light produced by the primary particle along its track.

4.5 QUENCHING OF ELECTRONS

We now turn to the total number of scintillation photons created by incident electrons. It is assumed in the following that the electrons do not have very high energies, so that the production of secondary electrons is negligible and does not have to be taken into account. The task is basically to integrate equation (4.10) with the respective formulas for σ and $\langle \mathrm{d}E/\mathrm{d}x \rangle$ for electrons. The subscript p will be omitted as long as the respective quantities refer to electrons.

Analytic formulas for these quantities were derived by Møller in his 1932 paper, which contains a full relativistic and quantum-mechanical treatment of the passage of electrons through matter.[55] The following formulas are taken from Møllers publication and were adapted to the notation of this thesis.

[1]It shall be especially noted here, that in the case of electrons with intermediate energies the total cross section can be approximated to be roughly proportional to the mean differential energy loss, i.e. $\sigma(E) \approx k \cdot \langle \mathrm{d}E/\mathrm{d}x \rangle$. In this case equation (4.51) is equivalent to Voltz' equation (4.3) for electrons, even though it was developed with a different approach.

4.5.1 Differential cross sections

Let E_0 denote the energy of the electron at rest and $E = E_0(\gamma - 1)$ its kinetic energy. β and γ are the Lorentz variables, and $\mathfrak{I}$ is the mean ionization energy of the atom.

There are three different cases to be considered: excitation into discrete atomic states, excitation of bound electrons into the continuum, and scattering off free electrons. These processes correspond to different amounts of the energy T transferred from the incident electron to the atomic electron.

Excitation of electronic states In the first case T is small and electronic states within the atom are excited. The corresponding cross-section is

$$\sigma_n = \frac{\chi}{\beta^2} \frac{\alpha^2}{\mathfrak{I}} |x_{0n}|^2 \left[\ln \frac{2\,a_n\,E_0^2\,\beta^2\gamma^2}{\mathfrak{I}} - \beta^2 \right] \tag{4.11}$$

for excitation of the nth state. The proportionality factor χ is given as

$$\chi := \frac{4\pi}{E_0^2} \cdot \frac{e^4}{(4\pi\epsilon_0)^2} \tag{4.12}$$

with e being the elementary charge and ϵ_0 the permittivity of free space. Its numerical value is $\chi = 5.1 \cdot 10^{-29}$ MeV m^2.

Ionization If the transferred energy is higher, bound electrons can be ejected from the atom into the continuum. The atom is ionized and the differential cross section is

$$\frac{\mathrm{d}\sigma}{\mathrm{d}\epsilon} = \frac{\chi}{\beta^2} \frac{1}{E\,\epsilon^2} \tag{4.13}$$

with $\epsilon = T/E$ being the fractional energy transfer.

Scattering off free electrons Finally, when the energy transfer to the atomic electron is so large that the latter can be considered free, the differential cross section becomes

$$\frac{\mathrm{d}\sigma}{\mathrm{d}\epsilon} = \frac{\chi}{\beta^2} \frac{1}{E^2} \left[\frac{1}{\epsilon^2} + \frac{1}{(1-\epsilon)^2} - \frac{2\gamma - 1}{\gamma^2} \frac{1}{\epsilon(1-\epsilon)} + \left(\frac{\gamma - 1}{\gamma} \right)^2 \right] \tag{4.14}$$

From the differential cross sections (4.11), (4.13) and (4.14) the total ionization cross section and the mean energy loss of a primary electron can be derived.

4.5.2 *Total cross section*

The total cross section is calculated by integrating the differential cross sections from the previous section over all possible energy transfers T. When the electron's kinetic energy is only of the order of several MeV, the number of interactions with high energy transfer are very rare compared to the number of soft collisions and it is sufficient to consider only equation (4.11).[55] This leads to

$$\sigma = \frac{\chi}{\beta^2} \frac{1}{\mathfrak{I}} \left(\ln \frac{2E_0^2 \beta^2 \gamma^2}{\mathfrak{I}} - \beta^2 \right) \tag{4.15}$$

where $\mathfrak{I}$ is the mean ionization energy, which results from the weighted summation over the possible electronic levels in (4.11).

4.5.3 *Mean energy loss*

The terms for soft and hard collisions merge smoothly at the cut value and one obtains (see for example [34])

$$\left\langle \frac{\mathrm{d}E}{\mathrm{d}x} \right\rangle = \frac{\chi}{\beta^2} n \left[\ln \left(\frac{E^2(\gamma + 1)}{2\mathfrak{I}^2} \right) - \beta^2 \right.$$
$$\left. + 1 - \frac{2\gamma - 1}{\gamma^2} \ln 2 + \frac{1}{8} \left(\frac{\gamma - 1}{\gamma} \right)^2 \right] \tag{4.16}$$

4.6 ESTIMATING THE QUENCHING RADIUS

The formulas of the previous paragraph already allow us to numerically compute the mean total light yield (4.10) for incident electrons. This is now used to estimate the critical distance R from a comparison of equation (4.10) and measured light yield data. Experimental light yield data for the Double Chooz scintillators is available from studies presented in [58].

The electron density n and the mean ionization energy $\mathfrak{I}$ can both be calculated from the chemical composition of the liquid.[56] For the Gamma Catcher it is $n = 2.731 \cdot 10^{29}$ m^{-3} and $\mathfrak{I} = 56.4$ eV.[2] With these values equation (4.10) was numerically integrated to produce the theoretical curve. Figure 4.1 shows this resulting light yield curve compared to the measured data points. A good concordance between (4.10) and the data points is obtained for values of R between 9 and 10 nm. This result is also in good agreement with the expectations. The range of the inter-molecular interactions is of a few nanometers, so R should be of a similar size. R is expected to be a bit larger though, since the excitations

---

[2]For the mineral oil Ondina 909 in the Gamma Catcher mixture an elementary composition of 14.6 %$_{\mathrm{mass}}$ Hydrogen and 85.4 %$_{\mathrm{mass}}$ Carbon was used, as it was measured in the CHN-analysis (see Chapter 3).
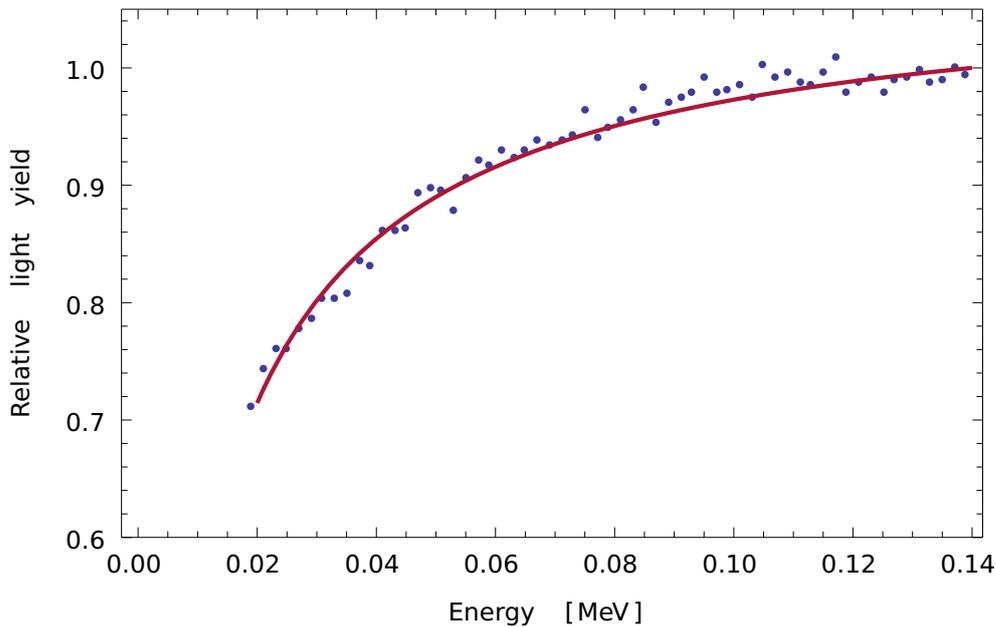
Figure 4.1: Comparison of experimental light yield data of the Gamma Catcher and the theoretical curve. The curve is obtained from a numerical integration of equation (4.10). A good agreement with the data points was achieved with R=9.5 nm for the quenching radius, as seen in the plot. The graph shows the relative deviation of the curve from an idealized linear behavior, as described in [58], and was normalized to the last data point at 139 keV. Since the energy of 139 keV is still too low for the assumption of linearity to be correct, the curve would continue to rise beyond 139 keV until the response is truly linear (at around 180 keV).

move through the medium and can come closer to each other. So two excitations can still quench each other, even though they were initially farther away.

The order of magnitude of R is an important intermediate result, since we can deduce the strength of ionization quenching from it. This helps especially in designing the approximations in the following sections. With $R = 9.5$ nm and the above values for n and $\Im$ the emission factor takes the form shown in Figure 4.2. Above 200 keV it is nearly constant and close to 1. This means that ionization quenching processes play only a minor role above this energy. At lower energies ionization quenching sets in and the light yield diminishes. This transition from the non-linear to the linear regime at 200 keV is in good accordance with what is reported by Birks.[30] The decrease continues until no light is produced any more at about 1 keV. It is expected that R is of the same order of magnitude for different types of liquid scintillators, so the qualitative behavior is thought to be rather general.
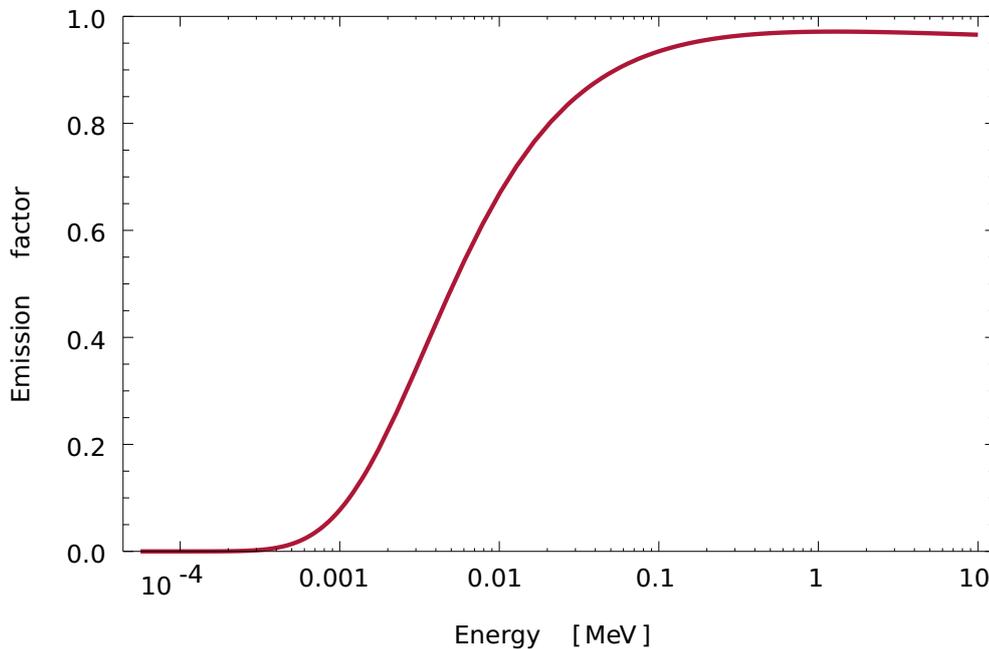
Figure 4.2: The emission factor in dependence of the electron energy, assuming a quenching radius of R=9.5 nm. While at higher energies the emission factor is nearly constant and close to 1, it starts to decrease below 200 eV. Below 1 keV the value is practically zero, and effectively no light is produced any more due to very heavy ionization quenching.

4.7 APPROXIMATION OF THE INTEGRAND

To calculate the mean total light yield $\langle L \rangle$ of an incident electron, the adequate formulas from the previous section for electrons have to be inserted into (4.10). This leads to a complicated expression that cannot be integrated. However, the integrand can be simplified in several ways. This section is concerned with approximating the integrand in a way that it becomes analytically integrable and retains the original form at the same time. It is challenging to find suitable approximations that fulfill both requirements, especially for the logarithms, and much effort was taken to find good substitutes. It was found that it is best to try and find approximations with the whole expression in mind, rather than approximating each part on its own. This way the errors of an approximation at one place in the equation can be mitigated by an approximation at another place. The emission factor (the exponential function in the integrand) is very useful for this task. Since it quickly drops to zero at very low energies, it suppresses many approximation errors in this energy range.

It is probably best to start with an expansion of the fraction $\sigma / \langle \mathrm{d}E/\mathrm{d}x \rangle$. A traditional Taylor series either quickly becomes inaccurate with the distance from

the expansion point, or must take many terms into account, which makes the approximation unwieldy. Instead, the expression is first expanded around an arbitrary expansion point $b > 0$.

$$\frac{\sigma}{\langle dE/dx \rangle} \approx \frac{1}{\Im n} \left[\frac{E_0^2}{(b+E_0)^2} - 1 + \ln \left(\frac{2b^2 + 4bE_0}{E_0 \Im} \right) \right] \Bigg/ \left[\left(\frac{b^2}{8} + E_0^2 \right.\right.$$
$$\left.\left. - (2bE_0 + E_0^2) \ln 2 \right) \Big/ (b+E_0)^2 + \ln \left(\frac{b^3 + 2b^2 E_0}{2E_0 \Im^2} \right) \right]$$

(4.17)

where the Lorentz-variables β and γ are already expressed as functions of E. In the second step we let $b \to 0$. At this point it is advantageous to factor the smallest power of b out of the logarithms

$$\ln \left(\frac{2b^2 + 4bE_0}{E_0 \Im} \right) = \ln \left(\frac{2b + 4E_0}{\Im} \right) + \ln(b/E_0) \tag{4.18}$$

$$\ln \left(\frac{b^3 + 2b^2 E_0}{2E_0 \Im^2} \right) = \ln \left(E_0 \frac{b + 2E_0}{2\Im^2} \right) + 2\ln(b/E_0) \tag{4.19}$$

so that one part can be evaluated and only the second part diverges when $b \to 0$. Close to zero the expression (4.17) becomes increasingly dominated by the logarithms while the other terms can safely approach $b \to 0$. It is therefore justified to "exclude" the logarithms from the expansion and retain them as functions. Using this procedure, $\lim_{b \to 0}$ is not a single number, but still a function of $\ln(E/E_0)$. The expression so asymptotically approaches

$$\frac{\sigma}{\langle dE/dx \rangle} \approx \frac{1}{\Im n} \frac{\ln(4E_0/\Im) + \ln(E/E_0)}{1 - \ln 2 + 2\ln(E_0/\Im) + 2\ln(E/E_0)}$$
$$= C \frac{A + \frac{1}{2}\ln(\epsilon)}{\phi + \ln(\epsilon)}$$

(4.20)

where the constants

$$C := \frac{1}{\Im n} \tag{4.21}$$

$$\phi := \frac{1}{2}\left(1 - \ln 2 + 2\ln(E_0/\Im)\right) \tag{4.22}$$

$$A := \frac{1}{2}\ln(4E_0/\Im) \tag{4.23}$$

were introduced for simplicity, and

$$\epsilon = E/E_0 \tag{4.24}$$

is the reduced energy, which will appear often due to the simplifications of logarithmic expressions. Whenever a logarithm is split, the reduced energy helps to maintain the arguments dimensionless.

While many approximations require a serious trade-off between accuracy and simplicity of the resulting expression, this procedure offers good accuracy and

simplicity alike. At the point of the biggest deviation from the original the error reaches about 3 %, but the overall approximation is good, especially towards low energies. In general the approximation is good up to the order of 10 MeV and thus valid throughout the region of interest. At much higher energies the approximation would become increasingly inaccurate.

Even though the fraction already became much simpler to handle, the logarithmic terms still pose a major obstacle to a later integration. At this point we have to eliminate the logarithms in the above formula. Again, the Taylor series of the logarithm

$$\ln(x) = \sum_{j=0}^{\infty} (-1)^j \frac{(x-1)^{j+1}}{j+1} \tag{4.25}$$

itself does not give satisfactory results for the given problem. It only yields a good approximation when $x \approx 1$ and converges only when $x \in (0, 2)$. Outside this interval the expansion diverges and is not applicable. However, with help of the identity

$$\ln(x) = m \ln(\sqrt[m]{x}) \tag{4.26}$$

which follows from the basic logarithm rules, the argument can be brought as close to 1 as desired, if only m is chosen large enough. And for sufficiently large values of m even the first-order term of the expansion (4.25) gives an accurate approximation:

$$\ln(x) \approx m \sqrt[m]{x} - m \tag{4.27}$$

This formula establishes an interesting connection between logarithms and roots, which can be exploited. With increasing m it also converges much faster against $\ln(x)$ than (4.25). In principle one would try to choose m as big as possible. But in our case it would also be desirable to eliminate the sum in the denominator of (4.20), i.e. to set $m = \phi$. Yet, in this case m would not be large enough to produce a good approximation.

A way to fulfill both requirements simultaneously is to modify equation (4.27) such that all instances of m are replaced by independently adjustable parameters.

$$\ln(x) \approx \alpha \sqrt[m]{x} - \mathfrak{B} \tag{4.27*}$$

Parameter $\mathfrak{B}$ is already fixed to be equal to ϕ by the above requirement.[3] So we are left with the two adjustable parameters α and m. We demand that at a certain

---

[3]Even though it is not necessary to set $\mathfrak{B} = \phi$ for the logarithm in the numerator too, it is a good idea to use the same values since the resulting terms then cancel nicely.

expansion point x_0 both the value of the function and its slope are equal to those of the original expression; mathematically:

$$\ln(x_0) \overset{!}{=} \alpha \sqrt[m]{x_0} - \phi \tag{4.28a}$$

$$\frac{\mathrm{d}}{\mathrm{d}x}\left[\ln(x)\right]\Big|_{x=x_0} \overset{!}{=} \frac{\mathrm{d}}{\mathrm{d}x}\left[\alpha \sqrt[m]{x} - \phi\right]\Big|_{x=x_0} \tag{4.28b}$$

Solving these equations for α and m yields

$$m = \ln(x_0) + \phi \tag{4.29a}$$

$$\alpha = \frac{\ln(x_0) + \phi}{x_0^{1/(\ln(x_0)+\phi)}} \tag{4.29b}$$

In the following the expansion point is set to $x_0 = 2$ (i.e. $E = 2E_0$), but its exact position does only have a minor impact on the curve, as long as $x_0 \gg \mathfrak{I}/E_0$. When (4.27*) is then plugged into equation (4.20), ϕ vanishes in the denominator and we obtain

$$\frac{\sigma}{\langle \mathrm{d}E/\mathrm{d}x\rangle} \approx C\frac{A - \phi/2}{\alpha}\epsilon^{-1/m} + \frac{C}{2} \tag{4.30}$$

Again, the error introduced by this approximation is almost completely absorbed by the exponential term, when it is inserted in (4.10). This is seen in Figure 4.5, in which the approximation (4.30) is compared to the original expression.

The pre-factor in the above equation will be referred to by the new constant

$$K := \frac{A - \phi/2}{\alpha} \tag{4.31}$$

which can be calculated from the mean ionization energy $\mathfrak{I}$ alone.

$$\star \qquad \star \qquad \star$$

We now turn to the emission factor in (4.10). Here it is more important to reproduce the function at the slope and the higher energies. With all quantities inserted it is

$$e^{-nR\sigma} = e^{nR\frac{\chi}{\mathfrak{I}}}\, e^{-nR\frac{\chi}{\mathfrak{I}}\frac{1}{\beta^2}\left(\ln\frac{2E_0}{\mathfrak{I}}+\ln\left(\beta^2\gamma^2\right)\right)} \tag{4.32}$$

The constants which appear in the exponent form the new dimensionless constant

$$W := nR\frac{\chi}{\mathfrak{I}} \tag{4.33}$$

With the values calculated earlier for the Gamma Catcher, W assumes a numerical value of $2.34 \cdot 10^{-3}$. Then, by expanding β^2 and $\beta^2\gamma^2$, and separating the energy-independent terms into a separate constant Y with

$$Y := e^{W\left(1-\ln\frac{2E_0}{\mathfrak{I}}\right)} \tag{4.34}$$
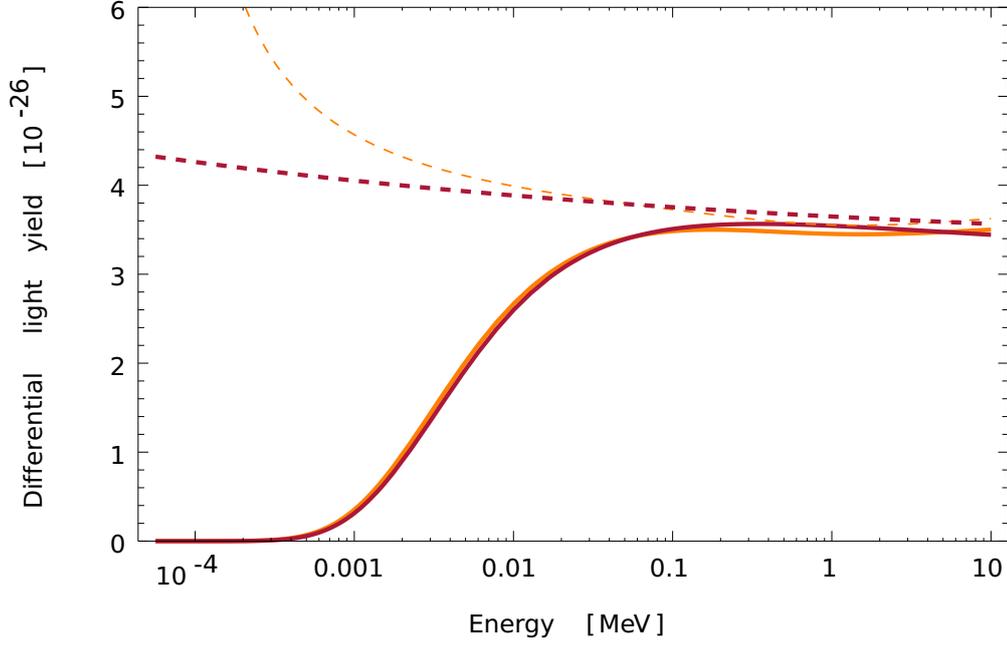
Figure 4.3: Accuracy of the approximation of the differential light yield. The dashed curves show the fraction $\sigma/\langle dE/dx \rangle$ in its original (orange) and approximated form (red). Both curves are in good agreement above about 50 keV, but they diverge from each other towards lower energies. In this energy range, however, the emission factor decreases rapidly and absorbs most of the approximation error, so that the shape of the integrand is represented well. The complete integrand (i.e. including the emission factor) is represented by the continuous lines, with the original formula again in orange and the approximation in orange.

we get

$$e^{-nR\sigma} = Y \, \exp\left[-W \left\{ \tfrac{1}{2\epsilon+\epsilon^2} \ln \tfrac{2E_0}{\Im} + \tfrac{\ln(2\epsilon+\epsilon^2)}{2\epsilon+\epsilon^2} + \ln\left(2\epsilon + \epsilon^2\right) \right\} \right] \tag{4.35}$$

The exponent has to be approximated further. We proceed by simplifying the occurrences of $2\epsilon + \epsilon^2$.

We seek a simpler expression for $2\epsilon + \epsilon^2$ which maintains the shape of the curve especially at the slope. First, it is observed that the omission of the second summand in (4.35) mainly results in a shift of the function, while leaving shape and size nearly unchanged. Second, the substitution of $2\epsilon + \epsilon^2$ with a linear expression $g\epsilon$ causes the curve to shift into the opposite direction. These observations are now used to compensate the errors of one simplification with the error of the other. By choosing an appropriate value of g both errors can nearly cancel and the net approximation becomes relatively accurate. A value of $g = 1.9$ MeV was found to yield a very good agreement between the original and the approximation. This seems to hold independently of the specific values of
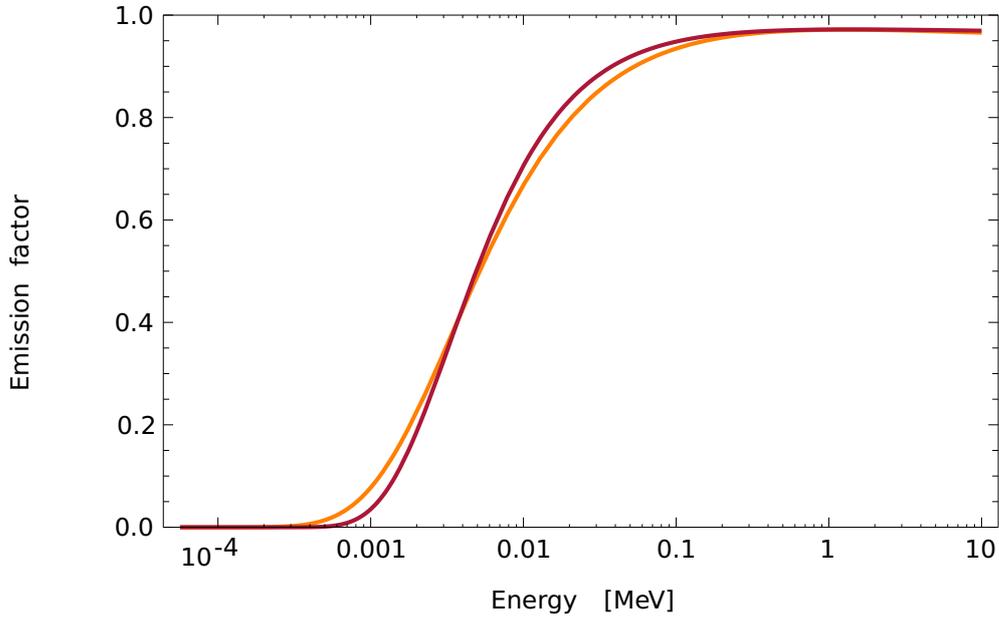
Figure 4.4: The original expression (4.32) of the emission factor (orange curve) and its approximation (4.38) (in red). The approximation slightly alters the shape of the slope, but in general the shape is conserved very well.

R and $\Im$, so $g = 1.9$ MeV can be taken as a standard value for different scintillators.

With this approximation we arrive at

$$e^{-nR\sigma} = Y \exp\left[-W\left\{\frac{E_0}{g\epsilon}\ln\frac{2E_0}{\Im} + \ln\left(\frac{g\epsilon}{E_0}\right)\right\}\right] \tag{4.36}$$

By defining the constant

$$D := W\frac{E_0^2}{g}\ln\left(\frac{2E_0}{\Im}\right) \tag{4.37}$$

and drawing the summand $\ln(\frac{g\epsilon}{E_0})$ from the exponent, we finally have

$$e^{-nR\sigma} \approx Y\left(\frac{g}{E_0}\right)^{-W}\left(\frac{E}{E_0}\right)^{-W}e^{-\frac{D}{E}} \tag{4.38}$$

when ϵ is replaced by E/E_0 again. The good accordance between equation (4.38) and the original function is shown in Figure fig:Approximation.of.emission.factor.

4.8 EVALUATING THE INTEGRAL

With the approximations (4.30) and (4.38) worked out in the previous section the mean total light yield of an incident electron can be written as

$$\langle L \rangle = \eta \, n \, C \, Y \, \frac{g}{E_0} \left[K \int_0^E \left(\tfrac{E}{E_0}\right)^{-W-1/m} e^{-\frac{D}{E}} \, \mathrm{d}E + \frac{1}{2} \int_0^E \left(\tfrac{E}{E_0}\right)^{-W} e^{-\frac{D}{E}} \, \mathrm{d}E \right] \qquad (4.39)$$

This integral can be evaluated analytically via *integration by substitution*. Let

$$\xi := \frac{D}{E} \qquad (4.40)$$

be the new integration variable, so that the exponent simply becomes $-\xi$. It is then

$$\mathrm{d}E = -D\xi^{-2} \, \mathrm{d}\xi \qquad (4.41)$$

Since $\lim_{E \to 0} \xi(E) \to \infty$, the integration then runs from ∞ to $\xi(E)$. The minus signs introduced by the $\mathrm{d}\xi$ can be absorbed by the integrals to switch the integration limits. Then, the constants in the integrands have to be adjusted such that all occurrences of E are replaced by ξ and we obtain

$$\langle L \rangle = \eta \, n \, C \, Y \, D \left(\tfrac{g \, D}{E_0^2}\right)^{-W} \left[K \left(\tfrac{D}{E_0}\right)^{-\frac{1}{m}} \int_\xi^\infty \xi^{W+\frac{1}{m}-2} \, e^{-\xi} \, \mathrm{d}\xi + \frac{1}{2} \int_\xi^\infty \xi^{W-2} \, e^{-\xi} \, \mathrm{d}\xi \right] \qquad (4.42)$$

The integrals are now equivalent to the *(upper) incomplete gamma function*

$$\Gamma(a, x) := \int_x^\infty t^{a-1} \, e^{-t} \, \mathrm{d}t \qquad (4.43)$$

with the parameter α equal to $W+1/m-1$ and $W-1$ respectively. Using this, the integral can be solved and we obtain

$$\langle L \rangle = \eta \, n \, C \, Y \, D \left(\tfrac{g \, D}{E_0^2}\right)^{-W} \left[K \left(\tfrac{D}{E_0}\right)^{-\frac{1}{m}} \Gamma\left(W+\tfrac{1}{m}-1, \tfrac{D}{E}\right) + \tfrac{1}{2}\Gamma\left(W-1, \tfrac{D}{E}\right) \right] \qquad (4.44)$$

as the final result.

It shall be especially noted that K and m can be calculated from the the mean ionization energy $\mathfrak{I}$ and the electron density n. The parameters W, Y and D additionally depend on the critical radius R as the only unknown quantity. For convenience, the constants and variables needed to evaluate equation (4.44) are summarized in Table 4.1. Despite its apparent complexity, equation (4.44) is predestined for an analysis of ionization quenching and easier to handle than Birks' formalism. The reason is that it describes the *total* light yield, which is experimentally directly accessible. Birks' formula involves the *differential* light yield, which is hard to measure. Therefore, the use of Birks' equation requires numerical integration.

η	scintillator efficiency
n	electron density
$\mathfrak{I}$	mean ionization energy
R	quenching distance (fit parameter)
χ	$5.1 \cdot 10^{-29}$ MeV m^2
g	≈ 1.9 MeV
C	$\frac{1}{\mathfrak{I} n}$
ϕ	$\frac{1}{2}\left(1 - \ln 2 + 2\ln(E_0/\mathfrak{I})\right)$
A	$\frac{1}{2}\ln(4E_0/\mathfrak{I})$
m	$\ln(2) + \phi$
α	$m/2^{1/m}$
K	$\frac{A - \phi/2}{\alpha}$
W	$n R \chi / \mathfrak{I}$
Y	$e^{W\left(1 - \ln\frac{2E_0}{\mathfrak{I}}\right)}$
D	$W\frac{E_0^2}{g} \ln\left(\frac{2E_0}{\mathfrak{I}}\right)$

Table 4.1: Summary of the constants and variables used in equation (4.44) for the mean total light yield.

4.9 VALIDITY

In the previous sections we started from the exact expression (4.10) for the mean total light yield $\langle L \rangle$ produced by electrons and used a series of simplifications to arrive at the analytical but approximative formula (4.44). It is now of interest how much the simplifications impact the result. Figure 4.5 shows the total light yield predicted by a numerical integration of the exact formula as well as by a direct evaluation of the approximate formula (both in relative representation). The parameters $\mathfrak{I}$ and n of the Gamma Catcher were used again and $R = 9.5 \cdot 10^{-9}$ m was set according to Section 4.6. It can be seen that equation (4.44) reproduces the shape of the exact function very well, but is some 6 % larger. This deviation is nearly constant for all energies and can be corrected by a simple scaling. The necessity of such a correction does not limit the usefulness of equation (4.44), as the factor can be incorporated into the light yield constant, which is treated a fit parameter anyway. With the scaling factor both curves can be brought to match over a very wide energy range.

Of course equation (4.44) represents the actual physics only up to a few MeV, even though the agreement with equation (4.10) exists up to much higher energies.
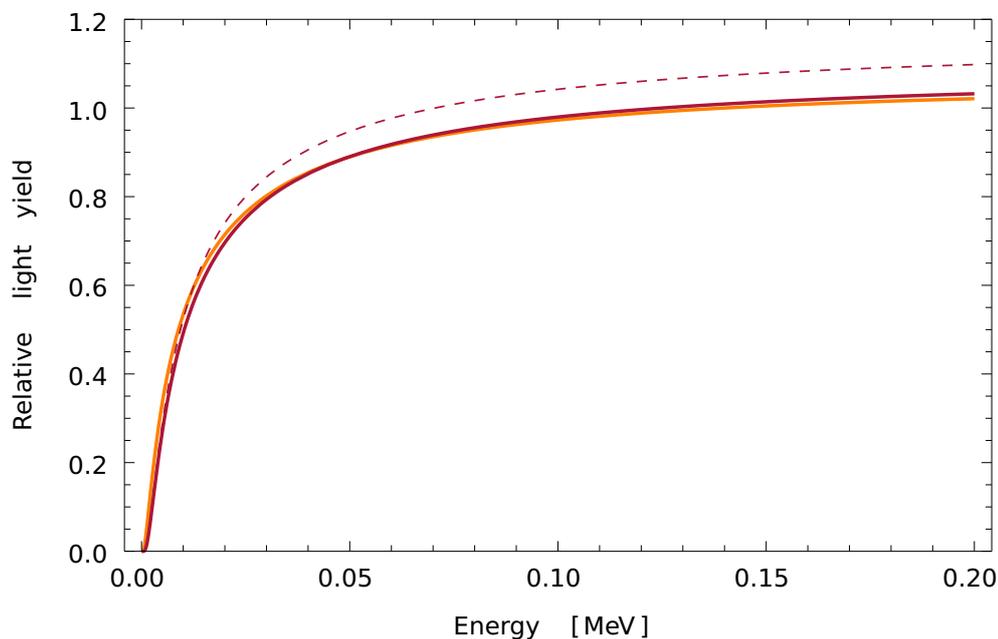
Figure 4.5: Comparison of the light yield predictions before and after the approximations, in the case of the Gamma Catcher scintillator. The light yield curve of the original model (orange) was created via a numerical integration of equation (4.10). The light yield curve given by equation (4.44) is represented by the dashed red line. It takes the shape of the original curve, but differs slightly in size. After scaling it with a constant factor (continuous red line) both curves match extremely well (up to 1 MeV and beyond). The scaling factor used here was 0.94.

One has to keep in mind that this formula was derived under the assumption that particle energies are not too high, so that hard collisions in $\sigma(E)$ can be neglected. When energies are high enough that hard collisions have to be taken into account, the incident electron itself can also create secondary electrons, which are again subject to ionization quenching.

Moreover, the functional form of $\sigma(E)$ changes. Formula (4.15), which was used for $\sigma(E)$ in this chapter, assumed that hard collisions are rare and do not contribute to the total ionization cross section. At higher electron energies these hard collisions become increasingly important and equation (4.14) has to be included into the calculation of the total cross section. The above derivation is then not adequate any more. Still, when a linear scintillation response is assumed at high electron energies, formula (4.44) can be extended with help of a linear function above a certain threshold energy.

4.10   IONIZATION QUENCHING AND LIGHT YIELD OF ELECTRONS

Equation (4.44) was derived for the purpose of including secondary electrons in the description of ionization quenching. It represents the mean total light yield
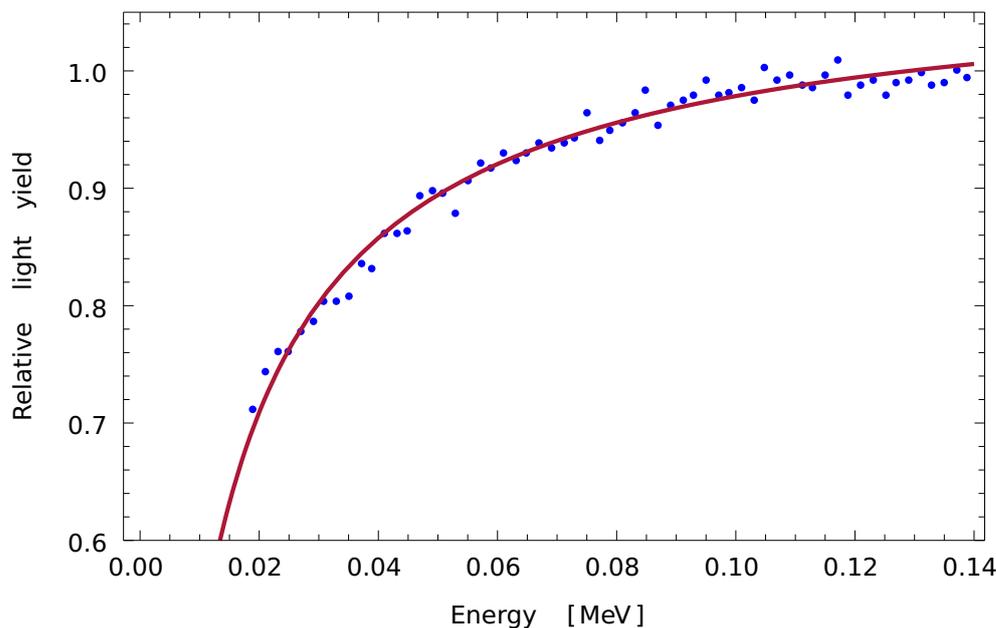
Figure 4.6: A direct fit of equation (4.45) to the Gamma Catcher data. The result is displayed as the light yield relative to a perfectly linear scintillator response, as it is described in [57].

obtained from a secondary electron with initial energy E. This is an important contribution for heavy particles, which can produce a number of secondary electrons in the scintillator. Incident primary electrons of moderate energies, however, only have a very small chance of creating secondary electrons. So equation (4.44) can be directly applied to incident electrons.

In most cases, especially in the case of large-scale scintillation detectors, this is more convenient than using Birks' differential version (4.1). Except for thin-film detectors or effects near the surface, an electron always deposits its whole energy in the scintillator and the total light yield is experimentally more easily accessible than the differential light yield. On the downside, this model employs with the incomplete gamma function a more complex function than Birks' model, but with well chosen starting values the fit generally converges quickly.

Figure 4.6 shows a fit of the formula to the Gamma Catcher data. While in Figure 4.1 a numerical integration of the formula was needed for each fitting step (which slowed down the evaluation significantly), equation (4.6) could now be applied directly. The form of the fit function used was

$$\langle L \rangle = \textbf{\textit{L}}_{\textbf{0}} \left[KD^{-\frac{1}{m}} \, \Gamma\left(W + \tfrac{1}{m} - 1, \, \tfrac{D}{E}\right) + \tfrac{1}{2}\Gamma\left(W - 1, \, \tfrac{D}{E}\right) \right] \tag{4.45}$$

where the common coefficients were combined into a single fit parameter $\textbf{\textit{L}}_{\textbf{0}}$, and the quantities D and W were implicit functions of the second fit parameter $\textbf{\textit{R}}$, representing the quenching radius R. K, m and g are constant in the fit. The

quantities were calculated with $\mathfrak{I} = 56.4$ eV and $n = 2.731 \cdot 10^{29}$ m^{-3} as in Section 4.6. The fit yielded $L_0 = 313 \pm 14$ and $R = (9.57 \pm 0.95) \cdot 10^{-9}$ m^{-3} as the best results for the parameters and their errors.

As L_0 is a function of R

$$L_0 = \eta \, n \, C \, Y \, D \left(\frac{g \, D}{E_0^2} \right)^{-W} \tag{4.46}$$

it describes an interesting relation between ionization quenching and the light yield.

This could only be verified if it is possible to measure the light yield of a scintillator in terms of scintillation photons per MeV of electron energy. The data points come from a measurement where the light yield was only qualitatively measured with a PMT, where the measured quantity is in fact the PMT current. While the current is proportional to the number of photons, to obtain the absolute number of scintillation photons would require a calibration of the PMT as well as a determination of its photon detection efficiency and of light loss in the experimental setup.

4.11 QUENCHING OF PARTICLES OTHER THAN ELECTRONS

Birks' also asserts that the quenching parameter kB in his model is independent of the primary particle, but studies show otherwise (for example [54]). It is therefore common to either use an empirically motivated "extended Birks model" like equation (4.2), or to use special values for each type of incident particle. Double Chooz uses the second approach. Both options involve considerable experimental efforts to determine the optimal parameters, often requiring high-level scientific equipment.

It would be convenient if the quenching model allowed to describe the behavior of all kinds of particles with the same quenching parameter. The results of the measurement with electrons could then be re-used for all other particles without the necessity of further laboratory experiments, thus saving time and money.

In the present model ionization quenching only depends on the quenching radius R, which is assumed to be equal for all types of particles. Therefore, when the quenching radius was determined for one species of particles (in this case electrons), it can also be applied to any other kind of particle. What differs are the ionization cross sections, and consequently the fraction of excitations with a mean distance above and below R. So the impact of ionization quenching is indeed different for different particle types, but it can be described by the same parameter R.

The formulas (4.8) and (4.44) for the mean differential light yield and the mean total light yield do not automatically work for particles other than electrons. It

must first be ensured that secondary electrons do not play a major role in the energy deposition. We start by separating the differential light yield into a sum of the contributions of the primary particle and of secondary electrons:

$$\left\langle \frac{dL}{dx} \right\rangle_{\text{total}} = \left\langle \frac{dL}{dx} \right\rangle_p + \left\langle \frac{dL}{dx} \right\rangle_{\text{sec}} \tag{4.47}$$

The term $\langle dL/dx \rangle_{\text{sec}}$ includes all the photons generated by the secondary electrons created within dx. The energy spectrum of the δ-electrons created within a distance dx is related to the differential cross section σ_p of the primary particle and given as

$$\frac{d^2N}{dT\, dx} = n\, \frac{d\sigma_p}{dT} \tag{4.48}$$

with T being the energy transferred from the primary particle to the electrons of the material. It is equivalent to the initial kinetic energy of the ejected electron. From this follows that the mean number of photons created by secondary electrons in dx is given by

$$\left\langle \frac{dL}{dx} \right\rangle_{\text{sec}} = \int_0^{T_{\text{max}}} n\, \frac{d\sigma_p}{dT}\, \langle L \rangle \, dT \tag{4.49}$$

where $\langle L \rangle$ is just given by equation (4.44). Here it is a function of the energy transfer T, since this is the starting energy of the secondary electron. T_{max} is the maximum energy a primary particle can lose in a single collision. In the energy range of interest T_{max} is given as [2]

$$T_{\text{max}} = 2E_0 \beta^2 \gamma^2 \tag{4.50}$$

where E_0 is again the rest energy of the electron. The Lorentz variables β and γ are now referring to the incident hadron. At kinetic energies of several MeV, the kinetic energy is much smaller than the particle's rest energy and $T_{\text{max}} \approx 4(E_0/E_p)E$. At a kinetic energy of 10 MeV, for example, the maximum transferable energy is about 20 keV for a proton, and only about 5 keV for alphas. From this it becomes evident that the contribution of secondary electrons is negligible. Equation (4.8) simply again becomes

$$\left\langle \frac{dL}{dx} \right\rangle_{\text{total}} = \eta\, n\, \sigma_p\, e^{-nR\sigma_p} \tag{4.51}$$

and the total light yield is again given as

$$\langle L \rangle_p = \eta\, n \int_0^E \frac{\sigma_p}{\langle dE/dx \rangle_p}\, e^{-nR\sigma_p}\, dE \tag{4.52}$$

For heavy particles $\langle dE/dx \rangle_p$ is described by the Bethe-Bloch energy loss equation. For the given problem, however, the Bethe-Bloch formula is not applicable, since

its accuracy significantly degrades below 2 MeV. Reliable values are needed down to a few keV in order to evaluate equation (4.52). For this reason it is best to resort to tabulated experimental values, which are also available at keV energies. A database of ionization cross sections is available at [59].

But apparently there are no experimental values available for the total ionization cross sections σ. Cross section data in this energy range exists for elements, [60] but not for compounds. It is not sufficient to calculate the cross section of the compound material from the constituent elements. As seen from equation (4.50) the maximum energy that an alpha particle of several MeV kinetic energy can transfer to a shell electron is only of the order of keV; the mean transferred energy is even lower. Under these circumstances the atomic electrons cannot be regarded as free and the effects of molecular bonds play a role, leading to significant modifications of the cross section of the compound material.

Unfortunately, the validity of the models for protons or alpha particles could not be tested within the scope of this thesis due to a lack of available cross section data for protons and alpha particles below 2 MeV kinetic energy.

PART II

ENERGY SCALE AND MONTE CARLO TUNING

Chapter 5

Energy reconstruction

The most obvious manifestation of neutrino oscillations is a decrease of the expected neutrino flux at a certain distance from the source. The mixing angle θ_{13} can be determined by a comparison of the predicted and measured number of neutrinos. This is a common technique and is used in many neutrino oscillation disappearance experiments, including Double Chooz. However, from equation (2.1) it can be seen that the survival probability does not only depend on the distance between the reactors and the detector, but also on the energy of the electron antineutrinos. As reactor neutrinos are not mono-energetic, different portions of the emitted neutrino energy spectrum are affected to a different extent, leading to a distortion of the spectral shape.

The spectral distortion and the deficit in the neutrino flux are both correlated manifestations of a non-zero θ_{13} and can be used together to measure the value of this mixing angle. The *rate+shape analysis*, which also exploits the shape of the spectrum, was already mentioned in Chapter 2. With the shape information θ_{13} can be further constrained and the uncertainty of its value is reduced compared to an analysis of the neutrino rate alone.

Figure 5.1 shows the expected shape of the antineutrino energy spectrum as detected in the Double Chooz Far Detector, as well as the distortion due to oscillations. These deviations from the original shape are more prominent at the low energy end of the spectrum. In order to be sensitive to the distortions it is necessary to have a solid knowledge about the detector's *energy scale,* i.e. the function which relates the detector's raw signals to the energy of the detected particle. It requires considerable efforts to understand the energy scale in detail. Of the new-generation reactor neutrino experiments to determine Double Chooz was the first one to perform a rate+shape analysis and published results in 2012.[1] A publication of a rate+shape analysis of the Daya Bay collaboration followed in 2014.[61]
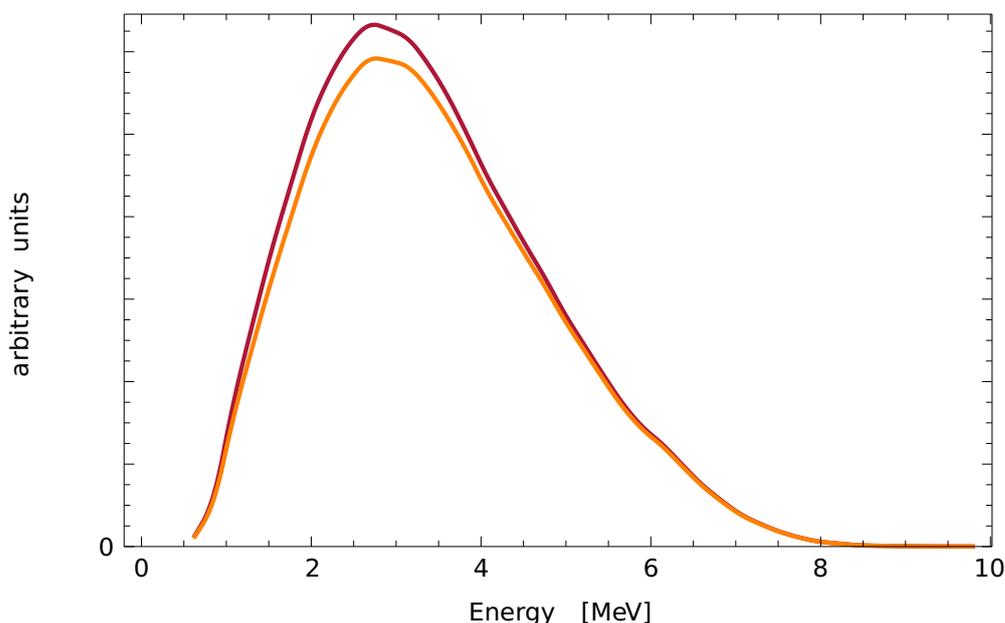
Figure 5.1: Expected shape of the electron antineutrino energy spectrum, as observed by the Double Chooz Far Detector. The red curve shows the predicted spectrum in the no-oscillation case ($\theta_{13} = 0$). The orange curve is the spectrum expected at the Far Detector for $\sin^2 2\theta_{13} = 0.10$. The effect of the spectral distortion is small, but can be seen, for example, at the peak of the curves. In addition it is seen that the oscillated spectrum loses more neutrinos at the left slope than at the right. This simulation considered neutrinos from both reactors at distances of 998 and 1115 m from the Far Detector, as well as the detector response.

5.1 THE ENERGY SCALE

An essential step in the Double Chooz analysis is to reconstruct the event energy from the observed light. The accuracy of the energy reconstruction has decisive impacts on the analysis results. In a θ_{13} analysis, any discrepancy between data and Monte Carlo influences the quality of the *final fit* and contributes to the systematic error of the result. In consequence, it is a prime concern to achieve a very good agreement between the energy scale in both data and simulation. This section summarizes the energy scale approach of [1].

The energy reconstruction takes the *energy non-linearity* of the detector response, the *non-uniformity* of the detector, and *variations with time* into account. These effects are either implemented in the Monte Carlo, such that the simulation can reproduce them, or measured and corrected in the detector data itself. This results in two different energy scales, one for data and one for the Monte Carlo. The base structure is

$$E_{\text{vis}} = \text{PE}\,(\rho, z, t)\; f_{\text{MeV}}\; f_{\text{u}}(\rho, z)\; f_{\text{s}}(t) \tag{5.1}$$

where $PE(\rho, z, t)$ is the number of photoelectrons (PE) reconstructed from the PMT charge and f_{MeV} is the conversion from PE to the event energy. These two terms alone represent a linear connection between the photoelectron yield and the event energy, so several corrections are applied in a second step. The factor $f_u(\rho, z)$ corrects for the non-uniformity of the detector, and $f_s(t)$ is a stability correction to compensate time variations of the detector response. All terms in equation (5.1) are different in data and Monte Carlo and are determined separately for both cases; the stability correction $f_s(t)$ is only applied to data, since there is no evolution with time in the Monte Carlo.

5.2 PE RECONSTRUCTION

The first step of the energy reconstruction is the determination of the number of the PE from the measured PMT currents. In principle this is as simple as integrating over the PMT signals to get the charge, and then dividing it by the *single photoelectron response*. In practice, the PE reconstruction may be biased by a dependence of the gain on the observed charge Q_i. To correct such effects the gain is parametrized with of a piecewise linear gain function $g_i(Q_i, t)$. The index i denotes an individual PMT, and the parametrization is done for each PMT separately. The gain properties might change over time and the characterization has to be repeated at regular intervals. The calibration is repeated at least on a weekly basis (which is much shorter than the typical timescale of possible gain drifts) and after power cycles. With the gain curves $g_i(Q_i, t)$ the number of PEs is finally reconstructed from the PMT charges Q_i via

$$PE(\rho, z, t) = \sum_i \frac{Q_i}{g_i(Q_i, t)} \tag{5.2}$$

5.3 ENERGY NON-LINEARITY

As it was already described in Section 3.3, liquid scintillation detectors are faced with two important effects that introduce a non-linear dependence of the scintillation signal with the event energy: Ionization quenching and Čerenkov radiation. These scintillator-related non-linearities are summarized as *light non-linearity*. In the context of the energy scale there is a second kind of non-linearity called *charge non-linearity*. It represents effects of the electronics and the DAQ, which might induce a non-linear behavior even in absence of light non-linearities. It includes remaining nonlinearities of the DAQ system, which could not be eliminated with the PE reconstruction function alone. The complete energy non-linearity is then given as a product of both the charge and the light non-linearity.

It is favorable to try and keep data-MC-discrepancies as small as possible in the first place. For this purpose it is necessary to implement an accurate model in

the Monte Carlo of how light is created and how it propagates and changes within the scintillator. The relevant scintillator properties were determined in laboratory measurements (Chapter 6), and the results were used as input for the simulation (Chapter 7).

PE-to-MeV conversion   For the conversion from photoelectrons to particle energy one exploits the fact that scintillators usually have a reasonably linear energy response to electrons above a few hundred keV. A linear connection between the particle energy and the amount of scintillation light usually serves as a first-order approximation. Under the assumption of proportionality it is enough to have one calibration point for the conversion from PE to MeV. In Double Chooz this anchor is the Hydrogen capture peak at 2.22 MeV.

For detector data the conversion factor f_{MeV} is determined from calibration runs with a ^{252}Cf source at the detector center. Neutron captures on Hydrogen are selected and the resulting peak is fitted with a Gaussian function. Its mean value gives the conversion factor. The procedure for Monte Carlo is identical. [1] The simulated primary light yield, in this case, is another input parameter and comes from laboratory measurements of the scintillator light yields performed at the MPIK. [35]

5.4   NON-UNIFORMITY

It must be furthermore considered that the detector response changes with the event position in the detector. This dependence has different reasons. For one, a basic variation of the light collection efficiency is caused by the fact that the PMTs and their surrounding shieldings are oriented towards the detector center. For events farther outward the PMT cathode may be partly obscured by the Mu-metal. As an extreme example, the light collection efficiency near the chimney is much lower than near the center, as the shieldings of the top-lid PMTs can block the line-of-sight to many PMTs at the Buffer wall. More importantly, some PMTs were deactivated during the detector run time due to an increased rate of light noise generated by them. The positions of those PMTs are unevenly distributed on the Buffer vessel and their deactivation causes an inhomogeneous light detection efficiency. Absorption by the scintillator, on the other hand, only plays a minor role due to the high attenuation lengths of the liquids (see Section 6.3).

For a correction only the z-coordinate and the distance ρ from the axis have to be taken into account and the non-uniformity can thus be corrected via a function $f_{\mathrm{u}}(\rho, z)$. A correction along the azimuthal angle ϑ is not necessary, as the deactivated PMTs are also "switched off" in the Monte Carlo. Due to the cylindrical geometry the detector response can in other respects be assumed to be independent of ϑ.
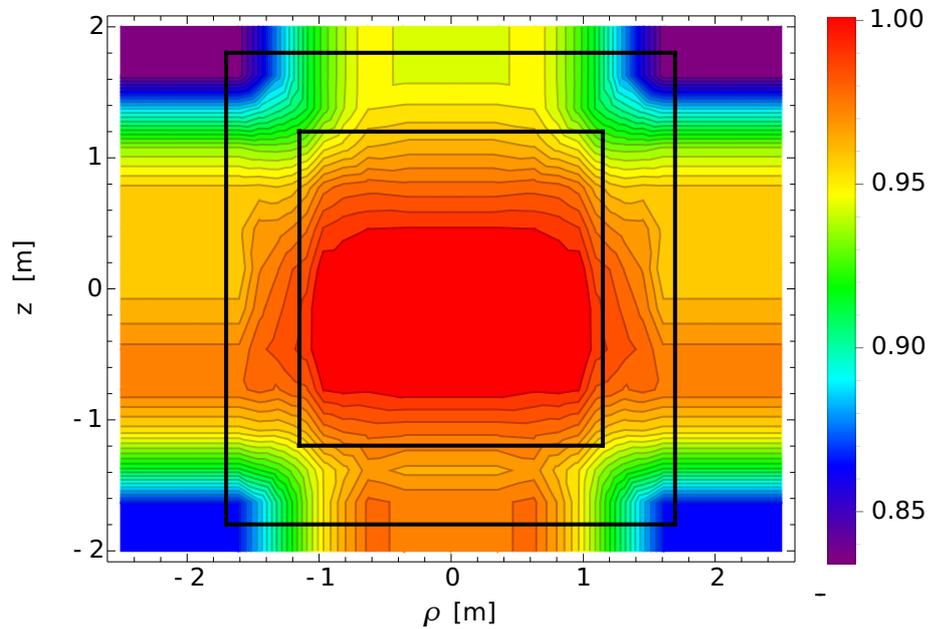
Figure 5.2: Detector map for data, as used in [1]. The map shows the detector response relative to the Target center and is given as a function of ρ and z due to the cylindrical symmetry of the detector. The response at each position was measured with help of the capture of spallation neutrons on Hydrogen, so the map is normalized to the Hydrogen peak at 2.2 MeV. In the Buffer volume the "response" is just an extrapolation of the Gamma Catcher response, which is done for computational reasons.

The detector non-uniformity is corrected with the help of *detector maps*. The detector geometry is displayed in the (ρ, z)-plane, which is rasterized into small cells. Then the detector response is scanned for each cell with help of the capture peak of spallation neutrons on Hydrogen. The more the peak deviates from the reference position at 2.22 MeV, the stronger the effect of non-uniformity on the particular cell. The result is a sampled "topographic" map of the detector response relative to the Target center.

With help of the maps the non-uniformity can be corrected for each event. The correction is applied in data as well as in the Monte Carlo, but for both cases individual maps were created. The detector response maps for data used in [1] can be seen in Figure 5.2. The correction applied is below 5 % throughout most of the Target volume, but can reach up to about 20 % in the edges of the Gamma Catcher. It is worth noticing here, that there is a smooth transition of the detector response between Target and Gamma Catcher. This is a consequence of the detailed light yield matching done, as it is described in Section 3.7.2. The detector map also serves as a confirmation that the underlying light yield model is valid and works as well on a large scale.
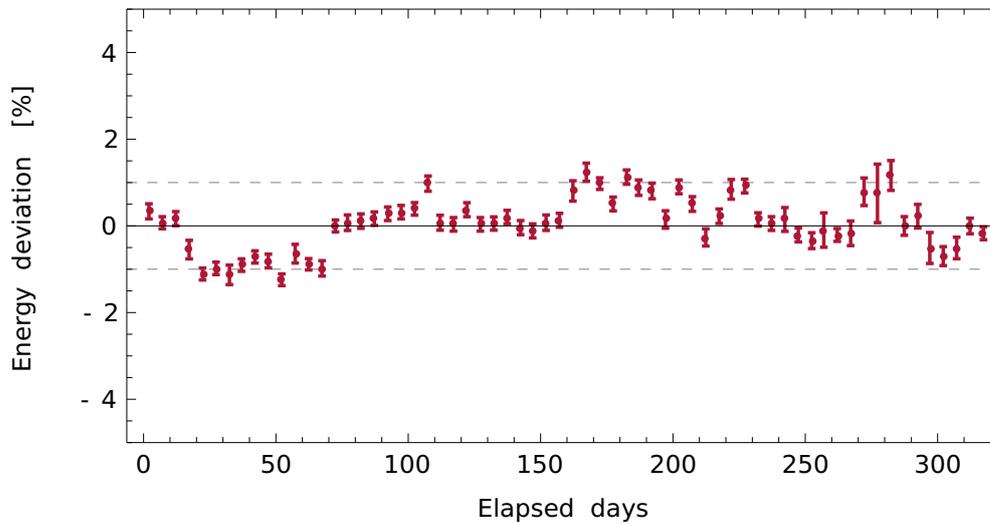
Figure 5.3: Stability of the energy scale over the runtime, as of [1]. The plot shows the stability of the Hydrogen capture peak position after correction of the detector response with the scintillator stability curve obtained from neutron capture events on Gadolinium. The "steps" in the curve are due to power cycles.

5.5 VARIATIONS WITH TIME

In contrast to the Monte Carlo, the visible energy of the detector data may suffer from variations of the detector response over time. The associated stability correction term $f_s(t)$ is applied after the other corrections were already performed.

The correction function is obtained from the scintillator time stability. It is measured with captures of spallation neutrons on Gadolinium, giving the characteristic narrow structure at about 8 MeV. The stability of the peak position is monitored over time and displayed in Figure 3.5. It can be seen that the scintillator response is stable within 1 %. This curve is then used to correct the time variations of the detector response. After correction, the detector stability is monitored with spallation neutron capture events on Hydrogen. Figure 5.3 shows the relative variation of the Hydrogen capture peak position over the runtime of [1], where the time stability is confirmed within 1 %.

5.6 SUMMARY

The energy scale in [1] takes several causes for a non-linearity of the detector response into account and corrects for non-uniformity, energy non-linearity and time variations. This way a relative uncertainty of only 1.13 % for the complete energy could be achieved.[1] The uncertainty is estimated from discrepancies between data and Monte Carlo and is composed of the uncertainties of the different effects. The detector non-uniformity contributes with a relative systematic error

of 0.43 %. Another 0.61 % are due to the remaining instability, and 0.85 % come from the non-linearity of the detector response with the event energy. It is seen that the latter is the dominant contribution to the systematic error of the energy scale. For this reason this work aims to further improve uncertainty the energy non-linearity by reducing the discrepancies between the behavior of the Monte Carlo and data. This becomes necessary as Double Chooz enters the precision phase and the energy scale uncertainty, though small, becomes an increasingly important contribution to the error on θ_{13}.

MEASUREMENT OF SCINTILLATOR PROPERTIES

This chapter deals with refinements made in the Monte Carlo and therefore starts with a short presentation of the Double Chooz simulation software.

The simulation of events in Double Chooz is done with DCGLG4sim. It is a module within the Double Chooz software framework and acts as a front-end to Geant4 which contains Double Chooz related definitions.[1] Above all, DCGLG4sim manages the detector geometry and material properties. They are defined and stored in Geant4-independent configuration files. The advantage is the high flexibility and easy customization of Double Chooz related properties without having to change internals of Geant4. For example, the changes of the optical model, which are described later on in this chapter, could so be implemented with relative ease. From this external information DCGLG4sim builds the detector geometry and sets required options, and puts them into an appropriate format for Geant4. Geant4 is then invoked with the configuration from DCGLG4sim. The simulation starts with the injection of the primary particles – either through Geant4's own generator or by tailored external modules.[2] Geant4 takes care of particle tracking and their interactions within the detector, including the creation of scintillation light. It simulates the physical processes from the production of particles up to the point when photoelectrons are produced at the PMTs.

Geant4's scope ends when photoelectrons are produced at the PMTs. At this point, another custom simulation software takes over. The RoSS module is designed to replicate the performance and characteristics of the Double Chooz

---

[1]DCGLG4sim is the Double Chooz flavor of the more general framework GLG4sim, which in turn is designed for the simulation of large liquid scintillator neutrino detectors.

[2]Most notably, the simulation of reactor antineutrinos is done with a dedicated Double Chooz software module called DCNuGen2. It contains all the relevant information to simulate the reactor antineutrino spectrum, e.g. the position of the reactors and detectors, reactor fuel composition and neutrino oscillation parameters.

read-out chain. Among others, it simulates PMT effects, the behavior of the Trigger system and the electronics, and characteristics of the FADC. After RoSS the simulation chain is finished and the Monte Carlo events can be processed like detector data.

6.1 THE OPTICAL MODEL

The so-called *optical model* is a part of DCGLG4sim, which takes care of the accurate simulation of optical photons in the detector. For this purpose it has to implement the optical properties of the Double Chooz liquids and pass them on to Geant4. It is a prime concern to minimize differences between the energy non-linearity in data and Monte Carlo. To this end, the mechanisms of light production and propagation in the detector have to reproduce the real behavior as closely as possible.

Scintillation, however, is a complex micro-physical process. It involves, among others, transitions between electronic states as well as interactions between atoms. Geant4 cannot reproduce all these mechanisms on a per-atom level. The computational requirements would be overwhelming and make a simulation outright impossible. Instead, the detailed micro-physics is ignored and the production of scintillation photons is treated on a macroscopic basis. For this to succeed without striking losses in the quality of the simulation, one has to provide suitable settings and information. These properties – all together constituting the optical model – have to be determined experimentally and made available to Geant4 as external input. The most important ones are

Emission spectrum: The primary emission spectrum of the scintillator is the radiative emission of the PPO–bis-MSB system, as described in Section 3.6. The optical photons in Geant4 are created with this spectrum and tracked individually. The primary spectrum was obtained from fluorimetric measurements. Its spectrum lies entirely above 340 nm and is shifted to higher wavelengths when the single photons are absorbed and reemitted by bis-MSB.

Molar extinction coefficients: The molar extinction coefficients of the substances are used for the calculation of the attenuation lengths of the scintillator mixtures. If a photon is absorbed, they are also needed to calculate on which components the absorption occurred. This is important for the decision if the photon can be reemitted and, eventually, with which spectrum (see below).

Reemission probabilities: The reemission probabilities describe how likely it is that one fluor molecule emits a photon after it was excited by photon absorption. They are intimately connected to the quantum yields of the fluors. As the measurement of the reemission probability is done in a relative manner, the quantum yield serves as the normalization and allows to convert the relative reemission curves to absolute values.

Light yield: The mean total amount of scintillation photons created per MeV deposited in the scintillator (under the assumption that there are no non-linearities with the energy). This parameter is of importance for the generation of primary scintillation photons and therefore the only property in this list which is not wavelength-dependent.

Refractive index: The refractive index is essential for the creation of Čerenkov light in the simulation. The Čerenkov effect is one of the prime sources of nonlinearities of the scintillator response with the particle energy. Apart from this, the refractive index is responsible for reflection and refraction at boundaries, for example when an optical photon propagates from the Target through the acrylic vessel into the Gamma Catcher.

quenching parameter: According to the currently implemented model by Birks, the influence of ionization quenching is described by one single parameter kB. In DCGLG4sim three parameters per liquid are used for the quenching of electrons, protons and alpha particles, in order to better represent the behavior of ionization quenching. The kB parameters were measured in laboratory measurements.

The optical model comes into play when optical photons enter the simulation. Optical photons are a separate class of particles within Geant4, as they exhibit wave-like properties and are subject to processes such as reflection or diffraction. This makes them different from other particles, including gamma rays.

Geant4 provides a flag to define if a material scintillates. When this flag is set, a certain number of optical photons are created per unit of energy deposited in it. The mean number of scintillation photons created per MeV is controlled by the light yield constant. As scintillation is a statistical process, the actual number of photons is sampled from a distribution around the mean value. The wavelength with which each of these photons is emitted is sampled from the primary scintillation spectrum (Section 3.6), which also has to be given as user input. It was experimentally measured for the Target and Gamma Catcher liquids[46] and ranges from about 350 to 500 nm (see Figure 6.1).

After the photons are created the software tracks each one individually. The probability that a photon is absorbed at some point is described by means of the attenuation length of the material. When absorption took place the question is whether the photon was absorbed by a non-fluorescent component (dodecane, PXE, Ondina 909, or the Gd-complex) or a fluorescent molecule (PPO or bis-MSB). PXE, which is in principle also fluorescent, has its emission spectrum in the near UV. It is not fluorescent any more in the wavelength region of primary spectrum, and can be considered non-fluorescent here. The probability for absorption on fluorescent or non-fluorescent molecules is calculated by Geant4 from material properties.

If the emitting molecule is bis-MSB, the reemission takes place with a pure bis-MSB spectrum. In the case of PPO there is also the possibility of non-radiative
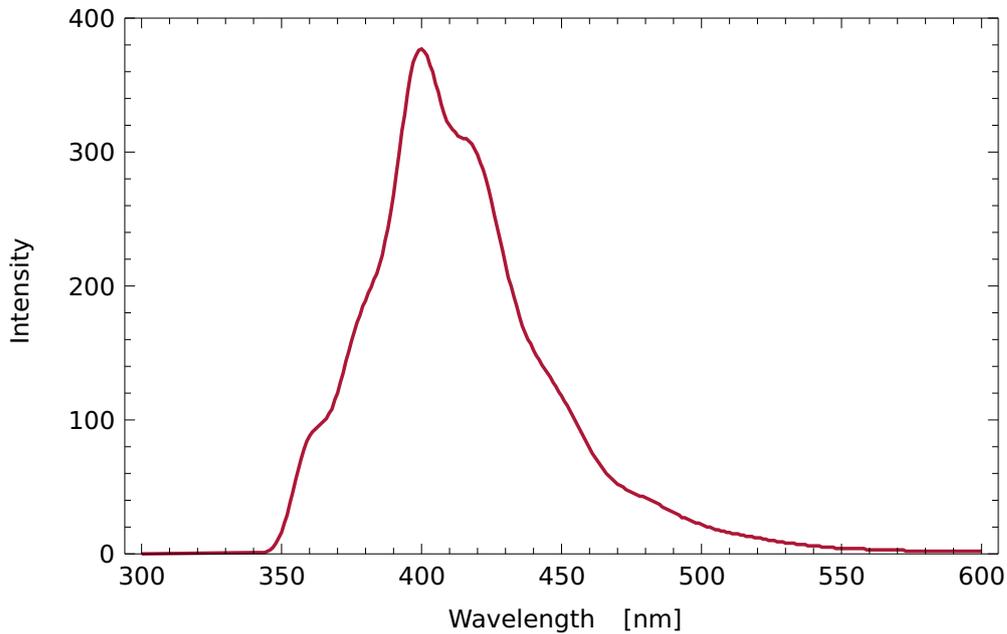
Figure 6.1: Measured primary scintillation spectrum of the Target scintillator, as it is implemented in the Monte Carlo. The spectrum extends from about 350 to 550 nm. Below 340 nm there is no emission of scintillation light.

energy transfer to bis-MSB. In this case the reemission occurs on bis-MSB, even if the photon was absorbed on PPO. This possibility is accounted for by using a combined PPO/bis-MSB-spectrum for the PPO reemission. In any case the wavelength of the new photon must be higher than that of the absorbed photon in order to obey the law of conservation of energy. The absorption of a photon and its subsequent reemission at a higher wavelength represents the wavelength-shifting property of the scintillator.

After reemission the photon is tracked again and the processes of absorption and reemission are eventually repeated. This continues until all photons are either lost due to absorption in the scintillator or on the boundary materials, or detected at the PMTs at the Buffer vessel.

The optical model is implemented through DCGLG4sim. The required properties are provided in form of simple text files. A dedicated module named `DChoozG4-BuildOptProperties` reads the raw data files and performs the required calculations if necessary. The results are put into Geant4 format and passed on to the simulation framework. Geant4 then constructs the detector with the defined optical properties and starts the simulation.

Nearly all optical properties are wavelength-dependent and as such stored in form of Geant4 property tables. Geant4 retrieves the information and interpolates

linearly between two entries. The properties in Double Chooz are implemented with a step size of 1 nm between two wavelengths and the interpolation error is completely negligible. At both ends of the parameter range Geant4 extends the value of the last available entry and so produces a flat continuation. A notable exception is the refractive index, which is not extended when Čerenkov light production is concerned (see Section 6.7).

In this work I was concerned with an exact adjustment of the optical model in order to reproduce the energy non-linearity. The processes of primary emission, absorption and subsequent reemission themselves are independent of the energy of the incident particle, but a non-linearity in the energy response is introduced by Čerenkov light and ionization quenching.

6.2 ČERENKOV TUNING

Čerenkov radiation leads to a non-linearity mainly due to the fact that it only sets in if the incoming charged particles have energies above a certain threshold. When primary Čerenkov light was created in the simulation, the photons propagate and are also subject to absorption and reemission processes, among others. The amount and shape of the Čerenkov contribution is consequently influenced by the details of the propagation of photons in the detector, i.e. by the optical model. Ionization quenching is treated differently, since it acts upon the scintillator *before* the primary photons are created. It reduces the number of photons before a single photon is tracked. The nonlinearity due to ionization quenching is therefore not influenced by the optical properties of the scintillator. For this reason the following sections concentrate on Čerenkov light.

At the beginning of this work the optical properties were implemented for a wavelength range between 340 and 600 nm. This range covers all processes associated with scintillation light. The emission spectrum only starts around 350 nm and has a tail which extends to about 500 nm. The spectrum of Čerenkov light, though, extends over a much wider range of wavelengths. It is created as long as the refractive index $n(\lambda)$ is greater than 1 and increases in intensity with growing $n(\lambda)$. Since the refractive index of the scintillator increases towards shorter wavelengths, so does the contribution of Čerenkov light. But since no values between 200 and 340 nm were available, the propagation of Čerenkov light in this wavelength range was not realistically simulated. The number of Čerenkov photons is small compared to the number of scintillation photons and the error so induced was also small. But now that Double Chooz has entered the precision era and the energy scale is very well known, such small errors may start to play a role. It is then of interest to refine the optical model. These efforts are presented in the following sections.

The extension of the wavelength ranges of the optical properties only affects Čerenkov light and the process was thence commonly dubbed *Čerenkov tuning*. This is a misnomer, though, as the primary *production* of Čerenkov light was never adjusted. The influence of Čerenkov radiation on the energy scale is only adjusted via the optical parameters, which are obtained from laboratory measurements. The quantities in question are the molar extinction coefficients, the reemission probabilities and quantum yields, and the refractive index.

6.3 MOLAR EXTINCTION COEFFICIENTS

For use in Geant4 the attenuation lengths are pre-calculated from the molar extinction coefficients of its components, rather than using them directly as an input to the simulation. This detour makes the optical model more flexible than otherwise. This was especially important in the earlier phases of Double Chooz when the scintillator composition was not yet fixed. Possible adjustments of the composition could so be implemented by simply updating the concentration without having to re-measure the attenuation lengths.

The molar extinction coefficient ϵ_i is a measure of how strongly a substance absorbs light of a certain wavelength. The ϵ_i and the attenuation lengths L_i are connected via the Beer-Lambert law. When a beam of light of initial intensity I_0 traverses the sample it is weakened according to

$$I(d) = I_0 \, e^{-c_i \, d \, \epsilon_i} \tag{6.1}$$

with ϵ being the molar extinction coefficient, c_i the molar concentration of the respective component in the solution (indicated by the subscript i), and d the path length through the cell. The ratio of the original intensity and the intensity $I(d)$ after the beam crossed the sample gives information about the absorption within the cell. It is commonly presented in terms of the *absorbance A*, which is the negative decimal logarithm of this ratio,

$$A_i = -\log_{10}\left(I/I_0\right) \tag{6.2}$$

Together with equation (6.1) then follows

$$\epsilon_i = \frac{A_i}{c_i \, d} \ln(10) \tag{6.3}$$

where the factor $\ln(10)$ accounts for the change of base.

The attenuation length L_i is the path length a beam of light has to cross so that its intensity is decreased to $1/e$ of the initial intensity. When the molar extinction coefficient of a substance and its molar concentration in the mixture

are known, the attenuation length L_i can be calculated from equation (6.1) as

$$L_i = \frac{1}{c_i\,\epsilon_i} \tag{6.4}$$

The total attenuation length L_{tot} is then calculated using

$$\frac{1}{L_{\mathrm{tot}}} = \sum \frac{1}{L_i} \tag{6.5}$$

It shall be noted that the Beer-Lambert law and the derived equations in this paragraph are, strictly speaking, only valid as long as the concentrations involved are small, while in particular the concentrations of the solvents dodecane and PXE is high. The equations hold nevertheless, since the transparency of both liquids is very high in the wavelength region of interest. Especially in the case of dodecane, but also for PXE, the absorbance in this region is completely dominated by the impurities. From this point of view the impurities have a very small concentration and the above equations are applicable again. The validity of equation (6.5) for the given scintillator composition was also confirmed in [62].

6.3.1 Measurement

The measurement of the molar extinction coefficients was performed with a Varian Cary 400 UV/Vis spectrometer. A Xenon lamp serves as the primary light source and provides a spectrum that reaches into the UV region. A monochromator then selects the wavelength with which the measurement is done. The wavelength range covered in these measurements is from 200 to 600 nm, which the instrument scans in 1 nm steps.

The primary beam is then guided along two different paths in quick succession. The beam is effectively split. One beam is sent through the sample of interest, while the other acts as the reference beam with the option to insert a reference sample into its beam path. For this experiment the reference compartment remained empty. The instrument then calculates the absorbance (6.2) from the intensity of the reference and sample beams.

The solvent used for most measurements is cyclohexane, because of its high transparency over a wide wavelength range. Since the absorption of dodecane, Ondina 909 and PXE (in the tail) is already very low, these samples were also measured in pure form, without an additional solvent. The samples are prepared beforehand and given enough time for the solutes to completely dissolve. The solutions are filled into UV-transparent quartz glass vials with path lengths between 1 and 10 cm and placed into the spectrometer.

The concentration of the solute must be such that the absorption is neither too low nor too high. In the first case the measurement may suffer from a low signal-to-noise ratio, in the second case the instrument may deviate from linearity.
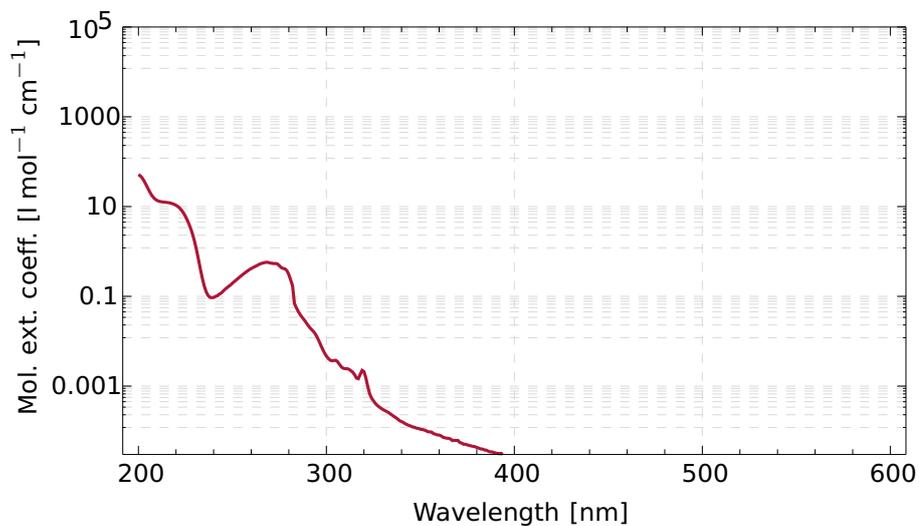
Figure 6.2: Molar extinction coefficient of dodecane.
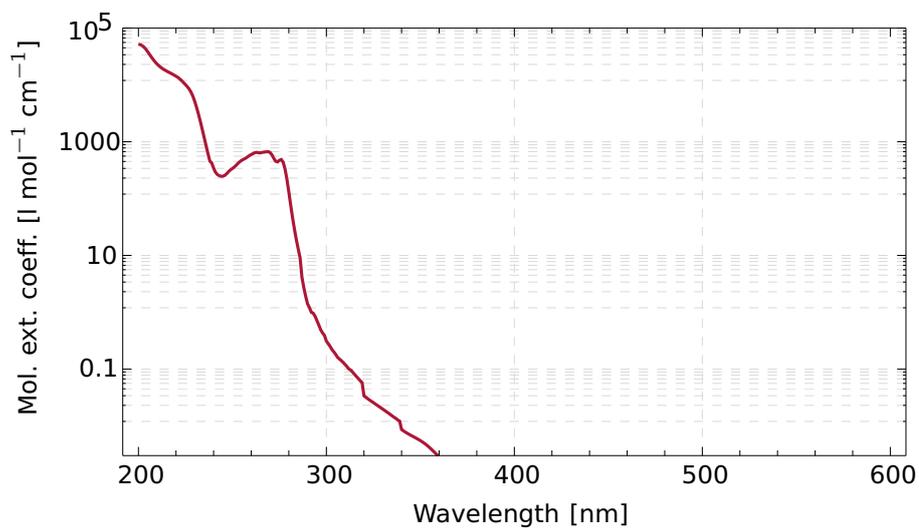
Figure 6.3: Molar extinction coefficient of PXE.
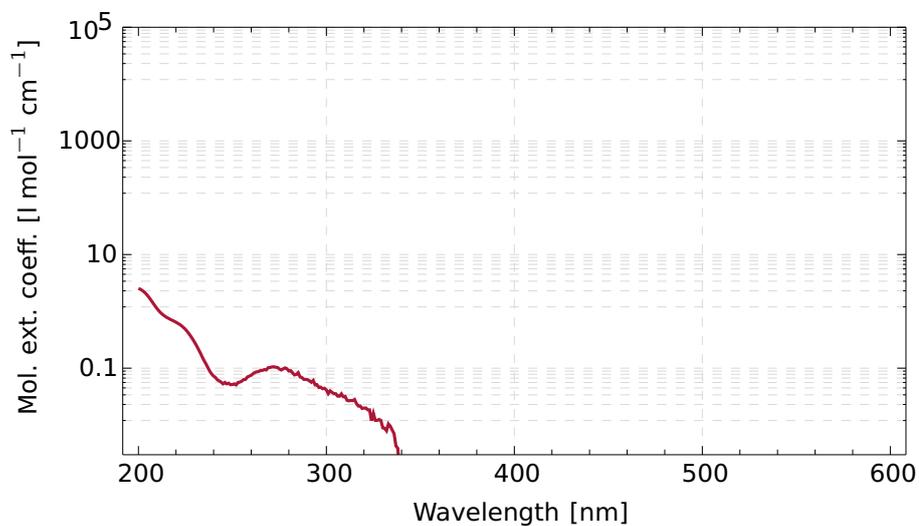
Figure 6.4: Molar extinction coefficient of Ondina 909.
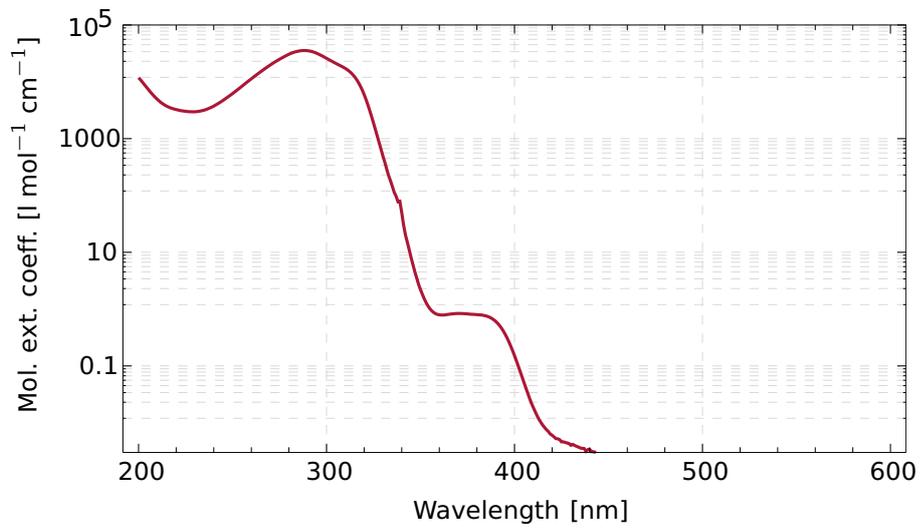
Figure 6.5: Molar extinction coefficient of Gd(dpm)$_3$.
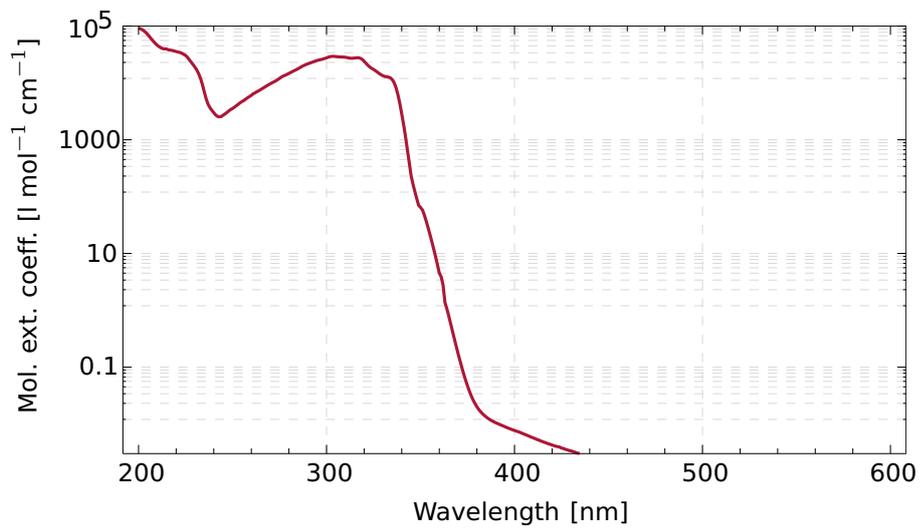
Figure 6.6: Molar extinction coefficient of PPO.
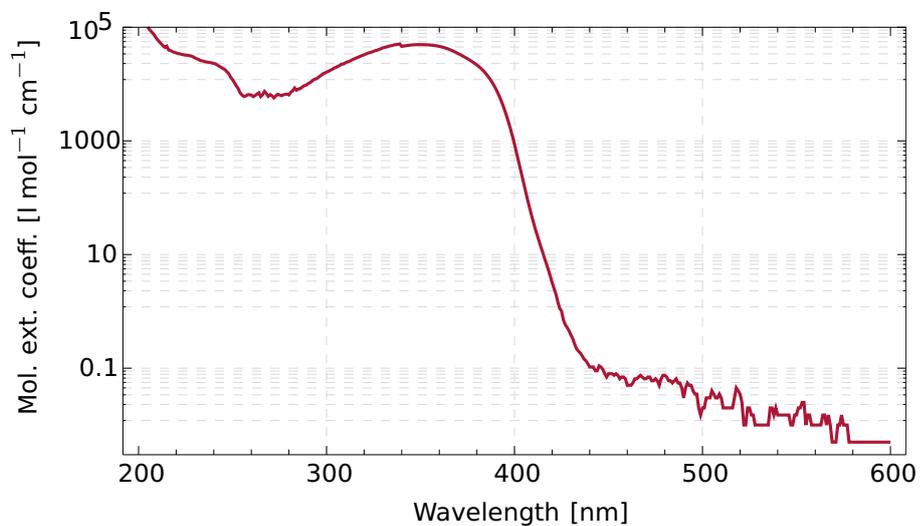
Figure 6.7: Molar extinction coefficient of bis-MSB.
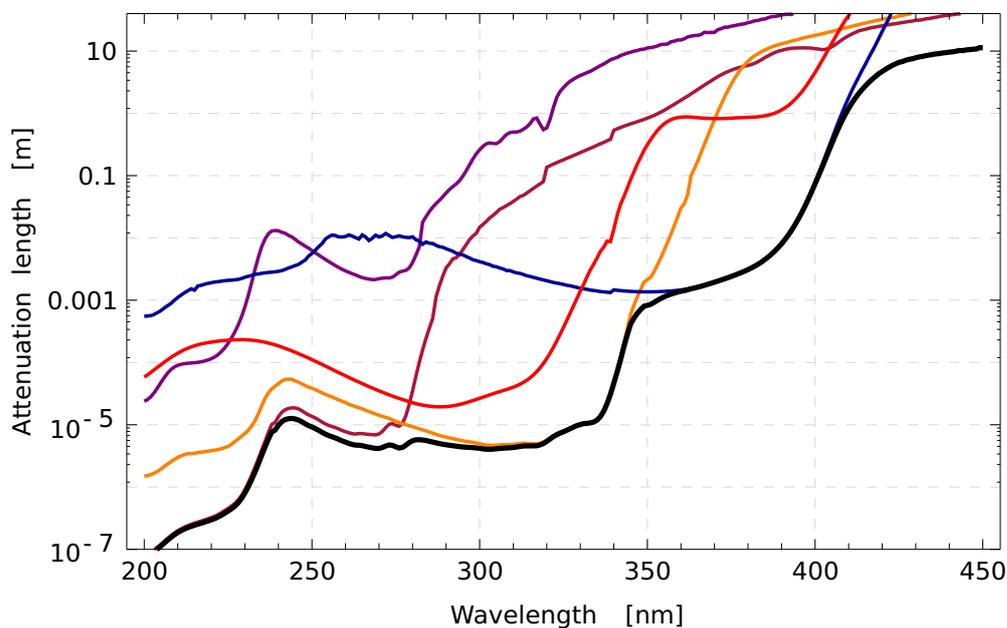
Figure 6.8: Attenuation lengths of the Target and its components. The thicker black line is the attenuation length of the complete mixture, while the colored lines represent the components dodecane (purple), PXE (dark red), the Gadolinium complex (red), PPO (orange), and bis-MSB (blue). It can be seen that the attenuation length of the Target is dominated by PXE until 270 nm, then by PPO until 350 nm, and finally by bis-MSB. At about 450 nm the attenuation length reaches 10 m and is comparable to the detector size. This plot complements Figures 6.2 to 6.7, where the molar extinction coefficients of the components are shown. In this picture the concentrations of the substances are also taken into account.

In general this requirement cannot be met for the whole range from 200 to 600 nm. Over the whole wavelength region the absorbance varies by as many as seven orders of magnitude and great care must be taken to avoid the influence of systematics. The measurement has to be performed on separate wavelength sub-ranges with different solute concentrations and/or different path lengths, so that the absorption is within reasonable limits in each sub-range.

As the measurement is done without a sample in the reference compartment, the issue arises that the sample beam is affected by wavelength-dependent reflections at the cell boundaries, while the reference is not. This might bias the result for measurements of the solvents. To compensate this effect, the measured absorbance curves are multiplied with a specifically determined correction function.[63]

As the fluors were measured in cyclohexane, the absorbance contains a contribution of the solvent. An additional measurement was made with pure cyclohexane. The absorbance of pure cyclohexane is then subtracted from the measured

fluor absorbances to obtain the values for the solutes only. In the subtraction the effect of the reflection bias cancels, so no correction is necessary in this case.

6.3.2 Results

The wavelength-dependent molar extinction coefficients were calculated from the measured absorbance and the respective concentrations used in the measurement. The results for the solvents are displayed in Figures 6.2 to 6.4 and for the solutes in Figures 6.5 to 6.7. The values between 340 and 600 nm were already implemented in the Monte Carlo, while the values from 200 to 340 nm are added in order to refine the optical model.

It can be especially noted that the solvents dodecane and Ondina 909 are extremely transparent. Even at short wavelengths their molar extinction coefficients is about four orders of magnitude lower than of the other substances. At wavelengths above around 320 nm the absorption is already at the limits of the instrument's precision. For the fluors the drop of the molar extinction coefficient happens at around 400 nm and above 440 nm the absorption is also negligible.

The occasional discontinuities occur when when the absorbance was measured with a different sample. This is mostly the case when the molar extinction is already extremely low. In this case the sample must often be replaced by a solution with higher substance concentration to keep the absorbance in an appropriate range. Some systematic errors might change in between the measurements of different samples, like the offset of the instrument or the uncertainty of the sample's concentration. The steps do not have any significant impact on the Monte Carlo. They only occur when the extinction coefficients are either extremely high or extremely low, so the steps only cause differences when the attenuation length is either extremely short (i.e. instant photon absorption) or much larger than the detector dimensions (i.e. no absorption at all). In both cases the *exact* attenuation lengths do not matter.

The attenuation lengths of the substances are calculated from the molar extinction coefficients via (6.4); the attenuation length of the mixture via (6.5). The concentrations are taken from Table 3.1 in Chapter 3. The results for the Target scintillator and its individual components are shown in Figure 6.8. It can be seen clearly which components dominate in which wavelength region. Below 330 nm the Gd-complex, despite its small concentration, is the second largest contributor to the total absorbance. It competes with PPO for the primary scintillation photons and reduces the Target light yield. Nevertheless, the PPO absorbance is nearly one order of magnitude larger, and is the dominating component until about 350 nm, where bis-MSB takes over.
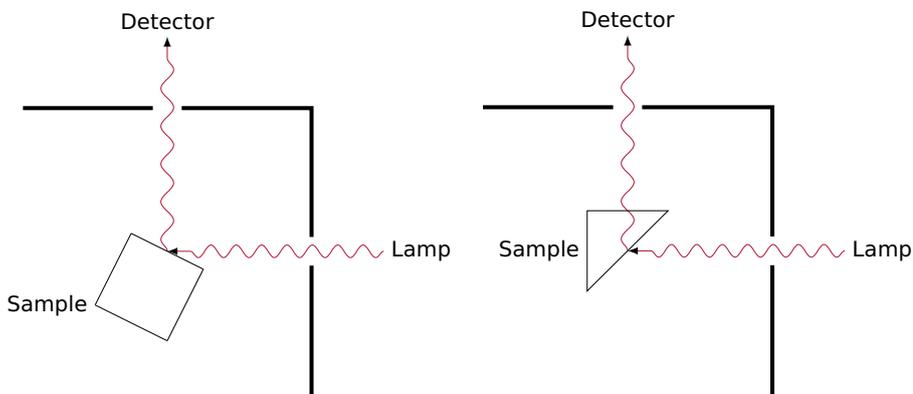
Figure 6.9: Front-face and back-face geometries used in fluorimetric measurements. In the front-face configuration (left) the light emitted by the excited sample does not cross the liquid on its way to the detector. Therefore the light is not shifted by scintillator components and the detector measures the primary spectrum. In the back-face geometry (right) the measured spectrum includes wavelength shifting, as the emitted light has to cross some of the scintillator material.

6.4 SCINTILLATOR EMISSION SPECTRUM

The shape of the emission spectrum depends on the spectra of the components and the radiative and non-radiative energy transfer paths between them, as explained in Section 3.6. Microscopic processes are not modeled in the Monte Carlo, so it makes sense to define the primary emission spectrum as the one which is emitted just after the non-radiative energy transfer processes have taken place.

The non-radiative transfer PXE→PPO has concluded and the primary spectrum mostly consists of the PPO spectrum. Since there is also a non-radiative transfer path from PPO to bis-MSB, the primary spectrum already contains some features of the bis-MSB emission spectrum. This primary spectrum is implemented in DCGLG4sim to create the first optical photons, which then propagate in the scintillator.

The measurement of the primary spectrum is not trivial, since there is a strong dependence of the spectral shape on the path length of the light through the scintillator. After the creation of the primary photons their spectral distribution is modified when they traverse the liquids. Especially the absorption and reemission by bis-MSB shifts the detected spectrum more towards higher wavelengths.

The measurement was performed with a Varian Cary Eclipse fluorimeter. Like the UV/Vis-spectrometer, it uses a Xenon excimer lamp as primary light source and selects the desired wavelength with a monochromator. The scintillator sample is contained in a quartz cell and placed in the sample chamber. The incident beam excites the scintillator and causes the emission of scintillation light with

its characteristic spectrum. For a given excitation wavelength λ_{ex} the fluorimeter scans the intensity of the emitted light for each wavelength, thus taking the emission spectrum $s(\lambda)$.

In a spectroscopic measurement the sample is irradiated from one side and the detected light is emitted around the center of the cell. In this configuration the scintillation light has to travel a macroscopic distance through the cell and is subject to absorption and emission processes and is so shifted to longer wavelengths. The primary spectrum would not be accessible this way. Instead, it is measured with help of a *front face* geometry. This arrangement is outlined in Figure 6.9. The cell is positioned such that the scintillator is excited at one side of the cell and the emitted light has to leave the cell immediately to be detected. Scintillation light which penetrates macroscopic distances in the scintillator and is shifted, does not reach the detector. The detected spectrum is therefore very close to the primary spectrum. A small contribution of shifted photons, which are backscattered into the direction of the detector, may still exist, but the contribution is assumed to be very small. [46] The primary spectrum, as implemented in the simulation, is shown in Figure 6.1.

6.5 REEMISSION PROBABILITIES

To begin with, the terms *reemission probability* and *fluorescence yield* refer to slightly different things. The fluorescence yield y_i of a substance is the probability that, after absorption, a single molecule of this substance reemits a photon. For a single molecule, the reemission probability $p_{\mathrm{reem.}}$ is equivalent to its fluorescence yield. In case of the *complete* scintillator cocktail, however, the reemission probability is somewhat different, for it also takes into account the interaction between molecules. For example, there is the possibility that the photon was absorbed on a non-fluorescent molecule and is lost. A molecule can also reemit a photon which was absorbed on a molecule of a different substance, if there is non-radiative transfer between them.

6.5.1 *Reemission probabilities above 340 nm*

At the beginning of this work the reemission probabilities were implemented for wavelengths above 340 nm. This was sufficient since there is no scintillation light to be simulated below this threshold; the primary spectrum is located entirely above 340 nm. In this wavelength range the scintillator is dominated by radiative energy transfer. PXE does not emit any more in this region and can be considered non-fluorescent, so only PPO and bis-MSB have to be considered. In the simulation the reemission probability of the scintillator mixture was calculated from the reemission probabilities of these two substances and their concentrations, as outlined below.

After absorption of a photon in the scintillator, Geant4 itself does not know on which component the process occurred. To simulate reemission it has to be verified first that the absorption of the photon took place on one of the two fluors. The probability μ_i for the absorption on the fluor i is given as

$$\mu_i(\lambda) = \frac{c_i \epsilon_i}{\sum_j c_j \epsilon_j} \tag{6.6}$$

where j runs over all the components of the scintillator. The index i can refer to either PPO or bis-MSB. In accordance with equations (6.4) and (6.5) it can also be expressed simply in terms of the attenuation lengths as

$$\mu_i(\lambda) = \frac{L_{\text{tot}}}{L_i} \tag{6.7}$$

The total reemission probability of the scintillator is the product of μ_i and the fluorescence yield y_i of the reemitting molecule:

$$p_{\text{reem.}}(\lambda) = \mu_{\text{PPO}}(\lambda)\, y_{\text{PPO}}(\lambda) + \mu_{\text{bis-MSB}}(\lambda)\, y_{\text{bis-MSB}}(\lambda) \tag{6.8}$$

The fluorescence yields of the components PPO and bis-MSB were experimentally determined with a fluorimeter measurement (see Section 6.5.3) and used in the calculation.

6.5.2 Reemission probabilities below 340 nm

Now, in the course of refining the optical model, the reemission process had to be extended to values between 200 and 340 nm. While there is no scintillation light in this region, Čerenkov photons in this wavelength region are absorbed and excite the scintillator. When they are reemitted with the scintillation spectrum, they contribute to the total light yield.

The scintillation mechanism in this region is fundamentally different from the region above 340 nm. PXE becomes dominant and the non-radiative transfer processes involved play an important role for the scintillator behavior. PPO receives the excitation energy and emits the photon in the place of PXE. Alternatively, there is some probability that PPO passes the excitation energy on to bis-MSB. In addition to these processes, an excitation of the non-radiative solvents n-dodecane and Ondina 909 can also lead to an efficient energy migration to PXE by exciton formation (as described in Section 3.1.2). This further increases the light output. None of these transfer mechanisms is covered by equation (6.8) and it cannot be used here.

The non-radiative energy transfer mechanisms cannot easily be dealt with mathematically. Instead the reemission probability in this wavelength range was measured for the liquid as a whole.

In order to extend the optical model to lower wavelengths, the division of the scintillation behavior into two domains was also realized in the Monte Carlo. Above 340 nm the simulation continues to use equation (6.8) and the fluorescence yields of pure PPO and bis-MSB and calculates the reemission probability of the mixture. Below this wavelength the simulation now uses the laboratory measurements of $p_{\mathrm{reem.}}(\lambda)$ of the whole Target and Gamma Catcher. This solution required a substantial modification of the DCGLG4sim source code. The modification was thoroughly tested.

6.5.3 Measurement

The reemission probabilities were studied together with B. Gramlich and L. Huth. The measurement apparatus and the procedure is the same as in Section 6.4. However, in this case the emission slit, where the emitted light of the sample is registered, is arranged at a $90°$ angle to the excitation beam. The sample is loaded into a triangular cell. It is then placed into the holder with the diagonal facing the excitation beam; the lateral face is oriented towards the emission slit, as it is also shown in Figure 6.9. This arrangement is called *back-face* geometry, as opposed to the *front-face* geometry used in Section 6.4, in which the beam directly hits the diagonal side. In the back-face configuration the emitted light has to cross some of the scintillator liquid before it can continue in the direction of the emission slit.

The division of the scintillator behavior in regions above and below 340 nm also impacts the measurement details. For the radiative domain above 340 nm the reemission probability of the single components is measured (see also Section 6.6). The substances are only present in low concentrations in a transparent solvent and non-radiative processes are negligible.

In the non-radiative regime below 340 nm, the reemission must be measured for the scintillator as a whole. This time the back-face geometry is required to fully include the radiationless transfers in the measurement.

The reemission probability $q(\lambda_{\mathrm{ex}})$ is then proportional to the integral

$$q(\lambda_{\mathrm{ex}}) \sim \int s(\lambda)\,\mathrm{d}\lambda \tag{6.9}$$

of the emission spectrum recorded by the fluorimeter. The integral should cover the whole reemitted spectrum. This can be difficult when the excitation peak (or higher orders of it) overlaps with the spectrum. But the overlaps are generally small and the errors negligible. The fluorimeter also offers a 3D-mode, in which the instrument records the emission spectrum belonging to a specific excitation wavelength, and automatically continues with the next excitation wavelength. This mode was used for the measurement with a step size of 1 nm.
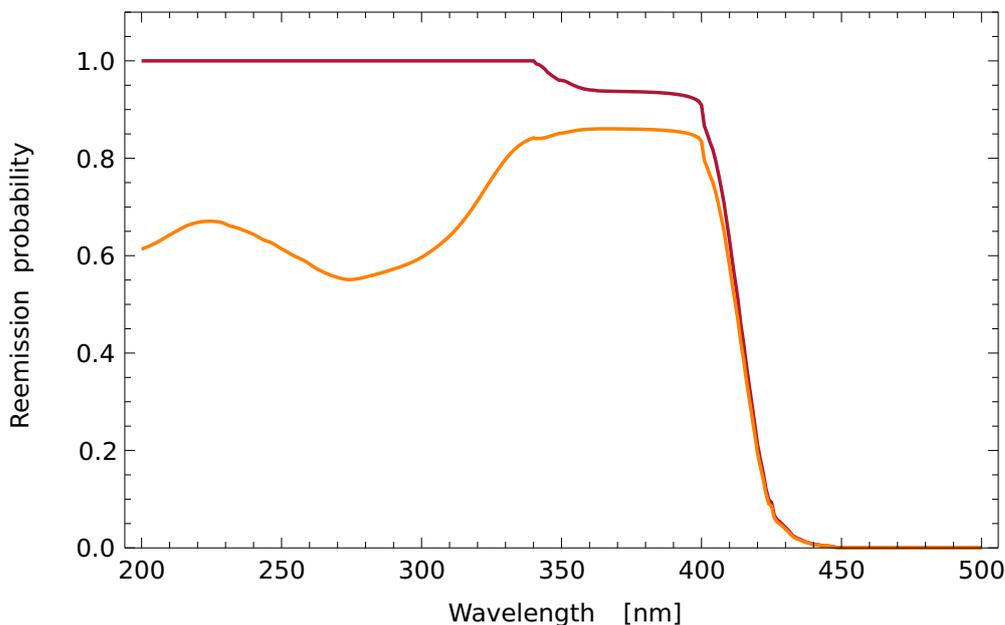
Figure 6.10: Target reemission probability as obtained from fluorimeter measurements. The red curve is the old reemission probability with the Berlman quantum yields ($\phi_{\mathrm{PPO}} = 1$, $\phi_{\mathrm{bis-MSB}} = 0.94$ at 340 nm). Above 340 nm the reemission probability of the mixture is calculated from the measured molar extinctions and the reemission probabilities of the Target components; the values were then extrapolated with a constant to wavelengths below 340 nm. The orange curve shows the new reemission probability. The shape of the curve between 200 and 340 nm was explicitly measured for the Target mixture as a whole to include radiationless processes, which are important in this region. Above 340 nm the values were again calculated from the properties of the components. This time the quantum yields used for the normalization at 340 nm were determined in the MPIK measurement ($\phi_{\mathrm{PPO}} = 0.842$, $\phi_{\mathrm{bis-MSB}} = 0.863$, see Section 6.6), resulting in a lower overall reemission probability.

In this experiment the reemission probability, as seen in equation (6.9), cannot be measured in absolute terms. The integrals are always given in a relative scale. To obtain an absolute value it is necessary to have an anchor point with known *quantum yield*, to which the values can be normalized. In the last version of the optical model these points were the quantum yields of PPO and bis-MSB at 340 nm. Berlman gives a value of 1 and 0.94 respectively, however without an uncertainty.[64] These values were used in [1]. A more recent measurement by Xiao *et al.* suggested a quantum yield of 0.77 for PPO and 0.96 for bis-MSB, both with a 3 % uncertainty.[65] The rather large variations between the quantum yield values cited in the different publications prompted an own measurement campaign at the MPIK. The results of these measurements are presented in Section 6.6.

In this experiment an anchor point for the complete mixture is also required. But since at 340 nm the scintillator is completely dominated by the PPO absorption, the PPO quantum yield also serves as a normalization for the whole scintillator in
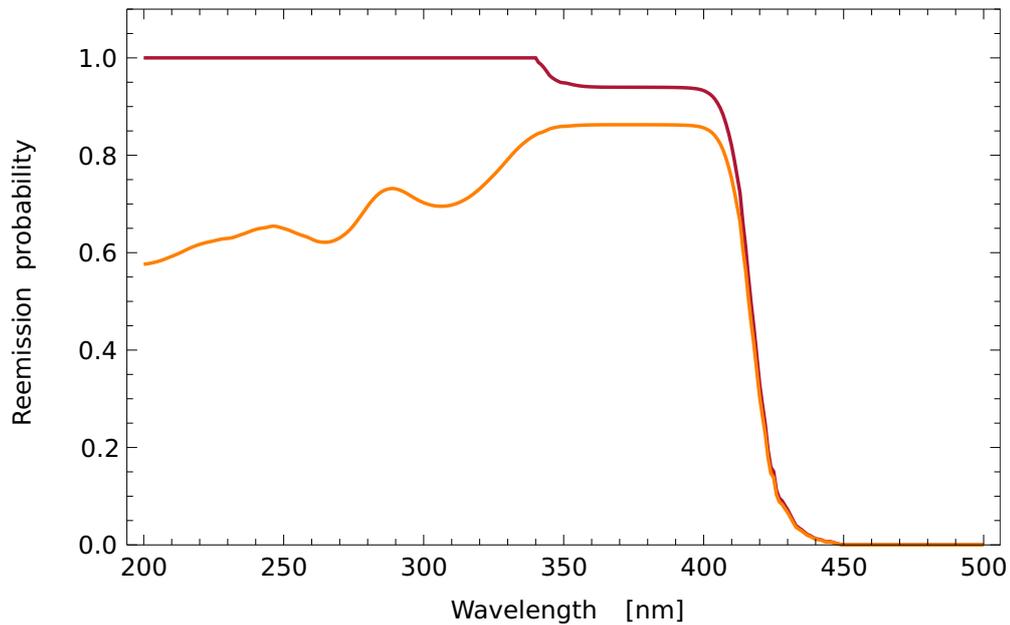
Figure 6.11: Gamma Catcher reemission probability as obtained from fluorimeter measurements. Please refer to Figure 6.10 for a detailed description. The new Gamma Catcher reemission curve differs from the Target curve mainly by the bump at around 290 nm, which is due to PXE. This structure is not seen in the Target, since the Gadolinium complex quenches the emission in the same region.

this case. This way the measured curve below 340 nm and the calculated curve above 340 nm both match at the transition.

6.5.4 Results

Figures 6.10 and 6.11 display the reemission probabilities for the Target and the Gamma Catcher. Between 200 and 340 nm the curves curves are directly measured for the scintillator cocktails. Above 340 nm the curves are calculated from the measured PPO and bis-MSB spectra and normalized to the quantum yields measured by us (see Section 6.6).

It can be seen that below 340 nm the reemission probabilities of the Target and GC mixtures are qualitatively similar. The two spectra differ mainly in the region around 290 nm, where the Gamma Catcher reemission is higher than that of the Target liquid, which shows a dip at this position. This can be attributed to the presence of the Gadolinium complex in the Target, which strongly absorbs in this region (compare Figure 6.5), but does not reemit light, leading to absorption losses in the Target.

Above 340 nm the curves are almost identical to the curves determined with the obsolete quantum yield values. Between 350 and 410 nm the reemission probability is now slightly higher, due to bis-MSB which dominates in this region

and of which the quantum yield was raised from 0.94 to 0.96. The significant reduction in the PPO quantum yield, however, does not have any impact on the region 340 nm. Its absorption spectrum lies nearly completely below this limit.

6.6 QUANTUM YIELDS

As seen in Figures 6.10 and 6.11, the use of the new PPO and bis-MSB quantum yields has a far larger impact on the reemission probability of the scintillator, than the actual extension of the data with the measured values, and in the case of PPO the old and new quantum yields values are even mutually exclusive. The big difference between the values of the substance's quantum yield in [64] and [65] created interest in an independent measurement of the quantum yields. For this purpose a series of laboratory measurements was carried out together with C. Buck and B. Gramlich. In addition to PPO and bis-MSB several other substances, which are used in scintillator design, were studied.

As before, a fluorimetric measurement can only determine the reemission probability of a substance relative to its reemission probability at another wavelength. To obtain the fluorescence quantum yields of the substances, their reemission probability must be compared to a scintillator standard with known quantum yield. With such a standard the quantum yield ϕ of a substance can be calculated via

$$\phi = \phi_0 \frac{1 - T_0}{T} \left(\frac{n}{n_0}\right)^2 \frac{\int s(\lambda)\,\mathrm{d}\lambda}{\int s_0(\lambda)\,\mathrm{d}\lambda} \qquad (6.10)$$

where T is the transmission of the sample and $s(\lambda)$ its emission spectrum. The integral $\int s(\lambda)\,\mathrm{d}\lambda$ extends from beginning to end of the reemission spectrum and yields the relative reemission probability. Quantities with index 0 refer to the standard. The factor $(n/n_0)^2$ is a correction for different refractive indices n and n_0 of the solvents in use. The experimental determination of ϕ involves a measurement of the fraction of absorbed light A and of the emission spectra $s(\lambda)$, and a calculation of the relative reemission probabilities and their comparison to the standard.

Fluors   The fluors were dissolved in pure cyclohexane at a concentration of 0.5 mg/l. The samples were bubbled with Nitrogen before the measurements in order to remove Oxygen from the liquid. Oxygen quenching is an important issue in this measurement. Due to their design the sample vials cannot be completely sealed, and Oxygen slowly enters the cell and dissolves again in the bubbled sample. In consequence, the absorbance and reemission probabilities change over time, and introduce a systematic error. For this reason, the measurement times themselves as well as the intervals between the different steps should be

kept as small as possible. The instrument offers several averaging speeds, each one improving the measurement speed at the expense of measurement quality. After several tests it was found that a medium speed yields good precision while requiring only a short amount of time, such that the degradation due to oxygen could be kept small. Additionally, the measurement of the reemission spectra was done first, as Oxygen predominantly affects the emission, while the absorbance of the sample is only slightly influenced.

The measurements were performed immediately after bubbling. The emission spectra are recorded in the Varian Cary Eclipse fluorimeter, as in Section 6.5. The measurement is done with rectangular quartz cells with path lengths between 2 and 10 mm in the standard position, instead of a front- or back-face arrangement. When the spectra have been taken for all excitation wavelengths, the first excitation wavelength is measured again. Due to Oxygen quenching the emission spectrum is slightly smaller in the second measurement. The relative decrease between the integrals over the two spectra gives an idea of the size of the influence of Oxygen, which is included in the uncertainty on the reemission probabilities for all excitation wavelengths. After the fluorimetric measurement the absorption was determined with the Varian Cary 400 UV/Vis spectrophotometer, in the same way as in Section 6.3.

Quinine sulfate standard A common standard is *quinine sulfate*[3] in diluted sulfuric acid, which was also used as a reference in these measurements. It has an absolute quantum yield of $\phi_{\mathrm{QS}} = 0.55$.[66]

It has the advantage that its emission spectrum extends smoothly over a wide range of wavelengths. It does not exhibit features like peaks or ridges. The emission spectrum is also far away from the excitation wavelength, so there is no overlap between them. The integration limits over the emission spectrum can so be set without ambiguity. In addition, quinine sulfate is practically unaffected by Oxygen and maintains stable absorbance and fluorescence over a very long time.

On the other hand, quinine sulfate does not dissolve well in cyclohexane. The solvent is an aqueous solution, which distinguishes it from the PPO and bis-MSB samples, which are dissolved in cyclohexane. Both solvents have different refractive indices which are corrected for in equation (6.10). The refractive indices are $n_{\mathrm{C_6H_{12}}} = 1.43$ for cyclohexane and $n_{\mathrm{H_2SO_4}} = 1.34$ for the 1 M sulfur acid.

Results PPO was measured at 290 nm as well as in 5 nm steps between 300 and 330 nm; Bis-MSB was measured in 5 nm intervals between 300 and 350 nm and in 10 nm intervals between 350 and 380 nm. For each excitation wavelength the quantum yield was calculated according to equation (6.10). Averaging over the results, the quantum yields were determined as $\phi_{\mathrm{PPO}} = 84.2$ % and $\phi_{\mathrm{bis-MSB}} = 86.3$ %. The empirical variance of the values was within 3 %.

---

[3]CAS number 6119-70-6

The measurement is prone to a variety of possible systematic errors, which must be carefully taken into account. The different systematic effects of the measurement have been investigated. For this purpose the measurements were repeated with different experimental parameters to study their influence on the measurement. The fluor concentrations were varied to test self-absorption and self-quenching effects, and cells with different path lengths between 2 and 10 mm were used to monitor the effect of "shadowing" by the sample holder. These measurements yielded results consistent with the ones obtained with the "standard" configuration. The influence of different solvents were also tested. When cyclohexane is replaced by n-dodecane, the measured quantum yields agree with the ones measured in cyclohexane within their errors. The aromatic solvents PXE and LAB show significant self-emission at lower wavelengths, which limits the measurement range and makes the measurement difficult. As a consequence, the solvent effect was only studied with bis-MSB, and a higher light yield by 5 to 10 % was found in LAB. In PXE a slight (but not significant) decrease of the light yield was observed for bis-MSB in PXE, compared to the measurement in cyclohexane.

According to the above measurements we assume a 5 % relative error on the results. This error should cover the above effects as well as the uncertainty of the quinine sulfate quantum yield, the wavelength dependence and the correction of the refractive indices, and a variation of the light yields over the measurement time due to quenching effects by oxygen entering the cell.

The ratio $\phi_{\mathrm{bis-MSB}}/\phi_{\mathrm{PPO}}$ is 1.02 for our results of the bis-MSB and PPO quantum yields. This agrees with $\phi_{\mathrm{bis-MSB}}/\phi_{\mathrm{PPO}} = 0.94$ obtained from Berlman's values, assuming that they also have a 5 % relative uncertainty. Another quantum yield measurement of these fluors by the Borexino collaboration also yields a ratio compatible with ours.[67]

The situation changes for the absolute values of $\phi_{\mathrm{bis-MSB}}$ and ϕ_{PPO}. With $\phi_{\mathrm{bis-MSB}} = 0.94$ and $\phi_{\mathrm{PPO}} = 1.0$ both values are significantly higher than in our case. The reason might be that Berlman overestimated the quantum yield of his scintillator standard, causing higher values for the fluors as well. This was already suggested by another study on quantum yields of common fluors, which assumed that Berlman's values might have to be corrected upward by about 17 %.[68]

The PPO quantum yield of 0.77 cited by by Xiao *et al.* is in agreement with our result within its 3 % relative error. However, their result for bis-MSB $\phi_{\mathrm{bis-MSB}} = 0.96$, again with 3 % relative uncertainty, is clearly higher. Consequently, the ratio of $\phi_{\mathrm{bis-MSB}}/\phi_{\mathrm{PPO}} = 1.25$ is also incompatible. This may be due to a different solvent used in their measurement. Their measurement was conducted with *linear alkyl benzene* (LAB), which is itself fluorescent. This might enable non-radiative transfer processes from LAB to bis-MSB, giving a seemingly higher bis-MSB light output.

6.7 REFRACTIVE INDEX

The intensity of Čerenkov light with wavelength λ depends upon the refractive index $n(\lambda)$ of the material. The Čerenkov spectrum emitted by a particle of velocity $\beta = v/c$ traversing a distance dx is given by

$$\frac{dN^2}{dx\,d\lambda} = \frac{2\pi\alpha z^2}{\lambda^2}\left(1 - \frac{1}{\beta^2\,n^2(\lambda)}\right) \tag{6.11}$$

Therein, α is the fine-structure constant and z the charge of the particle in units of the elementary charge. It can be seen from equation (6.11) that to a first approximation the intensity of Čerenkov light goes with λ^{-2}. A divergence is only prevented by the fact that the refractive index is a function of the wavelength as well. When $n(\lambda)$ drops below 1, the Čerenkov condition cannot be fulfilled any more and the spectrum is cut off at this wavelength.

If $n(\lambda)$ is not available for a certain λ, Geant4 cannot calculate the intensity of Čerenkov light of this wavelength and no light is produced. When this work on the optical model started, the refractive index was implemented for wavelengths between 200 and 600 nm. The fraction of Čerenkov radiation below 200 nm, which is present in data, was missing completely in the Monte Carlo.

To correct this, the refractive index $n(\lambda)$ as well as the molar extinction coefficients and reemission probabilities have to be extended to much lower wavelengths. However, it is very challenging to obtain values of $n(\lambda)$ below 200 nm. The principal problem is to find a suitable light source. Modern excimer lasers have wavelengths well below 200 nm (for example, $Ar_2^\star$ excimer lasers have a wavelength of 126 nm), but they only offer discrete wavelengths. A measurement to cover the wavelength range from 50 to 200 nm in narrow intervals would require a synchrotron light source. Another obstacle is the absorption of hard ultraviolet light in air (due to the photo-dissociation of oxygen, which occurs when $\lambda < 240$ nm). So the refractive index would have to be measured in vacuum, which is a problem for liquid samples.

However, experimental data is available for the normal alkanes tetradecane ($C_{14}H_{30}$) and heptadecane ($C_{17}H_{36}$) as well as for benzene. They originate from [69] and [70] and were already used in a study of the refractive index of the KamLAND scintillator. [71] They were made available to me by Y. Kamyshkov. [72]

For all three chemicals the data is given in terms of the photon frequency ω. First, it had to be converted to the wavelength scale. Then the data is interpolated with a linear function between the values. Finally, the resulting curve is sampled at 1 nm intervals to obtain $n(\lambda)$. The refractive index of dodecane is estimated from the data available for tetradecane and heptadecane. It is assumed that the refractive index of the normal alkanes is qualitatively identical, but scales linearly with the length of the hydrocarbon chain, i.e. with the number of carbon atoms. The resulting refractive index of dodecane has a less pronounced peak than tetra- or heptadecane, but is slightly higher at wavelengths above 211 nm. The refractive
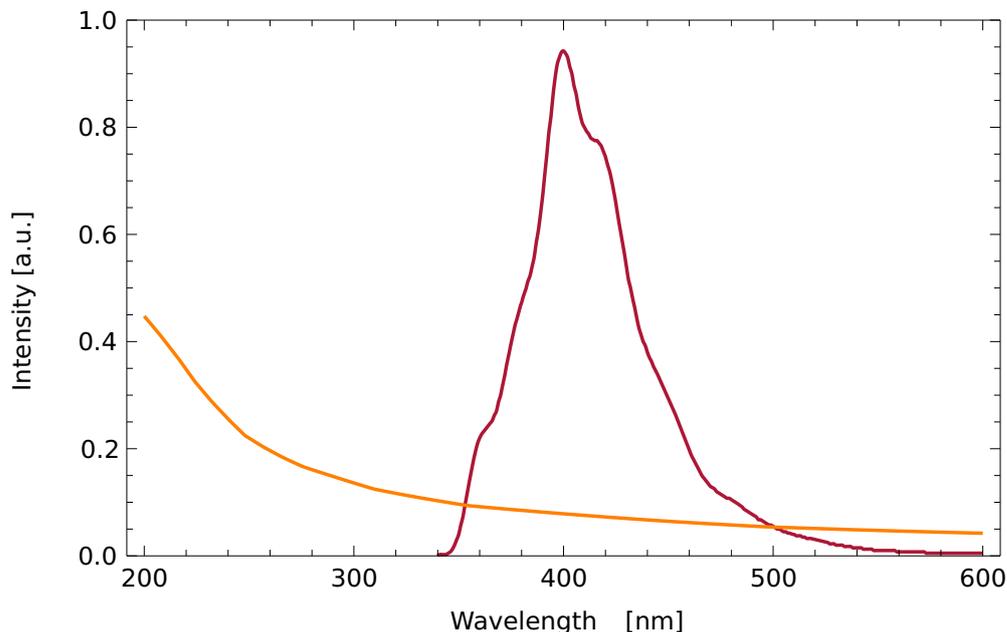
Figure 6.12: Spectra of scintillation and Čerenkov light. The scintillation spectrum displayed is the measured primary spectrum, while the Čerenkov spectrum was calculated from the refractive index for an electron of 0.5 MeV kinetic energy. The two curves are consequently not to scale. While scintillation light is confined to the wavelength region between 340 and 55 nm, the contribution of Čerenkov light rises towards lower wavelengths. In the detector the primary Čerenkov light below 340 nm is largely absorbed, but a part is reemitted again with scintillation wavelengths.

index of dodecane was measured to be 1.421 at 589 nm, while the above formula evaluates to 1.423 at this wavelength, which is already in good agreement. The estimated curve was finally scaled with a constant factor such that it matches the experimental value at this point.

Benzene is taken as representative for PXE. Even though the chemical structure of both compounds is different, it is believed that the refractive index of PXE is predominantly determined by the cyclic groups, and therefore similar to the refractive index of benzene. The benzene data is therefore simply scaled to match the measured refractive index of PXE of 1.570 at 589 nm. In contrast to the alkanes, the refractive index of benzene was only measured down to 120 nm; experimental values below this wavelength are unavailable. The available data was extrapolated with a linear function, so that there is a smooth transition at 120 nm. According to the extrapolation the refractive index of benzene becomes smaller than 1 at 60 nm. To find the refractive index of the mixture, Newtonian mixing is used:

$$n_{\text{Target}}^2 = p_{\text{C12}}\, n_{\text{C12}}^2 + p_{\text{PXE}}\, n_{\text{PXE}}^2 \tag{6.12}$$
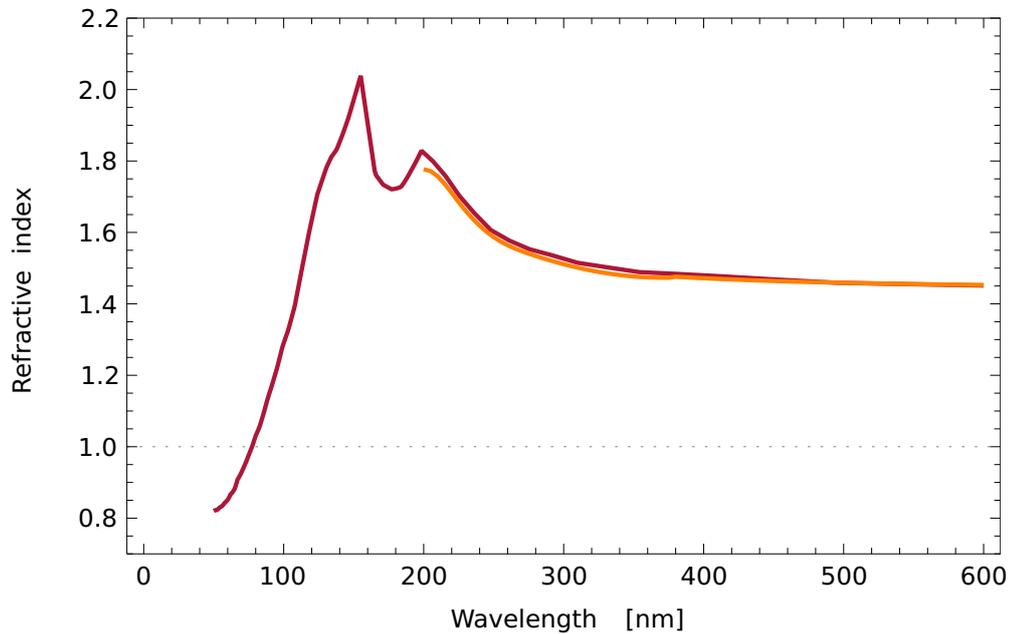
Figure 6.13: The wavelength-dependent refractive index of the Target liquid. The red curve represents the refractive index as calculated from measured values of benzene and higher normal alkanes. The orange curve is currently used in the Monte Carlo. It is created from measured values of the Target's refractive index above 400 nm and extrapolated to shorter wavelengths with help of the Sellmeier formula.[73] Both curves agree very well above 200 nm. According to the calculated curve, the refractive index peaks at 155 nm and drops below 1 at about 78 nm, which is the shortest wavelength that Čerenkov light can have in the liquid.

p_{C12} and p_{PXE} are the volume fractions of the respective substances. The contribution of the solutes is thought to be negligible. The resulting function $n_{Target}(\lambda)$ is displayed in Figure 6.13. It is worth noting that above 200 nm the calculated curve is practically identical with the refractive index as it is currently implemented in the Monte Carlo.

When Čerenkov light with wavelengths smaller than 200 nm is created, it is immediately absorbed due to the very short attenuation length of the Target in this wavelength region. The absorbed light is partly reemitted with the scintillation spectrum. In order to determine the contribution of Čerenkov radiation with $\lambda < 200$ nm to the total light output, the reemission probabilities of the scintillator below 200 nm is needed. Such a measurement would be faced with many experimental challenges, including the search for a suitable light source. The immense efforts needed to perform a successful measurement are probably not justified. A simple extrapolation of the values with a constant is probably sufficient for an estimate of the reemission probability.
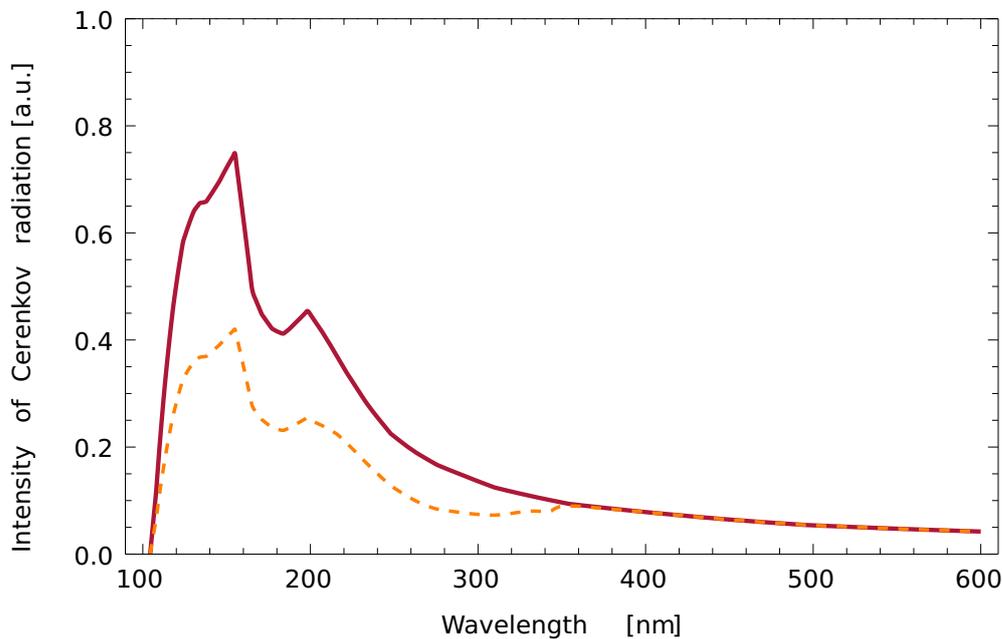
Figure 6.14: Spectrum of the Čerenkov radiation emitted by a 500 keV electron. The intensity of the primary Čerenkov light (red) was calculated with help of equation (6.11) and the estimated refractive index $n_{\text{Target}}(\lambda)$. The dashed curve shows the amount of Čerenkov light, which is not immediately lost again due to absorption, but reemitted at least once. Reemission occurs with the scintillation spectrum at wavelengths above 340 nm.

Figure 6.14 shows the intensity of the primary Čerenkov radiation resulting from the calculated refractive index. The spectrum was created for an electron of 500 keV kinetic energy. Below 200 nm the light is instantly absorbed, but has a chance to be reemitted again with wavelengths above 340 nm. The dashed curve shows the Čerenkov spectrum without the part which is immediately absorbed and lost, assuming the extended attenuation lengths and reemission probabilities from the previous sections. An integration of the spectrum above and below the 200 nm mark shows that both areas are approximately equal, i.e. the extension of the refractive index nearly doubles the amount of Čerenkov light produced per unit of length.

Often it is assumed that a fixed threshold energy exists, below which the charged particle does not irradiate Čerenkov light any more. Yet, this "threshold" is not so clearly defined. Čerenkov radiation can give a contribution even for particles with low kinetic energy, since the refractive index of the material is a function of the wavelength. In a wavelength region where $n(\lambda)$ is very high, the speed of light of these wavelengths is correspondingly lower, so that the particle may still fulfill the Čerenkov condition for these wavelengths and can still irradiate light. This behavior leads to a rather complex relation between the energy of the

particle and the intensity of Čerenkov light, which has to be considered for the treatment of the energy nonlinearity.

6.8 IONIZATION QUENCHING

The effect of ionization quenching is simulated before the first scintillation photons are created in the Monte Carlo. Geant4 uses equation (4.1) by Birks to model the reduction of scintillation photons. The parameter kB must be given as input. The effect of ionization quenching varies for different particles and DCGLG4sim attributes a separate parameter kB to electrons, protons and alpha particles. At the MPIK the parameter was measured experimentally for electrons and alphas.

6.8.1 Electrons

The measurement of kB for electrons is described in detail in [57]. In the experiment a quartz cell containing the scintillator sample is irradiated by a mono-energetic ^{137}Cs gamma source. The gammas undergo Compton scattering in the scintillator and create electrons directly within the sample. The Compton electrons deposit their energy in the liquid and create a flash of scintillation light, which is detected by a PMT. The second part of the setup is a cryogenically cooled Germanium gamma spectrometer placed above the sample. If the scattering angle is small (corresponding to an energy of <200 keV transferred to the electron) the photon is deflected in the direction of the Ge-spectrometer and its energy is measured with high precision. The energy of the Compton electron is determined from the difference between the initial and final photon energies. With help of a coincidence circuit the signals from the PMT and the Ge-spectrometer can be related to each other. After an analysis of the raw data the light yield in dependence of the electron energy was obtained. The data points taken for the Gamma Catcher were already shown in Figures 4.1 and 4.6 in Chapter 4.

With a numerical fit of equation (4.1) to the data points the quenching parameter was extracted as $kB_{\mathrm{Target}} = 0.159$ mm MeV^{-1} for the Target and $kB_{\mathrm{GC}} = 0.292$ mm MeV^{-1} for the Gamma Catcher. In a second approach different values of kB were plugged into the Double Chooz Monte Carlo and electrons with the same energies as the data points were simulated. This analysis searched for the best concordance of the simulation results with the experimental data. The analysis found $kB_{\mathrm{Target}} = 0.202$ mm MeV^{-1} and $kB_{\mathrm{GC}} = 0.335$ mm MeV^{-1}. These values are better suited for a use in the optical model and were implemented in the Monte Carlo. The difference between the numbers in the two approaches is caused by the different electron energy loss mechanisms.

6.8.2 Alpha particles

The measurement of *kB* for alpha particles is explained in [35]. Due to the very small range of alpha particles in matter the alpha emitters have to be brought directly into solution. This was done with help of Polonium-loaded PPO and Radon-purging of the sample. The light output of the scintillator for the was measured with a PMT. From the light yields and the known alpha decay energies, *kB* can be determined for alpha particles. As in the case of electrons the best *kB* values were determined from a comparison of simulation results to the experimental data. For alphas the results are $kB_{\text{Target}}^{\alpha} = 0.098$ mm MeV^{-1} and $kB_{\text{GC}}^{\alpha} = 0.134$ mm MeV^{-1}, which were implemented into the optical model. [35]

6.8.3 Protons

The quenching parameter for protons is not available yet and it has been set to the same value as for alpha particles in the Monte Carlo. Efforts to measure the proton quenching factor experimentally were undertaken at MPIK with a ^{252}Cf neutron source, [74] and at TUM with help of a proton accelerator. [75] In both cases the analysis is still ongoing at the time of this writing.

CHAPTER 7

MONTE CARLO TUNING

The optical model of [1] contained all the relevant properties only for wavelengths above 340 nm. This was motivated by the fact that the scintillation spectrum lies completely above this threshold and any light with shorter wavelengths does not survive long in the detector due to the very short attenuation lengths. This is also true for Čerenkov light, which can have much shorter wavelengths. But as there is a chance that absorbed light is reemitted at scintillation wavelengths, some of this Čerenkov light effectively survives and is not adequately accounted for in the Monte Carlo.

Now that Double Chooz has mastered many systematic effects, which previously dominated the error budget, the exact details of the optical model become more important. It is desired to reproduce the actual scintillator behavior also very accurately below 340 nm. To this end, the scintillator properties had to be determined in the wavelength region from 200 too 340 nm. The dedicated measurements of the optical properties of the Double Chooz scintillators and their components were presented in the previous chapter. The measured properties then have to be included in the Monte Carlo software. This chapter is concerned with the effects of these implementations on the energy non-linearity in the simulation.

7.1 PROCEDURE

To check the influence of the different modifications on the Monte Carlo output, each property was implemented individually and a simulation was run with the updated optical model. The optical model of [1] acts as the reference. The output of the modified Monte Carlo was then compared to the results of the reference model. The effect of each attribute on the simulation output is checked at 25 energies from 100 keV to 8 MeV. These energy is sampled at 100 keV intervals up to 1 MeV and at 200 keV intervals up to 3 MeV. Between 3 and 8 MeV only five points are taken with 1 MeV distance between them. The sample density is higher at low energies, since this is where the biggest effects are expected.

At each energy 10000 mono-energetic Gamma quanta are created. The vertex is set at the Target center with isotropic emission of the Gammas. Gammas were selected for comparability with detector data, since all available calibration sources are essentially gamma emitters. ^{252}Cf emits neutrons, but only the deexcitation gammas after the neutron capture on Hydrogen or Gadolinium are detected, and the positron from the decay of ^{68}Ge annihilates within the capsule, so that again only the annihilation gammas are detected. Gammas exhibit a stronger energy non-linearity than electrons. This is because they deposit their energy mainly through multiple Compton scattering processes. This creates a number of electrons with lower kinetic energies, which are individually more influenced by ionization quenching, than a single particle with the complete kinetic energy. The total contribution of Čerenkov light of these Compton electrons is also reduced. In total, the light yield is lower for many low-energy electrons than for a single electron that carries the complete energy.

The simulation is run with standard parameters, as they are used in official analyses. For each energy the simulation output is then analyzed with the Double Chooz analysis framework DOGS. Per event the property `TruthPE` is retrieved from the files and stored in a ROOT tree. This property denotes the true absolute number of photoelectrons created at all Inner Detector PMTs. The true number of photoelectrons was chosen, since the photoelectron creation marks the end of the optical model and the beginning of the readout simulation.

The `TruthPE`-values of all 10000 events are then put into a histogram. From the entries in the ROOT tree it is decided how the histogram is designed, including the number of bins and the upper limit (the lower limit is always zero). As `TruthPE` is an integer variable, the bins were only allowed to have integer values as their lower and upper edges. Around the value μ, which is the mean number of PEs created by Gammas of this specific energy, the entries are approximately distributed with a Gaussian function. To the left the distribution shows a slight tail towards lower PE values. The histogram is then fitted with a function $A \cdot \mathcal{G}(\mu, \sigma)$, where $\mathcal{G}(\mu, \sigma)$ is a Gaussian function with mean μ and width σ and normalized to height 1. A is used to adapt the function to the number of entries. At very low PE yields, a Poissonian distribution was used instead of a Gaussian function, but the results for μ differ only marginally. Due to the numerous fitting tasks, the curve fitting process was automated. The starting values A', μ' and σ' were chosen by a script. It sets μ' to the location of the bin with most entries and A' to the number of entries in this same bin. σ' is estimated as $\sqrt{\mu'}$. The fitting itself was done with help of the routines provided by ROOT. This was considered a preliminary fit. Since the data range was not limited, the result could be biased by the tail of the distribution to the left. To avoid this, the fit was repeated with a restricted fit range around the peak. This time the starting values A'', μ'' and σ'' were the results of the preliminary fit. The data range was limited to $(\mu'-1.5\sigma', \mu'+1.5\sigma')$, which excludes most of the tail, but still covers a sufficiently large number of bins
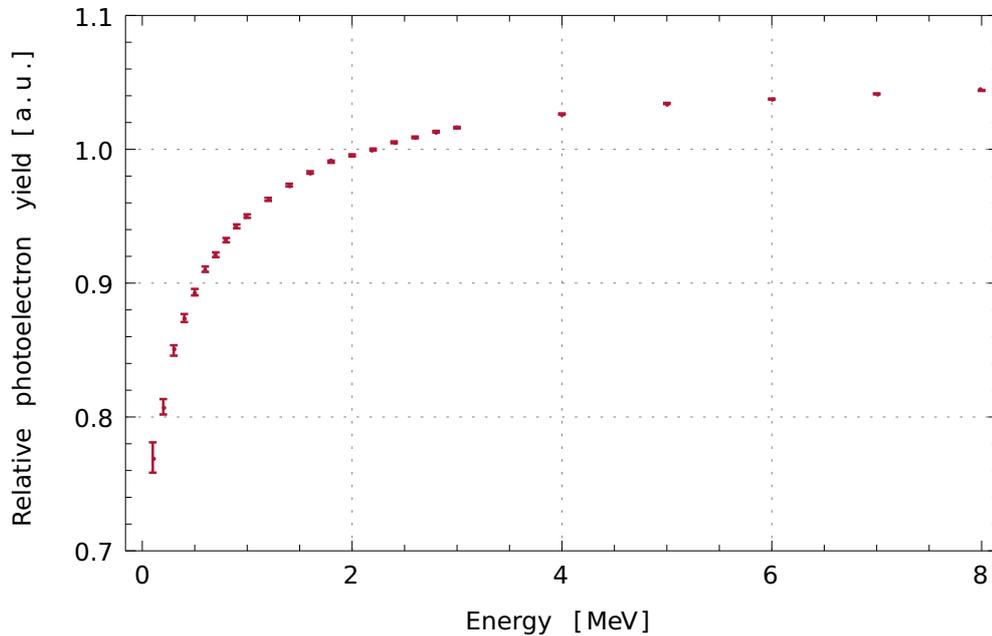
Figure 7.1: Energy non-linearity of simulated gamma events at the detector center. Each data point was obtained through a simulation of 10000 mono-energetic gamma events. This graphic shows the simulated light yield relative to the light yield expected in the case of full proportionality to the particle energy. The anchor point for this representation is the Hydrogen capture peak at 2.2 MeV, so the relative light yield at 2.2 MeV is 1 per definition. As the detector response is not yet fully linear at this point, the curve continues to rise beyond 2.2 MeV. The non-linearity is especially pronounced at low energies, where the curve has a rather steep slope.

and each included bin has at least around 100 entries. The fit result for μ and its mean error is the final result for the PE yield of a certain Gamma energy. The procedure is repeated for all Gamma energies and this way 25 data points are obtained.

7.2 SCINTILLATION AND ČERENKOV CONTRIBUTION

In the beginning the above procedure was done with the original Monte Carlo, as of [1]. This model serves as the reference for the further simulations. The relative energy non-linearity as the simulation results is shown in Figure 7.1.

Since it is expected that changes in the non-linearities are effectively due to changes of the ratio of Čerenkov and scintillation light, it is useful to gain an idea of the actual Čerenkov contribution to the signal. For this reason the simulation was repeated with the reference model, but this time the Čerenkov process was deactivated in Geant4. The result contains just the contribution of scintillation light. In turn, the difference in PE yield between the two simulation output gives

the contribution of Čerenkov light. The fraction of Čerenkov light is shown in Figure 7.2.

In the reference model the refractive index is implemented for wavelengths above 200 nm. As the function $n(\lambda)$ increases towards lower wavelengths, it reaches its highest value of 1.82 at this point. This corresponds to a threshold energy of nearly 100 keV for electrons, below which an electron does not emit Čerenkov light any more. The fact that the Čerenkov fraction is nearly zero for Gammas up to 600 keV indicates that the Compton electrons mostly receive energies below 100 keV from the Gamma. Only when the Gamma energy grows further it becomes likely that some electrons have kinetic energies above the threshold.

The content of Čerenkov light grows with the energy of the Gammas. Therefore, if a modification of the optical model causes a change of the ratio between scintillation and Čerenkov light, different energies are affected to a different extent. This causes the energy non-linearity to change as well.

The changes of the energy non-linearity connected to changes of the Čerenkov-scintillation-balance can be described with help of a simple model:

$$L_{\text{tot}}(E) = a \cdot L_{\text{scint}}(E) + b \cdot L_{\text{Čerenkov}}(E) \tag{7.1}$$

where the total light output is a sum of scintillation light and Čerenkov light. Considering that $L_{\text{scint}}(E)$ and $L_{\text{Čerenkov}}(E)$ have different functional forms, $L_{\text{tot}}(E)$ maintains its shape if and only if the ratio a/b remains nearly unchanged. From Figure 7.2 is can be seen that in the reference model $a/b \approx 19$ at high particle energies and even larger at low energies.

7.3 ABSORPTION AND REEMISSION

The implementation of the extended extinction coefficients and reemission probabilities required substantial modifications of the DCGLG4sim source code. An extension of the wavelength range was not envisaged in the original version of the respective module. Extensive testing of the modified code was done to remove bugs or biases introduced by the modifications.

With the extension of the molar extinction coefficients the attenuation lengths are now fixed. There are more degrees of freedom in the case of the reemission probabilities. While the shape of the reemission spectrum was measured below 340 nm, the actual reemission probability depends upon the quantum yields of bis-MSB and PPO. In the reference model Berlman's values ($\phi_{\text{PPO}} = 1$, $\phi_{\text{bisMSB}} = 0.94$) were used, but from the study in Section 6.6 it is advisable to replace them with values from more recent measurements. In the following I tested two different combinations of bis-MSB and PPO quantum yields, namely the values by Xiao et al. ($\phi_{\text{PPO}} = 0.77$, $\phi_{\text{bisMSB}} = 0.96$) and the results of our own quantum yield
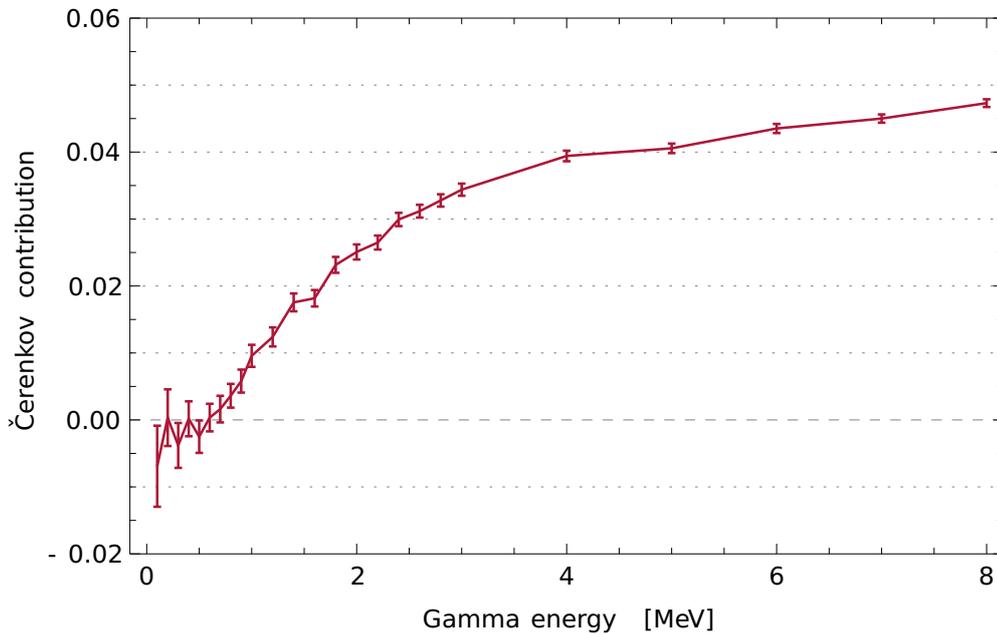
Figure 7.2: Contribution of Čerenkov light to the total light output for Gammas. Up to Gamma energies of about 600 keV the Čerenkov contribution is zero. It starts to rise for higher energy and approaches 5 %.

measurements ($\phi_{\mathrm{PPO}} = 0.842$, $\phi_{\mathrm{bisMSB}} = 86.3$, Section 6.6). In both cases the quantum yield of PPO is drastically reduced in comparison to the values used in the reference model.

With the new attenuation lengths, reemission probabilities and our quantum yields, the net light output was visibly decreased, which is predominantly caused by the smaller quantum yields. The attenuation lengths did not make any significant change, since they only changed in the micrometer range.

Even so, there were no significant changes of the energy non-linearity. This result seems surprising at first. The PPO reemission is only important at $\lambda < 340$ nm, so the change of its quantum yield only influences Čerenkov light, but leaves scintillation photons unaffected. This should change the ratio of Čerenkov light to scintillation, and this way also the energy non-linearity.

The fact that the energy non-linearity remained unaffected is explained when one looks at the size of the effects. Čerenkov light extends over a vary wide wavelength range and is created with λ between 200 and 800 nm.[1] Assuming that the refractive index $n(\lambda)$ is approximately constant over the whole range, the fraction between 200 and 340 nm is only about 20 % of the total Čerenkov light intensity. If this portion is now reduced by roughly 20 % due to the new PPO

---

[1]Light with very long wavelengths does not contribute much to the total light yield, though, because the PMT's efficiency decreases.

quantum yield, the total intensity of the Čerenkov light drops by only 4 %. At the highest Gamma energies, where Čerenkov photons make up about 5 % of the light yield, this reduction causes a total light decrease of only 0.2 %. At lower energies the effect is even smaller.

Instead, the change of the overall light yield is caused by the new bis-MSB quantum yield. Bis-MSB affects wavelengths between 340 and 430 nm, and thus a major part of the primary scintillation spectrum. But bis-MSB does not differentiate between scintillation and Čerenkov light: Čerenkov photons are only "seen" by bis-MSB if they have already been absorbed and shifted to scintillation wavelengths by PPO. Therefore the change of the bis-MSB quantum yield affects both mechanisms to the same extent. The balance between scintillation and Čerenkov light is thus only controlled by PPO.

To summarize, the fluor quantum yields only have an influence on the net light output, but do not change the energy nonlinearity. The resulting shift of the Čerenkov-scintillation balance is simply too small to have a relevant impact on the energy non-linearity. It can be concluded that under the given configuration of the optical model the energy nonlinearity is highly robust in the face of changes to the quantum yields.

7.4 LIGHT YIELD CONSTANTS

A more serious shift of the Čerenkov-scintillation balance happens when the Monte Carlo scintillation light yield normalizations are changed. In the reference model the light yield constant in the Target was set to $LY_{NT} = 9651$ scintillation photons per MeV deposited in the material, for the Gamma Catcher it was $LY_{GC} = 9651$ MeV^{-1}. However, changes of the Monte Carlo simulation might make a readjustment of these values necessary, for instance when changes are made in the readout simulation.

Of course, such a change would again alter the ratio between Černekov an scintillation light, but to a much larger extent than in the previous section. The effect on the energy non-linearity can be observed in Figure 7.3. As an example the Target light yield was decreased to 8152 MeV^{-1} there. At low particle energies the relative non-linearity decreases by about 1 %; above 2.2 MeV the new light yields increase the non-linearity by up to 0.5 %. It is worth noting that the shape of the curve in Figure 7.3 is qualitatively equivalent to the one in Figure 7.2, which shows the Čerenkov fraction. Since it was expected that a change of the light yield constants shifts the balance between scintillation and Čerenkov effect, the situation is described again by equation (7.1) and the relative change must be proportional to the Čerenkov content in the signal. This is beautifully reflected in the similarity of the two curves.
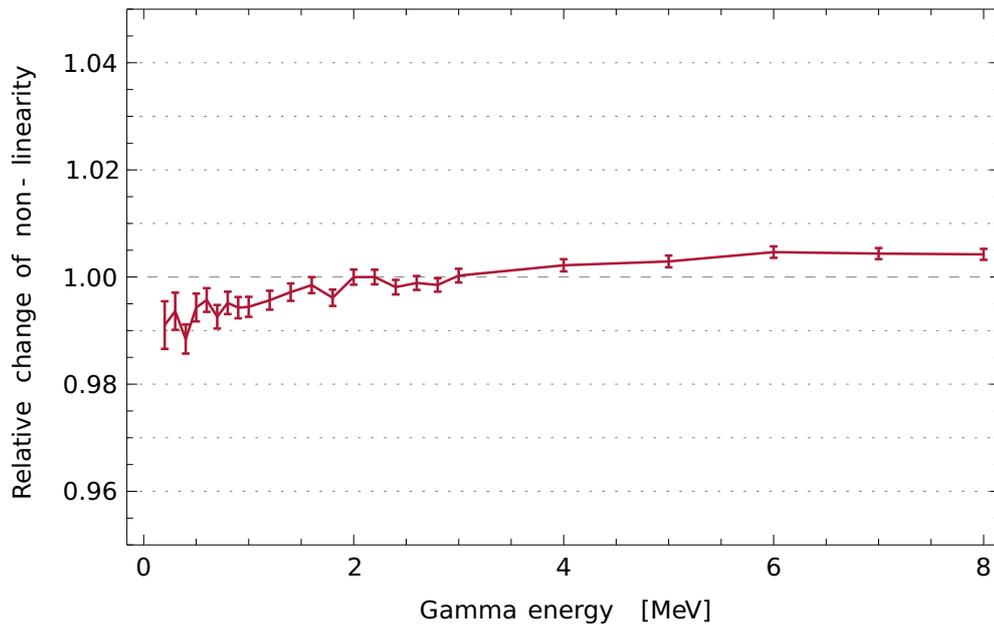
Figure 7.3: Relative change of the energy non-linearity in the Monte Carlo simulation using the new Target light yield constants of 8152 MeV^{-1}.

However, the situation is not as simple as setting the Monte Carlo light yields to the measured values, as the two contain different effects. The Monte Carlo light yield constants describe the number of primary photons per MeV, which are created *before* the processes of ionization quenching, absorption and reemission take place. The experimental values, on the other hand, include all these effects to a certain extent. Especially ionization quenching is expected to lead to a significant reduction of the number of photons that are actually created. The Monte Carlo light yields therefore have to be higher than the lab values, as a certain fraction of the photons will be lost. Consequently, even though lab measurements exist for the mean light yield per MeV, there is some freedom to adjust the values, and they should be chosen such that discrepancies between data and Monte Carlo are reduced as much as possible.

7.5 REFRACTIVE INDEX

As described in Section 6.7, Čerenkov light is only simulated in the wavelength range for which values of the refractive index are available. Since $n(\lambda)$ was only available from 200 nm upward, the portion of Čerenkov light with wavelengths below 200 nm was neglected. In order to include the contribution from this fraction in the simulation, the values of $n(\lambda)$ between 78 and 200 nm have to be added.

The effect of the extended refractive index cannot be described by a simple change of the ratio between Čerenkov light and scintillation according to (7.1). The extension increases the amount of Čerenkov light, but also the shape of the Čerenkov contribution changes. Above all, slow electrons can now still irradiate Čerenkov photons with wavelengths in the ultraviolet, so the increase affects smaller energies in particular. The ultimate threshold energy (given by the peak of $n(\lambda)$, as seen in Figure 6.13) is now decreased to about 80 keV. Without the extension this threshold was at about 100 keV electron energy. This may seem like a rather small effect, but considering that a single gamma creates several electrons with low energies, the effect is intensifies by the number of Compton electrons. Additionally, the extension also increases the amount of Čerenkov light emitted by electrons of higher energies.

The extension of $n(\lambda)$ was not yet implemented in the Monte Carlo. The reason for this is that the production of Čerenkov light is handled in a completely different manner than scintillation light. The process is also managed by DCGLG4sim, but the underlying mechanism is still governed by Geant4 itself. As such, the exact creation of Čerenkov photons is not only given by the refractive index, but also controlled by various methods of Geant4, which would have to be adjusted accordingly, as such effects could significantly influence the simulation and bias the result.

For example, the method `SetMaxNumPhotonsPerStep` sets the maximum number of Čerenkov photons that may be created by the primary particle within a step dx. When this threshold is reached and the refractive index is extended, the same number of Čerenkov photons is distributed over a wider wavelength range, reducing the number of photons in the original range to create photons with wavelengths below 200 nm. These have a smaller chance to survive, so the overall number of Čerenkov photons would be reduced instead of increased after the extension of $n(\lambda)$.

Even though there are no quantitative results available yet, an extension of $n(\lambda)$ is believed to make a significant change to the optical model and the performance of the simulation, and is worthwhile to be investigated further.

7.6 IONIZATION QUENCHING

Ionization quenching affects the energy non-linearity only at small energies, and has no influence on higher energies. The currently used value of kB in the Monte Carlo was obtained from the best concordance of the simulation output to data from a lab measurement. [35] However, as in the case of the light yield constants, changes in the simulation software might make a readjustment of the quenching parameters necessary.
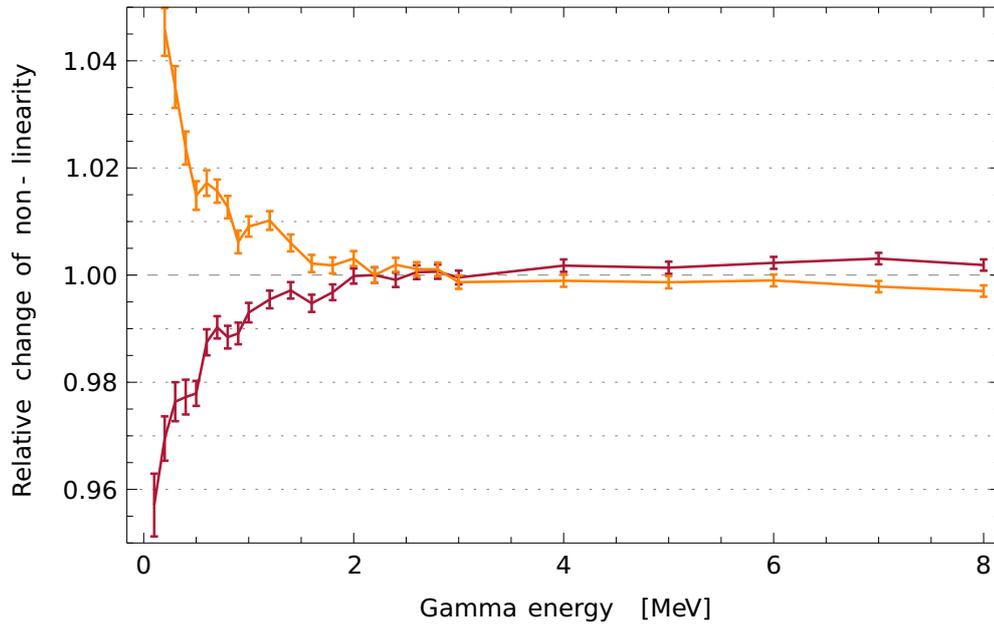
Figure 7.4: Relative change of energy non-linearity after implementation of higher and lower ionization quenching parameters kB. The curves show the effects of a higher (red) and lower (orange) value of kB by 1σ. It is seen that the changes are comparably large at lower energies, but do not affect the high energy regime very much.

Figure 7.4 shows the effect on the energy non-linearity when the standard value $kB = 0.202$ mm MeV^{-1} is changed to $kB = 0.250$ mm MeV^{-1} and $kB = 0.150$ mm MeV^{-1} (equivalent to a 1σ variation according to [35]). The effects are rather large at low gamma energies, but are nearly gone above 2 MeV. Considering the big impact of the quenching parameters on the energy non-linearity, it is probably best to not make manual adjustments in order to tune the optical model for data-Monte Carlo concordance. Instead, the kB values should be determined individually after each modification of the optical model, by comparing them to laboratory data. The kB that gives the best agreement between the simulation output and the measured curve should then be used in the Monte Carlo.

7.7 CONCLUSIONS AND OUTLOOK

At the time of this writing, the changes of the parameters mentioned above were not included in the official optical model of Double Chooz, and there remains the task to find the best combination of these parameters in order to decrease the discrepancies between data and Monte Carlo. The optical model is a complex system and it is not automatically clear what the outcome of a certain modification will be. Even less, what the effect of one modification will be in conjunction with a simultaneous change of another property. The best strategy is probably to

implement the best-known parameters first and then add the others in the order of the amount of knowledge we have about them.

In this context it is seems to be best to start with the extended molar extinction coefficients and the reemission probability curves. The results of the spectroscopic measurements are very accurate and there is practically no freedom to make changes. Next, the PPO and bis-MSB quantum yields should be set. Their error of about 5 % leaves some space for possible adjustments, but it was shown before that eventual changes have only a very minor impact. For this reason it does not make much sense to attempt to make adjustments of these parameters.

The remaining quantities have a larger influence on the simulation outcome. When the refractive index is extended to wavelengths below 200 nm, the high-frequency part of the Čerenkov spectrum is added to the simulation. While the refractive index itself is known relatively well, the scintillator's reemission probability can only be estimated. This creates a net uncertainty of the total amount of Čerenkov light added. So the total amount can be modified within certain bounds by letting the reemission probability below 200 nm vary.

The light yield constants also have an influence on the balance between scintillation and Čerenkov light and can be varied to some extent. The Birks parameter for ionization quenching is practically independent of the other parameters and can be fixed in the last step, as its value is determined by the best accordance of kB with experimental data.

To summarize, the properties should be implemented according to their measured values wherever possible. The light yield constants, the Birks parameter, and the the refractive index (by means of the reemission probability below 200 nm) offer a somewhat larger freedom for adjustment and can be modified within a certain range. Changing these properties thus presents a possibility to reduce the discrepancy between data and Monte Carlo.

PART III

EVENT CLASSIFICATION AND BACKGROUND SUPPRESSION

CHAPTER 8

AN UNSUPERVISED CLASSIFICATION APPROACH

This chapter and the following ones deal with the data analysis of Double Chooz. The studies in the present chapter are a precursor to the pulse shape analysis presented in Chapter 9. The pulse shape-based classification variable constructed in the next chapter will be optimized for several tasks using the classification technique presented here.

The usual way to start an analysis is to define the selection criteria. The first step is to design a cut with knowledge about the events which should be selected and which should be rejected.

For the θ_{13}-analyses the mission is to extract the IBD signals from the background. A list of possible backgrounds is given in Section 2.5. Due to the vast number of recorded events, the selection begins with a rejection of clearly non-IBD events, the *pre-selection*. It consists of

- rejection of light noise
- a veto of cosmic muons (by means of the Inner Veto and/or a very high energy deposition in the Inner Detector)
- a pre-selection of the right event energy range $E_{\text{vis}} \in (0.5, 20)$ MeV

The events that pass the pre-selection cuts are potential neutrino candidates and called *singles*, as no coincidence cut was applied yet. The pre-selection cuts as they are used in the present analysis are summarized in Table 8.1.

The rejection of light noise is an integral part of the pre-selection. It must be ensured that this rejection is as clean and efficient as possible. The first step is to identify characteristics that separate light noise events from physics. For example, it is well known that a particle interaction in the detector creates light isotropically and leads to a homogeneous distribution of the charge over all PMTs. Light noise events on the other hand are likely to create the majority of the charge in a single PMT. So the ratio of the highest charge seen by single PMT to the total charge

is a reasonable choice for such a selection variable. This reasoning has led to the Q_{max}/Q_{total}-variable, which is the ratio of the largest charge seen by a single PMT to the total charge observed in the detector.[1] In the next step a classifier is developed upon the variables (which is often a simple threshold) and its *efficiency* and *purity* must be determined.

The evaluation of a light noise rejection variable is far from trivial. The problem is that no clean sample of light noise is available – in contrast to physics events, for which calibration sources exist. Light noise is only extracted by means of dedicated cuts, which possess their own efficiency and purity. So we are faced with the problem that a new light noise cut can only be cross-validated against other existing light noise cuts. Consequently, the evaluation of a new light noise variable always requires a certain amount of confidence. The Monte Carlo can offer some relief when it comes to identifying the efficiency. An abundant sample of physics events can be generated and the number of events passing the cut determines its efficiency. The simulation cannot, however, give information about the purity, since light noise cannot be adequately modeled. Additionally, for pulse shape-based variables the simulation may be unreliable, because the scintillation pulse shapes are only roughly modeled with two parameters for the fast and the slow component. They rather represent a qualitative behavior of the scintillator, than to model it in detail. This is understandable, since the micro-physical processes of excitation, internal conversion, energy transfer, and so on, lie outside of Geant4's scope.

8.1 A CLASSIFICATION APPROACH

In the following I present a procedure to evaluate and optimize the Ω classifier independent of the results of other existing cuts. The analysis will be *blind*, in the sense that no *a priori* assumptions about light noise and physics events are required in the first place. In a more general context the procedure can also be used to construct a classifier when no or only very little information is available about the categories an event may be placed in. In addition, such a classifier would not be restricted to separate light noise from physics, but might separate arbitrary populations in a suitably chosen parameter space.

Cluster analysis (or *clustering*) is the task to group a set of data points in a multi-dimensional data space, and so to identify the underlying class member-ship.[76] It is based on the very basic assumption that events of the same class are close to each other in the parameter space: they "clump" together in a confined subspace and form a *cluster*. Conversely, events which are distant in the parameter space probably belong to different categories. Of course, this does imply that the

Pre-selection

$$E_{\text{vis}} \in (0.5, 20) \text{ MeV}$$
$$Q_{\text{max}}/Q_{\text{total}} < 0.15$$
$$Q_{\text{IV}} < 30000 \text{ DUQ}$$
$$\Delta T_{\text{muon}} > 1 \text{ μs}$$

Table 8.1: Selection criteria for the singles used in this analysis.

parameters have a reasonable connection to the classes in question, i.e. the class membership must be somehow reflected in the values of the parameter.[1]

Clustering is an example of an *unsupervised analysis* technique. This means that it can be done completely without supervision, i.e. the analysis is able to *automatically* group events into one of two or more categories, and does so without user input about the characteristics of the underlying categories. It works solely with the distribution of the points in the parameter space.

8.1.1 Singles selection

The idea is now to use clustering to find structures in the space of the selected variables and organize the singles data into clusters. This way it is attempted to discover characteristics of light noise and physics events, which help to effectively separate the two types of events.

We start with the *singles* data. The number of triggers in the available Double Chooz runs is overwhelming and would require an immense amount of processing time. For this study it suffices to look only at a subsample of the available data. Only one in every 100 physics runs has been used, which approximately equals two hours of data every week. This is sparse enough to significantly reduce the data, but still sufficiently frequent to capture possible evolutions of the light noise, which is known to vary over time.

Without loss of generality, a minimal light noise rejection was applied here. The $Q_{\text{max}}/Q_{\text{total}}$-cut is known from to be very efficient for a threshold of 0.09,[1] so a pre-selection with 0.15 should not impact the analysis at all. Here, it merely serves the purpose of reducing the amount of data, but can be done without. The same is valid for the energy cuts applied. A great number of non-physical triggers are below the energy threshold of $E_{\text{min}} = 0.5$ MeV, which is also used in many Double Chooz physics analyses. With these reductions the sample contains 5.1 million events.

---

[1] If there is no connection, or if the differences between the values is to small, it is trivially clear that clustering cannot resolve the task. There are no miracles, after all.

8.1.2 Feature selection

Now that the singles selection is fixed, we have to choose the variables (in the context of machine learning also called *features*) which will be used to characterize light noise and physics events. The following variables are used or proposed for the light noise rejection in Double Chooz. They are used rather frequently in the pre-selections of the analyses, and are therefore also chosen for an investigation here.

Q_{max}/Q_{total}: The largest fraction of the total charge, seen by a single PMT. As mentioned in the introduction to this chapter, scintillation light caused by physics events spreads out over the detector volume. The charge is thus expected to be distributed evenly over all PMTs, resulting in a small value of the variable. In contrast, light noise events originate at a single PMT, which is then expected to see a large fraction of the total light. This variable can reject a large portion of the total light noise contamination and has been used since [4].

T_{rms}: The root mean square (RMS) of the hit time distribution. This cut uses the fact that scintillation signals are very fast. The photons hit the PMTs within a very narrow time range and the RMS of the distribution is small. Light noise often consists of extended bursts of light. Such events have a broader hit time distribution and a larger T_{rms}. The hit time is defined as the time of the PMT pulse onset. If a PMT registers several photons within the readout time window, the hit times of all of them are taken into account. This variable has also been in use since [4].

Q_{rms}: The root mean square of the charge distribution. This variable is based on a similar reasoning as the T_{rms} variable. In physics events the PMTs are supposed to observe more or less the same amount of charge. The RMS of the charge distribution is therefore small. Outliers, as in the case of a flashing PMT, can significantly distort the distribution and lead to a larger RMS. This variable is relatively new and proposed for a future use in Double Chooz.[77]

Q_{diff}: The charge difference between the PMT with the highest charge (PMT_{max}) and the PMTs in its vicinity. It is defined as

$$Q_{diff} = \frac{1}{N} \sum_i^N \frac{(Q_{max} - Q_i)^2}{Q_i} \tag{8.1}$$

where Q_{max} is the highest charge seen by PMT_{max} and the Q_i are the charges of the PMTs within its vicinity. It is given as a 1 m sphere around PMT_{max} and N is the number of PMTs included. This variable uses the local inhomogeneity of the observed charge caused by light noise events. This variable is also rather new and envisaged for future use.[78]
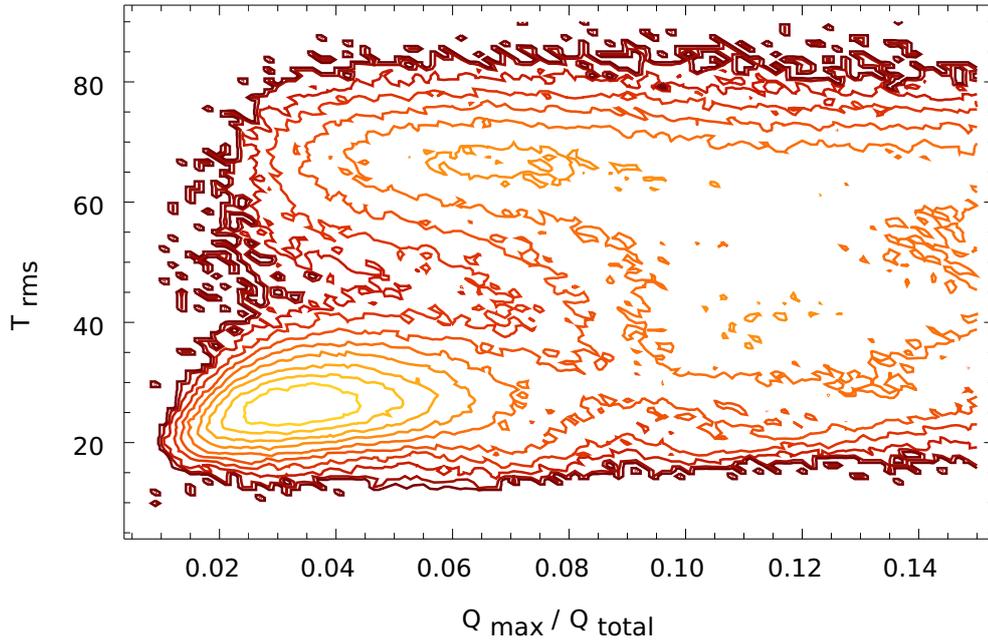
Figure 8.1: Contours of the distribution of the Q_{max}/Q_{total} and T_{rms} values for the singles events. Two main distributions are clearly recognizable: the dense population at about $Q_{max}/Q_{total} < 0.09$ and $T_{rms} < 45$ nm, and a larger and somehow sparser population around the first one. Smaller clusters, like the ones at $Q_{max}/Q_{total} \approx 0.01$ or at $T_{rms} \approx 30$ nm are also visible. It also becomes clear that two single one-dimensional cuts do not produce the most efficient and pure separation of the clusters.

These four variables are used to construct cuts to separate light noise from physics events. Four cuts, which are used or are suggested for use in Double Chooz, are presented in the following and will be investigated in this chapter.

- $Q_{max}/Q_{tot} < 0.12$
- $Q_{diff} < 30000$
- $T_{rms} < 36$ ns $\wedge$ $Q_{rms} < 464 - 8T_{rms}$ [77]
- $T_{rms} < 145 - 1500 \cdot (Q_{max}/Q_{tot})$ [79]

The first two are simple threshold cuts. The other two are two-dimensional piecewise linear cuts in the T_{rms}-Q_{rms}-plane and the T_{rms}-Q_{max}/Q_{tot}-plane respectively. In Figure 8.1 the advantage of two-dimensional cuts becomes immediately obvious. They can use more information simultaneously and allow for a much cleaner cut along the actual margins of the populations, which is not possible with one-dimensional threshold cuts. Still, the given cuts are linear or piecewise linear, whereas the limits of the distributions are curved. The clustering technique presented in Section 8.3 is able to construct non-linear decision boundaries around the distribution, which further increases efficiency and purity of the cut.

8.1.3 *Feature preparation*

For a successful cluster analysis it is preferable to work with values in a well-defined range in order to avoid that a cluster stretches out too much along a parameter axis. This might carry the risk that the cluster analysis is not able to "connect" all points of the same cluster, since they are too distant from each other. In general it should be taken care that the point density is comparable along all parameter axes. For this reason the values of all parameters are normalized such that they range from 0 to 1.

Q_{max}/Q_{total}: By definition the Q_{max}/Q_{total} variable can only take values between 0 and 1. But due to the pre-selection mentioned above, the remaining values now range from 0 to 0.15 and have to be projected onto the interval $[0, 1]$ again by dividing by 0.15.

T_{rms}: There is no general upper bound to T_{rms}, but it is empirically known that values are below 90 ns. This was taken as the upper bound and all values are divided by 90 ns to confine them to the interval $[0, 1]$. Sporadically occurring events with $T_{rms} > 90$ ns are neglected in this analysis.

Q_{rms}: In the case of Q_{rms} typical values lie below 600 DUQ,[2] but events with much higher values also exist. Since very large values of Q_{rms} become somehow equivalent to a large Q_{max}/Q_{total} ratio, is appears reasonable to use values in the $[0, 600]$ DUQ range and cut off larger values. The remaining events are divided by 600 DUQ, so that they stay within $[0, 1]$.

Q_{diff}: There is no inherent normalization in the Q_{diff} variable and values span over six orders of magnitude. Physics events are known to typically have $Q_{diff} < 30000$ DUQ. A simple rescaling would lead to an extremely packed cluster of physics events at very low values. The strategy here is to use $\log(Q_{diff})$ instead of Q_{diff} alone. The values are then spread out more evenly and contained in the interval $[0, 16]$. They can then be brought to the unity interval by dividing by $16 \log(\text{DUQ})$.

In this section some *a priori* knowledge was used in order to normalize the possible values of the parameters to the $[0, 1]$ interval. Another possibility would be to determine the mean and the variance of the sample for each parameter, and then to shift and scale the values so that the sample has mean 0 and variance 1 for all parameters. This method is applicable even if no prior knowledge about the data is available.

8.2 CLUSTERING TECHNIQUES

Now the clusters have to be identified in the parameter spaces spanned by the normalized parameters. There are various established algorithms to do this task.

---

[2]DUQ: *digital units of charge*, a measure of the PMT charges in Double Chooz.

Several of these methods were tested with the selected singles data. Very basic algorithms like the so-called *k-means clustering*, however, have many well-known limitations and are not fit to describe the data in question. For this reason they were not tested.

DBSCAN is a more sophisticated density-based method which is known to work well with a big variety of cluster shapes.[80] Density-based methods essentially define a cluster as a region of high density within the cloud of data points. For each data point DBSCAN searches for all neighboring points within a certain radius and recognizes regions with a high density of points as clusters. The search radius has to be given as an input parameter. Once chosen it remains fixed, which translates to the assumption that that all clusters have more or less equal densities. If they differ too much in density the algorithm might combine nearby separate clusters or divide a single cluster into several smaller ones. In the singles sample the cluster densities are very different and DBSCAN did not perform well enough.

The *Optics* algorithm is an advanced version of DBSCAN.[81] It eliminates the requirement of similar inter-cluster densities by allowing the search radius to vary. Still, the algorithm is prone to errors when the clusters have a varying internal density, as in the case of the singles sample. In experimental data the points are often distributed according to a Gaussian-like distribution and the density of a cluster thins out towards its border. OPTICS is then likely to recognize two clusters in its place: one for the denser region in the center and a separate one of lower density surrounding the first one. This is a serious limitation for the applying of this algorithm to the data at hand.

An entirely different class of clustering algorithms are distribution-based models. They might overcome these limitations and represent clusters with variable density well. An example is the *expectation-maximization-algorithm* (EM-algorithm). But distribution-based models are on their part restricted to specific distributions. The EM-algorithm, for instance, requires Gaussian distributions, or – more generally – to distributions of the exponential family. The underlying statistical distribution has to be given as external input, so that the algorithm is able to describe the data well. This would be contrary to the goal of organizing the data with as little input knowledge as possible; and more seriously, it is hardly possible to find a suitable statistical model for the distribution of the events in general and of light noise in particular.

All of the above techniques were found to be insufficient for the singles sample. In order to process detector data adequately, I devised a procedure which is better suited to cluster experimental data. It is called *contour clustering*, after its working mechanism, and will be described in the following.
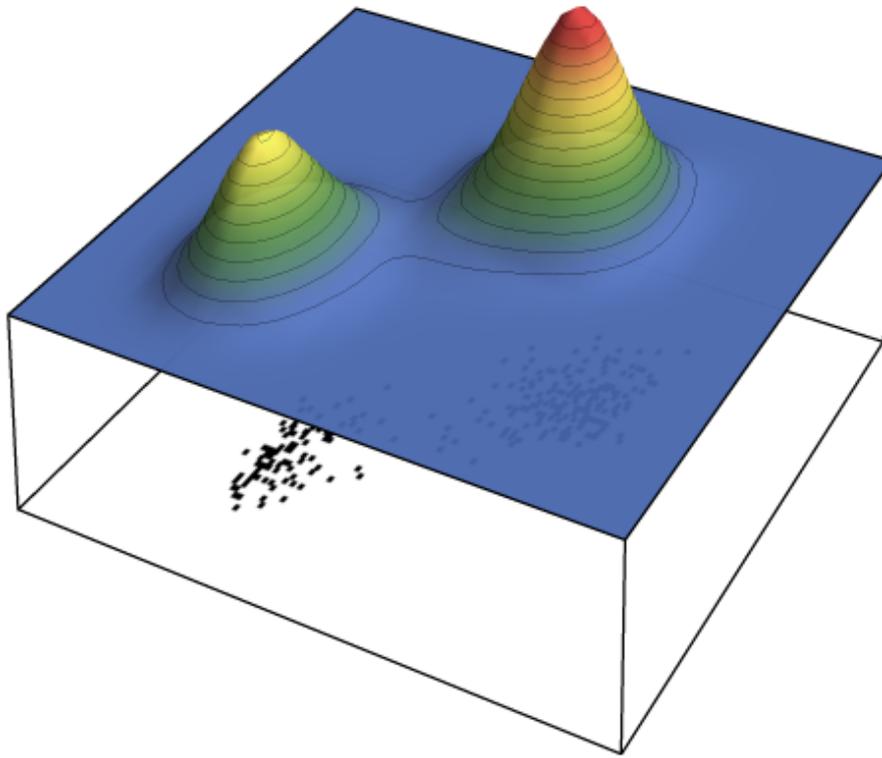
Figure 8.2: Illustration of the contour clustering concept with a two-dimensional parameter plane. The data points on the plane are interpreted as a landscape with different heights. Regions with high densities of data points show up as "mountains", which represent the clusters. The algorithm then identifies different clusters by means of their contour lines.

8.3 CONTOUR CLUSTERING

The idea behind *contour clustering* is to imagine the distribution of the data points in the two-dimensional parameter plane as some kind of "landscape" where the density of data points is represented by a *height* value. Like on a terrain map one can then use the contour lines to identify clusters. This concept is visualized in Figure 8.2.

To attribute a height to a certain location on the plane the data points were put into a histogram. The number of entries in a bin represents the height on the map and the bin coordinates give the location on the plane. The loss of accuracy due to binning is negligible, as long as the bin sizes are small. Of course there are also other (and possibly more precise) ways to determine a height value from the local density, such as counting the number of neighbors within a fixed radius like in Dbscan. Nevertheless, binning is a good choice in this situation, since it
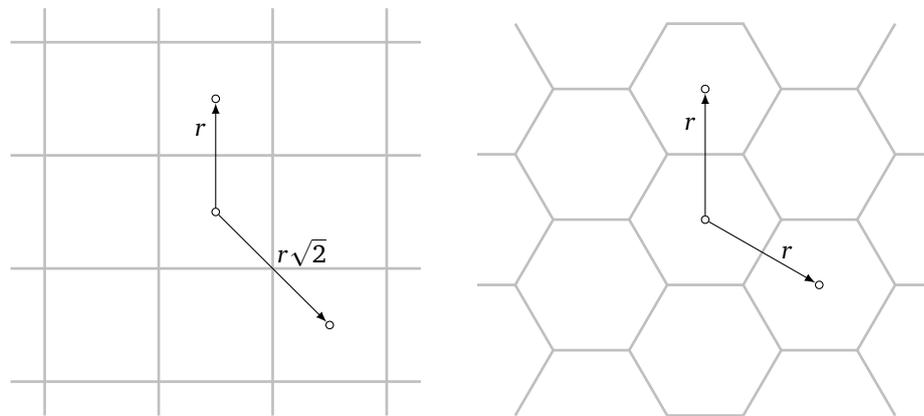
Figure 8.3: Quadratic and hexagonal binning. When measuring the distances to neighboring bins a histogram with standard rectangular bins (left) has the problem that the diagonal bins are a factor $\sqrt{2}$ farther away from the central bin. The clustering algorithm might be biased in favor of horizontal and vertical directions. The unconventional hexagonal bin shape in the right diagram circumvents this problem, since all neighboring bins have the same distance from the center.

also has the convenient side-effect to reduce the number of points to be processed, which speeds up the computation dramatically. The binning also provides a simple indexing structure, which gives a further performance boost. When working with individual points, the task of counting the number of neighbors within a distance d from a certain point can become computationally intensive. As it is not known beforehand where the other points are located, the distances to all other points have to be checked and the computing time increases accordingly. More advanced algorithms routinely employ some sort of indexing to reduce the number of queries and increase performance. This may be done with the help of more complex data structures such as k-d trees or range trees. In a histogram, on the other hand, a nearest-neighbor-query becomes trivial. The nearest neighbors are just the points in the surrounding bins, and for each bin it is known which bins to query.

From a clustering point of view, data binning can be seen as a simple form of density-based pre-clustering. However, there may be a pitfall when histogramming the data using standard rectangular bins. The situation is shown in Figure 8.3. Let b_0 be a bin of the histogram. The four bins which share a boundary with b_0 are closest, while the four other neighboring cells at the diagonals are a factor of $\sqrt{2}$ farther away. This impacts the nearest-neighbor-search (if the Euclidean metric is used as a distance measure) and introduces a preference for axis-parallel directions, especially if the search radius is small. To avoid this systematic effect, I decided to use a hexagonal grid to tessellate the two-dimensional plane.

Hexagonal combs have the advantage that all adjacent cells have exactly the same distance from the center and thus preserve the local symmetry much better.

8.3.1 The algorithm

Starting point is a filled grid of hexagonal cells. Each cell contains the number of events stored within its boundaries. In the beginning each cell is marked as *unprocessed* and is given the cluster number 0 (which means that no cluster is attributed to the cell yet). Then an ordered list is created, which contains the cells, sorted by their height values in descending order. This concludes the initialization phase.

The algorithm now loops over all cells, starting with the first one in the ordered list. The decision about the cluster membership of the active cell depends upon the status of the cells in its *neighborhood*. The neighborhood is defined as all the cells within a certain distance d of the currently active cell.[3] One can distinguish the following cases:

- All the cells in the neighborhood are marked as *uncategorized*, i.e. they have the cluster number 0. The active cell forms a new "peak" in the landscape, which means that a new cluster is found. The cell acts as a *seed* for a new cluster. The total number of clusters is augmented by 1, and this is the new cluster number of the active cell. When the algorithm processes the first bin in the list this condition is necessarily the case, i.e. the first bin always seeds a new cluster.

- In the other case at least one cell in the neighborhood already possesses a cluster attribute. Then the algorithm looks at all categorized cells in the neighborhood (uncategorized cells are not considered). Two options are now possible:

  - All categorized cells belong to the same cluster. The active bin is therefore close to an already existing cluster and considered part of it. The cell inherits the same cluster number as the cells around it.

  - The surrounding cells belong to different clusters. It cannot be (easily) decided which cluster the current cell belongs to. The cell is rather near the frontier between at least two clusters. So the cluster number of the active cell is set to *undecided*, encoded by the number -1. It is mostly a matter of taste how these undecided cells are handled. It might often make sense to attribute them to a certain cluster, but for this analysis they are considered *boundary points*. These boundary points form a mesh of connected lines

---

[3]This is the nearest-neighbor-query mentioned in the previous paragraph. If the data were not binned, an advanced routine would have to be employed here. Otherwise the performance of the algorithm would suffer and possibly make the algorithm useless if the number of cells becomes large enough.

on the plane, which conveniently represents the cluster boundaries. If it is desired, the coordinates of the boundary lines can already be used to construct a nonlinear classifier.

After that, the algorithm marks the cell as *processed* and proceeds with the next entry in the sorted list. This means that the algorithm descends to the next highest cell and checks its cluster membership. The algorithm continues this way until all cells are processed. Since cells with very few entries might be scattered around the landscape (due to outlier points), one might also introduce a minimum number of entries in a bin for it to be considered the seed of a new cluster.

Due to statistical fluctuations the distribution of the points in the histogram does not produce a smooth surface. The landscape is full of statistical spikes, which may be considered the seeds of a new cluster. Therefore the search radius around a cell has to extend over several cells to avoid finding a new cluster whenever a cell has no *categorized* cells in its immediate surroundings. Alternatively, the surface can be smoothed prior to the execution of the cluster search routine. This was the option used here for the singles data. One iteration with a simple Gaussian kernel can significantly reduce the number of clusters. The number of iterations can be chosen such that only a relatively small number of clusters, say, five to ten, remain in the end. As long as the number of iterations is not very large and the size of the smoothing kernel is small compared to the cluster size, the smoothing procedure should not substantially impact the cluster structure.

The algorithm described above is conceptually simple and remarkably fast. In the tests in this thesis it outperformed DBSCAN and the results were much better for the singles data set. The clusters are reliably identified. The basic structure of the algorithm is given in pseudocode on page .

8.3.2 *Clustering with two variables*

When the contour clustering algorithm is applied to the data, the resulting map (of the cluster memberships of each cell) is saved and the cluster membership of each cell is stored. The map can then be used to organize new events in clusters: When an unknown event is analyzed, it is placed on the parameter plane and the cluster membership is derived from its location on the map.

The cluster attribute serves as a very effective nonlinear classifier. It is also evident that it performs better than simple independent cuts on $Q_{\mathrm{max}}/Q_{\mathrm{total}}$ and T_{rms}, which would be equivalent to axis-parallel lines in the plane. The contour clustering approach was tested on three pairs of variables:

- $Q_{\mathrm{max}}/Q_{\mathrm{total}}$ and T_{rms}
- T_{rms} and Q_{rms}
- T_{rms} and $\log(Q_{\mathrm{diff}})$

The results are shown in Figures 8.4 to 8.6. The plots show the contour lines for the distribution of the singles events for the three pairs of variables, as well as the cluster boundaries found by the algorithm. It can be seen that the algorithm works very well with detector data. The main clusters are found and separated at reasonable positions. The sometimes "ragged" shape of the boundary lines is due to the hexagonal base structure of the underlying histogram. The algorithm also recognizes the two separate clusters with low densities, which may appear as a single cluster by their contour lines (the populations to the right in Figures 8.4 and 8.6). In Figure 8.5 it detects two additional clusters at high T_{rms} values, but the number of events in this region is already very low, so this region (and the clustering algorithm) is heavily influenced by statistical fluctuations.

```
1    create histogram H; // with hexagonal bin shape
2    create ordered_list L;
3    H.fill(raw_data);
4    H.smooth();
5    numberOfClusters = 0;
6
7    for each cell in H
8    {
9        cell.setClusterNumber(0);
10       L.insert(cell);
11   }
12
13   for each cell in L
14   {
15       this_cell = cell;
16       create list N = this_cell.getNeighbors(distance);
17
18       case (all 0): // new cluster found
19           numberOfClusters = numberOfClusters + 1;
20           this_cell.setClusterNumber(numberOfClusters);
21       case (all equal to C): // belongs to same cluster
22           this_cell.setClusterNumber(C);
23       case (unequal):
24           this_cell.setClusterNumber(-1); // i.e. undefined
25   }
```
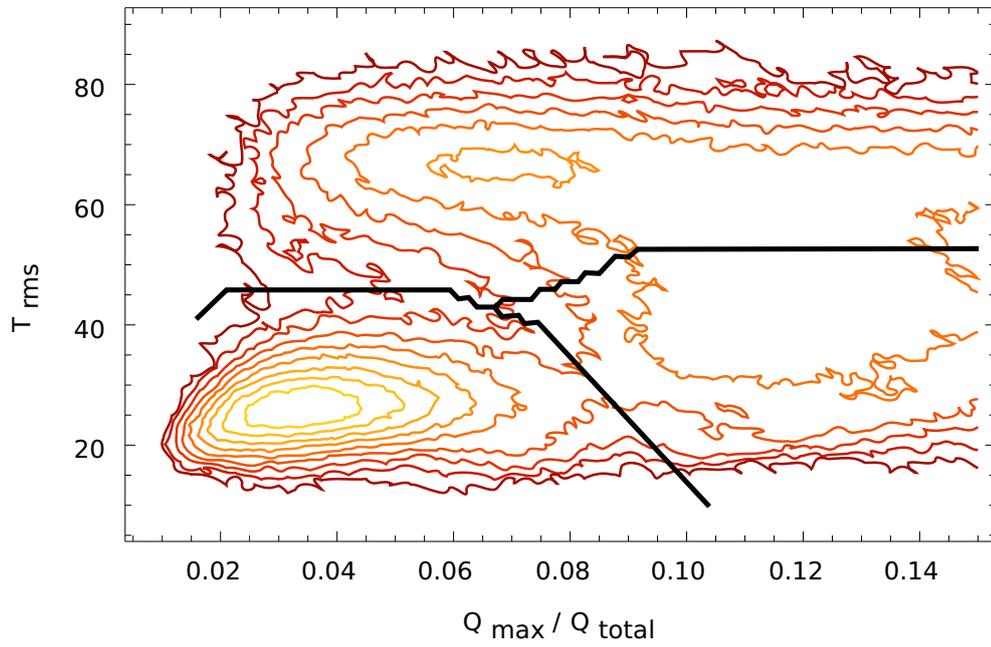
Figure 8.4: Clusters in the distribution of the Q_{max}/Q_{total} and T_{rms} values for the singles events. Two main distributions are clearly recognizable.
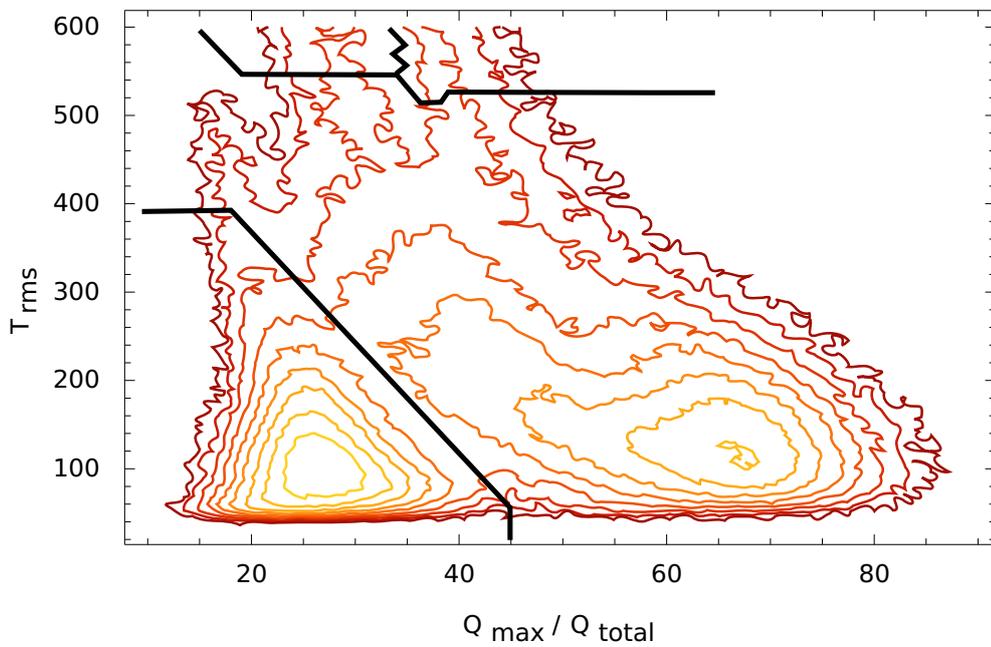
Figure 8.5: Clusters in the distribution of the T_{rms} and Q_{rms} values for the singles events.
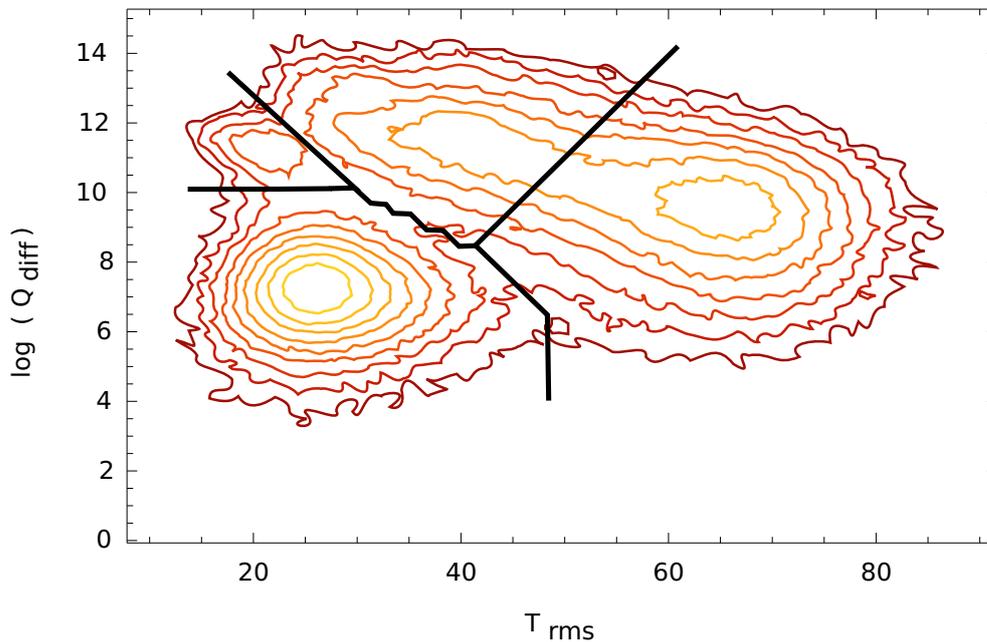
Figure 8.6: Clusters in the distribution of the T_{rms} and $\log(Q_{diff})$ values for the singles events.

8.3.3 Clustering with more than two variables

The concept that two-dimensional cuts are in general purer and more effective than two independent one-dimensional cuts can be thought further to include even more dimensions. Populations which cannot be separated in a two-dimensional parameter space, might be separable in three dimensions, and so on.

While in principle it may seem advantageous to include as many variables as possible, there are several problems connected to such an approach. First of all, the performance of the contour clustering algorithm in its given form will suffer significantly. If each dimension is equally divided into n bins, there are in principle n^d cells to process. This can either be resolved by completely disregarding empty bins, or by removing the binning and using a DBSCAN-like density measure. Then the computing time scales with the number of points, rather than with the number of dimensions. The honeycomb structure presented before must be replaced by the more general Voronoi-cells, which also makes the structure of the code more complex.

More seriously, when the number of dimensions grows too large, the points in the parameter space become increasingly sparse, so that in the end the concept of a cluster vanishes altogether. The best approach might therefore be to add new variables only until the desired degree of efficiency and purity is reached. At latest when the population of interest can be cleanly separated from the rest, there is no need to include further variables.

In the scope of this investigation it was found that an optimal separation can be already achieved when all three variables Q_{max}/Q_{total}, T_{rms} and $\log(Q_{diff})$ are used together in a three-dimensional parameter space. Physics and light noise clusters can even be linearly separated, i.e. the decision boundary is a simple plane. This is an optimal application for a linear *support vector machine,* which can find the best decision boundary in the case of separable populations. This possibility might be exploited and studied further for a light noise rejection with highest efficiency and purity.

8.4 PERFORMANCE AS A LIGHT NOISE REJECTOR

The cluster structure as determined by the contour clustering algorithm can already be used to reject light noise. It could already be seen in the Figures 8.4 to 8.6 that the boundaries found follow the cluster outlines very well. The cluster boundaries can be considered the decision boundaries for a new light noise rejection cut. In this section the efficiency of such a cut is quantified with calibration data.

Here, the cluster maps are exemplarily tested with the ^{252}Cf source in the Target center. A tight position cut of $\Delta R < 300$ mm around the source position was chosen to obtain a clean sample of physics events. Also, the standard muon veto $\Delta T_\mu > 1$ ms was applied, but no light noise cuts were used.

The neutrons from ^{252}Cf are captured on Gadolinium or Hydrogen, so two energy ranges around the respective deexcitation peaks were defined: $E_{vis} \in (1.8, 2.6)$ MeV and $E_{vis} \in (7.0, 9.3)$ respectively. Since ^{252}Cf also emits a sizable amount of gamma rays an additional time cut $\Delta T < 100$ µs to the last event is applied. A neutron is emitted simultaneously with a gamma, so the neutron capture signal is correlated to a preceding gamma event, and the time difference is given by the thermalization and capture time. After the basic event selection was performed, the different light noise rejection cuts were applied.

The results are shown in Table 8.2. It is seen that while all cuts have a very high efficiency, the cluster-based cuts have a slightly worse performance. The seemingly lower efficiency of the contour cuts can be explained by two main reasons: First, the sample is not completely free of light noise events. Certain populations of light noise events have even shown a tendency to be reconstructed at the detector center. Second, the other Double Chooz cuts are optimized for efficiency, but not for purity. They are designed such that they let a certain fraction of light noise events pass, in exchange for a higher efficiency. The contour lines, on the other hand, are found by searching for the deepest valley between two clusters. They represent the best compromise between efficiency and purity. If a very high efficiency is desired in exchange of reduced purity, the boundary lines can be extended farther into the region of the light noise cluster. This way they

cut	total number of events	determined efficiency
none	83128	100 %
C1	83067	99.927 %
C2	83056	99.913 %
C3	83036	99.889 %
Q_{max}/Q_{tot}	83124	99.995 %
T_{rms}-Q_{rms}	83068	99.928 %
T_{rms}-Q_{max}/Q_{tot}	83124	99.995 %
Q_{diff}	83110	99.978 %

Table 8.2: Evaluation of the contour cuts and the other cuts with the ^{252}Cf calibration source at the Target center. The row labeled "none" shows the total number of events after the ΔR, ΔT and energy selection, but before applying any of the light noise cuts. The rows labeled C1, C2 and C3 show the events selected with the cluster boundaries according to Figures 8.4 to 8.6 The definitions of the other cuts are given in Section 8.3.2.

could achieve an efficiency comparable to the Double Chooz cuts and still maintain a higher purity.

8.5 SUMMARY

The contour clustering algorithm serves as a method to discover the distributions of physics and light noise in the parameter spaces constructed by the variables Q_{max}/Q_{tot}, T_{rms}, Q_{rms} and Q_{diff}. It can be used to automatically find a non-linear decision boundary in these parameter spaces, which offers better efficiency and purity than linear cuts. However, the current strategy in Double Chooz is to design the cuts in favor of increased purity and accepts a lower purity in turn. The background events that pass the cuts are then attributed to the accidental spectrum and accounted for in the final analysis of θ_{13}. Even though, it was shown that the efficiency of the clustering-based cuts is almost equally high as for current and proposed cuts.

The prescription described in this chapter is also interesting from a computational point of view. The algorithm developed here is conceptually simpler than the established clustering techniques DBSCAN and OPTICS, and in the case of Double Chooz detector data (and probably experimental data in general) the contour clustering algorithm also performed better than the other two. The given contour clustering avoided fragmentation of the data (after adequate smoothing) and was able to separate different clusters well, regardless of their shape or density. Even varying inter-cluster density, which is often a hallmark of experimental data, presents no difficulties.

In test runs with the contour clustering algorithm and a homemade implementations of DBSCAN, contour clustering was also much faster than the latter.

Yet, much of the performance boost compared to Dbscan is probably due to the pre-clustering step. Depending on the analysis task at hand, this may not always be an option. The pre-clustering also limits the applicability of the algorithm to low-dimensional parameter spaces. Nevertheless, since clustering is a fundamental process in the area of machine learning, this algorithm may be of general interest.

A FOURIER-BASED METHOD FOR EVENT CLASSIFICATION

Pulse shape discrimination (PSD) is a collective term for methods to identify particles by means of the shape of the registered pulses. As explained in Section 3.2, particle identification by PSD is based on the fact that different particles deposit their energies differently when they traverse matter, which can lead to visible differences in the scintillation pulse shape. But PSD can also be used to distinguish between different scintillators. In Double Chooz the Target and Gamma Catcher compositions were chosen so that they show significant differences in their pulse shapes, precisely to make pulse shape discrimination between them possible. The PPO concentration of 7 g/l in the Target makes the scintillation much "faster" than in the Gamma Catcher (which contains just 2 g/l of PPO).

In a large-scale liquid scintillator experiment like Double Chooz an efficient PSD is often difficult to achieve. Many details of the original pulse can "wash out" over the large distances. One reason is that the photons of the scintillation pulse are distributed over many different PMTs. The different distances from the interaction vertex to the PMTs have to be taken into account. A time-of-flight correction of the individual PMT signals can be performed after the event vertex was reconstructed, but it introduces some uncertainty to the waveform. In addition, scattering and reflection of the scintillation photons occurs in the material. Finally, the DAQ can cause some distortion of the recorded pulses and add a certain degree of electronic noise to the signal.

Common methods for PSD include the *tail-to-total* and *late light ratios* (involving charge integration), or the pulse rise time approach.[82] and the comparison to a reference pulse shape (in specific implementations sometimes called *Gatti filter*[83]). However, the differences in the detector pulse shapes are so small that it is already very hard to discriminate between Target and Gamma Catcher pulses with the charge integration methods. Past studies with established methods could not provide a large enough separation, such that the parameter could be put

to a reasonable use for analysis. [84] The separation of different particles, which are expected to show even smaller pulse shape differences, would be extremely challenging if not impossible. In the following I present novel PSD technique, which can separate the event classes with currently unprecedented efficiency.

9.1 THE FOURIER TRANSFORM

The Fourier transform is a widely used technique to decompose a periodic signal into its frequency components. Mathematically, the Fourier transform $\mathscr{F}\{f(t)\}$ of a periodic function $f(t) : \mathbb{R} \to \mathbb{R}$ is defined as

$$\mathscr{F}\{f(t)\} = \int_{-\infty}^{\infty} f(t) e^{-2\pi i t \omega} \, dt \tag{9.1}$$

It is customary to denote functions in the time domain with minuscule letters and their Fourier transforms with the equivalent capital letters, i.e. $F(\omega) := \mathscr{F}\{f(t)\}$. This is now a function of the complex-valued *frequency* ω, which has the "classical" frequency as its absolute value, and the phase as the complex argument. Strictly speaking, the transform is only applicable to periodic functions with period T. Nonetheless, in practice the transform is commonly used on finite portions of arbitrary signals. In this case it is implicitly assumed that the signal is periodic with length T and repeats itself infinitely beyond both ends of the window. Usually this underlying premise does not lead to complications for the analysis of transformed signals.

The Fourier transform shows that every pulse can be analyzed into harmonic functions. One can turn this point of view around and imagine a pulse as a composition of many harmonic functions with different frequencies and phases. This is expressed by the inverse Fourier transform $\widetilde{\mathscr{F}}\{F(\omega)\}$. It is given by

$$\widetilde{\mathscr{F}}\{F(\omega)\} = \int_{-\infty}^{\infty} F(\omega) e^{2\pi i t \omega} \, d\omega \tag{9.2}$$

Furthermore, it is

$$\widetilde{\mathscr{F}}\{\mathscr{F}\{f(t)\}\} = f(t) \tag{9.3}$$

which means that no information is lost and the original signal can be fully retrieved from its transform $F(\omega)$.

The Fourier transform has many useful properties, by which the use of the Fourier transform for PSD was motivated. Some of which are summarized in Table 9.1. An ideal PSD variable would only describe the shape of the pulse independent of its size or its position within the readout window. A shift of the pulse in the time domain only causes a (complex) phase shift in Fourier space; the absolute value

	time domain	Fourier domain
LINEARITY	$f(t) = a \cdot g(t) + b \cdot h(t)$	$F(\omega) = a \cdot G(\omega) + b \cdot H(\omega)$
TRANSLATION	$f(t) = g(t - a)$	$F(\omega) = G(\omega) e^{-2\pi i a \omega}$
CONVOLUTION	$f(t) = g(t) \ast h(t)$	$F(\omega) = G(\omega) \cdot H(\omega)$

Table 9.1: Some important properties of the Fourier transform. The real-valued functions in the time domain are represented by minuscules, while their corresponding Fourier transforms are represented by capital letters.

of the Fourier components does not change. It does not matter where the pulse is located in the readout window, and consequently no correction has to be applied. Also, as stated above, no information about the original time-domain pulse is lost due to the transform. In contrast, sampling the waveform at certain points around its maximum, which is also often applied in PSD, discards much of the original information.

To some extent the Fourier transform also separates signal- and noise-related features. Noise is usually distributed over a broad frequency range or dominates at high frequencies, while features of the pulse are mainly encountered in the lower frequency range. If the high-frequency components are not considered, a substantial amount of noise is already removed from the pulse analysis and pulse smoothing or other noise reduction is not necessary.

9.1.1 *The discrete Fourier transform*

In Double Chooz the analog signals from the detector are discretized at a very early stage of the data acquisition chain. The *waveform digitizer* samples the incoming signals at 2 ns intervals, and quantizes it into 256 channels in the y-direction.[85] Henceforward we deal with digital signals.

The sampling has an immediate impact on the transform. As the transform (9.1) acts upon a continuous function, it is not applicable on the digitized data from the detector. The transform can be done instead by the closely related *discrete Fourier transform* (DFT):

$$F_\omega = \mathscr{F}\{f_t\} = \sum_{t=0}^{N-1} f_t \, e^{-2\pi i t \omega / N} \tag{9.4}$$

where N is the number of samples, taken at discrete times t. The result is also discrete. The most important difference to the continuous case is that with a finite window size T only harmonics of certain discrete frequencies can be present in the pulse. After the constant ω_0 the lowest frequency is ω_1, which completes exactly one oscillation within T. There can only be integer multiples of this base frequency present in the signal, else there would be a discontinuity at the window limit. So the next frequencies are $\omega_2 = 2/T$, $\omega_3 = 3/T$ and so on. The highest frequency which can be represented is ω_{64}, at which the sinusoid alternates between two

subsequent samples. This is formally described by the *Nyquist-Shannon theorem*. It essentially states that in the discrete case the number of *independent* frequency components is limited to $n/2 + 1$, where n is the number of samples per period, and one frequency is the constant. With the 128 samples available in Double Chooz, the DFT of the pulses returns only 65 independent components.[1] This is a convenient reduction of data, especially when computationally intensive methods (like the neural network in Chapter 10) are used with the pulses.

9.1.2 *The Fourier power spectrum*

The DFT of a real-valued pulse yields complex-valued Fourier components $F_j = a_j + i b_j$. Instead of using the Cartesian picture it is more convenient to write the complex components in the polar representation $F_j = R_j e^{i\varphi_j}$. The modulus R and the phase φ can be directly interpreted. R is the magnitude of the given frequency component in the original signal. The argument φ represents the phase shift of the frequency[2] in the time domain. For the purpose of PSD it is difficult to extract useful information from it. The valuable information for event classification is mostly contained in the absolute value R of the coefficients. The set of all R_j is the *power spectrum*, also called *Fourier spectrum* or *spectral density*. In physical processes it represents the power carried by a certain frequency within a periodic signal.

9.2 PULSE PREPARATION

We now build a classifier from the Fourier spectrum. The idea of a Fourier-based classifier is that the frequency domain might reveal characteristics which are concealed in the time domain. First, the scintillation pulse shape of the event has to be restored. In Double Chooz the Inner Detector volume is observed by 390 PMTs. When a particle interaction occurs within this volume, the flash of light spreads out and is ultimately distributed over all PMTs. In order to recreate an approximation of the original signal, the waveforms recorded at all PMTs must be summed up again. The procedure is described in the following.

9.2.1 *Baseline correction*

The baselines of the recorded PMT pulses have an offset. Since the Fourier transform is sensitive to additive constants (see Table 9.1), the baseline has to be determined and subtracted from the single pulses prior to the analysis. It is

---

[1] The Fourier coefficients are complex, which means that they in fact consist of two components: the absolute value and the complex phase. From this point of view no data reduction takes place, but it is shown that the complex phases carry nearly no relevant information for PSD and they may be discarded for these purposes, so that in the end really only 65 independent components remain.

[2] In the context of Fourier analysis the term *frequency* often denotes a sinusoid function of a given frequency

important that this correction happens before the time-of-flight correction in order to avoid discontinuities when the pulse is shifted: the shift may leave empty values in the array that stores the pulse, which might be filled with zeros. If the baseline is not at zero, sharp edges can be created at these positions.

Due to the characteristics of the Double Chooz PMTs, the raw pulses are recorded with negative amplitude. In the present analysis they were also inverted for positive amplitudes. The reason for this is that several methods which were investigated in the course of this thesis required positive values to work with.

9.2.2 *Time-of-flight correction*

There is the question if it is beneficial to correct the relative positions of the single PMT pulses by the time of flight of the photons. In general such a correction would always have to be taken into account to retrieve the original waveform. The times of flight from the reconstructed event position to each PMT are calculated and the pulses are shifted accordingly before adding them up. The drawback is that this procedure might affect the pulse shapes. If a PMT pulse has a tail that extends beyond the end of the readout window, it is simply cut off. When shifted to the left, the cut-off portions would have to be replaced with zeros, and there is then a sharp step in the waveform at that point. If this happens with sufficiently many PMT signals, the sum of the time-of-flight-corrected pulses might be distorted at its end, which influences the Fourier spectrum. In numerous tests it could be shown that if the baseline is subtracted before the time-of-flight correction, the distortions are minimal and their influence on the performance of the classifier (see Section 9.3) is small. Even so, both approaches have different advantages and disadvantages, and have been used in the following.

9.2.3 *Summation and normalization*

The baseline- and time-of-flight corrected pulses of all Inner Detector PMTs are now summed up. The integral[3] over the sum pulse scales with the event energy, and consequently also the Fourier components. As we want to have an energy-independent classifier, the sum pulse $p(t)$ has to be normalized to $\sum p(t) = 1$. As it follows from the definition of the Fourier transform, the zeroth spectral component represents just the integral over the pulse in the time domain. After normalization the zeroth component is therefore always 1 by construction. When this last step is completed the DFT can be executed and the power spectrum is built.

---

[3]Strictly speaking, in the discrete case the "integral" is the sum over the samples, but the terminology is often adapted from the continuous case.
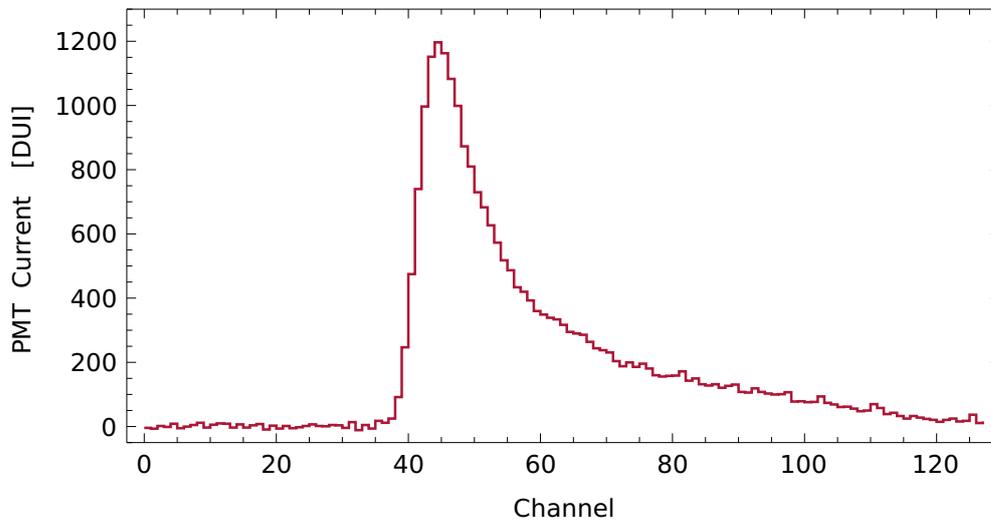
Figure 9.1: Sum pulse of a physics event in the Target volume. The PMT pulses were baseline- and time-of-flight corrected before addition. They were also inverted, so the signal is represented here as a positive pulse with baseline zero (while the actual PMT pulses are negative). The energy of the event in display is ca. 3 MeV.
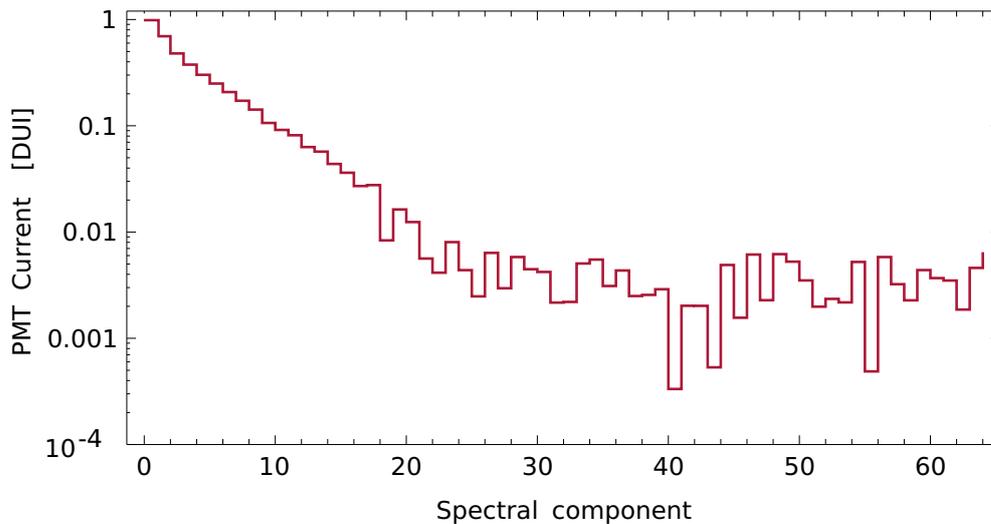
Figure 9.2: Normalized power spectrum of the pulse displayed in Figure 9.1. The zeroth component is always 1, as it represents the integral of the pulse, which was normalized before the transform. Only the 65 independent coefficients are shown.

9.3 A FOURIER-BASED PSD CLASSIFIER

Figure 9.1 shows an unnormalized sum pulse of a Target event before the transform; Figure 9.2 is its normalized Fourier power spectrum on a logarithmic scale. It is exemplary for the Fourier spectrum of most physics events. It can be seen that the size of the spectral coefficients decreases sharply and enters the noise regime at
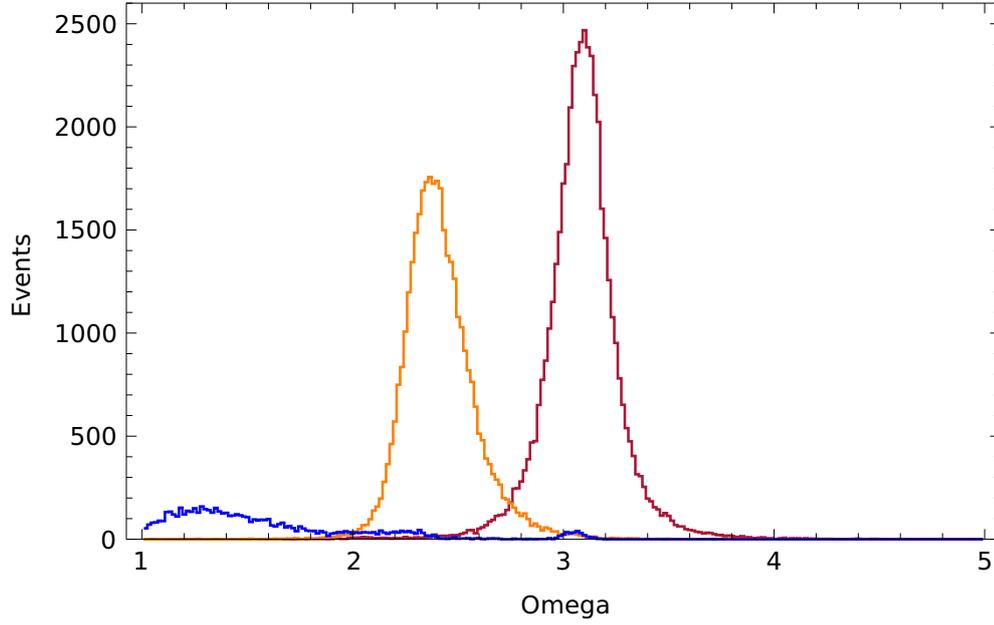
Figure 9.3: Distribution of the Ω variable for the ^{252}Cf source in the Target center (red) and the Gamma Catcher the middle of the Gamma Catcher (orange) at $\rho = 1429$ mm. Target and Gamma Catcher events are separated very clearly by Ω and only a very small overlap exists. Furthermore, selected light noise events (blue) typically have much lower values of Ω and can be separated from physics events.

about component 20. The information about the pulse shape is mostly contained in the lower components. With this in mind we can define a PSD variable

$$\Omega := \sum_{j=1}^{20} \left| \mathcal{F}_j \left\{ p(t) \right\} \right|, \tag{9.5}$$

where $\left| \mathcal{F}_j \left\{ p(t) \right\} \right|$ is the jth spectral component of the sum pulse $p(t)$. The zeroth component is not included in the summation, since it is always 1 by construction. The upper limit was chosen 20, as this is where the spectra of most pulses start to transition into the noise regime. The choice of components will later be optimized in Section 9.5.

9.3.1 Performance of Ω

The performance of the Ω variable is tested with calibration data. The ^{252}Cf source is chosen, as it produces events up to very high energies. It was positioned once in the Target center and once at $\rho = 1429$ mm in the Gamma Catcher. Apart from a volume cut of $\Delta R < 50$ cm around the source position, only the light noise cuts $Q_{\text{max}}/Q_{\text{tot}} < 0.09$, $T_{\text{rms}} < 40$ ns and $Q_{\text{diff}} < 30000$ DUQ were applied. In addition, light noise was selected from the singles sample of Section 8.1.1 when
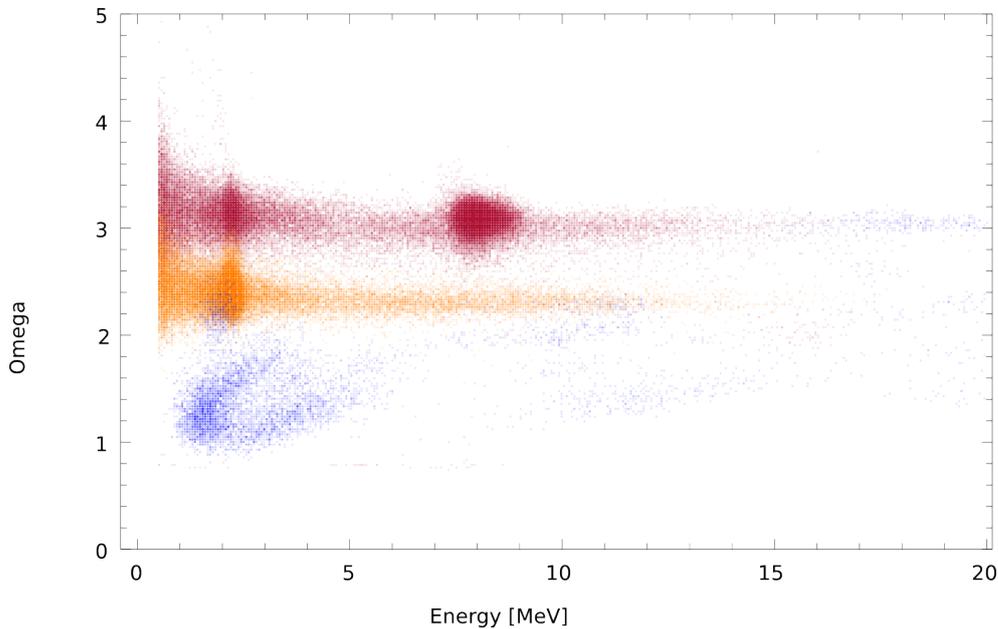
Figure 9.4: The Ω variable plotted against the event energy. The plot involves the same calibration data as Figure 9.3. The physics events for two horizontal bands for the Target (red) and the Gamma Catcher (orange) respectively. The dense population at 8 MeV is caused by Gd-capture events and is only seen in the "Target band" with $\Omega \approx 3$. Light noise events (blue) have a very different structure and form several clusters. The plot also shows that the overlap of the curves in Figure 9.3 is mainly caused by low energy events, for which the bands get broader.

$Q_{\text{diff}} > 30000$ DUQ or $Q_{\text{max}}/Q_{\text{tot}} > 0.09$. The result is shown in Figure 9.3. The variable provides a very clear separation of physics events in the Gamma Catcher and in the Target. Moreover, the selected light noise events predominantly show up at values between 1 and 2, and are therefore rather far away from the physics events, especially from the Target distribution which peaks at around $\Omega = 3$. The variable may consequently be used as an efficient light noise rejector.

It is also interesting to investigate the distribution of Ω together with the event energy. This is done in Figure 9.4. There it can be seen that physics events form narrow, horizontal bands. This shows that the energy dependence of Ω is relatively small. There is only a slight upward curvature towards lower energies. This region is also where most of the overlap between the Target and Gamma Catcher bands occurs. Events identified as light noise show an entirely different behavior. These events form multiple separate populations at different positions in the plane. Yet, the majority of the light noise populations have $\Omega < 2$ and can be removed from the sample with a threshold on Ω without cutting much into the physics bands. Remaining light noise events with $\Omega > 2$ would have to be removed with other cuts, though.
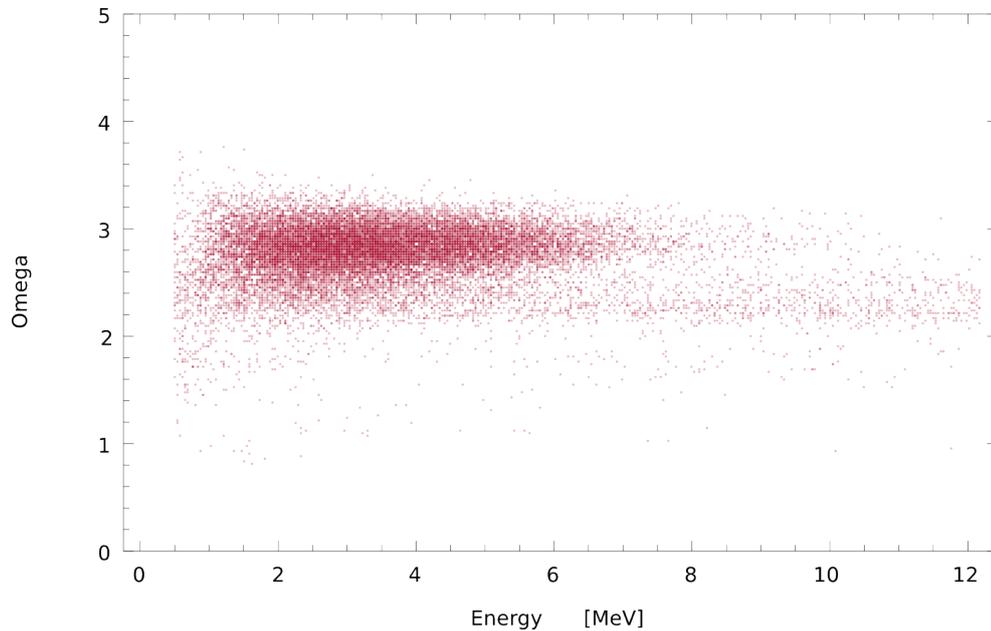
Figure 9.5: Distribution of Ω for events from a loose Gadolinium selection. The events are mostly contained in the Target volume, but a band of Ω values between 2.0 and 2.6 exists, indicating events in the Gamma Catcher. A further investigation shows that events in this band show characteristics of stopping muons.

There is also a small position dependence of Ω, which broadens the bands if events of the whole detector are taken into account. But the separation of the two bands comes indeed from the two different scintillator pulse shapes, as it was confirmed with the ^{252}Cf source at the Target wall. The source is then still positioned in the Gamma Catcher, but close enough to the Target, that the neutrons are captured in the different volumes. In this case the two distinct bands can still be observed, even though the events take place more or less at the same position.

The position dependence can be nearly completely removed if the pulses are time-of-flight corrected. Interestingly, the overall separation of the Target and Gamma Catcher bands becomes worse in this case.

9.4 STOPPING MUONS

Now I look at the distribution of Ω in a Gadolinium analysis. For this a selection similar to Table 2.1 was performed, but with rather loose cuts in order to increase the background content on purpose.

Figure 9.5 shows Ω against the event energy for this selection. It is seen that most events are contained in a population around $\Omega \approx 3$. This was expected from the findings before. Since neutron captures on Gadolinium can only occur in
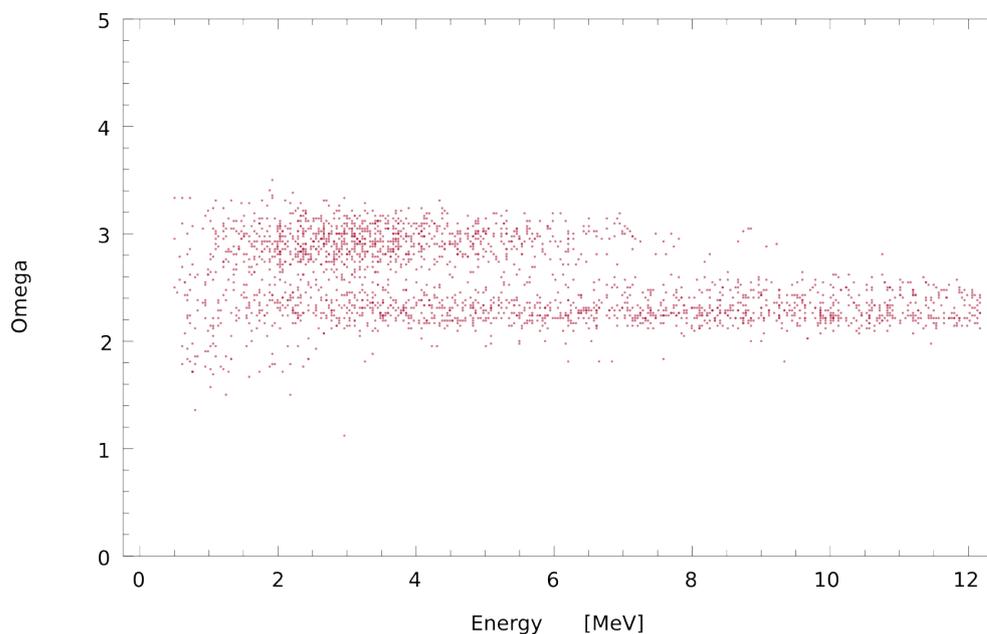
Figure 9.6: This graphic shows Ω for the same selection as in Figure 9.5, but with events confined to a sphere of 500 mm radius around the point $z = 750$ mm. The position reconstruction algorithm places stopping muons preferably into this region, due to the very inhomogeneous charge distribution of chimney events. Two bands can be clearly seen here. The upper band with $\Omega \approx 3$ corresponds to "normal" Target events. The lower band is caused by stopping muons and vanishes if a stopping muon cut is applied. The band is also not visible for Target events outside the sphere.

the Target, most events should have an accordingly high Ω value. Nevertheless, there is a second, horizontal band visible with $2.0 < \Omega < 2.6$, which would hint at Gamma Catcher events. But a look at the event vertices shows that the events in this band are still located in the Target. More precisely, they cluster in a region in the detector around the point $(0, 0, z = 750$ mm), which is typical for stopping muon events. This can be confirmed by applying the stopping muon cut FV$< 1.23 \cdot \ln(E/0.068)$.[26] This cut removes most of the events in the Gamma Catcher band, confirming that they were indeed stopping muons.

Apparently stopping muons are reconstructed in a certain Target region, but have an Ω according to a Gamma Catcher event. This gives another handle for stopping muons. Figure 9.6 shows the distribution of Ω when the events are restricted to a sphere with 500 mm radius around the point $(0,0,z = 750$ mm). The two bands can now be clearly seen again, since the events are confined in a rather small space and the spread due to the position dependence of Ω is practically removed in this case. The two bands can be selected with a threshold cut on Ω. The events with $\Omega < 2.6$ are now selected.

Stopping muons are characterized by a short time separation between the prompt event (the muon) and the delayed event (the decay electron), given by
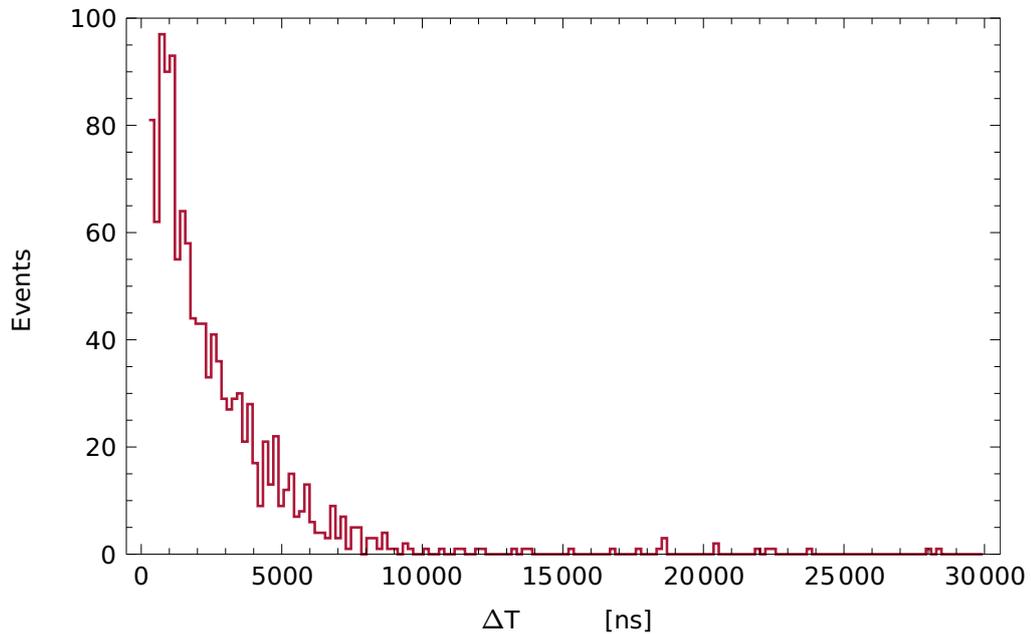
Figure 9.7: Time distribution of the events in the "stopping muon band" selected from Figure 9.6 with $2.0 < \Omega < 2.6$. A fit of the distribution with an exponential function between 0.5 and 6000 µs yields a time constant of (2.146 ± 0.099) µs. This is in agreement with the mean life time of muons and shows that stopping muons can be identified by Ω.

the mean muon life time of 2.197 µs. Figure 9.7 shows the ΔT distribution of the selected events. A fit of a single exponential function to the fit between 0.5 and 6.0 µs yields a time constant of (2.146 ± 0.099) µs, which is in excellent accordance with the muon life time. This method thus provides a very clean sample of stopping muon events and can be used both for studying the stopping muon contribution and rejecting it.

9.5 OPTIMIZATION

The previous definition of the classifier Ω sums up the spectral coefficients in a predefined range. This yields very satisfying results, but the definition is not yet optimized. As the rejection of light noise is needed in most studies and analyses, an approach will be presented in the following to optimize Ω for the identification of light noise. Nevertheless, it could also be adapted for an improved separation of Target and Gamma Catcher events, e.g. for use in spill-in/out studies, for which it is important to know in which volume an event took place. One possibility to further improve the separation capability of Ω is to give the spectral components different weightings. If a single component has the same central value and the same variance for both event categories, it does not carry any usable information about the class an event belongs to. This is for example the case for the zeroth

component, which is always 1 per definition. But the first few components do not perform much better. Their mean values do not differ significantly for physics events and light noise events, and they are always compatible with the other event class within their respective errors. The spectral components 5 to 10 tell more about the class membership of the event. Their mean values for events of one class do not agree with the other class, and their error bars do not overlap. These components contain more information and should be given more importance. One can so define a weighting

$$w_j = \frac{\mu_{j,1} - \mu_{j,2}}{\sigma_{j,1} + \sigma_{j,2}} \tag{9.6}$$

for each of the summands in (9.5). The $\mu_{j,k}$ and $\sigma_{j,k}$ are the mean values and variances of the jth spectral coefficient for events of class 1 and 2 respectively.

Such an approach has the disadvantage that it depends on a selection of light noise in the first place. There already has to be a working light noise selection in order to optimize Ω for light noise rejection. An independent way to select light noise and physics events is given by the contour clustering algorithm from the previous chapter. With its help rather pure physics and light noise samples can be obtained. The mean power spectrum and the variances of the components can then be determined for both samples and used in equation (9.6). The resulting optimized variable provides a better separation between the two event classes than the standard Ω with flat weightings and has also a reduced inter-class variance, i.e. the bands get narrower.

This optimization procedure can be used for all classes of events from which a pure sample of sufficient size can be obtained. For example, an optimization for PSD between electrons and alphas could be achieved with help of a sample of BiPo events. They provide a large sample of alpha events, which can be used to create an average power spectrum for alphas. If it is possible to obtain a large sample of fast neutron events, Ω could also be adapted for their detection. However, it is expected that even with help of the optimization procedure, Ω cannot separate different particles as cleanly as physics and light noise events. A PSD between particle types is preferably performed with the technique presented in the following Chapter.

9.6 SUMMARY

It has been shown that the pulse shape-based variable Ω allows a very good discrimination between Target and Gamma Catcher events by the different pulse shapes of the two scintillators. This was not possible before with standard PSD techniques like a tail-to-total ratio and suggests that PSD can be done much more effectively in the frequency domain than in the time domain. The capability to differentiate between the two volumes can be useful for measurements of the spill-in/out effect, for example.

In addition, Ω is highly effective as a light-noise rejection variable. It is able to detect light noise populations that are not seen by other variables and can reject them with nearly negligible influence on physics events. The performance of Ω for light noise rejection is furthermore virtually independent of the event energy. Another advantage is that Ω is the first real pulse shape-based variable in Double Chooz. As such it is independent of and complementary to other variables and approaches used in the experiment.

It could also be seen that with the help of Ω one is able to identify stopping muons amidst other physics events. Stopping muons are reconstructed in the Target volume, but show an Ω according to Gamma Catcher events. They can thus be selected by looking for Target events with a Gamma Catcher-like Ω. The removal of stopping muons is particularly important, since they constitute a part of the correlated background in Double Chooz.

The weighting of the spectral components can be adjusted to adapt Ω for different analysis tasks. With the prescription presented it is possible to further improve the performance of Ω and to create different flavors specialized for a separation of Gamma Catcher from Target events, light noise from physics events, alphas from electrons, and so on. These considerations raise the question if it is possible to adapt Ω in such a way that the identification of different particles becomes possible. This question is addressed in Chapter 10, where a much more general procedure to discriminate between event classes is presented.

Chapter 10

Machine learning for background suppression

In the previous chapter it was shown how to optimize Ω for special tasks. By modifying the weight of the individual Fourier components, the separation of different event populations could be maximized in Ω-space, allowing for a cleaner cut than with a flat weight. Nevertheless, this method only leads to different linear combinations of the Fourier components, and thus to a linear separation of event populations. This has proven to be sufficient for the separation of Target and GC events, light noise from physics events, or even the identification of stopping muons. A reasonable discrimination between particles, however, could not be achieved yet.

In a high-dimensional data space, this previous method is equivalent to finding a hyperplane which optimally divides the space into two parts: each one containing only events from one category. But of course, such a perfect separation is rarely possible. Under common circumstances there will always be at least some events which belong to one class, but are encountered in the half-space of the other. And even in low-dimensional spaces a linear classifier is not always the best possible solution, as already seen in Chapter 8. A more precise classification can be achieved through *non-linear classification*. This corresponds to constructing a hypersurface of a more complex shape in the parameter space.

Considering this, the full potential of the Fourier power spectrum has probably not yet been exploited. The differences between the spectra of electrons and positrons are most probably of non-linear nature and a linear classifier is no longer sufficient for this task. Hence, the goal of this chapter is to find a non-linear classifier for electron-positron discrimination. An established technique to effectively deal with such high-dimensional non-linear optimization problems are *artificial neural networks*, which will be employed here for this task.

10.1 NEUTRINO SIGNATURE

One advantage of antineutrinos over neutrinos is that the IBD reaction creates a coincidence signature in the detector. The search for two consecutive signals allows to reduce the background content dramatically, since most background consists only of single events. On the other hand, correlated background still remains an issue, since it can mimic this coincidence pattern.

A second advantage of antineutrinos is that the prompt event is a positron, while most of the physics background in Double Chooz comes either from gammas or electrons, including the prompt events of correlated backgrounds (in particular the cosmogenic β^-n-emitters ^{9}Li and ^{8}He). This opens up the possibility to reject these kinds of events by the different pulse shapes that electrons and positrons create in the detector.

Even though the energy deposition of electrons and positrons is very similar, they differ fundamentally by the two annihilation gammas at the end of the positron trail. While the electronic stopping of the positrons can be considered point-like, the gammas can move several decimeters away from the interaction point, leading to a slightly delayed energy deposition. This leads to distortions in the scintillation pulse shape, compared to electron events. Still, the differences between them are very small and the reliable separation of electrons and positrons is a challenging task. To my knowledge a pulse shape-based event-by-event discrimination of these particles has not yet been successfully achieved in a large-volume liquid-scintillation neutrino detector. The main obstacle is that the time difference between the primary ionization signal and the annihilation is usually too short to observe.[1] However, positrons differ from electrons in a second way. They can form positronium with an electron from the surrounding matter, which delays the annihilation.[86]

In vacuum o-positronium has a relatively long lifetime of $\tau = 142$ ns, because the annihilation is suppressed by the spin orientation. In matter interactions with nearby electrons reduce the effective lifetime to several nanoseconds. This can lead to a detectable delay between the ionization signal of the stopping positron and the signals from the two annihilation gammas. The pulse shape can then be fitted with two Gaussian functions, one for the positron stopping signal and one for the subsequent gammas. Positronium events can then be identified if the time separation of the two Gaussians is above a certain threshold.[86] The Borexino collaboration has used the positronium formation to reject a fraction of their positron background from ^{11}C, and could so measure solar *pep*-neutrinos.[87] However, in this context Borexino is in the opposite situation as Double Chooz. Its detection channel is neutrino-electron scattering (so that the particles to look for are electrons), and positrons are undesired background to be rejected. Unfortu-

---

[1]In Double Chooz the pulse digitization has a resolution of 2 ns, which is too coarse to resolve a sub-nanosecond broadening of the pulse.

nately, this procedure is not as well applicable for background rejection in Double Chooz. Since o-positronium formation only occurs in a fraction of positron events, many positrons would appear as background and the method would probably throw away many neutrino events. Nevertheless, considering the previous success in Borexino, the method is investigated and improved further for a possible use in Double Chooz.

Another proposed technique to separate positrons from electrons is to use the event topology instead of the differences in timing. It would exploit that the annihilation gammas deposit their energy at different places, so that positrons have three points of interactions, while electrons have only one. A likelihood approach could then be used to check if the event is more compatible with one or three vertices, and consequently if it is more compatible with electrons or positrons.[88]

10.2 ARTIFICIAL NEURAL NETWORKS FOR CLASSIFICATION

Artificial Neural Networks (ANNs) are a widely-used tool for machine learning and data mining. ANNs began as mathematical abstractions of biological neural networks and they have picked up much of the biological terminology. Nowadays, they have evolved far beyond that initial concept, and are widely used as analysis tools for different kinds of tasks. This high versatility made them very popular in many different fields. The following gives a short introduction to ANNs; the interested reader can find more detailed information in textbooks on the topic, for example [89; 90].

The basic unit of an ANN is called a *neuron* or *node*. It essentially it takes the sum of a number of input variables and computes an output via its *activation function*. The output can then be used other nodes, which in turn process the signal as one of their input values. In analogy to biological neurons the activation function is mostly sigmoid, so that the node "fires" (i.e., it gives an output signal close to 1) when the sum of the inputs is above a certain threshold. In the other case the neuron stays inactive and returns an output close to 0. This function is called the *activation function*. This behavior might be produced with a Heaviside step function, but for several reasons it is desirable to use differentiable functions, so that sigmoid functions are most often used instead. Other types of activation functions can also be used, including unbounded functions like linear or quadratic functions. However, sigmoid functions and *radial basis functions* play special roles in ANN theory: they form a *universal basis* and a suitable network using such functions can approximate any continuous function to any desired level of accuracy, which is formulated in the so-called *universal approximation theorem*.[91]

A single node cannot do much more than respond to a given stimulus. The power of ANNs arises from the connections of many different neurons. In principle, each neuron may receive the output of any other node as their input, and send its own output to any other node (or even itself). A natural exception are the *input nodes*, which receive their input externally, and the *output nodes* at the end, which make the network's response available to the user again. The structure of the connections between them can be designed quite freely, giving rise to many different types of neural networks. In the following I will only consider *multi-layer feed-forward networks*, also called *multi-layer perceptrons*. One example of such a network is the one which will be used later for electron-positron-discrimination and is shown schematically in Figure 10.2.

Even though multi-layer perceptrons are the simplest kind of ANNs, they are very versatile and capable of solving many different problems. Pattern recognition has to be especially noted. Multilayer perceptrons were used very efficiently to discover previously unknown patterns in the input data, and to classify the inputs accordingly. [89] The attempt to to identify electrons and positrons based on possible structures in their Fourier power spectra is an example of pattern recognition. Multilayer perceptrons were thus considered the method of choice for this task.

From the universal approximation theorem mentioned before follows that (under mild assumptions) a multi-layer perceptron with sigmoid activation functions is able to approximate any continuous function to any desired level of accuracy, if only the number of hidden neurons is chosen large enough. [91;92] This is important for our problem statement, since it guarantees that an appropriately designed multi-layer perceptron is able to emulate a non-linear decision boundary in the high-dimensional space of Fourier coefficients. This is, if the spectral coefficients of electrons and positrons form two separable populations in the 64-dimensional space, there exist multi-layer perceptrons which are able to find the best separation between them.

Finally it shall also be noted that many types of neural networks are the counterpart of a "classical" statistical technique. The multi-layer perceptron in particular is essentially performing a nonlinear regression. [93]

10.2.1 *Network training*

When the basic network structure is fixed, the artificial neural net can "learn" to solve different tasks, i.e. it can adapt itself to a problem statement in such a way that it reproduces the desired output. The network is fed with different input patterns, from which it discovers the characterizing features by itself. Over time, it gets sensitive to the characteristic patterns in the input. This procedure is called *training*. Neural network training is an optimization procedure. The networks' weights are adjusted such that after many iterations the error is minimized.

In the present case the network shall learn to differentiate particles by discovering patterns in the Fourier spectra of the events[2] and assign categorical labels ("electron" and "positron", represented by 0 and 1) to the input patterns.

For the given classification task the *supervised learning* paradigm was adopted. This means that the neural network is trained with a set of input patterns of which the class membership is already known. The class labels are called *targets*. The network usually starts with randomly initialized weights, but educated guesses are also possible. During the training phase the network is presented different input patterns and it creates a response according to the weights of its nodes. **style!** It is then checked if the answer matches the right class attribute. If yes, then the weights of the nodes which contributed to the answer are increased, in the other case their weights are decreased. There are different ways how the weight adjustment is done exactly; a widely used algorithm is *error backpropagation*.[89;94]

This procedure is repeated for all patterns in the input set. When all patterns were presented to the network, one *training cycle* has been completed. The readjustment of the weights takes place after each training cycle, rather than after each input. This is known as *batch learning* and avoids the risk that the order of input patterns influences the training progress, e.g. that more recent patterns have a stronger influence than older patterns. Over time, the weights change in such a way that the network becomes sensitive to features in the input data, which are relevant to the classification task. The nodes associated with less important features are assigned smaller weights. This way, on average, the network's response will come closer to the target.

Training is a crucial part in the design of an artificial neural network and determines its performance on real data. The user has to ensure that the training process is in fact suited to the problem at hand. A well-known problem is the so-called *overfitting*. In this case the network was too excessively trained, so that it allowed to become sensitive to smallest details in the input data (e.g. to statistical fluctuations), but loses its generalizability. This is, on real data the network will often give wrong results, especially when the input patterns are close to the decision boundary. One solution to this problem is to monitor the training progress. After each cycle, the network performance is evaluated with a validation set, for which the class memberships of its patterns are also known. A simple method to avoid overfitting is then to stop the training process when there is no improvement on the validation set any more.

---

[2]This assumes, of course, that there exist useful characteristic patterns in the Fourier spectra of electrons and positrons. It may well be that the differences are too small to be of any use. A network could then only find a meaningless pattern due to overfitting.
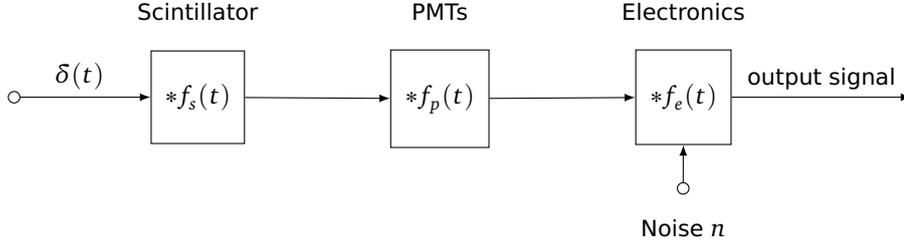
Figure 10.1: Creation of the pulse shape in the linear time-invariant approximation.

10.3 THE NETWORK FILTER AND DECONVOLUTION

Artificial neural networks have already been used for pulse shape discrimination in the past. What is new in this approach is that it works entirely in the Fourier domain. This gives the neural network several advantages over similar techniques in the time domain. It is well known that several problems can be solved more easily in Fourier space and this is also true in this case. In particular, an important tool to which the network has access to in the Fourier domain, but not in the time domain, is *deconvolution*.

If the Double Chooz detector is considered a *linear time-invariant system*, the detection mechanism in Double Chooz can be considered a chain of subsequent convolution processes in different sub-systems.[95] Each sub-system possesses its own *impulse response*, i.e. a characteristic function with which the system responds to a δ-like input signal, and modifies the primary signal accordingly. The process is depicted in Figure 10.1. The energy deposition of the primary particle can be regarded as a δ-like function, which is then convolved with the impulse response functions of the scintillator, the PMTs and the electronics. Altogether, the response of the detector to a δ-like[3] input is

$$h(t) = \delta(t) \ast f_{\text{scint}}(t) \ast f_{\text{PMT}}(t) \ast f_{\text{elec}}(t) + n \qquad (10.1)$$

In the detector the impulse responses of the subsystems cannot be decoupled, and what is seen is a single impulse response $f(t)$ of the whole detector.

$$f(t) = f_{\text{scint}}(t) \ast f_{\text{PMT}}(t) \ast f_{\text{elec}}(t) \qquad (10.2)$$

In this picture a positron is described by three clearly separated δ-like input functions, which follow in quick succession. This information is still contained

---

[3]By this, I refer to a function that is so sharp that it takes a value c at $x = 0$, and is practically zero at all other samples. It is similar, yet not equivalent, to the δ-distribution, which goes to infinity. The δ-function considered here may be best imagined as an extremely narrow Gaussian function.

in the output function, but it is washed out. This is where the Fourier transform comes in. The convolution processes are described by simple multiplications in the Fourier domain (see Table 9.1). The above equation transforms to

$$H(\omega) = c \cdot F_{\text{scint}}(\omega) \cdot F_{\text{PMT}}(\omega) \cdot F_{\text{elec}}(\omega) + N = c \cdot F(\omega) + N \qquad (10.3)$$

and is now described by simple multiplications. The inverse process of deconvolution is also easy to achieve in the Fourier domain. In principle, the original signal can be restored by dividing $H(\omega)$ by the total transfer function $F(\omega)$.[4] In practice, this is hindered by the additive noise N. Due to its statistical nature the exact shape of N is always unknown and it cannot be simply subtracted. Often, as in this case, it can be assumed that N is additive, white and Gaussian, and several techniques can then be used to restore a certain approximation of $H(\omega)$.

A second and more severe problem is that the system under consideration is not really an LTI system. Especially the scintillator and the PMTs have a stochastic output. Both the number of photons in a single scintillation pulse and the number of electrons per PE follow a Poisson distribution (or a Gaussian distribution in the limit of many particles). The exact shape of the transfer function is then unknown and has to be estimated. *Blind deconvolution* approaches usually make heavy assumptions on the signal and the noise content, which are generally not fulfilled here.

This can now be handled by the artificial neural network. With N supposed to be *additive white Gaussian noise*[5] and stochastically determined response of the sub-systems, we are in a situation in which the data points scatter around the "true" output curve.

This is just the situation encountered in typical curve fitting problems. As it was mentioned in Section 10.2, a multi-layer perceptron essentially performs a nonlinear regression. In other words, the neural network can remove removes the (electronic and stochastic) noise from the Fourier spectrum and restores the "true" output function $H(\omega)$. Then, since it can be assumed that on a statistical basis the transfer function $F(\omega)$ is on average equal, $H(\omega)$ only needs to be divided by the average transfer function $\tilde{F}(\omega)$ to retrieve the original function.[6]

---

[4]The power spectrum is just the absolute value of this equation, so the power spectrum of the input signal can also be restored from the power spectrum of the output signal by a simple division.

[5]This means the noise content is added on top of the output signal, has an amplitude distributed according to a Gaussian and equal power in all frequency bands.

[6]Of course the network does not "divide" one function by another. The aim was to show that the information about the input signal is still contained in $H(\omega)$ and that the network can access it. The net rather looks for patterns in $H(\omega)$, which hint towards the structure of the input pulse, and so towards the type of particle.
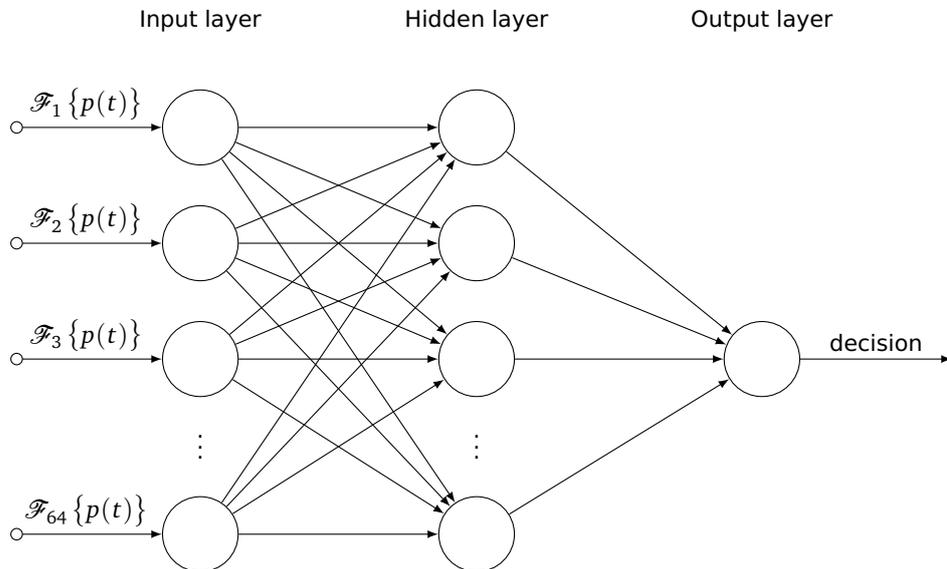
Figure 10.2: Structure of the artificial neural network used for the Fourier Network Filter. It is a feed-forward network with a single hidden layer and a single output node. Each node of the input layer is connected to every node in the hidden layer. The activation functions are all logistic functions. The 64 spectral components are fed into the input nodes and the final output is in the range $(0, 1)$, as required for binary classification.

10.4 AN ARTIFICIAL NEURAL NETWORK FOR BACKGROUND SUPPRESSION

The ultimate goal of this chapter is to create an artificial neural network capable of separating positrons from electrons (and other background events), based solely on the event pulse shapes. Based upon the findings of the previous chapters, the network described in the following works on the Fourier spectrum, rather than the actual pulse shape.

10.4.1 *Network design*

The neural network used in this thesis was implemented with help of the Shark machine learning framework.[96] The basic layout is a *multi-layer feed-forward network*. This is the simplest class of artificial neural networks. Its nodes are organized into different *layers*, as seen, for example, in Figure 10.2. *Forward-feeding* means that the output of a node can only be used as an input in one of the following layers. In a stricter sense (and as is it the case here), a node's output may only feed nodes in the layer directly behind it.

As input the Fourier spectrum of the sum pulse, as constructed in Section 9.2, is used. Here we only use time-of-flight corrected sum pulses. As it is yet unknown which spectral components are the most important ones for this task, the complete Fourier spectrum is used as an input for the network and it is given 64 input nodes. One hidden layer with another 64 nodes is implemented and each input node is connected to each neuron of the hidden layer. Note that this is not necessarily the optimal configuration. It is normally more advisable to start with a small hidden layer and increase it step-by-step until a satisfactory performance is achieved.[90] But since this process of repeated training and evaluation can potentially take very long for a 64-input network, the approach is reversed and the network is first evaluated with a 64-node hidden layer, which may eventually be reduced later on.

As the problem of positron-background-separation is a binary classification task, only a single output node is used. The output itself should be between 0 and 1, representing the two classes. So sigmoid functions are a natural choice for the activation functions of the neurons in the hidden layer as well as for the output node. More precisely, the *logistic function*

$$f_{\text{act}}(x) = \frac{1}{1 + e^{-x}} \tag{10.4}$$

was selected. Its advantage over other possible sigmoid functions is that its derivative can be calculated easily, which speeds up calculations in the training phase. Also, they have a special importance for classification tasks.[90] The complete network structure used here is schematically displayed in Figure 10.2.

10.4.2 Network output

When sigmoid activation functions are used, the output can only be in the range $(0, 1)$. This is comfortable, since it can be interpreted as a probability for the class membership. Output values very close to 0 or 1 generally indicate a big certainty about the decision, i.e. the decisive features in the input pattern allow for a clear distinction between the classes and the network is very "confident" about its decision. In the other case, when the response is distant from either bound, the respective features are not very prominent.

Therefore, the classifier built upon the network response d is defined as

$$\text{event} \in \text{class A} \qquad \text{if } d \geqslant 0.5$$
$$\text{event} \notin \text{class A} \qquad \text{otherwise.}$$

The value $d = 0.5$ represents the situation in which the network finds both class memberships equally likely.

Pre-selection

$E_{\text{vis}} > 0.4$ MeV
$\Delta T_{\text{muon}} > 1$ ms
$T_{\text{rms}} < 36$ ns $\vee\ Q_{\text{rms}} < 464 - 8\,T_{\text{rms}}$
$Q_{\text{max}}/Q_{\text{tot}} < 0.09$
$Q_{\text{diff}} < 30000$ DUQ

Prompt event

$E_{\text{prompt}} \in [4, 7]$ MeV

Delayed event

$E_{\text{delayed}} \in [4, 10]$ MeV
$\Delta T \in [10, 150]$ μs

Purity

No valid triggers in the 200 μs before the prompt event.
No valid triggers in the 600 μs after the prompt event,
except for the delayed candidate.
$\Omega > 2.2$
$\text{FV} < 1.23 \cdot \ln\left(E_{\text{prompt}}/0.068\right)\ \wedge\ \text{FV} < 6$
$\rho < 1100$ mm $\wedge\ |z| < 1100$ mm

Table 10.1: Selection criteria for the positron candidates used in the training of the neural network.

10.4.3 *Training samples*

For the training phase suitable data samples have to be used. A clean sample of electrons can be obtained from a selection of ^{12}B events, while the only sizable and clean sets of positrons come from the inverse beta decay in the antineutrino analyses. The prompt events of the Gd-analysis were used as a positron sample, since the Hydrogen analysis is not sufficiently pure for the purposes of training. The selection criteria for the training sets are summarized in Tables 10.1 and 10.2. The cuts are designed in favor of very clean samples, rather than to preserve the number of events. They were thus chosen rather strict and the resulting sample size is relatively small.

The positron sample   This selection differs from the usual Gd-selection[1] mainly in that the energy window for the prompt event was narrowed from $[0.5, 20]$ MeV to $[4, 6]$ MeV. The energy window is chosen considering the different energy spectra and background contributions in the two samples. The ^{12}B spectrum has a significant background content below 4 MeV, which defines the lower limit. The antineutrino spectrum, on the other hand, only has few events above 7 MeV, which

Prompt event	
	$E_{\text{prompt}} > 520$ MeV
Delayed event	
	$E_{\text{delayed}} \in [4, 7]$ MeV
	$\Delta T \in [2, 62]$ ms
	$T_{\text{rms}} < 36$ ns $\vee Q_{\text{rms}} < 464 - 8\,T_{\text{rms}}$
	$Q_{\text{max}}/Q_{\text{tot}} < 0.09$
	$Q_{\text{diff}} < 30000$ DUQ
	$Q_{\text{IV}} < 10000$ DUQ
Purity	
	$\rho < 1100$ mm $\wedge\ |z| < 1100$ mm
	No coincidence in the IV or OV with the delayed event.

Table 10.2: Selection criteria for the electron candidates used in the training of the neural network.

is therefore chosen as the upper limit. Both samples should only contain events of the same energy range, the window is set to $E_{\text{vis}} \in [4, 6]$ MeV for both the positron and the electron sample.

The pre-selection applies three light noise cuts to remove non-physics events as well as possible. Additional cuts (under "Purity" in Table 10.1) are a cut on Ω, according to Chapter 9, together with a cut on the functional value to reduce remaining light noise as well as stopping muons.[26]

Since only the Target volume is loaded with the Gd-complex, the events from the Gd-sample are predominantly located in the Target volume (let aside spill-in events). Events close to the boundary with the Gamma Catcher have a higher chance to be in fact accidental coincidences. Therefore an additional volume cut was imposed on the candidates, so that only events in the Target volume are selected.

The electron sample The cosmogenic isotope ^{12}B is created by a high-energy cosmic muon crossing the detector. For this reason, the prompt event in the ^{12}B selection is a muon (defined by the extremely high energy deposition), and the electron from the β^--decay of ^{12}B constitutes the delayed event. The selection used here is given in Table 10.2 and based upon the prescription in [97].

The ^{12}B selection is adapted to the Gadolinium cuts so that they only differ in the fact that once they are electrons and once positrons. This is necessary so that the neural network has no other way to discriminate between the event classes than by the Fourier spectra. This is why the ^{12}B selection also contains a volume cut, even though the events vertices are distributed over the whole Inner Detector. In contrast to the Gd selection no pre-selection is applied, since the light noise

cuts might have an impact on the high energy muons. Light noise cuts are only applied on the delayed candidates.

10.4.4 Training

Now the network is trained with the selected positron and electron events. The training sample consists of an equal number of positron and electron events. 1000 events of each species were randomly chosen, so that the training set contains 2000 events in total. The class labels are 0 for electrons and 1 for positrons.

The 64 independent spectral components of each event are included in the training sample together with the class label ("positron" or "electron"). The latter serves as the *training target*, i.e. to control if the network has made the right decision so that the weights can be adjusted accordingly. Apart from the spectral coefficients and the class labels no other information is made available to the net.

In the beginning the weights are randomly initialized to a value between -0.1 and $+0.1$. The network is then trained with a cross entropy error measure. Cross entropy is a concept from information theory, and defined as

$$H(y) \; = \; -p\ln(y) \; - \; (1-p)\ln(1-y) \tag{10.5}$$

where p is the probability, that an event belongs to class 1, and y is the network output. It is better suited for classification than, say, a traditional mean squared error, and takes into account different class membership probabilities in the training sample. For example, if among 1000 patterns only 1 belongs to class "A", the cross entropy error puts much emphasis on a correct determination of this one event. A mean squared error would happily train the network such that the output is always "B". The choice of a cross entropy error is also theoretically motivated if the network's output is to be interpreted as a probability.[89] The training algorithm used for the network filter is `iRpropPlus`, as described in [94].

For technical reasons the training progress was not monitored with an independent validation set. Instead, the network configuration was saved after every 100 cycles and the behavior of each of these configurations was checked afterwards on a validation sample. After the successful training the neural net is now configured for the classification of positron and electron events. The network is then applied to the Hydrogen sample. Before I present the results, I turn to the structure of the trained network, as it gives an insight to its decision making process.

10.5 THE NETWORK STRUCTURE

When a neural network is set up it is not immediately clear how it makes its decisions and it is of interest to find out how it works internally. In general it is difficult to gain detailed information about the inner workings of a neural net, but a some methods exist to provide at least some knowledge.
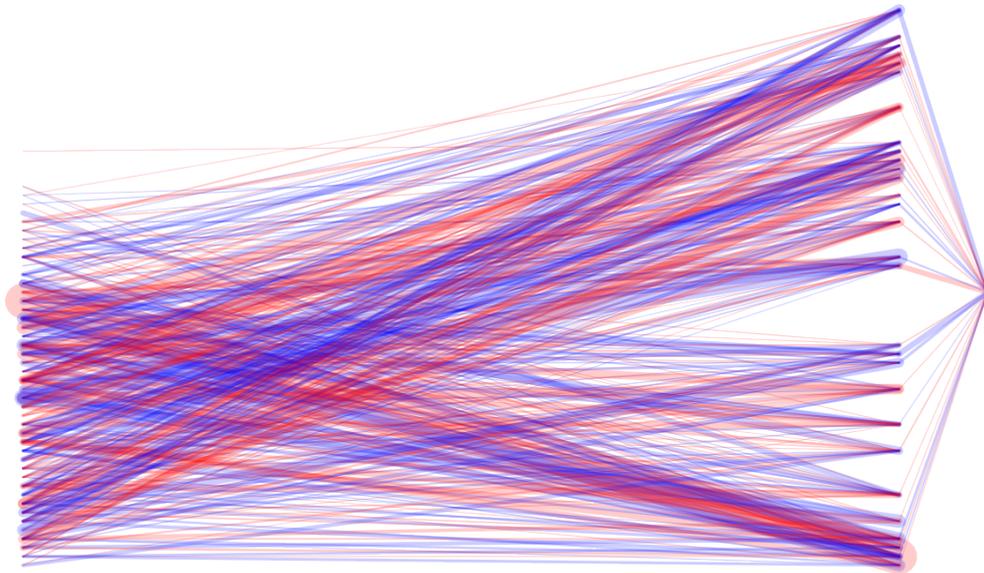
Figure 10.3: A network graph of the trained network filter in *parallel coordinates*. It displays the weights of the connections between the input layer and the hidden layer, as well as between the hidden layer and the output node. The stroke widths indicate the strength of the connection. Red and blue lines indicate a positive or negative weight respectively. It is seen that the first 20 input nodes do not have any connections, which means that the first 20 spectral coefficients have no impact for the task of particle identification.

I created a network graph of the network trained in the manner described in the previous section. This graph shows the weights of the connections between the single nodes. The thickness of each line is a measure of the absolute value of the weight of the connection, and the color represents its sign. Connections with large weights have a big importance, while connections with weights close to zero do not contribute much to the decision making process. The resulting graph is rather confusing because of the $64 \times 64 = 4096$ connections between the input layer and the hidden layer. However, it is seen that the node weights are distributed rather unequally: most connections have very low weights, and in turn there are relatively few strong connections which are responsible for the network's decision. If the 1000 faintest connections are removed from the graph, it becomes more "readable" and one obtains Figure 10.3. It is seen that the first 20 input nodes have no or only very faint connections, which means that they have the least importance for the network's output. In other words, the network is most sensitive to the spectral components of higher frequencies.

This is an important observation. It shows that Ω and the neural network approach are somewhat complementary: apparently the "scintillator information" is contained in the lower frequency components, and the "particle information" in

Pre-selection

$E_{\text{vis}} > 0.4$ MeV
$\Delta T_{\text{muon}} > 1$ ms
$T_{\text{rms}} < 36$ ns $\vee$ $Q_{\text{rms}} < 464 - 8\,T_{\text{rms}}$
$Q_{\text{max}}/Q_{\text{tot}} < 0.09$
$Q_{\text{diff}} < 30000$ DUQ

Prompt event

$E_{\text{prompt}} \in [0.5, 12.2]$ MeV

Delayed event

$E_{\text{delayed}} \in [1.8, 2.6]$ MeV
$\Delta T \in [0.5, 600]$ μs
$\Delta R < 600$ mm between prompt and delayed events

Purity

No valid triggers in the 600 μs before the prompt event.
No valid triggers in the 900 μs after the prompt event,
except for the delayed candidate.
$\Omega > 1$

Table 10.3: Selection criteria for the Hydrogen candidates, which were used to evaluate the performance of the neural network.

higher frequency components. This opens the possibility to use the network filter, although only trained with Target data, on Gamma Catcher events too.

This increases the applicability of the Fourier network dramatically. The Hydrogen analysis suffers from a much larger background content than the Gadolinium analysis and an effective background filter is an extremely useful analysis tool. This possibility was not clear from the beginning. If instead the lower frequency components had a decisive role for the network output, this would not work.

10.6 THE NEURAL NET ON HYDROGEN CANDIDATES

The network's performance was tested on antineutrino candidates from a Hydrogen selection. The Hydrogen candidates provide an independent sample to the Gadolinium training set. Due to the small energy of the delayed event and the longer coincidence time window the candidate sample has a large background contamination. The selection criteria used here are summarized in Table 10.3 and is based on [21] with some changes. The present selection aims to reduce light noise (in the pre-selection) and stopping muon background (with the functional value cut). As shown in the previous section, the network should also work with
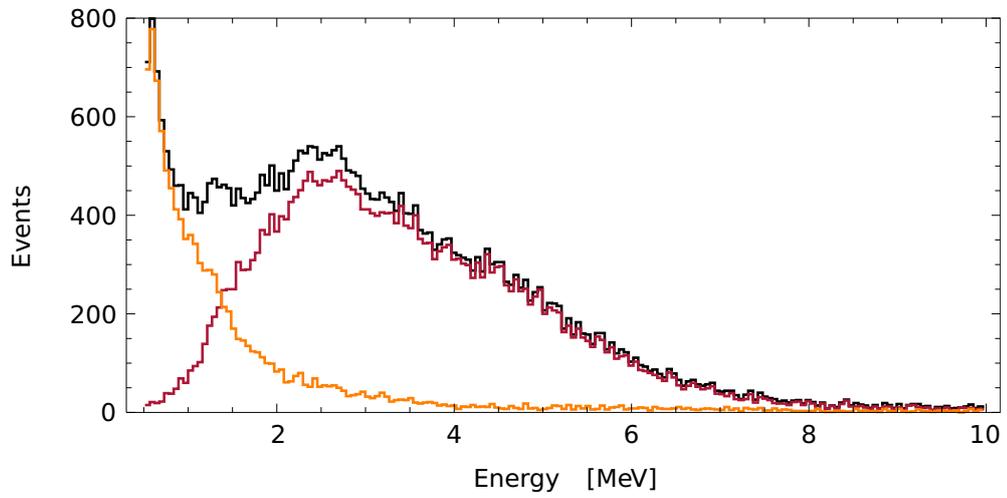
Figure 10.4: Energy spectrum of Hydrogen events processed with the network filter.
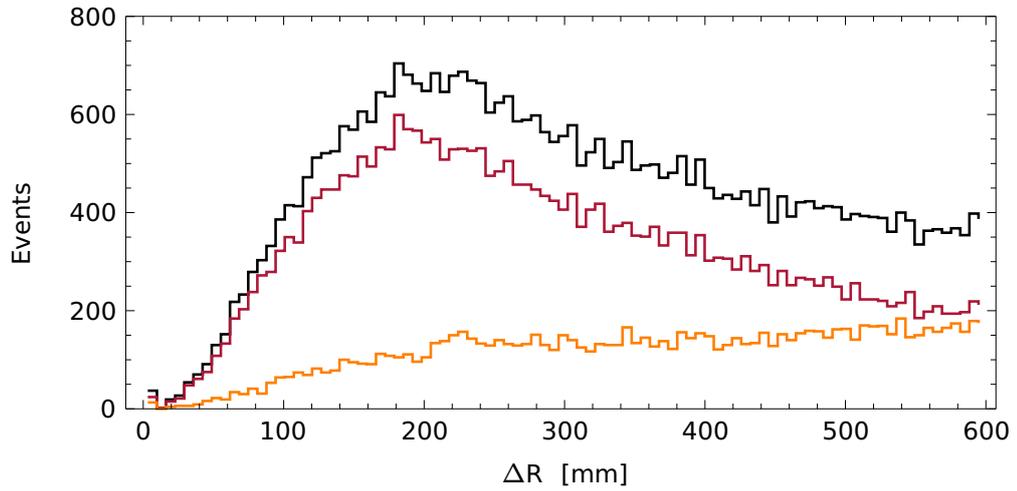
Figure 10.5: ΔR spectrum of Hydrogen events processed with the network filter.
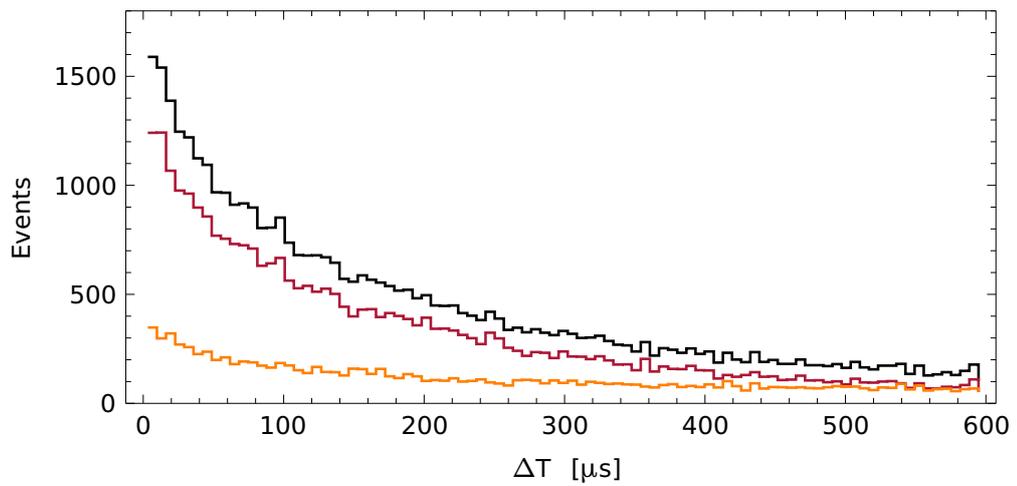
Figure 10.6: ΔT spectrum of Hydrogen events processed with the network filter.

Gamma Catcher events and we do not have to restrict the selection to the Target volume here.

The selected prompt events (the antineutrino candidates) are processed with the network filter. Events are considered positron-like if the decision is greater than 0.5 and as electron-like in the other case. Figures 10.4 to 10.6 show the performance of the filter. The black lines are the events selected according to Table 10.3, red lines show the remaining events after the filter and orange lines are rejected events. The results are explained in the following.

10.6.1 The energy spectrum

A first glance at the energy spectrum in Figure 10.4 already exhibits remarkable properties of the Fourier network filter. While the unprocessed energy spectrum is clearly contaminated with background (seen especially below 2 MeV), the spectrum of the remaining events is already very similar to the expected shape of a pure antineutrino spectrum. Especially above 3 MeV, where the spectrum is already rather clean, the shape is very well preserved. At lower energies there are some deviations from a pure reactor neutrino spectrum, which may be due to remaining accidentals or distortions induced by the filter. This is investigated in more detail in the next section.

The energy distribution goes towards zero at around 1 MeV, as it would be expected by the IBD spectrum (due to the 1 MeV energy deposition of the annihilation gammas). This is an outstanding result, considering that the network was only trained with events between 4 and 6 MeV and has no direct access to energy information. The power spectrum, which was used as the input, was calculated from the normalized sum pulse. Information about the energy would be contained in the integral over the signal, but due to the normalization step it is equal for all energies. So the decision can be only based on the spectral coefficients, i.e. the shape of the pulse. This is a strong indication that the network was in fact trained to be sensitive to relevant pulse shape features in the Fourier spectrum.

10.6.2 ΔR-distribution

Not only the energy spectrum indicates that the network is indeed sensitive to positron characteristics. The ΔR- and ΔT-spectra, i.e. the distribution of the spatial distances and time differences between prompt and delayed events, give information about the correlation of the two events. As the network was never exposed to the delayed events, these spectra are a very good benchmark for the network performance.

In the process of thermalization the IBD neutron can move away from the vertex of neutrino interaction, but it is expected to be captured rather close to the place of its origin. Typical neutron migration distances are about 20 cm. The

ΔR-distribution is displayed in Figure 10.5, where the neutron captures can be seen as a bump at about 20 cm. After the network filter is applied, the bump is more pronounced than before. The number of rejected events increases instead with the distance, as it is expected for accidental events. Around 20 cm a very small bump is also visible in the spectrum of rejected events, which could be due to inefficiencies of the network, or to correlated background events like ^{9}Li, where ΔR is given by the neutron capture, but the prompt event is an electron.

One has to keep in mind that the network only has access to the Fourier components of the *prompt* events. If the network somehow made its decision depending on the event energy, it could not improve the ΔR-spectrum of the coincidence. This can therefore be regarded as a very strong indication that the network indeed distinguishes between particle types.

10.6.3 ΔT-distribution

The situation is similar for the time differences between prompt and delayed events. Accidental coincidences show a flat ΔT-distribution, while correlated events follow an exponential distribution with a time constant determined by the neutron thermalization and capture time.

Figure 10.6 shows the ΔT distribution before and after application of the Fourier network filter. It is clearly seen that the events that passed the neural net essentially follow the same exponential shape as the unselected events, while the rejected events display a rather flat shape. Between 500 and 600 µs, where the distribution is dominated by background, the network removes about half of the events, which gives an idea of the purity of the filter.

Together with the other two distributions it can now be concluded with reasonable certainty that the network is indeed able to separate electron and positron events by their pulse shapes. Furthermore it appears that the efficiency for positrons is high.

10.6.4 Positronium

Other approaches for electron/positron discriminations are studied which make use of the formation of positronium in the scintillator, as mentioned in Section 10.1. This raises the question if the network is sensitive to positronium formation rather than to positron events in general. This was qualitatively tested with a sample of tagged positronium events within the Gadolinium analysis, which was kindly provided to me by C. Jollet and A. Minotti.[98] When the network is used with these events, no significant difference was found in the performance of the neural network, as compared to the complete set of Gadolinum events or just the non-tagged events. It can be concluded that the filter is not sensitive to positronium formation. This also indicates that the network triggers more on the three-point

structure of the positronium energy deposition rather than on time differences between the positron and the annihilation gamma signals.

Furthermore, the positronium formation rate is too low (40 to 60 %)[99] to explain the observed high efficiency of the network on Hydrogen candidates. From Figures 10.4 to 10.6 the efficiency for positrons is estimated to be above 90 %.

10.7 ENERGY DEPENDENCE

Even though the network shows a remarkable performance, the energy dependence is a special concern. Since Double Chooz performs a rate+shape analysis, distortions of the energy spectrum would be fatal if they are not accounted for. For this reason the energy dependence of the network filter has to be investigated. It was already seen in Figure 10.4 that the filtered energy spectrum shows some deviations in respect to the expected shape.

The pulse shape differences between electrons and positrons comes from the two annihilation gammas. They always create two additional energy depositions of 511 keV each, regardless of the kinetic energy of the positron. In high energy events the positron creates the highest energy deposition, while the two gammas only give small signals in comparison. In the other case, at small positron energies, the gammas are responsible for the major part of the deposited energy. This causes variations of the positron signature in the pulse shapes and may lead to an overall energy dependence of the network's decision.

This is checked with the two training samples from Section 10.4 again. It shall be noted that the energy window from 4 to 7 MeV was (partially) used for network training, so these ranges are not independent from the network structure and must be excluded from all considerations.

Figure 10.7 shows the performance of the network on the Gadolinium events in the Target. The sample is very clean and essentially all events are IBD positrons. Even so, the network rejects a sizable amount of events and its efficiency has a rather strong dependence on the energy. Especially around 1.5 the network removes more events in proportion. This causes a severe distortion of the shape of the energy spectrum and would be unacceptable for the rate+shape analysis.

The performance on the ^{12}B electron sample is displayed in Figure 10.8. Again, the shape of the energy spectrum is distorted visibly by the network. The β^--spectrum of ^{12}B should extend down to zero and have a maximum around 7 MeV. Instead, the filtered spectrum has a maximum around 9 MeV.

10.7.1 *Network training with two energy ranges*

The energy dependence of the network's decision is not acceptable for the rate+shape analysis and must be eliminated. As mentioned above, the energy dependence is probably caused by the varying signature of positron events with the event energy. During training the network only had access to electron and positron
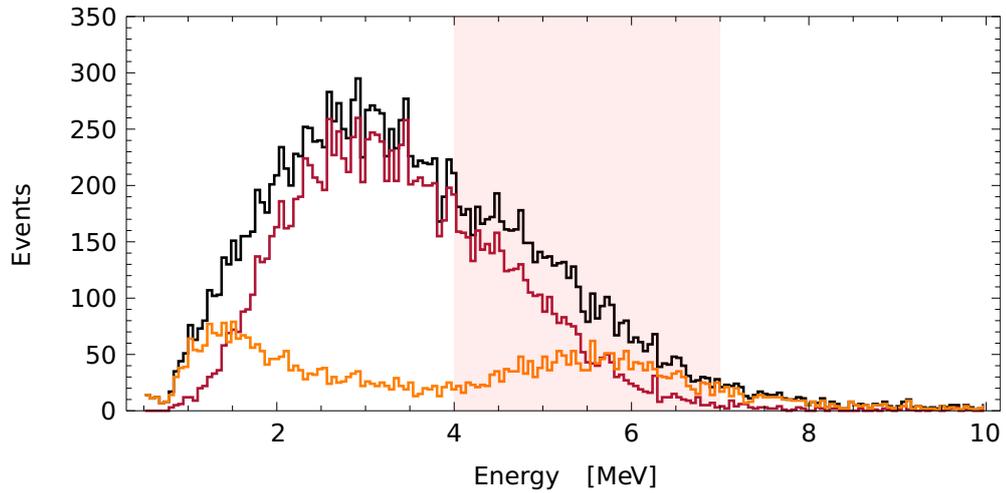
Figure 10.7: Energy spectrum of Gadolinium events processed with the network filter. It is observed that the spectral shape is visibly distorted after application of the network filter (red). The energy dependence of the selection efficiency is seen even more clearly in the rejected events (orange). The energy ranges $E \in [4, 7]$ MeV was already used for network training and may not be included for an interpretation of the results.
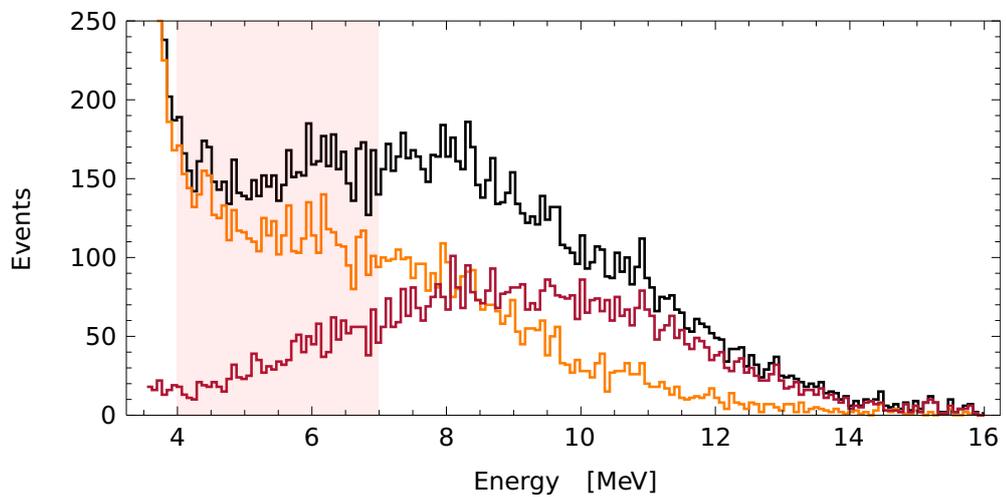
Figure 10.8: Energy spectrum of ^{12}B events processed with the network filter. This graphic is equivalent to Figure 10.7 for ^{12}B.

Pre-selection	
	$\Delta T_{\mathrm{muon}} > 1$ ms
	$T_{\mathrm{rms}} < 40$ ns
	$Q_{\mathrm{max}}/Q_{\mathrm{tot}} < 0.09$
Prompt event	
	$E_{\mathrm{prompt}} \in [1.5, 2.0]$ MeV
Delayed event	
	$E_{\mathrm{delayed}} \in [0.35, 1.2]$ MeV
	$\Delta T \in [0.5, 5.0]$ μs
Purity	
	$\Delta R < 500$ mm

Table 10.4: Selection criteria for the electron candidates from BiPo events.

events between 4 and 7 MeV. It could not learn the signature of low-energy events, where the annihilation gammas play a more decisive role.

Consequently, the idea to reduce the energy dependence of the network is to train it with electrons and positrons of lower energies too, in addition to e^+ and e^- between 4 and 7 MeV. Low-energy positrons can be readily obtained from the Gadolinium selection as in Table 10.1, but the ^{12}B sample cannot be used any more, due to its high background contamination below 4 MeV. Instead, a low-energy electron sample is created from Bismuth-Polonium events (BiPo events).

Electrons from BiPo events are predominantly encountered in the Target and are just in the right energy range. ^{212}Bi is an isotope of the Thorium decay chain and is created when Radon entered the detector. It decays after a half-life of about 60 minutes via β^--decay, giving a prompt event. The daughter nucleus ^{212}Po then produces a delayed event when it emits an alpha particle after a half-life of about 299 ns. The very short coincidence time produces a very clean sample. The prompt electrons with $E \in [1.5, 2.0]$ MeV are taken for network training. The selection of BiPo-events is based on [100] and summarized in Table 10.4.

With these samples the network is trained again as in Section 10.4.4. The training set now consists of 4000 events:

- 1000 positrons from the Gadolinium selection with $E \in [4.0, 7.0]$ MeV
- 1000 positrons from the Gadolinium selection with $E \in [1.5, 2.0]$ MeV
- 1000 electrons from the ^{12}B selection with $E \in [4.0, 7.0]$ MeV
- 1000 electrons from the ^{212}BiPo selection with $E \in [1.5, 2.0]$ MeV
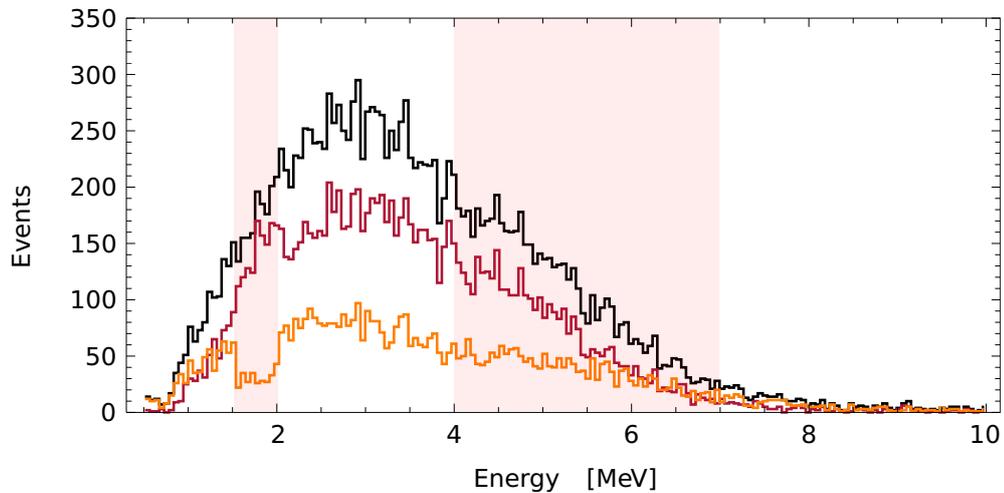
Figure 10.9: Energy spectrum of the events selected with the Gadolinum cuts before and after application of the improved network. The energy dependence of the selection efficiency is greatly reduced, as it can be seen by the fact that the spectra of the unselected (black), accepted (red), and rejected (orange) events have very similar shapes. The energy ranges $E \in [1.5, 2]$ MeV and $E \in [4, 7]$ MeV have been used for network training and may not be included in an interpretation.

The resulting network filter is tested on the energy spectrum of the Gadolinium sample again. The results are shown in Figure 10.9. Again, the energy ranges used for training have to be excluded from an interpretation, as they are not independent. It is now seen that the strong energy dependence of the network decision as in Figure 10.7 is mostly gone. Over the whole energy range the proportion of rejected events is now constant, indicating an energy-independent behavior of the neural net. An exception is the region between 0.5 and 1 MeV, where nearly all events are rejected. At such low energies the positron nearly does not carry any kinetic energy any more and the energy deposition comes only from the two gammas. It might be that without the positron signal the two annihilation gammas are mistaken for ordinary background gammas. However, the inefficiency at such low energies may be compensated in the future by other PID approaches.

In exchange for the energy independence the overall positron efficiency is now decreased compared to Figure 10.7.

10.7.2 *The improved network on Hydrogen candidates*

Now the improved network is applied again on the antineutrino candidates from the Hydrogen selection. The results are shown in Figures 10.10 to 10.12. As before, the black lines are the selected Hydrogen events before the filter, the red and orange curves show the accepted and rejected events respectively. The spectra are very similar to the results before the improvement of the neural network

(Figures 10.4 to 10.6). The number of rejected events is now slightly smaller than before, which could mean that the purity is now lower or the efficiency is higher. The most important difference is seen in the shape of the energy spectrum in Figure 10.10: even though the change is small, the left flank of the accepted spectrum between 0.5 and 2.5 MeV is now "rounder" and is more consistent with the accepted shape of the IBD spectrum plus low-energy background.

The results are more surprising due to another reason. In Figure 10.7 the efficiency was visibly decreased after the training with two energy ranges, but this cannot be seen in the Hydrogen samples. This may be a hint that the network's efficiency is not the same in the Target and the Gamma Catcher. It was stated before that the information whether the event took place in the Target or the Gamma Catcher is encoded in the first 20 Fourier components. And even though it was found in Section 10.5 that they only have little importance, they are not completely negligible.

That the Target and Gamma Catcher are not treated exactly equal is also seen at another point. If a volume cut is applied to the rejected events in Figure 10.6, it is observed that the exponential part of the slope between 0 and 80 µs vanishes almost completely when only the Gamma Catcher is selected. This is, the rejected correlated events are predominantly from the Target volume.

10.8   SUMMARY

The artificial neural network was found to be sensitive to the faint differences between electron and positron pulse shapes and can successfully extract the relevant information from the Fourier power spectrum. With the network an efficient discrimination between electrons and positrons was achieved, as it was seen by the distributions of ΔT and ΔR, as well as by the energy spectrum of the events from a Hydrogen selection. This way the network was able to reject a large part of the background in the Hydrogen analysis, but kept most of the IBD candidates. This is the first time that a reliable e^+/e^--discrimination is achieved in a large-scale scintillation detector, which does not rely on positronium formation. This result can be extremely valuable for Double Chooz (in particular for the Hydrogen selection with a rather large background content) and other scintillator-based neutrino experiments.

The exact efficiency and purity of the filter remains to be determined, which will be an important task for the future. The energy dependence of the network's decision was already investigated and could be significantly reduced by a careful training with samples in different energy ranges. Nevertheless, a certain energy dependence may still be present and has to be studied. An exact determination of the efficiency may prove difficult, as there is no calibration source for positrons
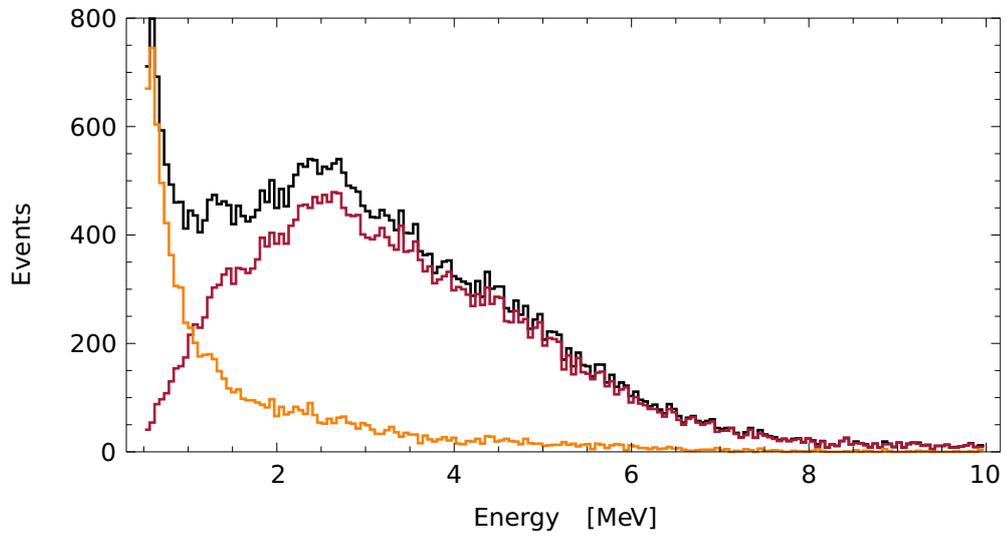
Figure 10.10: Energy spectrum of Hydrogen events processed with the improved network filter.
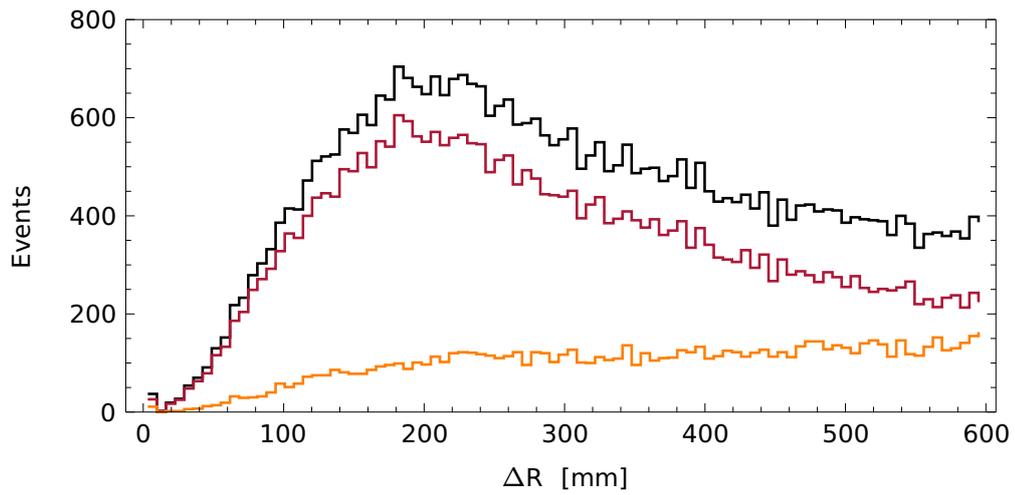
Figure 10.11: ΔR spectrum of Hydrogen events processed with the improved network filter.
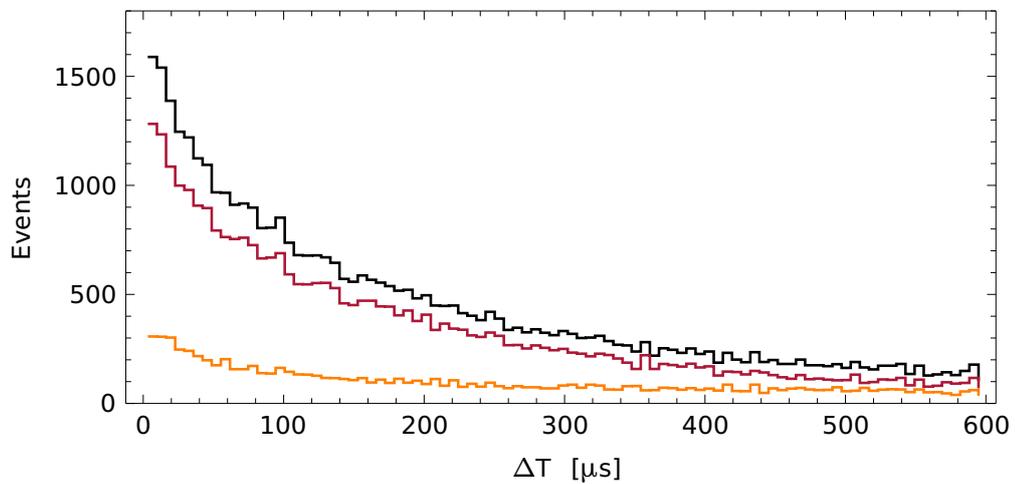
Figure 10.12: ΔT spectrum of Hydrogen events processed with the improved network filter.

yet available. The Monte Carlo is not suited for this task due to an insufficient precision of the scintillator pulse shapes.

SUMMARY

This thesis described the properties of the liquid scintillators in Double Chooz and their impact on the analysis of detector data. The design, composition and large-scale production of the Double Chooz scintillators were presented and their properties were investigated. A special importance was given to the non-linearity of the scintillator response with the energy. These are caused mainly by ionization quenching, which reduces the light output at low particle energies, and the emission of Čerenkov light, which causes an additional contribution at higher energies.

As Double Chooz includes the shape of the spectral distribution of the IBD events into the analysis of θ_{13}, the energy non-linearity has to be modeled precisely in the Monte Carlo so that it recreates the behavior of the real scintillator. The remaining discrepancies between the data and the Monte Carlo create an uncertainty of the shape of the IBD spectrum and should be kept as small as possible, as they directly influences the error of θ_{13}.

For this reason, the experimental part of this thesis was concerned with a refinement of the optical model, in order to further reduce uncertainty on the energy non-linearity. Various optical properties of the scintillator mixtures and the single components were studied. The molar extinction coefficients of the scintillator components were determined with UV/Vis spectrometry. The relative reemission probabilities were experimentally determined for the mixtures as well as the components. Their absolute values, however, depend on the quantum yields of the fluors. This triggered a series of experiments to determine the quantum yields of PPO and bis-MSB amongst other substances. Despite numerous sources of systematic errors, the quantum yields could be measured with good accuracy.

The implementation of the measured quantities in the Monte Carlo required a substantial modification of the source code. The effects of the changes were studied in a dedicated simulation campaign. The influence of the individual parameters on the energy non-linearity was presented, which may prove valuable for a future modification of the optical model.

In addition, I developed a theoretical model for ionization quenching. It relates the behavior of ionization quenching to a single parameter R, which (in contrast to Birks' quenching parameter kB) has a physical representation as the

distance between two excited molecules. An expression for the mean total light yield $\langle L \rangle$ for electrons is given. For practical use it can often be used more conveniently than Birks' formula for the mean differential light yield $\langle \mathrm{d}L/\mathrm{d}x \rangle$ and can be fitted directly to experimental data. Furthermore, it is predicted that the same parameter R can be used regardless of the incident particle. This way, the scintillation light output of protons and alpha particles could be derived from the measurement with electrons. This would be especially important for protons, for which no experimental data is available yet. However, this could not yet be confirmed experimentally, since no suitable cross section data for alpha particles was available.

The data analysis started with a separation of light noise events from physics. For this purpose I developed a novel clustering algorithm, which is able to process clusters with varying internal density, as it is often the case with experimental data. This is an improvement over established clustering techniques, which often have difficulties in such situations. The algorithm was then used to identify physics data in a two-dimensional parameter space and to create a non-linear classifier to reject light noise events. It has higher efficiency and purity as typical one-dimensional threshold cuts. The clustering technique was also used later for an optimization of the classifier Ω.

The classification variable Ω is built from the Fourier power spectrum of the scintillation pulses. The variable is a measure for the pulse shape of an event and can be used to distinguish between different event classes. It is able to cleanly separate Gamma Catcher and Target events via their different pulse shapes, which was previously not possible in Double Chooz. Moreover, typical light noise events can be cleanly separated from physics events with a simple threshold on Ω. This offers a novel method to reject remaining light noise in Double Chooz. It was also shown that the variable can be used to identify stopping muons. This may prove especially important, since stopping muons are a correlated background in the experiment.

In the end I developed a particle identification technique to separate electrons and positrons in detector data via their pulse shapes. It employs an artificial neural network, which is used to discover non-linear patterns in the Fourier power spectrum, which indicate the nature of the particle. Since IBD events are practically the only class of events which involve positrons, such a method may be used to reduce backgrounds, including the correlated cosmogenic backgrounds ^{9}Li and ^{8}He, which are otherwise hard to reject. First tests showed that the network is indeed able to remove a substantial amount of background, while it has a high efficiency for positrons. The network was then tuned such that its decision is mostly independent of the event energy. I also presented a model why the neural network technique in the Fourier domain may be better suited for PSD than similar methods in the time domain.

To my knowledge this is the first working electron-positron discrimination in a large-scale scintillation detector without relying on positronium formation. The technique is applicable to a series of other neutrino experiments and it is expected to "meet a general interest in the neutrino community."[101]

Bibliography

Where possible, ISB numbers, digital preprint references and/or DOI codes are given in order to facilitate access to the publications.

[1] Y. Abe *et al.* (Double Chooz collaboration): *Reactor $\bar{\nu}_e$ disappearance in the Double Chooz experiment*, Phys. Rev. D **86** 5, p. 052008 (2012) DOI: 10.1103/PhysRevD.86.052008 [arXiv:1207.6632]

[2] J. Beringer *et al.* (Particle Data Group), *2013 Review of Particle Physics*, Phys. Rev. D **86**, p. 010001 (2012) and 2013 partial update for the 2014 edition [http://pdg.lbl.gov]

[3] M. Apollonio *et al.* (CHOOZ collaboration): *Limits on neutrino oscillations from the Chooz experiment*, Phys. Lett. B **466** 2–4, p. 415 (1999) DOI: 10.1016/S0370-2693(99)01072-2 [arXiv:hep-ex/9907037]

[4] Y. Abe *et al.* (Double Chooz collaboration): *Indication of reactor $\bar{\nu}_e$ disappearance in the Double Chooz experiment*, Phys. Rev. Lett. **108** 13, p. 131801 (2012) DOI: 10.1103/PhysRevLett.108.131801 [arXiv:1112.6353]

[5] F.P. An *et al.* (Daya Bay collaboration): *Observation of electron-antineutrino disappearance at Daya Bay*, Phys. Rev. Lett. **108**, p. 171803 (2012) DOI: 10.1103/PhysRevLett.108.171803 [arXiv:1203.1669]

[6] J.K. Ahn *et al.* (RENO collaboration): *Observation of Reactor Electron Antineutrino Disappearance in the Reno Experiment* (2012) [arXiv:1204.0626]

[7] A. Gando *et al.* (KamLAND collaboration): *Constraints on θ_{13} from a three-flavor oscillation analysis of reactor antineutrinos at KamLAND*, Phys. Rev. D **83**, p. 052002 (2011) DOI: 10.1103/PhysRevD.83.052002, [arXiv:1009.4771]

[8] K. Abe *et al.* (Super-Kamiokande collaboration): *Search for differences in oscillation parameters for atmospheric neutrinos and antineutrinos at Super-Kamiokande*, Phys. Rev. Lett. **107**, p. 241801 (2011) DOI: 10.1103/PhysRevLett.107.241801 [arXiv:1109.1621]

[9] M. Agostini *et al.* (GERDA collaboration): *Results on neutrinoless double beta decay of ^{76}Ge from Gerda phase I*, Phys. Rev. Lett. **111**, p. 122503 (2013) DOI: 10.1103/PhysRevLett.111.122503 [arXiv:1307.4720]

[10] C. Kraus *et al.* (Mainz collaboration): *Final results from phase II of the Mainz neutrino mass search in tritium beta decay*, Eur. Phys. J. C **40** 4, p. 447-468 (2005) DOI: 10.1140/EPJC/S2005-02139-7 [arXiv:hep-ex/0412056]

[11] V.N. Aseev et al (Troitsk collaboration): *Upper limit on the electron antineutrino mass from the Troitsk experiment*, Phys. Rev. D **84** 11, p. 112003 (2011) DOI: 10.1103/PhysRevD.84.112003 [arXiv:1108.5034]

[12] A. Osipowicz *et al.* (KATRIN collaboration): *Katrin: A next generation tritium beta decay experiment with sub-eV sensitivity for the electron neutrino mass* (2001) [arXiv:hep-ex/0109033]

[13] F.X. Hartmann, R.A. Naumann: *Observation of N and M orbital electron capture in the decay of ^{163}Ho*, Phys. Rev. C **31** 4, p. 1594 (1985) DOI: 10.1103/PhysRevC.31.1594

[14] A. Nucciotti *et al.* (MARE collaboration): *Neutrino mass calorimetric searches in the Mare experiment*, (2010) [arXiv:1012.2290]

[15] L. Gastaldo *et al.* (ECHO collaboration): *The electron capture ^{163}Ho experiment Echo: an overview*, contribution to the LTD15 conference proceedings (2013) [arXiv:1309.5214]

[16] T.A. Mueller, D. Lhuillier, M. Fallot *et al.*: *Improved predictions of reactor antineutrino spectra*, Phys. Rev. C **83**, p. 054615 (2011) DOI: 10.1103/PhysRevC.83.054615 [arXiv:1101.2663]

[17] G. Mention, M. Fechner, T. Lasserre *et al.*: *The reactor neutrino anomaly*, Phys. Rev. D **83**, p. 073006 (2011) DOI: 10.1103/PhysRevD.83.073006 [arXiv:1101.2755]

[18] D. Benchekroun *et al.* (STEREO collaboration): *Proposal of a search for sterile neutrinos at ILL: the Stereo experiment*, (2012) [http://ruphe.fsac.ac.ma/Neutrino_ILL_experiment/STEREO/Stereo_Proposal.pdf]

[19] P. Adamson *et al.* (MINOS collaboration): *Measurement of the neutrino mass splitting and flavor mixing by Minos*, Phys. Rev. Lett. **106** 18, p. 181801 (2011) DOI: 10.1103/PhysRevLett.106.181801 [arXiv:1103.0340]

[20] F. Ardellier *et al.* (Double Chooz collaboration): *Double Chooz, A search for the neutrino mixing angle θ_{13}* (2006) [arXiv:hep-ex/0606025]

[21] Y. Abe *et al.* (Double Chooz collaboration): *First measurement of θ_{13} from delayed neutron capture on Hydrogen in the Double Chooz experiment*, Phys. Lett. B **723** 1–3, p. 66 (2013) DOI: 10.1016/J.PhysLetB.2013.04.050, [arXiv:1301.2948]

[22] Y. Abe *et al.* (Double Chooz collaboration): *Background-independent measurement of θ_{13} in Double Chooz* (2014) [arXiv:1401.5981]

[23] Y. Abe *et al.* (Double Chooz collaboration): *Direct measurement of backgrounds using reactor-off data in Double Chooz*, Phys. Rev. D **87**, p. 011102 (2012) DOI: 10.1103/PhysRevD.87.011102 [arXiv:1210.3748]

[24] G.L. Fogli, E. Lisi, A. Marrone, D. Montanino, A. Palazzo: *Getting the most from the statistical analysis of solar neutrino oscillations*, Phys. Rev. D **66** 5, p. 053010 (2002) DOI: 10.1103/PhysRevD.66.053010 [arXiv:hep-ph/0206162]

[25] E. Conover: *The ^9Li likelihood veto*, Double Chooz internal note **5160** (2013)

[26] A. Cabrera, L.F. Gomez Gonzalez: *Fine tuning the functional value cut*, Double Chooz internal note **5041** (2013)

[27] F. Kaether, B. Gramlich, R. Hofacker, K. Jänner, S. Wagner: *PMT glowing studies at MPIK*, Double Chooz internal note **2282** (2011)

[28] E. Calvo, M. Cerrada, J.I. Crespo, I. Gil-Botella, S. Jiménez, M. López, P. Novella, C. Palomares, R. Santorelli, A. Verdugo: *Light production in the Double Chooz PMTs*, Double Chooz internal note **3224**

[29] J.B. Birks: *Photophysics of aromatic molecules*, John Wiley & Sons (1970) ISBN: 978-0471074205

[30] J.B. Birks: *The theory and practice of scintillation counting*, Pergamon Press (1964) ISBN: 978-1483123646

[31] C.T. Peng, D.L. Horrocks (eds.): *Liquid scintillator solvents*, Academic Press (1970)

[32] F.H. Brown, M. Furst, H. Kallmann: *Light and high energy induced energy transfer in liquid and rigid organic scintillators*, Discuss. Faraday Soc. **27**, p. 43 (1959) DOI: 10.1039/DF9592700043

[33] D.L. Andrews: *A unified theory of radiative and radiationless molecular energy transfer*, Chem. Phys. **135** 2, p. 195 (1982) DOI: 10.1016/0301-0104(89)87019-3

[34] F. Rohrlich, B.C. Carlson : *Positron-electron differences in energy loss and multiple scattering*, Phys. Rev., **93** 1, p. 38 (1954) DOI: 10.1103/PhysRev.93.38

[35] C. Aberle: *Optimization, simulation and analysis of the scintillation signals in the Double Chooz experiment*, PhD thesis, Heidelberg University (2011)

[36] C. Buck, F.X. Hartmann, S.Schönert, U. Schwan: *An optically pure Gd-β-diketonate for the liquid scintillator of anti-neutrino detectors*, article in preparation

[37] C. Aberle, C. Buck, B. Gramlich, F.X. Hartmann, M. Lindner, S. Schönert, U. Schwan, S. Wagner, H. Watanabe: *Large scale Gd-beta-diketonate based organic liquid scintillator production for antineutrino detection*, J. Inst. **7** 6,

p. 06008 (2012) DOI: 10.1088/1748-0221/7/06/P06008
[arXiv:1112.5941]

[38] C. Aberle, C. Buck, F.X. Hartmann, S. Schönert: *Light yield and energy transfer in a new Gd-loaded liquid scintillator*, Chem. Phys. Lett. **516** 4–6, p. 257 (2011) DOI: 10.1016/J.CPLett.2011.09.067

[39] H.O. Back *et al.* (Borexino collaboration): *Study of phenylxylylethane (PXE) as scintillator for low energy neutrino experiments*, Nucl. Instrum. Meth. A **585** 1–2, p. 48 (2008) DOI: 10.1016/J.NimA.2007.10.045
[arXiv:physics/0408032]

[40] K. Eguchi *et al.* (KamLAND collaboration): *First results from KamLAND: evidence for reactor antineutrino disappearance*, Phys. Rev. Lett. **90**, p. 021802 (2003) DOI: 10.1103/PhysRevLett.90.021802 [arXiv:hep-ex/0212021]

[41] F. Boehm *et al.* (Palo Verde collaboration): *Final results from the Palo Verde neutrino experiment*, Phys. Rev. D **64** 11 (2001) DOI: 10.1103/PhysRevD.64.112001 [arXiv:hep-ex/0107009]

[42] C. Buck, F.X. Hartmann, S. Schönert, U. Schwan: *Development of an optically pure In-β-diketonate for the scintillator of an ^{115}In-loaded solar neutrino detector*, J. Radioanal. Nucl. Ch. **258** 2, p. 255 (2003) DOI: 10.1023/A:1026273318339

[43] F.X. Hartmann: *Double Chooz and the search for short range electron antineutrino oscillations*, in: *Proceedings of the Carolina International Symposium on Neutrino Physics*, J. Phys.: Conf. Ser. 173, p. 012023 (2009) DOI: 10.1088/1742-6596/173/1/012023

[44] J.E. Sicre, J.T. Dubois, K.J. Eisentraut, R.E. Sievers: *Volatile lanthanide chelates. II. Vapor Pressures, heats of vaporization, and heats of sublimation*, J. Am. Chem. Soc. **91** 13, p. 3476 (1969) DOI: 10.1021/JA01041A011

[45] M. Apollonio *et al.* (Chooz collaboration): *Search for neutrino oscillations on a long base-line at the Chooz nuclear power station*, Eur. Phys. J. C **27**, p. 331 (2003) DOI: 10.1140/EPJC/S2002-01127-9 [arXiv:hep-ex/0301017]

[46] D. Motta: *Discussion about the Scintillation Primary Spectrum*, Double Chooz internal note (2008)

[47] n-Dodecane data sheet, Japan Energy

[48] R. Queval: *Characterization, modelization and optimization of the Double Chooz acrylic vessels: Physics impact*, PhD thesis, Paris 7 (2010)

[49] C. Buck, B. Reinhold: *Proton numbers in the Double Chooz detector*, Double Chooz internal note **4211** (2012)

[50] J.B. Birks: *Scintillations from organic crystals: Specific fluorescence and relative response to different radiations*, Proc. Phys. Soc. A, **64** 10, p. 874 (1951) DOI: 10.1088/0370-1298/64/10/303

[51] A. Ferrari, P.R. Sala, A. Fasso, J.Ranft: *Fluka: a multi-particle transport code*, CERN-2005-10 (2005), INFN/TC_05/11, SLAC-R-773

[52] C.N. Chou: *The nature of the saturation effect of fluorescent scintillators*, Phys. Rev., **87** 5, p. 904 (1952) DOI: 10.1103/PhysRev.87.904

[53] R. Voltz, G. Laustriat: *Radioluminescence des milieux organiques. I. Étude cinétique*, J. Phys. France, **29** 2–3, p. 159 (1968) DOI: 10.1051/JPhys:01968002902-3015900

[54] R. Voltz, H. Dupont, G. Laustriat: *Radioluminescence des milieux organiques. II. Vérification expérimentale de l'étude cinétique*, J. Phys. France, **29** 4, p. 297 (1968) DOI: 10.1051/JPhys:01968002904029700

[55] C. Møller: *Zur Theorie des Durchgangs schneller Elektronen durch Materie*, Ann. Phys., **406** 5, p. 531 (1932) DOI: 10.1002/AndP.19324060506

[56] S.M. Seltzer, M.J. Berger: *Evaluation of the collision stopping power of elements and compounds for electrons and positrons*, Int. J. Appl. Rad. Isot., **33** 11, p. 1189 (1982) DOI: 10.1016/0020-708X(82)90244-7

[57] C. Aberle, C. Buck, F.X. Hartmann, S. Schönert, S. Wagner: *Light output of Double Chooz scintillators for low energy electrons*, J. Inst. **6** 11, p. 11006 (2011) DOI: 10.1088/1748-0221/6/11/P11006

[58] S. Wagner: *Ionization quenching by low energy electrons in the Double Chooz scintillators*, diploma thesis, Heidelberg University (2010)

[59] M.J. Berger, J.S. Coursey, M.A. Zucker, J. Chang: *Stopping power and range tables for electrons, protons, and helium Ions*, NIST (2011) [http://www.nist.gov/pml/data/star/index.cfm]

[60] M.G. Pia, G. Weidenspointner, M. Augelli, L. Quintieri, P. Saracco, M. Sudhakar, A. Zoglauer, *PIXE simulation with Geant4*, IEEE Trans. Nucl. Sci. **56** 6, p. 3614 (2009) [http://www.ge.infn.it/geant4/physics/pixe/datalib.html]

[61] F.P. An *et al.* (Daya Bay collaboration): *Spectral measurement of electron antineutrino oscillation amplitude and frequency at Daya Bay* Phys. Rev. Lett. **112**, p. 061801 (2014) DOI: 10.1103/PhysRevLett.112.061801 [arXiv:1310.6732]

[62] C. Buck: *Development of metal loaded scintillators for future detectors to investigate neutrino properties*, PhD thesis, Heidelberg University (2004)

[63] D. Motta: *Study of the systematics affecting the spectro-photometric determination of the attenuation lengths due to the wavelength dependence of the refractive index*, Double Chooz internal note (2006)

[64] I.B. Berlman: *Handbook of fluorescence spectra of aromatic molecules*, 2nd ed., Academic Press, New York (1971)

[65] H.L. Xiao, L. Xiao-Bo, Z. Dong, C. Jun, W. Liang-Jian, W. Nai-Yan: *Study of absorption and re-emission process in a ternary liquid scintillation system*, Chinese Phys. C **34** 11, p. 1724 (2010) DOI: 10.1088/1674-1137/34/11/011

[66] W.H. Melhuish: *Quantum efficiencies of fluorescence of organic substances: Effect of solvent and concentration of the fluorescent solute*, J. Phys. Chem. **65** 2, p. 229 (1961) DOI: 10.1021/J100820A009

[67] M.C. Johnson: *Scintillator purification and study of light propagation in a large liquid scintillator detector*, PhD thesis, Princeton University (1998)

[68] J.N. Demas, G.A. Crosby: *The measurement of photoluminescence quantum yields. A review*, J. Phys. Chem. **75** 8, p. 991 (1971) DOI: 10.1021/J100678A001

[69] R.A. MacRae, M.W. Williams, E.T. Arakawa: *Optical properties of some aromatic liquids in the vacuum ultraviolet*, J. Chem. Phys. **61** 3, p. 861 (1974) DOI: 10.1063/1.1680744

[70] T. Inagaki: *Optical absorption of pure liquid benzene in the vacuum ultraviolet*, J. Chem. Phys. **59** 9, p. 5207 (1973) DOI: 10.1063/1.1680744

[71] Y. Kamyshkov: *Non-linearity of energy response in neutrino liquid scintillator detectors*, talk at *Advances in Neutrino Technology* conference, University of Hawai'i, Mānoa (2009)

[72] Y. Kamyshkov, personal communication (2012)

[73] W. von Sellmeier: *Zur Erklärung der abnormen Farbenfolge in Spectrum einiger Substanzen*, Ann. Phys. und Chem. **143**, p. 272 (1871)

[74] C. Aberle, C. Buck, B. Gramlich, M. Lindner, S. Wagner, H. Watanabe: *Study of Liquid Scintillator Properties in Double Chooz*, Verhandlungen, T 100.7, 77th Spring Conference of the German Physical Society (2013)

[75] V. Zimmer: *Measurements of proton quenching factors and PSD parameters for the DC IV scintillator*, Double Chooz internal note **4052** (2013)

[76] L. Kaufman, P.J. Rousseeuw: *Finding groups in data: An introduction to cluster analysis*, John Wiley & Sons (2008) ISBN: 9780471878766, DOI: 10.1002/9780470316801

[77] R. Roncin, T. Konno, A. Cabrera: *Light noise reduction*, Double Chooz internal note **4935** (2013)

[78] T. Konno: *Studies for reduction of remaining noise events*, Double Chooz internal note **4179** (2012)

[79] J.M. López Castaño: *Accidentals and additional light noise cuts*, Double Chooz internal note **4954** (2013)

[80] M. Ester, H.P. Kriegel, J. Sander, X. Xu: *A density-based algorithm for discovering clusters in large spatial databases with noise*, in: E. Simoudis, J. Han,

U. Fayyad (eds.): *Proceedings of the 2nd ACM International Conference on Knowledge Discovery and Data Mining (KDD)*, p. 226, AAAI Press (1996) ISBN 1-57735-004-9 [http://www.dbs.ifi.lmu.de/Publikationen/Papers/KDD-96.final.frame.pdf]

[81] M. Ankerst, M.M. Breuning, H.P. Kriegel, J. Sander: *OPTICS: Ordering Points To Identify the Clustering Structure*, in: A. Delis, C. Faloutsos, S. Ghandeharizadeh (eds.): *Proceedings of the ACM SIGMOD International Conference on Management of Data*, p. 49, ACM Press (1999) ISBN 1-58113-084-8 [http://www.dbs.ifi.lmu.de/Publikationen/Papers/OPTICS.pdf]

[82] G.F. Knoll: *Radiation detection and measurement*, 4th ed., John Wiley & Sons (1989) ISBN: 978-0-470-13148-0

[83] E. Gatti, F. de Martini: *A new linear method of discrimination between elementary particles in scintillation counters*, Proceedings of the Conference on Nuclear Electronics II, IAEA, p. 265 (1962)

[84] J. Haser: *Update on spill-in/out and late light studies*, Double Chooz internal note **3669** (2012)

[85] Y. Abe, T. Akiri, A. Cabrera *et al.*: *The waveform digitiser of the Double Chooz experiment: Performance and quantisation effects on photomultiplier tube signals*, J. Inst. **8**, p. 08015 (2013) DOI: 10.1088/1748-0221/8/08/P08015 [arXiv:1307.4917]

[86] G. Consolati, D. Franco, S. Hans, C. Jollet, A. Meregaglia, S. Perasso, A. Tonazzo, M. Yeh: *Characterization of positronium properties in doped liquid scintillators*, Phys. Rev. C **88**, p. 065502 (2013) DOI: 10.1103/PhysRevC.88.065502 [arXiv:1308.0493]

[87] G. Bellini *et al.* (Borexino collaboration): *First evidence of pep solar neutrinos by direct detection in Borexino*, Phys. Rev. Lett. **108** 5, p. 051302, (2012) DOI: 10.1103/PhysRevLett.108.051302 [arXiv:1110.3230]

[88] Y. Abe, A. Cabrera, M. Ishitsuka: *Topological e^+/e^- identification*, Double Chooz internal document **5533** (2014)

[89] C.M. Bishop: *Neural networks for pattern recognition*, Oxford University Press (1995) ISBN: 978-0198538646

[90] G.B. Orr, K.R. Müller (eds.): *Neural networks: Tricks of the trade*, Lecture Notes in Computer Science 1524, Springer (1998) ISBN: 3540653112

[91] G. Cybenko: *Approximations by superpositions of a sigmoidal function*, Math. of Contr. Sign. Syst. **2** 4, p 303 (1989) DOI: 10.1007/BF02551274

[92] A.N. Kolmogorov: *On the representation of continuous functions of many variables by superposition of continuous functions of one variable and addition*, Dokl. Akad. Nauk SSSR **144**, p. 953 (1957)

[93] W.S. Sarle: *Neural networks and statistical models*, Proceedings of the 19th Annual SAS Users Group International Conference, p. 1538 (1994)

[94] C. Igel, M. Hüsken: *Empirical evaluation of the improved Rprop learning algorithms*, J. Neurocomp. 50, p. 105 (2003) DOI: 10.1016/S0925-2312(01)00700-7

[95] B.P. Lathi: *Linear Systems and Signals*, 2nd ed., Oxford University Press (2009) ISBN: 978-0195392562

[96] C. Igel, V. Heidrich-Meisner, T. Glasmachers: *Shark*, J. Machine Learning Res. **9**, p. 993 (2008), [http://jmlr.org/papers/volume9/igel08a/igel08a.pdf]

[97] C. Aberle: ^{12}B *studies*, Double Chooz internal document **4735** (2013)

[98] C. Jollet, A. Minotti, personal communication (2013)

[99] C. Jollet, A. Meregaglia, A. Minotti, D. Franco, S. Perasso, A. Tonazzo: *Ortho-positronium formation in the Double Chooz experiment*, Double Chooz internal document **5423** (2014)

[100] M.A. Hofmann: *Liquid scintillators and liquefied rare gases for particle detectors*, PhD thesis, Technische Universität München (2012)

[101] Franco, D.: *Positronium signature in liquid and plastic scintillator*, talk at *Advances in Neutrino Technology* conference, Philadelphia (2011) [https://indico.fnal.gov/conferenceDisplay.py?confId=4887]

LIST OF FIGURES

LIST OF TABLES

Acknowledgements